CHARACTERIZATION OF MACRO-SCALE AND MESO-SCALE PERFORMANCE OF ASPHALT CONCRETE MIXTURES UNDER COMPRESSION

A Dissertation

by

AHMED MOHAMED METWALY AWED

Submitted to the Office of Graduate and Professional Studies of
Texas A&M University
in partial fulfillment of the requirements for the degree of

DOCTOR OF PHILOSOPHY

Chair of Committee,	Eyad Masad
Committee Members,	Dallas Little
	Amy Epps Martin
	Amine Benzerga
	Emad Kassem
Head of Department,	Robin Autenrieth

August 2016

Major Subject: Civil Engineering

ABSTRACT

Researchers at Texas A&M University have developed the Pavement Analysis using Nonlinear Damage Approach (PANDA) for predicting the performance of asphalt concrete mixtures. PANDA offers substantial improvements in mechanistic modeling and simulation of pavement performance over other existing approaches. However, in order to facilitate the use of PANDA, there is a need to develop a systematic approach for determining the input parameters of its constitutive models.

In this dissertation, a well-designed experimental testing protocol is developed to characterize the resistance of asphalt concrete mixtures to permanent deformation. This approach involves conducting two experimental tests in order to extract the PANDA model parameters: the dynamic modulus test (DMT) and repeated creep-recovery test at various stresses (RCRT-VS). Then, a systematic analytical approach is used to determine the linear viscoelastic, nonlinear viscoelastic, and viscoplastic PANDA model parameters for different types of asphalt mixtures and at different temperatures, air void contents, and aging levels. The analytical method employs DMT data to determine the long-term linear viscoelastic properties and time-temperature shift factors, and it employs the RCRT-VS data to determine the nonlinear viscoelastic and viscoplastic properties.

A significant part of this dissertation focuses on the implementation of the global sensitivity analysis (GSA) approach to determine the sensitivity of the asphalt mixture performance to the PANDA's input parameters. This analysis is performed in order to reduce the output uncertainty to input uncertainty, focus the experimental methods on evaluating the key parameters that influence performance, and simplify the analytical approach to extract significant model parameters from experimental data. The GSA results show that the viscoelastic nonlinearity parameter (g_2), viscoplastic hardening function parameters (k_1 and k_2), and viscoplasticity-relaxation time ($1/\Gamma^{vp}$) are the most significant and sensitive parameters.

The PANDA constitutive modeling framework is used to efficiently simulate and predict the viscoelastic and viscoplastic responses of asphalt pavements. Two different scales of asphalt mixture performance are investigated: macro-scale (full dense-graded mixture, DGM) and meso-scale (fine aggregate matrix, FAM, and coarse aggregate matrix, CAM). The computational results show that the FAM controls the viscoelastic response of asphalt mixtures, while the CAM properties primarily influence the viscoplastic response of asphalt mixtures.

DEDICATION

*To my dear **Nancy***

for her endless support, encouragement, patience, and most importantly, love

*To my lovely **Dareen***

Mercy from Allah

I am truly blessed

ACKNOWLEDGEMENTS

I am sincerely grateful to many people who helped me complete this strenuous journey. First of all, I would like to acknowledge my committee chair, Dr. Eyad Masad, for providing me with opportunities and shaping my career and for his precious guidance, constructive encouragement, and endless support throughout the course of this research. I would like to thank my advisory committee member, Dr. Dallas Little, for his valuable guidance, knowledge, encouragement, and support throughout my graduate path. I would like to express my gratitude toward my advisory committee member Dr. Emad Kassem for his continuous support, fruitful guidance, valuable insight, and priceless advice regarding this research. I would like to thank my advisory committee members Drs. Amy Epps-Martin and Amine Benzerga for their pertinent comments and their patience in reviewing my dissertation manuscript. I also would like to thank Dr. Masoud Darabi, whose expertise and advice led the Asphalt Research Consortium (ARC) team members to achieve their academic endeavors. Thanks also go to my fellow colleagues, Drs. Maryam Shakiba, Taesun You, Eisa Rahmani, Lorena Garcia Cucalon, Husam Sadek, and Mohammed Sadeq, who were supportive and very insightful. Last but not least, I gratefully acknowledge Southwest Region University Transportation Center (SWUTC), ARC through the US Federal Highway Administration (FHWA), and Qatar National Research Fund (QNRF), which provided financial support for various aspects of this research.

TABLE OF CONTENTS

Page

LIST OF FIGURES

Page

LIST OF TABLES

Page

CHAPTER I

INTRODUCTION

1.1 Background

Recent studies at Texas A&M University have led to the development of an advanced constitutive model called Pavement Analysis Using Nonlinear Damage Approach (PANDA) for predicting the performance of asphalt concrete including fatigue damage, permanent deformation, and overall life span (Darabi et al. 2012a, 2012b, 2012c, and 2013). PANDA incorporates Schapery's (1969a) nonlinear viscoelastic model with Perzyna's (1971) viscoplastic model and continuum damage principles in order to predict the performance of asphalt concrete under various loading and environmental conditions. Schapery's nonlinear viscoelastic model accounts for the impact of stress level on the nonlinear material response, time-temperature shift, time-stress shift, and environmental factors (Huang et al. 2007, Saadeh et al. 2007, Masad et al. 2008, Masad et al. 2009). Perzyna's theory, with extended Drucker-Prager yield surface, is used to represent the material viscoplastic response. The model contains parameters to account for various frictional characteristics, anisotropy, hardening, and dilation (Tashman et al. 2005a, Tashman et al. 2005b, Saadeh et al. 2007, Masad et al. 2007).

The objective of developing PANDA is to analyze and predict the performance of asphalt concrete, and compare the utility of various material constituent combinations. In order to achieve this goal, systematic and well-designed experimental methods are needed to determine PANDA model parameters, which define the asphalt concrete material properties. There are traditional experimental methods currently in use to characterize material response:

1. Static creep tests: Applying a static load to a test specimen and measuring recoverable and irrecoverable (or permanent) deformation when the load is removed. Test results generally do not correlate well with actual in-service pavement rutting measurements (Brown et al. 2001).
2. Repeated load tests: Applying a repeated load at a constant frequency to a test specimen for many repetitions (often in excess of 1000) and measuring the specimen's recoverable strain and permanent deformation. In general, test results correlate with in-service pavement rutting measurements better than static creep test results (Brown et al. 2001). Test observations and theoretical analysis indicate that asphalt concrete in compression experiences primary, secondary, and tertiary deformation stages. During the three stages, two types of deformation are developed simultaneously: recoverable viscoelastic deformation and irrecoverable viscoplastic deformation. The rate of accumulation of viscoplastic strain during early cycles is higher than during the preceding cycles.
3. Dynamic modulus tests (DMTs): Applying a repeated load at varying frequencies to a test specimen over a relatively short period of time and measuring the specimen's recoverable strain and permanent deformation. DMTs are also used to measure the lag between peak applied stress and peak resultant strain, providing insight into a material's viscous properties. The test captures only the small portion of permanent

deformation associated with viscous deformation, but it does not account for viscoplastic deformation.

4. Laboratory wheel-tracking tests: Test results can correlate well with in-service pavement rutting measurements, but these tests do not provide any fundamental material parameters.

In addition to developing an experimental protocol to measure material properties, there is a need to develop analytical methods to extract PANDA model parameters from the experimental measurements. The experiments and analytical methods need to be implemented, and their efficacy should be evaluated for different mixture types, temperatures, air void contents, and aging levels. Once the model parameters are determined, the next step is to assess the sensitivity of asphalt material performance to changes in model parameters. This sensitivity analysis reduces output uncertainty and increases model robustness.

1.2 Problem Statement

The behavior of asphalt materials (binders, mastics, and asphalt composite mixtures) is complex and is influenced by temperature, stress/strain level, and stress/strain rate. Furthermore, the total response of asphalt materials subjected to an applied stress contains recoverable (viscoelastic) and irrecoverable (viscoplastic) strain components that could occur simultaneously. The viscoelastic component of the response becomes more dominant as temperature decreases and loading rate increases. The relationship between stress and the recoverable strain component can be nonlinear, depending on the applied stress/strain limits and temperature. The viscoplastic response is also complex, and it becomes more dominant as temperature increases and loading rate decreases.

The microstructure of asphalt concrete is a combination of coarse and fine aggregate matrices. A fine aggregate matrix (FAM) is a composite of fine fillers, fine aggregates, air voids, and asphalt binder, while a coarse aggregate matrix (CAM) is composed of coarse aggregates coated with asphalt binder and surrounded by air voids. By designing FAM and CAM as derivatives of a dense-graded mixture (DGM) based on their aggregate gradation, they can represent typical fine-graded and coarse-graded mixtures, respectively. This approach allows for exploring the effects of FAM and CAM on the overall mechanical response of asphalt concrete, which is controlled by the properties of its constituents. For example, it can be postulated that the viscoelastic response of asphalt concrete is mainly controlled by the FAM properties. On the other hand, aggregate structure, aggregate orientations, friction between aggregate particles, and aggregate interlocking in a CAM mainly control the viscoplastic response of asphalt concrete, especially in compression. Therefore, investigation of the performance of each matrix is required to correlate asphalt mixture characteristics to constituents. In order to effectively and efficiently predict asphalt pavement deformation, the viscoelastic and viscoplastic responses of asphalt material should be modeled rigorously in order to reflect their effects on pavement performance.

PANDA offers substantial improvements in modeling and simulating capabilities of pavement performance with mechanistic approaches, replacing the empirical methods of pavement design and analysis. The mechanistic method is based on fundamental aspects of pavement mechanics, as well as the properties of the material components that comprise asphalt pavements, such as asphalt binder, mastic, and aggregate. This approach allows the user to readily compare the utility of various material constituent combinations. The main challenge in using PANDA is the complexity of its constitutive models. This requires the development of robust experimental and analytical methods to determine the parameters of these models. Improving the robustness of PANDA predictions is also achieved by identifying model inputs that have significant effect on the output. In summary, the main motivations of this dissertation are the need to develop experimental and analytical methods to calibrate PANDA models and the importance of determining the sensitivity of the models' response to their parameters.

1.3 Research Objectives and Scope

The overall objectives of this research are to develop methods to characterize the response of asphalt concrete materials, determine PANDA model parameters for various types of mixtures under different loading and environmental conditions, and assess the sensitivity of the PANDA response to model parameters. These objectives are achieved through the following tasks:

1. Review of literature: The goal of the literature review is to fully understand the behavior of asphalt materials under complex states of stress, strain, and environment. A brief literature review is presented in order to describe different domains of behavior for asphalt materials, as well as research efforts in modeling and defining

the characteristics of each domain. A summary of PANDA capabilities is also documented.

2. Development of experimental methods: Experiments are developed to characterize the resistance of asphalt concrete materials to permanent deformation. Experiments are conducted on FAM, CAM, and DGM mixtures. In addition, DGM specimens are fabricated with different air void contents and aging levels. Cylindrical specimens are prepared to conduct dynamic modulus test (DMT) and repeated creep-recovery test at various stresses (RCRT-VS). Different test protocols are conducted to obtain the desired model parameters. Experimental tests are conducted in a multiaxial compression setup, in which axial and radial deformations are measured by axial and radial linear variable differential transformers (LVDTs), respectively.
3. Application of a robust analytical procedure to identify linear viscoelastic, nonlinear viscoelastic, and viscoplastic PANDA model parameters: The systematic analysis procedure can separate recoverable and irrecoverable components and obtain model parameters in order to calibrate PANDA constitutive models. Experimental data from the DMT and RCRT-VS are analyzed in order to identify linear (time-temperature shift factor and Prony series coefficients of long-term response) and nonlinear (g_1 and g_2) viscoelastic PANDA model parameters, respectively. After extracting linear and nonlinear viscoelastic parameters, the viscoplastic response can be determined by separating the recoverable response out of the total response. RCRT-VS output data are analyzed in order to identify viscoplastic PANDA model parameters.

4. Investigation of testing temperature, air void content, and aging level effects on asphalt mixture performance: After identifying linear viscoelastic, nonlinear viscoelastic, and viscoplastic PANDA model parameters, different temperatures (20, 40, and 55°C), confinement levels (70 and 140 kPa), air void contents (4, 7, and 10%), aging levels (0, 3, and 6 months), and asphalt mixture types (DGM, FAM, and CAM) are investigated for their effects on asphalt mixture response.
5. Global sensitivity analysis (GSA) of PANDA model parameters: This sensitivity analysis tests the robustness of the PANDA model prediction results in the presence of uncertainty and increases the understanding of the relationships between the input and output variables. The sensitivity analysis can be used to simplify the PANDA model by fixing the values of the model inputs that have no significant effect on the output and by identifying and removing the redundant parts of the model structure. GSA methods based on the Fourier amplitude sensitivity test (FAST) and Sobol sequence approach are implemented in the Global Sensitivity Analysis Toolbox (GSAT) in MATLAB.
6. Finite element (FE) simulation of asphalt concrete mixtures using PANDA: Two-dimensional (2D) axisymmetric FE models of four-layer pavement structure under pulse wheel loading are used to conduct FE simulations. These simulations are used to show PANDA capabilities in predicting rutting and to compare the performance of different asphalt pavements that incorporate different materials, mixture designs, air voids, and aging levels.

1.4 Dissertation Organization

This dissertation is organized in eight chapters as follows.

- Chapter I presents the introductory discussion, purpose, objectives, and scope of this research.
- Chapter II presents a comprehensive literature review related to asphalt material response, modeling, characterization, and PANDA capabilities and research efforts.
- Chapter III describes the design of asphalt mixtures and test specimen fabrication and instrumentation, as well as testing protocols and setup.
- Chapter IV presents an extensive characterization of asphalt mixtures by determining viscoelastic and viscoplastic properties using PANDA models. In addition, the evolution of shear strength parameters determined from the RCRT-VS data is compared with the traditional method of Mohr-Coulomb criteria.
- Chapter V discusses the effects of temperature, air void content, and aging level on the linear viscoelastic, nonlinear viscoelastic, and viscoplastic responses of asphalt mixtures.
- Chapter VI describes the implementation of FAST and Quasi-Monte Carlo simulation approaches in the GSAT to investigate the sensitivity of the viscoelastic and viscoplastic PANDA models to their parameters.
- Chapter VII presents 2D FE simulation of the viscoelastic and viscoplastic behaviors of different asphalt concrete mixtures at different temperatures, air void contents, and aging levels.

- Chapter VIII is dedicated to summarizing the research effort and presenting the conclusions and recommendations obtained from this research.

The dissertation includes three appendices that describe the design of FAM and CAM as derivatives of a DGM, the American Association of State Highway and Transportation Officials (AASHTO) standard for calibration of PANDA and its constitutive relationships, and an overview of the PANDA user interface (PUI).

CHAPTER II

LITERATURE REVIEW

2.1 Introduction

The mechanical behavior of asphalt materials is affected by complex states of stress, strain, and environmental factors (Lemaitre 2001). Calculating the mechanical behavior of asphalt materials under different conditions requires the different parameters involved in defining the behavior to be linked to the following fundamental equations (Findley and Davis 2013): (a) the equilibrium equations stating the relationships among the various stress components at any given point required for equilibrium; (b) the kinematic equations expressing the strain components in terms of displacements, which in turn describe the deformation of the body; (c) the compatibility equations stating the relationship required among the several strain components so that the strain components in a continuous medium do not produce discontinuities; and (d) the constitutive equation describing the relationship among stress, strain, and time in terms of the material constants (Haddad 1995).

2.2 Asphalt Material Behavior

2.2.1 Elastic Behavior

Most materials behave elastically (or can be approximated as such) under small stresses and certain climatic conditions. In Figure 2.1, the solid curve represents an immediate elastic strain response, which is obtained upon loading (Lemaitre 2001, Lakes

2009). The strain remains constant as long as the stress is fixed and disappears immediately upon removal of the load. The main characteristic of elastic is reversibility. Most elastic materials are linearly elastic so that there is a proportional relationship between stress and strain.

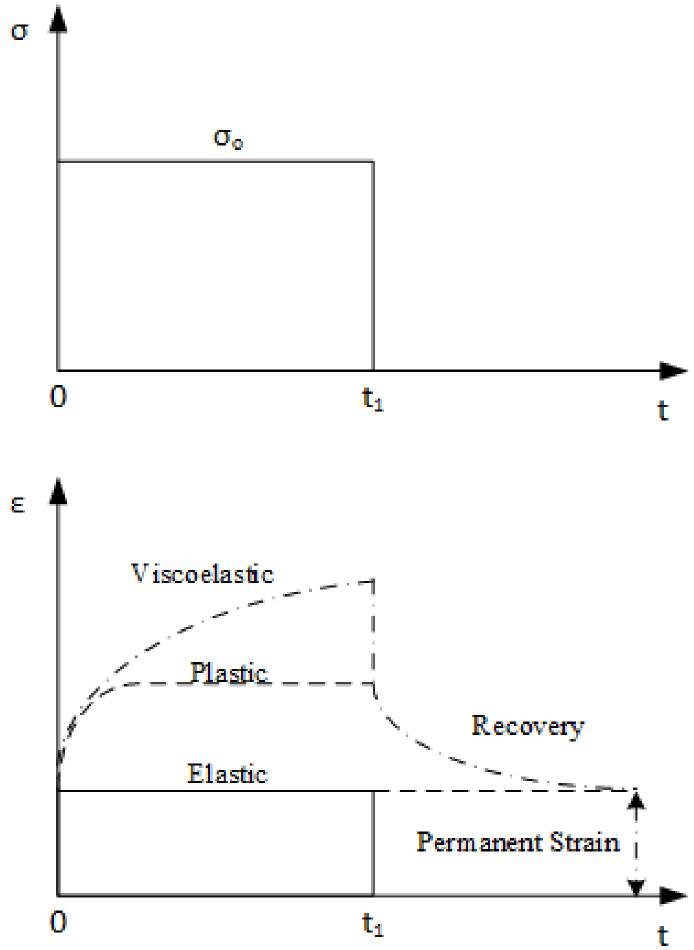

Figure 2.1 Various Strain Responses to a Constant Load (adapted from Parente Jr et al. 2014)

2.2.2 Plastic Behavior

If stress exceeds a certain limit, behavior is no longer elastic (Lemaitre 2001, Findley and Davis 2013). The limiting stress under which behavior is no longer elastic is called the elastic limit. The strain that does not disappear after removing the stress is called the inelastic strain. In some materials, the strain continues to increase for a short while after the load is fully applied and then remains constant under a fixed load. When the stress is removed, a permanent (residual) remains, as shown by the dashed curve in Figure 2.1. Plastic strain is defined as time-independent, although some time-dependent strain is often observed accompanying plastic strain.

2.2.3 Viscoelastic Behavior

Some materials exhibit elastic action upon loading if loading is rapid enough, followed by a slow and continuous increase of strain at a decreasing rate (Haddad 1995, Lakes 2009, Findley and Davis 2013). When the stress is removed, a continuously decreasing strain follows an initial elastic recovery. Such materials are significantly influenced by the rate of straining or stressing; e.g., the longer the time to reach the final value of stress at a constant rate of stressing, the larger the corresponding strain. These materials are called viscoelastic, as shown by the dotted-dashed curve in Figure 2.1.

Asphalt materials exhibit viscoelastic behavior at various temperatures. Because time is a very important factor in their behavior, they are also called time-dependent materials. As its name implies, viscoelasticity combines elasticity and viscosity. The time-dependent behavior of viscoelastic materials is expressed by a constitutive equation, which includes time as a variable, in addition to the stress and strain variables.

Even under a simple loading pattern, as shown in Figure 2.1, the shape of the strain-time curve (creep curve) may be rather complicated. Because time cannot be kept constant, reversed, or eliminated during an experiment, the experimental study of the mechanical behavior of such materials is much more difficult than the study of time-independent materials. Creep (including recovery following creep), stress relaxation, and constant rate stressing (or straining) experiments are used to explore the time-dependent behavior of materials under a quasi-static state (Findley and Davis 2013).

2.2.4 Creep Behavior

Creep is a slow, continuous deformation of a material under constant stress (Lemaitre 2001, Findley and Davis 2013). Creep behavior is the result of viscoelastic and/or viscoplastic behaviors. In general, creep may be described in terms of three different stages, as illustrated in Figure 2.2.

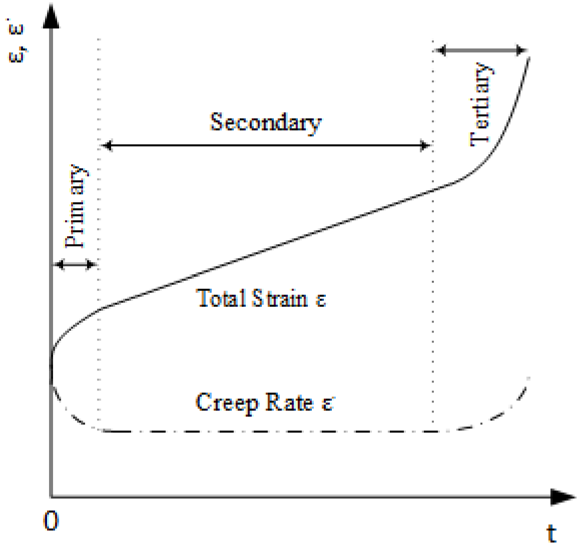

Figure 2.2 Three Stages of Creep (adapted from Findley and Davis 2013)

The first stage in which creep occurs at a decreasing rate is called primary creep; the second, called the secondary stage, proceeds at a nearly constant rate; and the third, or tertiary stage, occurs at an increasing rate and terminates in fracture. Most creep experiments are performed under a constant load, even when the cross-section of the specimen changes significantly with time. Total strain, ε, at any instance of time, t, in a creep test of a linear material is represented as the sum of the instantaneous elastic strain, ε^e, and the creep strain, ε^c.

$$\varepsilon = \varepsilon^e + \varepsilon^c \tag{2.1}$$

The strain rate, $\dot{\varepsilon}$, is found by differentiating Equation (2.1) and noting that ε^e is a constant, as shown below.

$$\frac{d\varepsilon}{dt} = \frac{d\varepsilon^c}{dt} = \dot{\varepsilon} \tag{2.2}$$

2.2.5 Recovery Behavior

If the load is removed, a reverse elastic strain, followed by recovery of a portion of the creep strain, occurs at a continuously decreasing rate (Haddad 1995; Lakes 2009; Kim at al. 2009). The amount of the time-dependent recoverable strain during recovery is generally a very small part of the time-dependent creep strain for metals, whereas for plastics it may be a large portion of the time-dependent creep strain that occurred, as shown in Figure 2.3. The amount of recovered portion of the time-dependent creep strain curve for asphalt materials varies depending on the surrounding temperature; it increases as temperature increases. Strain recovery is also called delayed elasticity.

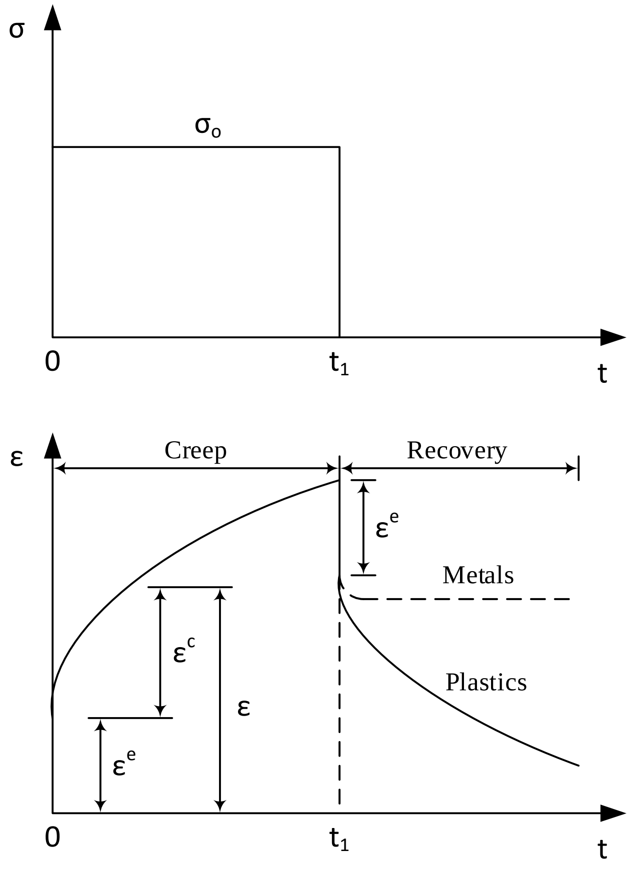

Figure 2.3 Creep and Recovery of Different Materials (adapted from Kim at al. 2009)

2.2.6 Relaxation Behavior

Viscoelastic materials subjected to a constant strain relax under constant strain so that the stress gradually decreases, as shown in Figure 2.4 (Junisbekov et al. 2003, Liu et al. 2015).

Asphalt materials may be subjected to one of the three time-dependent responses explained above or to a mixture; i.e., creep and relaxation may occur simultaneously under combined loading, or the load or strain history may be a cyclic or random variation.

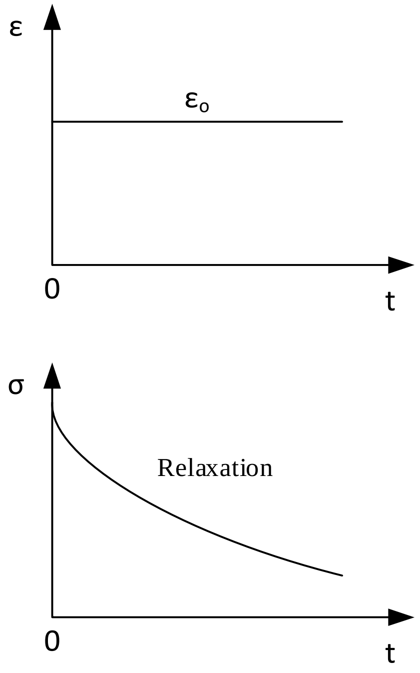

Figure 2.4 Stress Relaxation at Constant Strain (adapted from Liu et al. 2015)

2.2.7 Linearity Behavior

A material is said to be linearly viscoelastic if stress is proportional to strain at a given time and if the linear superposition principle holds (Starodubsky et al. 1994; Nguyen et al. 2015). Most materials, including asphalt materials, are nearly linear over certain ranges of stress, strain, time, and temperature variables; they are nonlinear over larger ranges of some of the variables. The maximum permissible deviation from linear behavior of a material, which allows a linear theory to be employed with acceptable accuracy, depends on stress distribution, type of application, and background of the experience. Under a very short duration of loading and small deformation, asphalt materials behave linearly, even at stresses for which considerable nonlinearity is found if the duration of loading is much longer. In fact, the strain during creep can be separated into a time-dependent linear part and a time-dependent nonlinear part.

2.3 Mechanical Modeling for Viscoelasticity

Viscoelastic mechanical models are helpful in representing viscoelastic behavior of materials. Various combinations of the basic rheological elements may create complex models. The basic elements considered, as shown in Figure 2.5, are the Hookeian element (spring), which is perfectly elastic, and the Newtonian element (dashpot), which is perfectly viscous. In the spring, all energy imparted to the specimen is stored as strain energy, while all energy is dissipated in the dashpot (Tanaka and Eijden 2003).

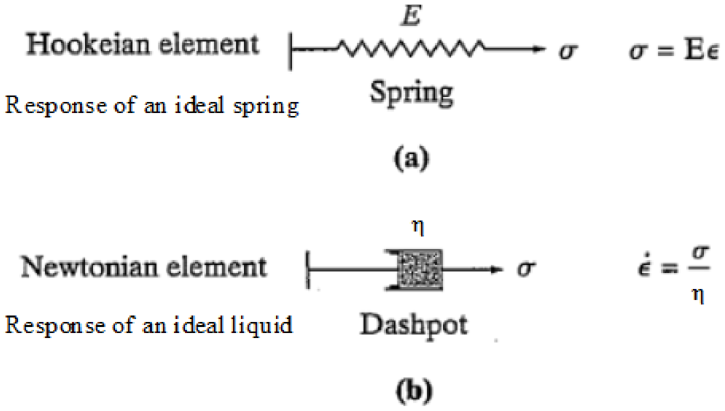

Figure 2.5 The Basic Elements (adapted from Tanaka and Eijden 2003)

With the basic rheological elements, increasingly complex rheological models may be built to account for the simulation of viscoelastic material behavior. The simplest rheological models are the Maxwell model and the Kelvin model.

2.3.1 Maxwell Model

The Maxwell model consists of a spring and a dashpot in series. The same stress acts on both elements, so the total strain is equal to the sum of the strains of the two elements. The extension of the spring is given by $\varepsilon_s = \sigma/E$; the extension of the dashpot obeys the relationship $\dot{\varepsilon}_d = \sigma/\eta$ (Tanaka and Eijden 2003). Differentiating ε_s with respect to time and summing produces the following equation:

$$\dot{\varepsilon}_s + \dot{\varepsilon}_d = \dot{\varepsilon} = \frac{\dot{\sigma}}{E} + \frac{\sigma}{\eta} \tag{2.3}$$

The response of the Maxwell model is limited to two loading cases: constant stress and constant deformation. Under constant stress, $\dot{\sigma} = 0$ and $\dot{\varepsilon}_s = \frac{\sigma}{\eta}$. At an instantaneous elastic strain, given by σ/E, which is recoverable, is going to be followed by a linearly increasing strain, which is irrecoverable, as shown in Figure 2.6.a. This type of behavior is referred to as creep. On the other hand, if a strain is suddenly applied to the system and held constant, $\dot{\varepsilon} = 0$, then stress is a function of time and is given by $\frac{\dot{\sigma}}{E} + \frac{\sigma}{\eta} = 0$. The following equation is thus produced:

$$\sigma = \sigma_o e^{-Et/\eta} \tag{2.4}$$

This means that there is an exponential stress relaxation, as shown in Figure 2.6.a.

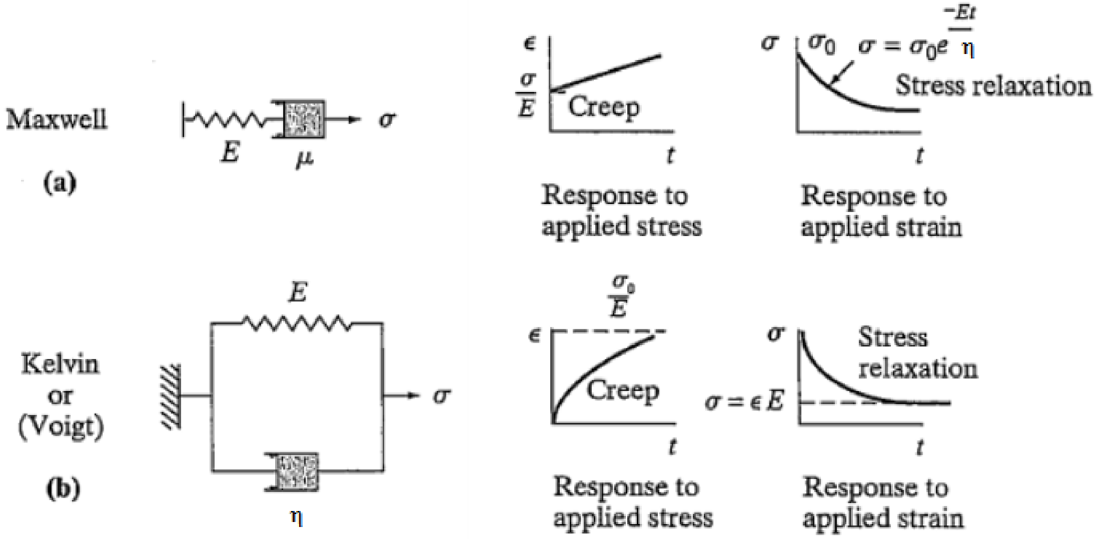

Figure 2.6 Two Element Rheological Models (adapted from Tanaka and Eijden 2003)

2.3.2 Kelvin (Voigt) Model

The Kelvin model consists of a spring and a dashpot in parallel. In this case, the elongation in each element remains the same (Tanaka and Eijden 2003). Therefore, $\sigma_s = E\varepsilon$, and $\sigma_d = \eta\dot{\varepsilon}$, so that the following exists:

$$\sigma = \sigma_s + \sigma_d = E\varepsilon + \eta\dot{\varepsilon} \qquad (2.5)$$

Under a constant stress, σ_o, a creep behavior is obtained, with the solution of differential Equation (2.5):

$$\varepsilon = \frac{\sigma_o}{E}\left(1 - e^{-Et/\eta}\right) \tag{2.6}$$

Then, the strain σ_o/E, which is obtained instantaneously in the absence of a dashpot, is instead approached exponentially. Under a constant strain, $\acute{\varepsilon} = 0$, there will be some stress relaxation, and then the stress remains constant at $\sigma = E\varepsilon$, as shown in Figure 2.6.b. If the material is given a sudden displacement and then released, there is an exponential strain relaxation as follows:

$$\varepsilon = \varepsilon_o e^{-Et/\eta} \tag{2.7}$$

2.3.3 Complex Rheological Model: Burger's Model

Burger's model is a combination of Maxwell and Kelvin elements in series, as shown in Figure 2.7 (Feng et al. 2015). Under a constant stress, σ_o, three types of deformation are distinguished: spring deformation, which is $\varepsilon_1 = \sigma/E_1$, Kelvin element deformation, which is $\varepsilon_2 = \frac{\sigma_o}{E_2}\left(1 - e^{-E_2 t/\eta_2}\right)$, and dashpot deformation, which is $\varepsilon_3 = \frac{\sigma_o t}{\eta_1}$. The total deformation is as follows:

$$\varepsilon = \sigma_o\left[\frac{1}{E_1} + \frac{1}{E_2}\left(1 - e^{-E_2 t/\eta_2}\right) + \frac{t}{\eta_1}\right] \tag{2.8}$$

This means that the material response includes spontaneous elastic deformation, delayed elastic deformation, and irreversible creep.

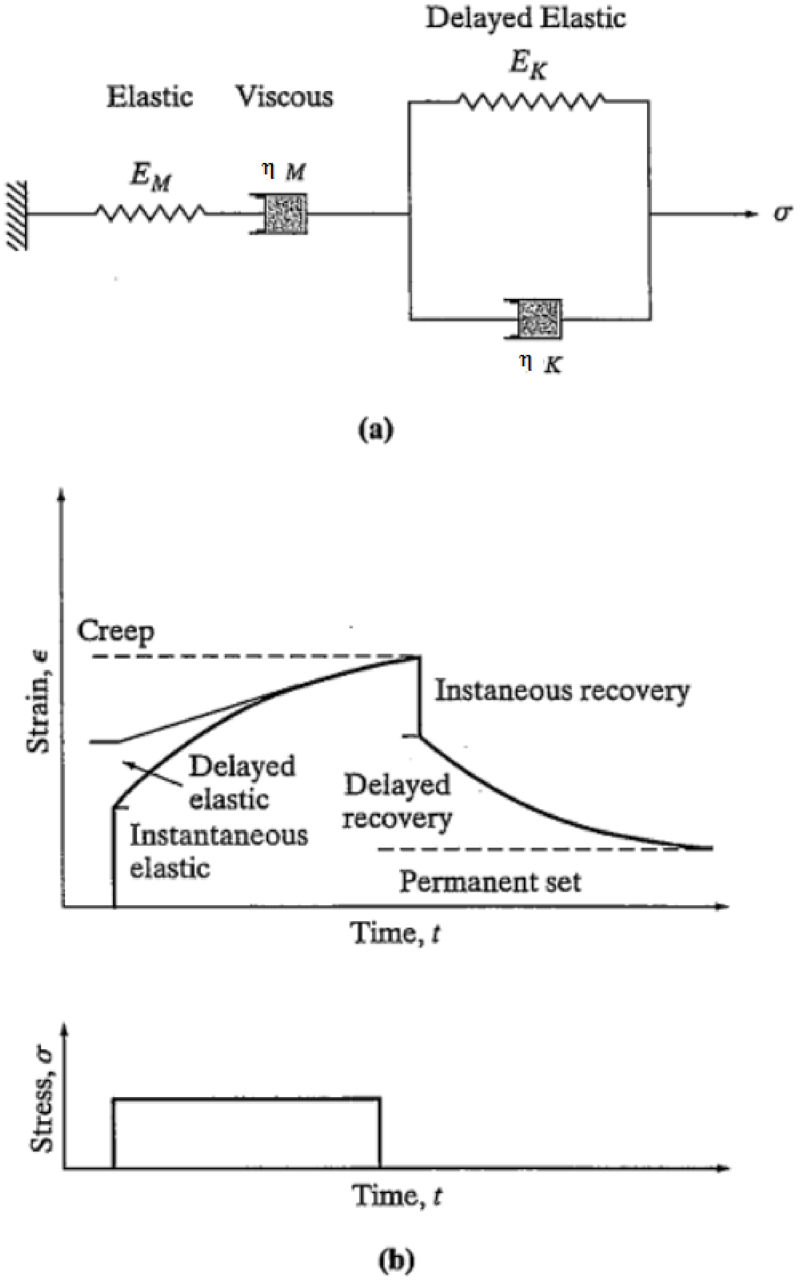

Figure 2.7 Burger's Model (adapted from Feng et al. 2015)

The viscoelastic behavior of asphalt materials with the greatest practical significance is creep. The rheological models described in the previous section provide mathematical formulations to describe creep curves. The characteristic rheological model and the constants composing the basic rheological units are usually determined by matching a model to an experimental creep curve. Therefore, to understand creep behavior, it is essential to address experimental creep curves, as well as the mechanisms by which creep is generated in asphalt material. Creep behavior is discussed in detail in Section 2.2.4.

2.4 Yield Surface Criteria for Plasticity

Defining the onset of plasticity or the point at which the elastic relations cease to be valid is necessary. Yield conditions and strength parameters are very important in understanding the behavior of asphalt materials. Many yield surface models have been proposed to characterize the yielding properties of an asphalt mixture. The most widely used yield surface criteria are the Mohr-Coulomb model, Drucker-Prager model, extended Drucker-Prager model, Matsuoka-Nakai model, hierarchical single-surface model (HISS), etc. The typical functions and problems associated with these yield surface models are presented as follows.

2.4.1 Mohr-Coulomb Model

The function of the Mohr-Coulomb yield surface model is shown as follows (Fwa et al. 2004):

$$\tau - \sigma \tan \phi - C = 0 \tag{2.9}$$

where τ is the yield shear stress; σ is the normal stress; and C and ϕ are cohesion and internal friction angle of the asphalt mixture, respectively. Researchers found that ϕ is primarily a function of aggregate contacts and interlocks, which are insensitive to temperature and strain rates, whereas C depends on testing temperature, strain rate, and properties of binder and fine aggregates (Tan et al. 1994). Figure 2.8 shows an example of a Mohr-Coulomb yield surface, which is an irregular hexagon on the octahedral plane.

2.4.2 Drucker-Prager Model

The Drucker-Prager yield surface model is expressed as follows (Tan et al. 1994, Seibi et al. 2001, Park et al. 2005):

$$\sqrt{J_2} - \alpha I_1 - \kappa_o = 0 \tag{2.10}$$

where $J_2 (= \frac{1}{2} S_{ij} S_{ji})$ is the second invariant of the deviatoric stress tensor, $S_{ij} (= \sigma_{ij} - \frac{1}{3}\delta_{ij} I_1)$; δ_{ij} is Kronnecker delta; $I_1 (= \sigma_{kk})$ is the first invariant of the stress tensor (σ_{ij}); and α and κ_o are material properties, which can be determined by the cohesion and internal friction angle. By matching the Drucker-Prager yield surface with the external apices of the Mohr-Coulomb criterion (as shown in Figure 2.8), the following relationships are obtained (Chen and Mizuno 1990, Tashman et al. 2004):

$$\alpha = \frac{2\sin\phi}{\sqrt{3}\left(3 - \sin\phi\right)} \tag{2.11}$$

$$\kappa_o = \frac{6C\cos\phi}{\sqrt{3}\left(3 - \sin\phi\right)} \tag{2.12}$$

2.4.3 Extended Drucker-Prager Model

The extended Drucker-Prager yield surface model is expressed as follows (Argyris et al. 1974, Dessouky and Masad 2006, Saadeh et al. 2007, Darabi et al. 2011a and 2011b):

$$\frac{\sqrt{3J_2}}{2}\left[1+\frac{1}{d}+\left(1-\frac{1}{d}\right)\frac{3J_3}{\left(3J_2\right)^{3/2}}\right]-\alpha I_1-\kappa=0 \tag{2.13}$$

where $J_3(=\det\left(S_{ij}\right))$ is the third invariant of the deviatoric stress tensor; κ is the strain-hardening parameter and is a function of viscoplastic strain; and *d* is an extension ratio that is the ratio of yield strength in extension to that in compression, which is the length ratio of segment PE to segment PF in Figure 2.8. *d* is related to the internal friction angle of geomaterials as follows (Bardet 1990, Maiolino and Luong 2009):

$$d=\frac{3-\sin\phi}{3+\sin\phi} \tag{2.14}$$

The value of the *d* range from 1 to 0.5 corresponds to the internal friction angle value from 0 to 90°. A *d* value less than 1 indicates that the yield strength in extension is lower than that in compression, which is true for an asphalt mixture. When *d* = 1, the extended Drucker-Prager model reduces to the Drucker-Prager model. To ensure convexity of the extended Drucker-Prager yield surface, the *d* value is limited to between 1 and 0.778 (Lin and Bazant 1986, Maiolino 2005, Masad et al. 2007, ABAQUS 2010), which corresponds to the internal friction angle from 0 to 22° based on Equation (2.14). Examples in Figure 2.8 show that the extended Drucker-Prager model is convex when ϕ =15° and is concave when ϕ = 35°.

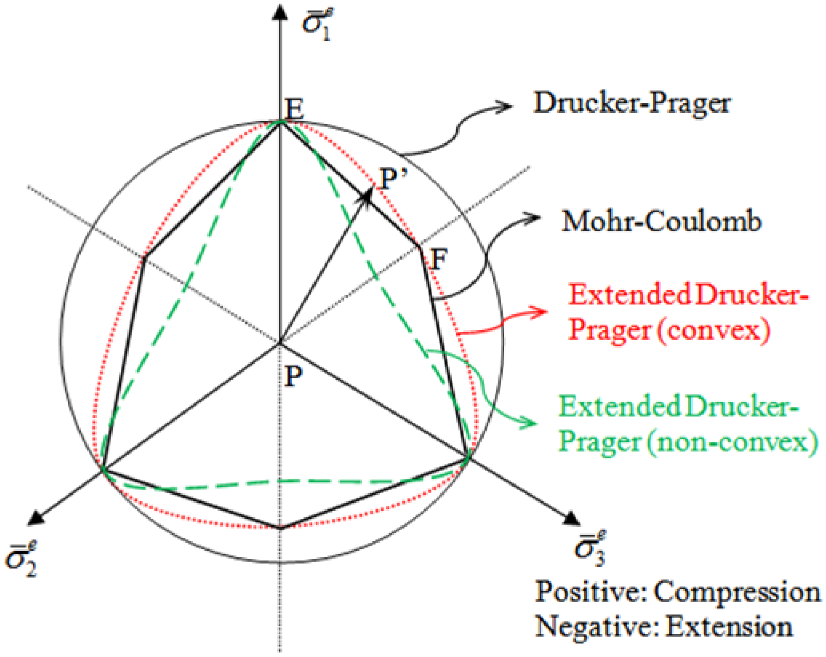

Figure 2.8 Yield Surfaces on an Octahedral Plane (adapted from Chen and Liu 1990; Chen and Mizuno 1990)

To consider the strain-hardening and temperature effect on the yield surface, κ can be written as follows (Abu Al-Rub et al. 2010):

$$\kappa = \kappa_o + \kappa_1 \left[1 - \exp\left(-\kappa_2 \varepsilon^{vp} \right) \right] \tag{2.15}$$

where κ_o, κ_1, and κ_2 are material parameters related to strength and hardening; κ_o defines the initial yield strength; κ_1 determines the amplitude of strain hardening; κ_2 is the strain-hardening rate; and ε^{vp} is the effective viscoplastic strain, the rate of which is expressed as follows (Dessouky 2005, Huang et al. 2011a):

$$\dot{\varepsilon}^{vp} = \left[1+2\left(\frac{0.5+\beta/3}{1-\beta/3}\right)^{2}\right]^{\frac{-1}{2}} \sqrt{\dot{\varepsilon}_{ij}^{vp}\;\dot{\varepsilon}_{ij}^{vp}} \tag{2.16}$$

where β is the slope of the viscoplastic potential and $\dot{\varepsilon}_{ij}^{vp}$ is the rate of viscoplastic strain tensor.

In addition to the above three well-known yield surface models, pavement researchers also introduced yield surface models of geomaterials into the viscoplastic modeling of asphalt mixtures, which are briefly discussed as follows.

2.4.4 Extended Matsuoka-Nakai Model

Bahuguna et al. (2006) extended the Matsuoka-Nakai model (Matsuoka and Nakai 1974, and 1985) and proposed the following yield surface equation:

$$I_1 I_2 + \alpha I_3 - Hk = 0 \tag{2.17}$$

where $I_1 (= \sigma_{kk})$, $I_2 (= \frac{1}{2}\left(\sigma_{ii}\sigma_{jj} - \sigma_{ij}\sigma_{ji}\right))$, and $I_3 (= \det\left(\sigma_{ij}\right))$ are first, second, and third invariants of the stress tensor; H is an isotropic hardening parameter; and *k* is a friction-dependent parameter. The Matsuoka-Nakai model is an excellent yield surface model for cohesionless geomaterials (e.g., sands), and it is inherently smooth and convex (Haythornthwaite 1985, Mortara 2008). However, Equation (2.17) cannot address the effect of rate- and temperature-dependent cohesion and strain hardening on the yielding properties of the asphalt mixture.

2.4.5 Di Benedetto Model

Di Benedetto et al. (2007) proposed a yield surface based on the Lode angle and a hardening variable. The yield surface is expressed as follows:

$$\sqrt{J_2}\cos\left(\frac{\pi}{3}-\psi\right)-R\frac{I_1+3S_o}{\sqrt{3}}=0 \tag{2.18}$$

where R is a scalar hardening variable; S_o is a parameter; and ψ is the Lode angle, which is defined as follows:

$$\psi=\frac{1}{3}\arccos\left[\frac{3\sqrt{3}}{2}\frac{J_3}{\left(J_2\right)^{3/2}}\right],\in\left[0,\frac{\pi}{3}\right] \tag{2.19}$$

The value of ψ, as shown in Figure 2.8 as <EPP’, is 0 in extension and π/3 in compression. The yield surface derived by Equation (2.18) is an equilateral triangle on the octahedral plane. Thus, the yield strength ratio of extension to compression is always 0.5 (i.e., d = 0.5, ϕ = 90), which is not reasonable for asphalt mixtures, as the d-value is recommended to not be less than 0.778 to ensure convexity of the yield surface.

2.4.6 Desai’s HISS Model

Desai et al. (1986) proposed a HISS model to constitutively model geologic materials, and the yield surface function has a form as follows:

$$J_2\left[1-B\cos\left(3\theta\right)\right]^m-\left[\gamma\left(I_1+S\right)^2-\alpha\left(I_1+S\right)^n\right]=0 \tag{2.20}$$

where γ is a softening parameter; α is a hardening parameter, S is a cohesion-related parameter; n is a parameter determining yield surface shape in the deviatoric-hydrostatic stress ($\sqrt{J_2}-I_1$) plane (or meridian plane); and B and m are parameters determining yield surface shape on the octahedral plane. Pavement researchers used Desai’s HISS model for asphalt mixtures by setting m as 0.5 (Muraya et al. 2009) and sand/aggregate base by setting m as 1 (Bonaquist and Witczak 1996). Several problems exist in Desai’s HISS model when applied to model asphalt mixture:

- The value of *m* must be 0.229 to ensure a convex yield surface for the full range of the internal friction angle from 0 to 90° (Van Eekelen 1980).
- Desai’s HISS model exhibits a spindle shape, and the yield surface becomes nonlinear at relatively high confining pressures, which are normally used to characterize the nonlinear softening of soils or granular base. In contrast, the confinement in an asphalt layer cannot reach a very high level, and the yield surface remains linear on the meridian plane for the asphalt mixture.
- Too many fitting parameters in the HISS model require complicated laboratory experiments for the determination of the model parameters.
- Rate- and temperature-dependent strain hardenings are not accounted for in Desai’s HISS model.

2.5 Hot-Mix Asphalt (HMA) Characterization for Constitutive Models

Tashman (2003) developed an isotropic viscoplastic continuum damage model describing the permanent deformation of asphalt concrete at high temperatures. His model is based on Perzyna’s viscoplasticity theory associated with a modified Drucker-Prager yield function. The Drucker-Prager yield function was modified to account for the dependency of strain rate and confining level, dilation, aggregate friction, anisotropy, and damage. The capabilities of the model and its sensitivity to changes in the microstructure distribution and loading conditions were investigated using laboratory experimental measurements from the Federal Highway Administration (FHWA) Accelerated Loading Facility (ALF). The model parameters were determined by conducting a comprehensive set of compressive triaxial strength tests with different confining levels and strain rates. This set of experiments describes hardening, anisotropy, and damage within asphalt concrete. In addition, damage evolution was captured by a predefined triaxial compression setup, as well as X-ray computed tomography (CT) and image analysis techniques.

Saadeh (2005) integrated the damage viscoelasticity model developed by Schapery (1969) with a viscoplasticity model based on Perzyna's theory. The damage viscoelastic constitutive relationship was employed to demonstrate the recoverable response, while the viscoplastic relationship was employed to present the irrecoverable response. After integration, the anisotropic damage viscoelastic-viscoplastic model was capable of predicting HMA performance under a wide range of temperatures, loading rates, and stress states. A set of experimental testing, including triaxial repeated creep and recovery tests, as well as monotonic constant strain rate tests, was conducted to quantify both the viscoelastic and viscoplastic response. X-ray CT and image analysis were also included to characterize the three-dimensional (3D) aggregate orientation and air void distribution.

Dessouky (2005) developed an elastic-viscoplastic continuum model to predict HMA performance taking into account the effects of microstructure distribution in modeling the macroscopic behavior of HMA. The model includes a modified Drucker-Prager yield surface to capture the impact of stress path direction on material response and material parameters, which reflect the directional distribution of aggregate and damage density at the micro-scale.

2.6 PANDA

Pavement design and analysis have gradually moved from empirical approaches to include more mechanistic principles. Various types of tests and mechanistic-based models have been used to characterize the response of asphalt concrete materials. PANDA seeks to provide an advanced mechanistic approach to predict rutting and fatigue damage subjected to general loading and environmental conditions. The goal for PANDA is to be used by both researchers at academic institutions and practitioners.

2.6.1 Advantages of PANDA

- PANDA is a comprehensive mechanistic-based modeling approach that can predict the response of asphalt pavements subjected to traffic loading and environmental conditions. PANDA includes constitutive relationships and evolution functions for the most important mechanisms occurring in pavements, such as viscoelastic, viscoplastic, viscodamage, micro-damage healing, moisture-induced damage, moisture damage, and oxidative aging constitutive relationships.
- The constitutive relationships implemented in PANDA are developed for general multiaxial stress states. It represents the behavior of asphalt concrete materials under general 3D stress states and realistic environmental conditions that actually occur in the field.
- PANDA captures the interactions and coupling among different components of constitutive relationships, enabling the model to predict the performance life of asphalt pavement more accurately.

- PANDA includes evolution functions coupled with other components of the model in order to consider the effect of environmental factors, such as moisture damage and oxidative aging, on pavement performance. PANDA is capable of predicting change in failure mode, as well as the location of crack initiation due to moisture presence or aging effects.
- PANDA is used to simulate asphalt concrete microstructure and investigate the effect of asphalt concrete constituents on the response and performance of asphalt mixes. Pavement design engineers can use the model and the software to analyze and predict the performance of pavements of various material combinations and, thus, select the best and most cost-effective materials for a proposed project.

2.6.2 PANDA Research Efforts

Asphalt concrete materials clearly display viscoelastic, viscoplastic, viscodamage, and healing responses. Huang (2008) presented a nonlinear viscoelastic-viscoplastic model for predicting the behavior of asphalt concrete mixtures under different conditions. The model employs both the Schapery nonlinear viscoelastic theory and Perzyna's theory for viscoplasticity with modified Drucker-Prager yield surface. In addition, he presented a new method for separating viscoelastic and viscoplastic responses from the total response of asphalt concrete materials. The nonlinear viscoelastic-viscoplastic constitutive model was implemented in the ABAQUS FE package using the user material (UMAT) subroutine to simulate fatigue and permanent deformation distresses of asphalt concrete pavements.

Darabi (2011) proposed a thermodynamic-based framework to derive thermo-viscoelastic, thermo-viscoplastic, thermo-viscodamage, and micro-damage healing constitutive relationships for asphalt concrete mixtures. In addition, he proposed a hardening-relaxation model to account for the viscoplastic hardening and relaxation response of asphalt concrete subjected to cyclic loading. The proposed framework, PANDA, is validated with comprehensive experimental testing including creep, creep and recovery, dynamic modulus, constant strain rate, and cyclic stress/strain-controlled tests in both compression and tension modes and over a wide range of testing conditions. The PANDA model demonstrates that it is capable of predicting time-rate and temperature-dependent performance of asphalt concrete mixtures subjected to different loading conditions.

Abu Al-Rub et al. (2012) investigated the effects of different FE modeling techniques and material constitutive models on predicting asphalt concrete performance under repeated loading patterns. Different coupling techniques of PANDA constitutive relationships, such as elasto-viscoplastic, viscoelastic-viscoplastic, and viscoelastic-viscoplastic-viscodamage, were used to evaluate permanent deformation predictions of asphalt concrete performance. In addition, different modeling techniques (2D and 3D) and loading patterns (pulse and equivalent) were used to evaluate and compare rutting predictions in asphalt pavements.

You (2013) used the coupled thermo-viscoelastic, thermo-viscoplastic, and thermo-viscodamage constitutive model in developing 2D and 3D methods to represent the microstructure of asphalt concrete materials. X-ray CT images were used to generate

2D representative volume elements (RVEs) based on identifying three phases of aggregate, matrix, and interfacial transmission zone (ITZ), representing the interface between the aggregate and the matrix. Then, the generated 2D X-ray CT images were gathered to construct a 3D microstructure of asphalt mixtures. You (2013) used the 2D and 3D microstructural modeling in investigating the effect of aggregate shape, distribution, volume fraction, ITZ strength, strain rate, loading rate, loading type, and temperature on the asphalt concrete response. In addition, the nonlinear constitutive model, FE analysis, and X-ray CT were combined to link the microstructural properties represented in the FAM with the macroscopic response of the full asphalt mixture.

Shakiba (2013) developed a physically based constitutive relationship that captures the moisture-induced damage of asphalt concrete. Based on the principle of virtual power and the laws of thermodynamics, Shakiba coupled the effects of moisture diffusion and pore water pressure to propose the Continuum Moisture-Mechanical Damage Mechanics (CMMDM) theory, which captures moisture degradation effect. The proposed moisture-induced damage constitutive relationships are implemented in PANDA to simulate moisture damage effect on pavement performance. The PANDA framework is used to fundamentally analyze combined mechanical and moisture-induced damage effect on the complex environmental-mechanical response of asphalt concrete. In addition, 2D and 3D micromechanical simulations were performed using the proposed framework to predict the microstructural response of asphalt concrete under the combined effect of moisture diffusion and traffic loading.

Rahmani (2015) developed a mechanistic-based aging constitutive relationship that captures oxidative aging damage in asphalt concrete. Based on continuum theory, an aging-state variable, which is correlated with oxygen content via an evolution function, was proposed to represent the thermo-dynamical change in mechanical and macroscopic properties of asphalt concrete due to oxidative aging damage. The developed aging constitutive relationship is implemented in PANDA by introducing the aging-state variable to Schapery's viscoelastic model. PANDA models the oxidative aging damage in asphalt concrete based on oxygen content, temperature, and level of aging at a certain time.

2.7 Summary

Asphalt concrete materials exhibit complex mechanical behavior under general traffic loading and environmental conditions. The literature review, presented in this chapter, describes the general behavior aspects for asphalt materials and research efforts to model this behavior. During the last decade, several research efforts have been conducted at Texas A&M University to better model asphalt concrete based on mechanistic approaches. PANDA is the comprehensive product of these efforts; it is capable of analyzing the performance of asphalt materials based on a nonlinear damage approach.

One advantage of PANDA is that it compares the utility of several material constituent combinations, which affects the whole mechanical response. Therefore, determining the response of PANDA model parameters to these material components is essential for knowing which mixture component affects which parameter. Various environmental conditions, as well as a wide range of asphalt mixtures based on different aggregate gradations, should be investigated to assess the sensitivity of model parameters. In order to perform these investigations, robust experimental tests and standard analytical methods are needed to determine PANDA parameters and calibrate its models. In addition, the complex response of asphalt materials should be modeled rigorously using noncomplex and sensitive models in order to effectively and efficiently predict performance under traffic loading and environmental conditions. The complexity of PANDA constitutive relationships is the motivation for this dissertation to develop experimental and analytical methods to identify PANDA model parameters and test the model sensitivity to its parameters, as described in detail in the following chapters.

CHAPTER III

EXPERIMENTAL WORK

3.1 Introduction

This chapter describes the materials and asphalt mixtures used in the experimental program. In addition, it presents detailed information of test specimen fabrication and instrumentation, testing setup, laboratory testing techniques, and testing protocols. An asphalt mixture is composed of two matrices: CAM and FAM, and the properties of these constituents control the overall mechanical response of the mixture. FAM and CAM mixtures are designed as derivatives of a DGM in order to represent a wide range of mixtures. Consistent and controlled methods are followed in preparing FAM, CAM, and DGM specimens, as well as aging specimens for 3 and 6 months. A robust experimental setup is established to control temperature, confinement level, loading stress, and rate of loading. This experimental setup is used to apply various states of stresses in order to determine the material parameters of the PANDA model. DMT is used to identify linear viscoelastic parameters and time-temperature shift factors. RCRT-VS is used to identify nonlinear viscoelastic and viscoplastic parameters. The material parameters, or constants, determined experimentally using the proposed testing technique, are used in PANDA constitutive relationships to predict the performance of asphalt pavements.

3.2 Mixtures Overview

The DGM used in this study follows the gradation design of C-type mixtures in the state of Texas, as presented in Table 3.1 (TxDOT 2004). The C-type mixture is produced by combining 30% C-rock, 36% F-rock, 24% washed screening, and 10% sand of limestone materials, which are provided with its gradation from stockpiles of the asphalt plant. An unmodified binder of PG 67-22 is used to produce DGM specimens with 4.4% asphalt binder; its crude oil source is Venezuela.

Table 3.1 Specification Limits of Aggregate Gradation for Designing C-Type Asphalt Mixture (TxDOT 2004)

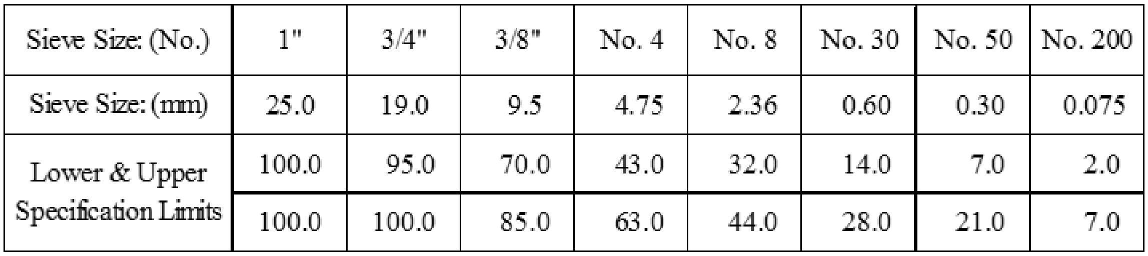

Sieve Size: (No.)	1"	3/4"	3/8"	No. 4	No. 8	No. 30	No. 50	No. 200
Sieve Size: (mm)	25.0	19.0	9.5	4.75	2.36	0.60	0.30	0.075
Lower & Upper Specification Limits	100.0	95.0	70.0	43.0	32.0	14.0	7.0	2.0
	100.0	100.0	85.0	63.0	44.0	28.0	21.0	7.0

The composition of asphalt concrete consists of two matrices: FAM and CAM. FAM is a composite of fine fillers, fine aggregates, air voids, and asphalt binder, while CAM is a coarse aggregate coated with asphalt binder and surrounded by air voids. Figure 3.1 represents the DGM composition.

The FAM and CAM asphalt mixtures are designed based on the gradation and composition of the reference DGM. The FAM consists of the fine portion of the mixture with aggregates passing sieve #16 (1.18 mm) (Sousa et al. 2013), while the CAM consists of the coarse portion of the mixture with aggregates retained on sieve #16 (1.18

mm). The proportions of fine aggregates comprising the FAM are kept the same as in the full mixture aggregate gradation, but they are normalized with respect to the largest sieve in the FAM (#16). This means that 100% of the aggregate in the FAM passes sieve #16, and the percentage passing the smaller sieves is calculated as follows:

$$\text{Cumulative percent passing sieve x in FAM} = \frac{\text{Cumulative mass of aggregate passing sieve x in reference mixture}}{\text{Cumulative mass of aggregate passing sieve \#16 in reference mixture}} * 100\% \qquad (3.1)$$

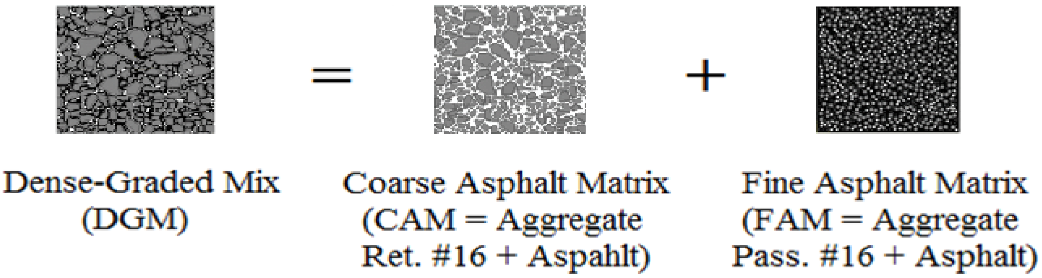

Figure 3.1 Composition of DGM

The proportions of the coarse aggregates comprising the CAM are kept the same as in the full mixture aggregate gradation, but they are normalized with respect to the lowest sieve in the CAM (#16). This means that 100% of the aggregate in the CAM remains on sieve #16. The percentage passing the larger sieves is calculated as follows:

$$\text{Cumulative percent passing sieve x in FAM} = 100 - \left[\frac{\text{Cumulative mass of aggregate retained on sieve x in reference mixture}}{\text{Cumulative mass of aggregate retained sieve \#16 in reference mixture}} * 100\%\right] \qquad (3.2)$$

After determining the percentage passing each sieve in the FAM and CAM, FAM and CAM aggregate gradations and the corresponding DGM gradation are compared, as given in Figure 3.2. Appendix A explains in detail the procedure of designing the FAM and CAM as derivatives of a DGM.

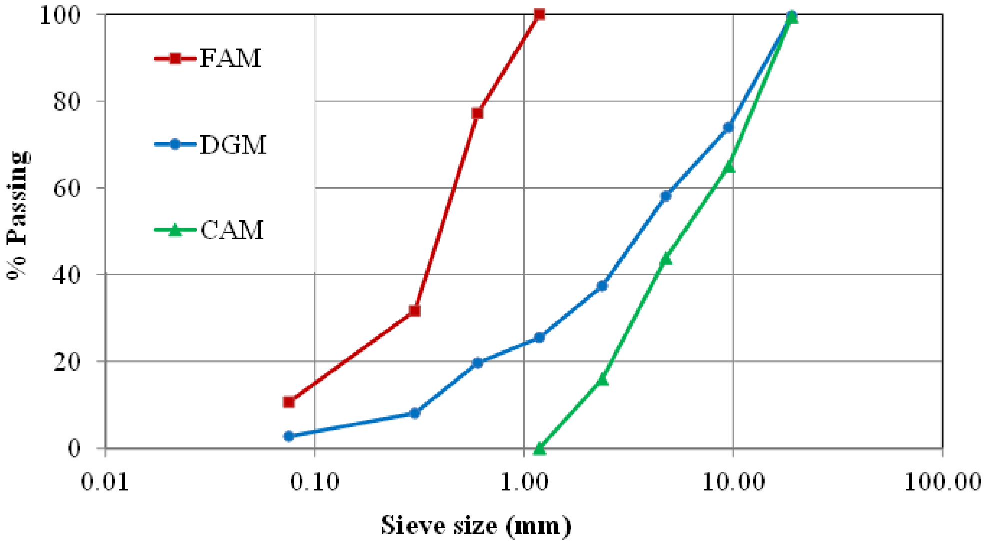

Figure 3.2 Different Proportioning of Aggregate Gradations

3.3 Test Specimen Fabrication and Instrumentation

HMA specimens are prepared, as illustrated in Figure 3.3, in accordance with AASHTO standard T 312 (AASHTO 2016). The Superpave gyratory compactor (SGC) is used to compact cylindrical 170±1-mm-height and 152.4±1-mm-diameter HMA specimens. The SGC specimens are cored to 101.6±1-mm diameter and are trimmed using a double or single saw cut to 152.4±1-mm height. The sides and ends of test specimens are required to be smooth and parallel. The ends of test specimens are kept perpendicular to the axis of specimens. Each specimen is checked using a machinist's square. The air void content of test specimens is determined in accordance with AASHTO standard T 269 (AASHTO 2016). A tolerance is allowed of 0.5% from the target-percent air voids. Any specimen exceeding this tolerance is discarded. At least two specimens are tested at each test condition.

The method for determining binder content relies on experimentally separating the fine portion of the mixture (passing sieve #16) from the coarse portion and determining the asphalt content of the fine portion and the coarse portion individually, as described in detail in Appendix A (Sousa et al. 2013). The determined asphalt contents are used to mix and compact FAM and CAM specimens in the SGC. The method takes advantage of the procedures described in AASHTO standards T 209 and T 308 (AASHTO 2016) for determining the theoretical maximum specific gravity and binder content in asphalt mixtures, respectively.

Drying aggregates Sieving aggregates Mixing aggregates with binder Molding specimen

Coring specimen Cutting specimen Test specimen after coring/cutting Measuring density Target AV±0.5%

Figure 3.3 Steps for Preparation of Test Specimens

Three axial LVDTs are mounted to the sides of the test specimens at 120° apart. Figure 3.4 presents a schematic view of the test setup with mounted axial LVDTs. The gauge length of the axial LVDTs is 101.6±1 mm. Metal studs are mounted at a distance of 25.4 mm from the top and bottom of the test specimens. The mounting studs for axial LVDTs are glued directly to test specimens. Three metal studs for the radial LVDTs are mounted in the center of the test specimens at 120° apart and 60° from the axial LVDTs. The gauge length of the radial LVDTs is equal to the radius of the test specimens (50.8±0.5 mm). The mounting studs for radial LVDTs are glued directly to test specimens. When confining pressure is required, a latex membrane is stretched over the test specimen. O-rings are used to seal the membrane to the top and bottom plates.

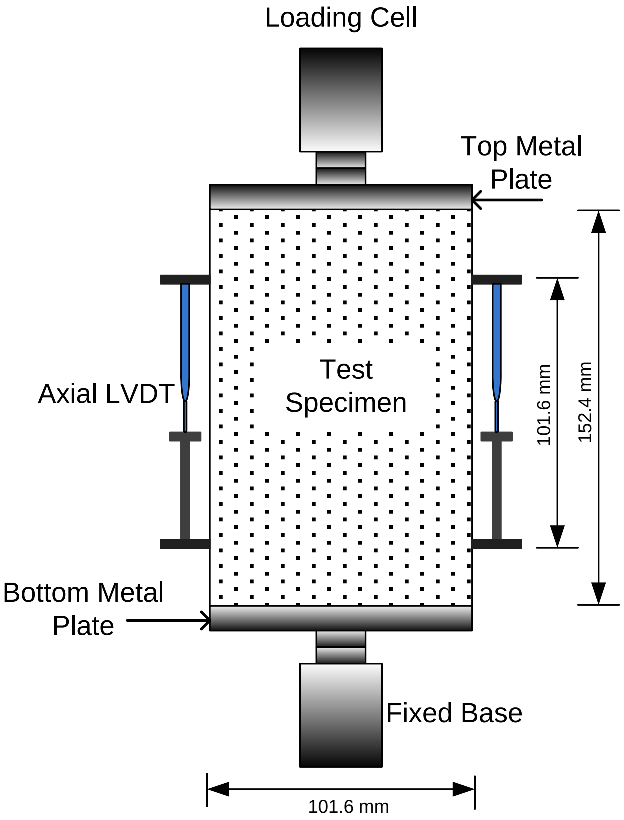

Figure 3.4 Schematic View of Test Setup with Mounted Axial LVDTs

3.4 Testing Setup

Some general principles and precautions are considered in setting up the experimental apparatus and executing creep and recovery experiments. In order to obtain desirable results with high precision and consistency, specific apparatus parts and methods are used, as described in detail below.

3.4.1 Loading Apparatus for Creep Testing

For constant load creep testing, loading weight is the simplest and generally the most satisfactory. For applying higher weights, this method is not very satisfactory because of difficulty in applying the load without undesirable disturbances. Loading weights applied to a lever may be employed for greater loads. Some situations require servo control to be used to obtain a controllable and repeatable loading pattern during application of the load. The force on the specimen is determined by a load cell or other force-measuring device, and the stress is determined directly from the load and the geometry of the specimen.

As long as load application method includes hydraulic or pneumatic (by means of pistons) and power screws, friction must be kept to a minimum if the stress is to be controlled and measured separately by means of a load-measuring device placed between the specimen and any apparatus subject to friction. Devices for applying load, such as pistons involving sliding seals and rings, generally involve too much friction to either control the load or determine stress from the fluid pressure. The challenge is to reduce the coefficient of friction as much as possible by either replacing sliding friction with rolling element friction or improving overall lubrication.

The supporting frame of the MTS machine, which is used for applying creep testing, must be stiff enough that its deflection under loading does not disturb the load-measuring or strain-measuring systems. The machine should be capable of producing controlled load in both compression and tension. It should be equipped with a ±22-kN (5,000-lb) load cell. The load cell should be calibrated in accordance with ASTM standard E 4 “Standard Practices for Force Verification of Testing Machines” (ASTM 2015). The system should be fully computer-controlled, capable of measuring and recording time, load, deformation, and confining pressure.

3.4.2 Load Application

During analysis and interpretation of the creep tests, it is usually assumed that load is applied instantaneously and remains constant after application. This is, of course, impossible to achieve because of the dynamics of the spring-mass system involved in the used machine. Thus, in practice, the load is applied gradually over a very short time span by using automated systems of load application to avoid bouncing, vibration, or overshooting the desired load. When servo control is employed, a step-change in input is a satisfactory means of load application if overshoot and vibration results are smoothed and minimized. While different rates of loading are applied, programmed loading is employed in order to have no difficulty achieving repeatable and consistent creep results.

3.4.3 Test Specimen

The common asphalt mix specimens for creep testing are cylindrical ones of 101.6±1-mm (4-in) diameter and 152.4±1-mm (6-in) height (TxDOT 2004). It is important for all specimens that the cross-sectional area be uniform over gauge length covered by the LVDT.

3.4.4 Uniform Application of Stresses and Strains

Application of uniform stress is very important in creep testing in order to accurately determine stress and strain. In order to achieve uniform stress or strain, it is necessary to eliminate bending stresses as much as possible. This can be accomplished by adjusting the axis of the loading rod with respect to the specimen axis. Positioning the specimen properly requires the use of three strain gages on the specimen or the use of a bending detector. These tools are used to observe bending that may occur when a small test load is applied. When bending occurs, one of the three strain gauges will detect more strain than the others.

3.4.5 Strain Transducers

LVDTs are used to measure strain during the creep test. LVDTs are robust, absolute linear position/displacement transducers and are inherently frictionless. As LVDTs do not contain any electronics, they are designed to operate at high temperatures, under high vibration, and under shock levels with high sensitivity, stability, repeatability, and accuracy.

During long-term experiments, the stability of LVDTs becomes more important. It is very difficult to keep the alignment of the LVDT axis accurate enough while the specimen deforms, especially at high temperatures. Errors due to such misalignment are difficult to avoid. Factors such as creep of the adhesive or creep of the gauge backing can result in unacceptable drift of the gauge output. Frictional effects should be checked by placing small loads on the specimen in the elastic range and removing them to verify that the strain indicated by the LVDT returns to the original value. Sensitivity of the LVDT may be verified by reducing test load size. For some situations, it is convenient to employ manual data observations in order to ensure consistent deformation in the attached LVDTs. Three LVDTs are used to record axial deformation, as well as three other LVDTs to record radial deformation. The three LVDTs that measure radial deformations are mounted 120° apart at the mid-height of the specimen and 60° from the LVDTs used to record axial deformations.

3.4.6 Temperature Control

Temperature control is essential during creep experiments, not only because temperature affects creep rate, but also because asphalt concrete behavior is temperature-dependent. Various means of temperature control and temperature distribution are employed. The testing machine includes a temperature-controlled chamber to provide a well-controlled environment for the testing specimen. Rapid air circulation is used around the specimen to counteract the stack effect and improve temperature distribution. Temperature-sensing instrumentation may include resistance elements (thermistors) or voltage elements (thermocouples). The temperature-controlled chamber is provided with closed-loop servo-type automatic controllers for controlling heat input. It should be capable of controlling the temperature of test specimens over a temperature range of -10 to 55°C. Opening the temperature-controlled chamber during creep experiments is not allowed to minimize change in environment temperature surrounding the specimen during testing. Any possible room in the interior of the building with heating and cooling temperature control is desirable. The room should involve circulation of air through some type of duct work, which may also serve to distribute air uniformly throughout the room. This allows for controlling the room's relative humidity, which introduces the most problems affecting the test specimen.

3.4.7 Internal Pressure

Maintaining an internal pressure in creep experiments is a challenging task. Air is the most common pressurizing medium in this type of experiment. The other media, liquids and gases, are hard to use without affecting creep behavior. A rubber membrane is used to cover the specimen during testing to ensure consistent distribution of confining pressure on the circumferential face of the specimen. As an asphalt specimen has air voids, the rubber membrane prevents air from flowing through the specimen during testing. Therefore, good-quality rubber membranes with enough thickness are required for creep experiments involving internal pressure. It is recommended to use one rubber membrane per experiment, especially at elevated temperatures.

A triaxial cell is required for applying a confining pressure on the test specimens. The cell should withstand a working pressure up to 400 kPa (air). The cell should accommodate test specimens, with each having the dimensions of 101.6-mm (4-in) diameter × 152.4-mm (6-in) height. The cell should facilitate up to three “through-the-wall” radial strain transducers, as shown in Figure 3.5.

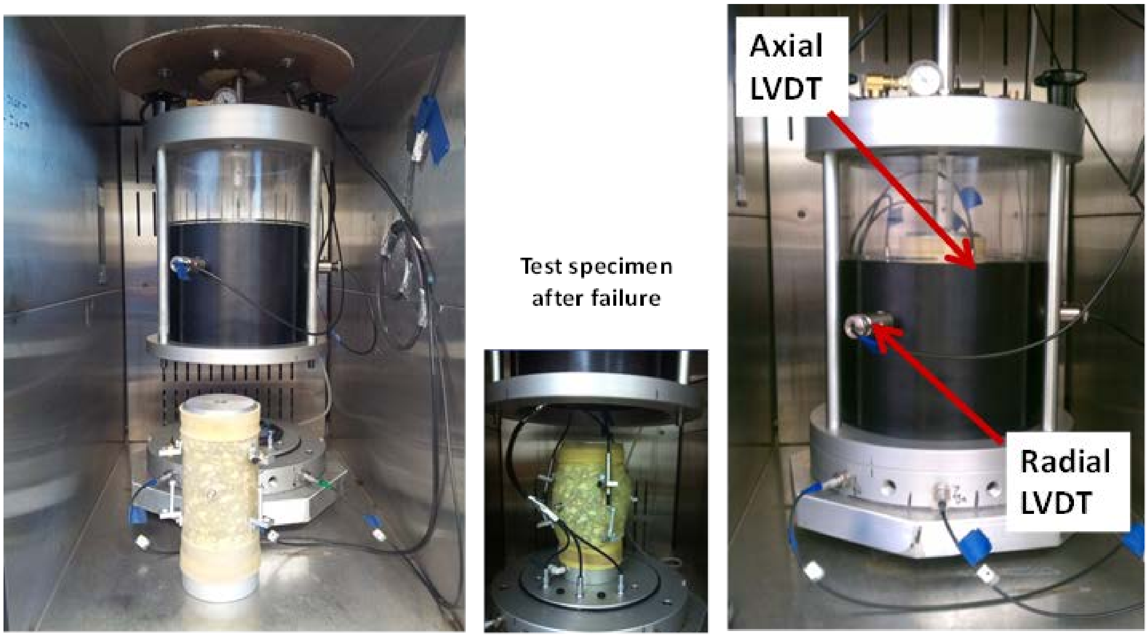

Figure 3.5 Laboratory Testing Setup

3.5 Testing Protocols

3.5.1 DMT According to AASHTO TP-62

A DMT is used to determine linear viscoelastic model parameters and time-temperature shift factors. This test is conducted in accordance with AASHTO standard TP 62 (AASHTO 2016) using Universal Testing Machine-25 (UTM-25), as shown in Figure 3.6. This test is conducted at five different temperatures (−10, 4.4, 21.1, 37.8, and 54.4°C) and six loading frequencies (0.1, 0.5, 1.0, 5, 10, and 25 Hz) at each temperature. Each test specimen, individually instrumented with LVDT brackets, should be tested for each of the 30 combinations of temperature and frequency of loading, starting with the lowest temperature and proceeding to the highest. Testing at a given temperature should begin with the highest frequency of loading and proceed to the lowest. Sinusoidal loading is applied and adjusted to obtain axial strain between 80 to 110 microstrains in order to remain within the linear viscoelastic response. Testing starts from the lowest to highest temperature and from the highest to lowest frequency. The applied stress and recorded strain are used to calculate the dynamic modulus and phase angle.

Figure 3.6 UTM-25

3.5.2 RCRT-VS

The MTS machine with a triaxial cell is used to conduct the RCRT-VS, as shown in Figure 3.7. The RCRT-VS is conducted at different temperatures with different confinement levels to identify nonlinear viscoplastic model parameters. The RCRT-VS includes six loading blocks. Each loading block consists of eight creep-recovery cycles with increasing applied deviatoric stress levels. The loading and unloading times of each loading cycle remain constant through the entire test. The loading time is 0.4 seconds while the unloading time is 30 seconds. The deviatoric stress of the first loading cycle of the first loading block is 140 kPa, and it increases by a factor of $1.2^{(n-1)}$; where n is the number of loading cycle in a specific loading block for the next loading cycle until the eighth loading cycle. The first deviatoric stress of the subsequent loading blocks equals the third stress level in the previous loading block, and it increases by the same factor of $1.2^{(n-1)}$ for the next loading cycle until the eighth loading cycle of that loading block. The test is conducted at different confining pressures (e.g., 70, 140 … kPa). Each applied confining pressure is maintained during the entire test. Figure 3.8 shows an example of the first three sequences of loading blocks of the RCRT-VS.

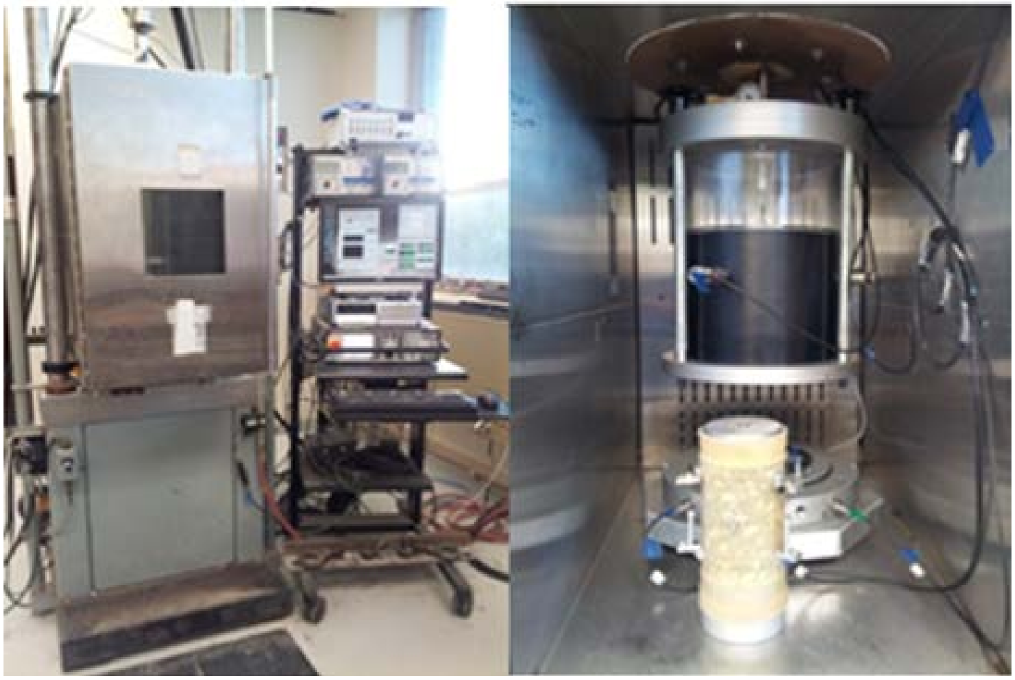

Figure 3.7 MTS Machine with a Triaxial Cell

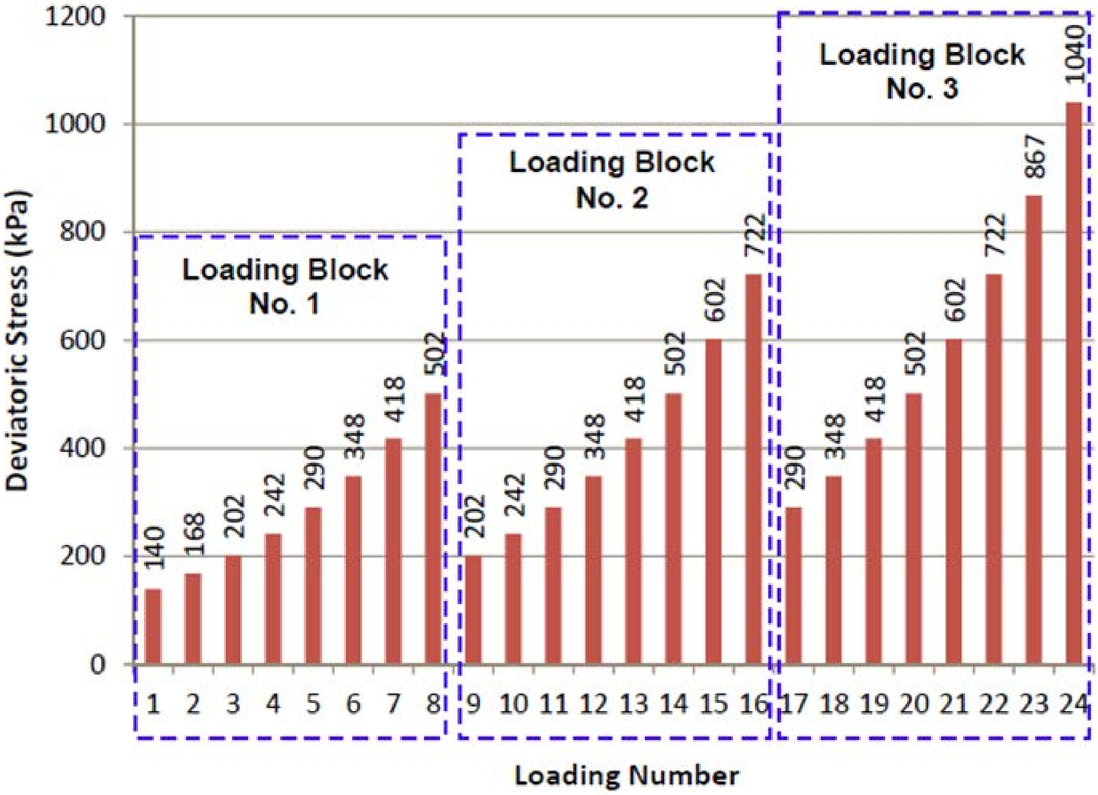

Figure 3.8 Applied Deviatoric Stresses in the First Three Loading Blocks of the RCRT-VS

3.5.3 Uniaxial Constant Strain Rate Compression Test (UCSRCT)

A constant uniaxial strain rate of 0.021 mm/sec is applied to test specimens in compression until failure. This test is conducted at different levels of confining pressure and temperature. Two replicates are tested at each confining level. The test is performed to determine the shear strength parameters of the Mohr-Coulomb failure criterion: cohesion (C) and internal friction angle (φ).

3.6 Summary

PANDA incorporates several material constitutive relationships that define the behavior of asphalt mixtures at a wide range of stress and temperature levels. In order to better utilize PANDA capabilities, there is a need to develop a robust experimental approach to determine its parameters and to evaluate the influence of asphalt material composition on these parameters. This chapter presents the design of derivative mixtures, which represent the composition of DGM, to assess the sensitivity of model parameters to a wide range of mixture types. In addition, it describes the experimental setup and factors used to test asphalt mixtures at various testing conditions. A DMT is used to characterize linear viscoelastic parameters and time-temperature shift factors, while an RCRT-VS is used to characterize nonlinear viscoelastic and viscoplastic parameters.

CHAPTER IV

VISCOELASTIC AND VISCOPLATIC PROPERTIES OF ASPHALT CONCRETE MIXTURES

4.1 Introduction

This chapter presents the characterization of viscoelastic (recoverable) and viscoplastic (irrecoverable) behavior of asphalt mixtures. The Schapery viscoelastic model is employed to represent the recoverable behavior, while the irrecoverable component is modeled by a modified Perzyna viscoplastic theory. First, the linear viscoelastic properties are obtained by measuring the dynamic modulus and phase angle at certain combinations of temperatures and frequencies. Then, an RCRT-VS is conducted at different temperatures (20, 40, and 55°C) and confinement stresses (70 and 140 kPa). This test identifies Schapery nonlinear parameters and viscoplastic parameters.

The systematic analytical procedure described in this chapter is used to determine the parameters of viscoelastic and viscoplastic PANDA models for three mixture types at different temperatures. Then, the results from the RCRT-VS are used to determine the evolution of shear strength parameters.

4.2 Background

Asphalt concrete mixtures consist of two matrices: (a) FAM, where fine aggregates passing sieve #16 are coated with asphalt binder and are surrounded by air voids (Sousa et al. 2013), and (b) CAM, where coarse aggregates retained on sieve #16 are coated with asphalt binder and are surrounded by air voids. The complex interactions between these matrices are affecting the total mechanical response of asphalt concrete mixtures. By designing the FAM and CAM as derivatives of a DGM, a wide range of mixtures is considered in the study.

Numerous experimental studies have shown that asphalt mixtures have a time-, rate-, and temperature-dependent response. Various types of experimental tests and models have been used to characterize the mechanical response of asphalt concrete mixtures, which exhibit nonlinear responses under different loading conditions (Schwartz and Carvalho 2007). Nonlinear responses are exhibited, even at very small strain or stress levels, due to the combined effect of different phenomena (Masad et al. 2005; Saadeh et al. 2007; and Im 2012), such as the difference between stiffness of the aggregate and the binder, interaction between aggregates and binder during the loading process, rotation and slippage of aggregates, temperature sensitivity of asphalt mixtures, and the evolution of micro-cracks and rate-dependent plastic response of asphalt concrete mixtures.

Most numerical models are developed to predict responses under specific test conditions. Therefore, they do not represent the behavior of asphalt materials under general 3D stress states and realistic environmental conditions that actually happen in the field (AASHTO 2008 and Roque et al. 2010). This raises another challenging task: identifying proper computational techniques for asphalt pavement performance predictions. The long life of pavements, a very large number of loading cycles (millions of loading cycles), complex constitutive relationships, and the complex nature of applied loading conditions make developing accurate and affordable computational techniques a challenging task.

This chapter contributes to filling the gap in constitutive modeling and computational techniques of a wide range of asphalt concrete mixtures under the compression state of cyclic creep loading by describing the coupled viscoelastic and viscoplastic constitutive relationships of PANDA. PANDA constitutive relationships are developed to model the complex response of these materials under more realistic conditions (Darabi et al. 2012a, 2012b, 2012c and 2013). The viscoelastic response can be dominant at low temperatures and low stress levels, whereas both viscoelastic and viscoplastic responses become significant at high temperatures. The developed constitutive relationships are calibrated, validated, and subsequently implemented in the well-known FE code ABAQUS using the UMAT subroutine. A robust and straightforward analytical procedure is developed to extract material parameters associated with each component of the PANDA model. This procedure is based on raw data analysis of the designed tests, which are described in the previous chapter. Then, the implemented constitutive model of PANDA is used to predict the complex mechanical response of asphalt mixtures and to conduct performance simulation of asphalt pavements.

4.3 PANDA Constitutive Model

In this section, a summary is presented of the main constitutive equations for the derived viscoelastic and viscoplastic PANDA models by Abu Al-Rub et al. (2010) and

Darabi et al. (2011a, 2011b, and 2012). Assuming small deformations, the total strain is decomposed into a viscoelastic (recoverable) strain and viscoplastic (irrecoverable) strain, such that:

$$\varepsilon_{ij} = \varepsilon_{ij}^{ve} + \varepsilon_{ij}^{vp} \tag{4.1}$$

where $\boldsymbol{\varepsilon}$, $\boldsymbol{\varepsilon}^{ve}$, and ε^{vp} are the total, viscoelastic, and viscoplastic strain tensors, respectively.

4.3.1 Linear Viscoelastic PANDA Model

Schapery's (1969a, 1969b) nonlinear viscoelastic model is implemented in PANDA. The nonlinear viscoelastic model can be written as follows:

$$\varepsilon_{ij}^{ve} = g_o D_o \overline{\sigma}_{ij}^{t} + g_1 \int_0^t \Delta D\left(\psi^t - \psi^\tau\right) \frac{d\left(g_2 \overline{\sigma}_{ij}^{\tau}\right)}{d\tau} d\tau \tag{4.2}$$

where

$$D\left(\psi^t\right) = \sum_{n=1}^{N} D_n \left[1 - \exp\left(-\lambda_n \psi^t\right)\right];\ \psi^t = \int_0^t \frac{d\xi}{a_T} \tag{4.3}$$

where ε_{ij}^{ve} is the viscoelastic strain tensor; $\overline{\sigma}_{ij}$ is the stress tensor; D_o is the instantaneous compliance; ΔD is the transient compliance; D_n and λ_n are the Prony series coefficients; N is the number of Prony series; a_T is the time-temperature shift factor; and g_o, g_1, and g_2 are the nonlinear viscoelastic model parameters. For the linear viscoelastic model, $g_o = g_1 = g_2 = 1$ is assumed. Table 4.1 lists the parameters associated with the linear viscoelastic constitutive relationship and their physical significance.

Table 4.1 List of Linear Viscoelastic Parameters and Their Physical Significance

Parameter	Physical Meaning
a_T	Time-temperature shift factor. Captures the response at different temperatures.
D_0	Instantaneous compliance. Related to the instantaneous viscoelastic response.
D_n	n^{th} Prony series coefficient related to transient compliance.
λ_n	n^{th} Retardation time associated with the n^{th} transient compliance D_n.
N	Number of Prony series to acquire desired accuracy. $N = 9$ is recommended. No need to be determined. It should be assumed.

4.3.2 Nonlinear Viscoelastic PANDA Model

Using the RCRT-VS protocol (Schapery 1969b, Masad et al. 2008, and Rahmani et al. 2013), three nonlinear parameters, g_o, g_1, and g_2, can be determined, as listed in Table 4.2. However, the nonlinear parameter g_o only affects the instantaneous response of asphalt mixes. Due to the time-dependent response of asphalt mixes, it is very difficult to measure the instantaneous strain response of asphalt mixes to characterize g_o. Even if measured, the instantaneous strain response has a high level of variability. Therefore, it is assumed that $g_o = 1$. Viscoelastic nonlinearity is captured through parameters g_1 and g_2.

Table 4.2 List of Nonlinear Viscoelastic Parameters and Their Physical Significance

Parameter	Physical Meaning
g_0	Affects the instantaneous response. It is recommended to assume $g_0 = 1$ because it is very difficult to measure the instantaneous response of asphalt mixtures. Nonlinear viscoelastic response is captured through nonlinear parameters g_1 and g_2. Time-temperature shift factor captures the response at different temperatures.
g_1	Controls nonlinearity in the transient compliance. Affects viscoelastic nonlinearity mostly during the loading stages.
g_2	Controls the nonlinear response during the recovery and at different loading rates.

To capture the effect of the multiaxial state of stresses on the nonlinear viscoelastic response of asphalt mixes, the total nonlinear viscoelastic strain tensor, ε_{ij}^{nve}, is decomposed into deviatoric strain tensor e_{ij}^{nve} and volumetric component ε_{kk}^{nve}, such that:

$$\varepsilon_{ij}^{nve} = e_{ij}^{nve} + \frac{1}{3}\varepsilon_{kk}^{nve}\delta_{ij} \tag{4.4}$$

Deviatoric and volumetric components of the viscoelastic strain can be expressed as:

$$e_{ij}^{nve,t} = \frac{1}{2} g_o J_o \overline{S}_{ij}^{t} + \frac{1}{2} g_1 \int_0^t \Delta J \left(\psi^t - \psi^\tau \right) \frac{d\left(g_2 \overline{S}_{ij}^{\tau} \right)}{d\tau} d\tau \tag{4.5}$$

$$\varepsilon_{kk}^{t} = \frac{1}{3} g_o B_o \overline{\sigma}_{kk}^{t} + \frac{1}{3} g_1 \int_0^t \Delta B \left(\psi^t - \psi^\tau \right) \frac{d\left(g_2 \overline{\sigma}_{kk}^{\tau} \right)}{d\tau} d\tau \tag{4.6}$$

where $\overline{S}_{ij}$ are the components of the deviatoric stress tensor and $\overline{\sigma}_{kk}$ is the volumetric stress.

Shear and bulk instantaneous (J_o and B_o) and transient (ΔJ and ΔB) compliances are calculated based on the identified linear viscoelastic model parameters using the following equations:

$$J_o = 2\left(1+\nu\right) D_o ; \Delta J\left(\psi\right) = 2\left(1+\nu\right) \Delta D\left(\psi\right) \tag{4.7}$$

$$B_o = 3\left(1-2\nu\right) D_o ; \Delta B\left(\psi\right) = 3\left(1-2\nu\right) \Delta D\left(\psi\right) \tag{4.8}$$

Deviatoric and volumetric components of the stress for the RCRT-VS under confinement stress, $\overline{\sigma}_c$, and additional axial stress, $\Delta\overline{\sigma}$, are calculated as follows:

$$\frac{1}{3} \overline{\sigma}_{kk} \delta_{ij} = \left(\sigma_c + \frac{\Delta\sigma}{3} \right) \delta_{ij} ; \overline{S}_{ij} = \begin{bmatrix} \frac{2}{3}\Delta\sigma & 0 & 0 \\ 0 & -\frac{1}{3}\Delta\sigma & 0 \\ 0 & 0 & -\frac{1}{3}\Delta\sigma \end{bmatrix} \tag{4.9}$$

4.3.3 Viscoplastic PANDA Model

Perzyna's (1971) viscoplastic model with modified Drucker-Prager yield surface is implemented in PANDA. The viscoplastic flow rule can be written as:

$$\dot{\varepsilon}_{ij}^{vp} = \dot{\gamma}^{vp} \frac{\partial F}{\partial \bar{\sigma}_{ij}}; \quad \dot{\gamma}^{vp} = \Gamma^{vp} \left\langle \frac{f}{\sigma_y^o} \right\rangle^N \tag{4.10}$$

where ε_{ij}^{vp} is the viscoplastic strain tensor and $\dot{\gamma}^{vp}$ is the viscoplastic multiplier. Perzyna expressed the viscoplastic multiplier in terms of an overstress function and a viscosity parameter that relates the rate of viscoplastic strain to the current stresses. *N* is the viscoplastic rate-sensitivity exponent parameter, $\langle \ \rangle$ are the Macaulay brackets defined by $\langle X \rangle = \left(X + |X| \right) / 2$, and σ_y^o is a yield stress quantity used to normalize the yield surface and can be assumed as unity.

Drucker-Prager yield surfaces have been used by a number of researchers for describing the viscoplastic flow behavior of HMA because they consider confinement, aggregate friction, aggregate interlocking, and HMA dilative behavior. A modified Drucker-Prager yield function, *f,* is employed that distinguishes between HMA behavior in compression and extension and also considers pressure sensitivity and plastic potential function *F*, such that:

$$f = \tau - \alpha I_1 - \kappa(p); \quad F = \tau - \beta I_1; \quad \tau = \frac{\sqrt{3J_2}}{2}\left[1 + \frac{1}{d^{vp}} + \left(1 - \frac{1}{d^{vp}}\right)\frac{3J_3}{\sqrt{3J_2^3}}\right] \tag{4.11}$$

where α and β are the pressure-sensitive material parameters; *k(p)* is the isotropic hardening function associated with the cohesive characteristics of the material and depending on the effective viscoplastic strain *p*; $I_1 = \overline{\sigma}_{kk}$ is the first stress invariant; τ is the deviatoric effective shear stress modified to distinguish between HMA behavior under compression and extension loading conditions; $J_2 = \frac{1}{2}\overline{S}_{ij}\overline{S}_{ij}$ and $J_3 = \frac{1}{2}\overline{S}_{ij}\overline{S}_{jk}\overline{S}_{ki}$ are second and third deviatoric stress invariants, respectively; and d^{vp} is the model parameter that distinguishes the viscoplastic responses during extension and contraction modes of loadings.

The d^{vp} value should have a range of $0.778 \leq d^{vp} \leq 1$ to ensure that the yield surface convexity condition is maintained. The effect of parameter d^{vp} on the viscoplastic response of bituminous materials is shown schematically in Figure 4.1. Point A in this figure represents a point under hydrostatic pressure. Increasing the axial stress causes both the first stress invariant, $\overline{I_1}$, and the second deviatoric stress invariant, $\overline{J}_2$, to increase. Hence, point A follows the stress path AB until the material yields at point B. On the other hand, by decreasing the axial stress (extension test), point A follows the stress path AC. The modified Drucker-Prager yield surface ($d^{vp} = 0.778$) shows that the material yields sooner at point C because the inclusion of the d^{vp} parameter reduces both the internal slope, α, and the hardening, κ, (at point B) to α' and κ' (at point C), respectively. This feature of the modified Drucker-Prager yield function helps distinguish the yield behavior in the compression or extension mode of loading.

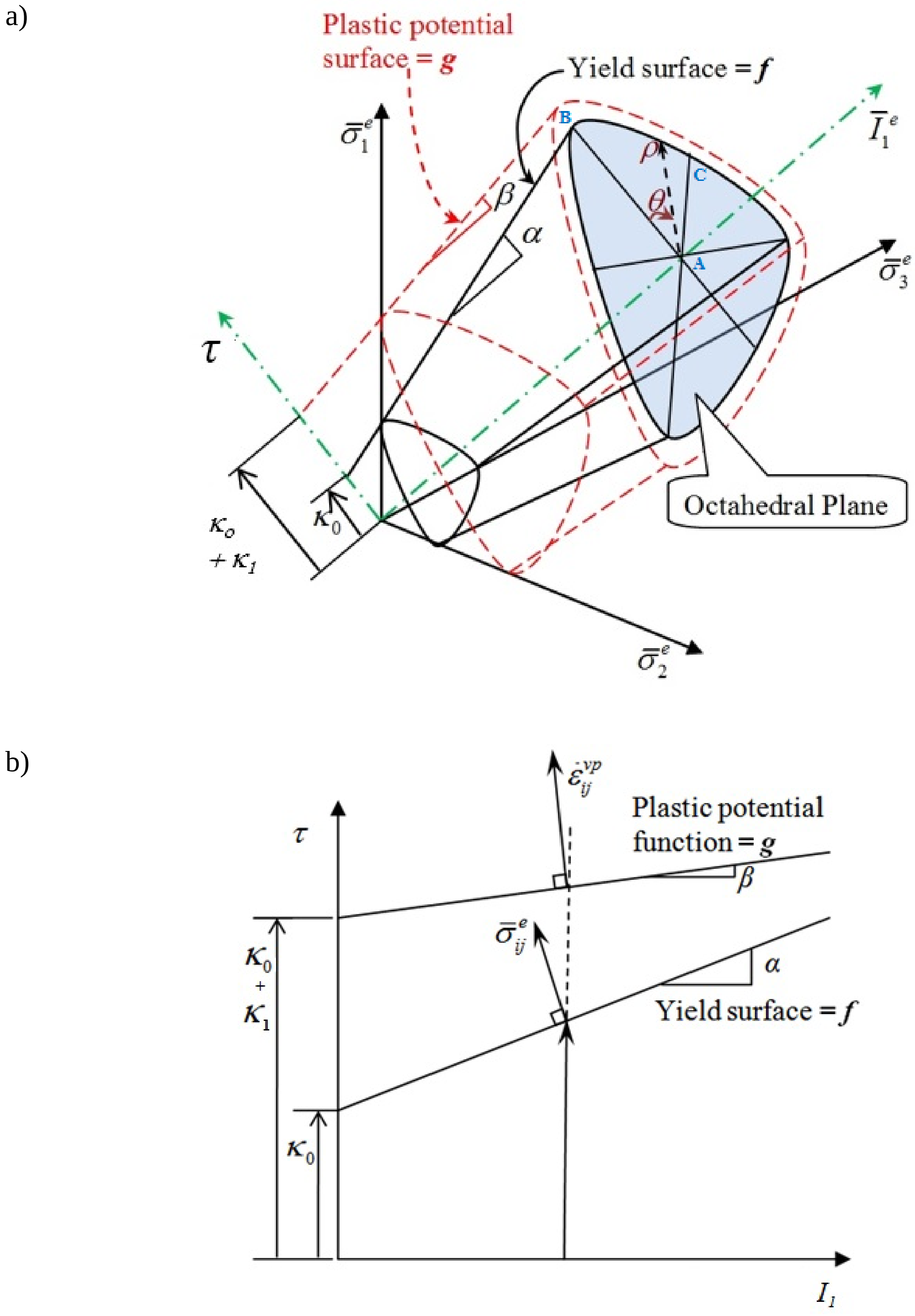

Figure 4.1 Graphical Schematic Illustration of the Influence of the Stress Path on the Modified Drucker-Prager Yield Surface

Table 4.3 List of Viscoplastic Parameters (Huang 2008, Abu Al-Rub et al. 2009, and Darabi et al. 2012c)

Parameter	Physical Significance
α	Related to the angle of friction of the asphalt mixtures and ranges from 0.1 to 0.3.
β	Material parameter describing dilation or contraction behavior, related to the angle of friction and the dilation characteristics of asphalt mixtures.
σ_y^o	Yield stress quantity used to normalize the overstress function and can be assumed unity.
Γ^{vp}	Viscoplastic fluidity parameter such that its inverse has the units of time and represents the viscoplasticity-relaxation time.
d^{vp}	Ratio of yield strength in tension to that in compression. Fixed for most asphalt mixes = 0.778.
N	Viscoplastic rate sensitivity exponent.
κ_0	Initial yield strength. It has a very low value at high temperatures. Does not affect the results very much and can be assumed to have a small value between 50 and 150 kPa for most asphalt mixtures.
κ_1	The hardening limit of asphalt mixtures against viscoplastic deformation. Is in the order of compressive strength of asphalt mixtures at 40^{o}C.
κ_2	Strain-hardening rate.

The isotropic hardening function, κ, is expressed as an exponential function of the effective viscoplastic strain, *p*, such that:

$$\kappa(p) = \kappa_o + \kappa_1\left[1 - \exp\left(-\kappa_2 p\right)\right]; \quad \dot{p} = \left[1 + 2\left(\frac{0.5 + \beta/3}{1 - \beta/3}\right)\right]^{-0.5} \sqrt{\dot{\varepsilon}_{ij}^{vp}\ \dot{\varepsilon}_{ij}^{vp}} \tag{4.12}$$

Table 4.3 lists the viscoplastic parameters and their physical significance (Huang 2008, Abu Al-Rub et al. 2009, and Darabi et al. 2012c).

4.4 Calibration of PANDA Constitutive Model Parameters

The procedure for identifying linear viscoelasticity, nonlinear viscoelasticity, and viscoplasticity parameters for the DGM, FAM, and CAM is presented as follows.

4.4.1 Calibration of Linear Viscoelastic PANDA Model Using DMT

This section presents a systematic procedure to identify time-temperature shift factors, as well as linear viscoelastic parameters based on DMT data. Dynamic modulus *E** and phase angle θ at each frequency and temperature are the outputs of the DMT. Values of complex compliance *D** is determined such that:

$$\log D^* = -\log E^* \tag{4.13}$$

A sigmoidal-type function is used to fit the experimental data and to obtain the time-temperature shift factors. The sigmoidal function for the complex compliance can be written as:

$$-\log\left|D^*\right| = \delta + \frac{\alpha}{1 + \exp\left[\beta + \gamma \log\left(\omega_r\right)\right]} \tag{4.14}$$

where ω_r is the reduced frequency, δ is the maximum value of the dynamic compliance, $\delta + \alpha$ is the minimum value of the dynamic compliance, and β and γ are parameters describing the shape of the sigmoidal function. Figure 4.2 represents the development of the dynamic modulus master curve before and after the time-temperature shifting. Time-temperature shift factor is defined as:

$$a_T = \frac{\omega_r}{\omega} \tag{4.15}$$

where ω is the angular frequency. The term a_T is the time-temperature shift factor at each temperature, as presented in Figure 4.2. Equations (4.14) and (4.15) introduce 4 + (n_T –1) unknowns that should be determined: $\alpha, \beta, \delta, \gamma, a_T(n_1), a_T(n_2), ...a_T(n_T\text{-}1)$; where n_T is the number of temperatures at which the test is conducted. It should be noted that the number of unknown time-temperature shift factors are (n_T –1) because a_T is known at the selected reference temperature T_r (i.e., $a_T\left(T_r\right) = 1$). The error function is defined as:

$$R^2 = 1 - \frac{SSE}{SST} \tag{4.16}$$

where $SSE = \sum_{i=1}^{M}\left(\log D_{\mathrm{exp}} - \log D_{fit}\right)^2$, $SST = \sum_{i=1}^{M}\left(\log D_{\mathrm{exp}} - \overline{\log D}\right)^2$, M is the number of data points obtained from the DMT, $\log D_{\mathrm{exp}}$ is the experimentally measured compliance, $\log D_{fit}$ is the compliance fitted using Eq. (4.14), and $\overline{\log D}$ is the mean value of the measured compliance.

The $4+(n_T-1)$ unknown variables are determined by minimizing the error function, R^2, using the Generalized Reduced Gradient (GRG) algorithm, which is also available in the Microsoft Excel® solver. Initial values for the unknown variables are set in the Excel solver by selecting the corresponding cells for each variable. The objective cell is the calculated value of R^2. The sigmoidal function parameters and time-temperature shift factors are identified by minimizing R^2. The fitting parameters are determined by a numerical optimization using the solver function in Excel.

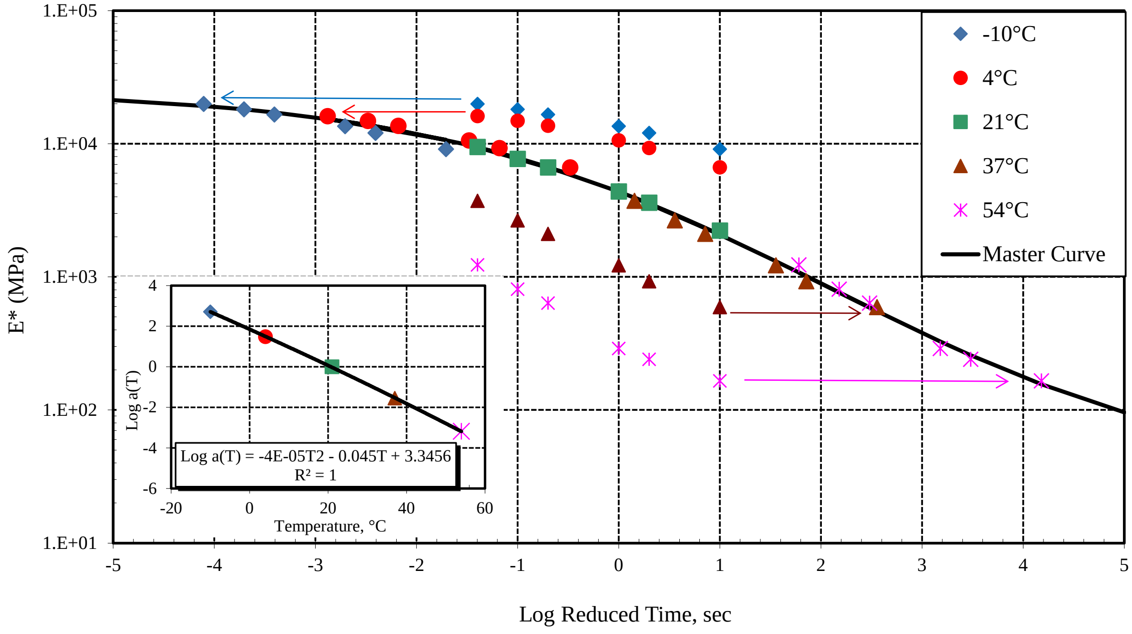

Figure 4.2 Development of a Dynamic Modulus Master Curve

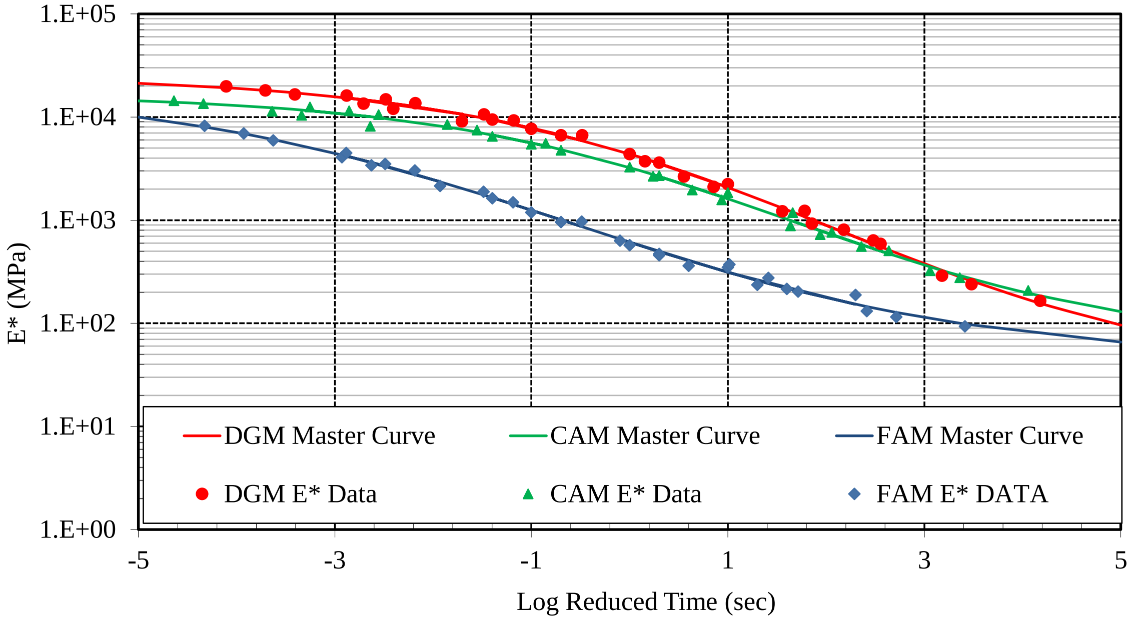

a) Dynamic Modulus Master Curves

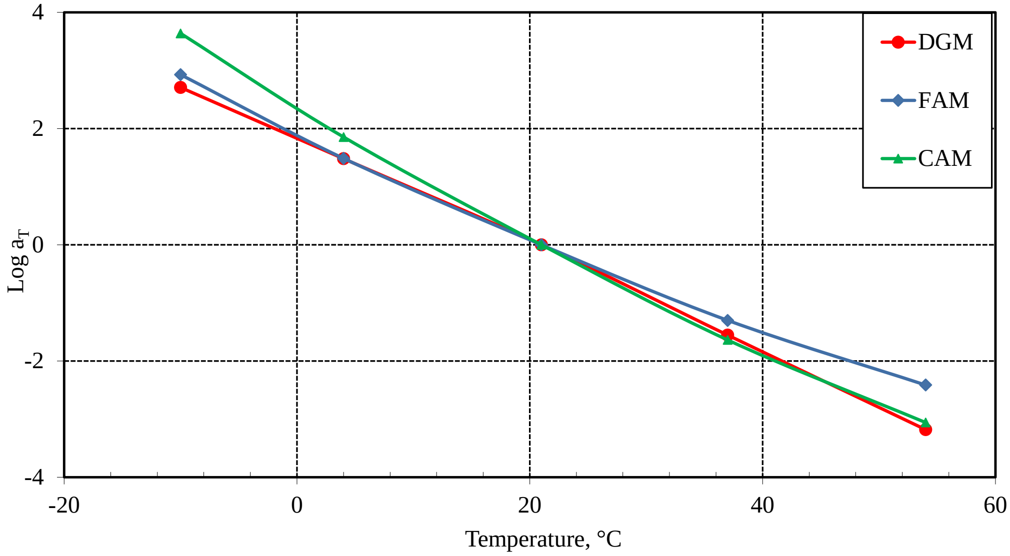

b) Time-Temperature Shift Factors

Figure 4.3 Development of Dynamic Modulus Master Curves for DGM, FAM, and CAM

Figure 4.3 shows the dynamic modulus master curves generated for the three types of asphalt mixtures (DGM, FAM, and CAM). The master curves show that CAM behaves like DGM at high temperatures. The similarity in both mixtures' behavior can be related to the drop of the viscoelastic role of the FAM in the DGM. In addition, the binder contents of the DGM and CAM are close: 4.4 and 3.4% by mixture weight, respectively. However, the FAM behaves differently due to a high binder content of 8%. This proves that the viscoelastic response could be dominant at low temperatures, whereas both viscoelastic and viscoplastic responses become significant at high temperatures.

Once the time-temperature shift factors are identified, linear viscoelastic model parameters can be determined. Using the experimental data, storage compliance, $D' = \left|D^*\right|\cos\delta$, and loss compliance, $D'' = \left|D^*\right|\sin\delta$, are calculated, as shown in Figure 4.4.a. The Prony series coefficients shown in (Eq. 4.16) can be obtained by minimizing the error function, shown in (Eq. 4.17).

$$D'_{Model} = D_0 + \sum_{n=1}^{N} \frac{D_n}{1+\omega^2/\lambda_n^2}; D''_{Model} = \sum_{n=1}^{N} \frac{\omega/\left(\lambda_n D_n\right)}{1+\omega^2/\lambda_n^2} \tag{4.16}$$

$$ERR = \left(\frac{D'_{Model}}{D'_{Exp}} - 1\right)^2 + \left(\frac{D''_{Model}}{D''_{Exp}} - 1\right)^2 \tag{4.17}$$

where *N* is the number of Prony series coefficients, D_o is the instantaneous compliance, and D_n is the n^{th} transient compliance associated with the n^{th} retardation time, λ_n.

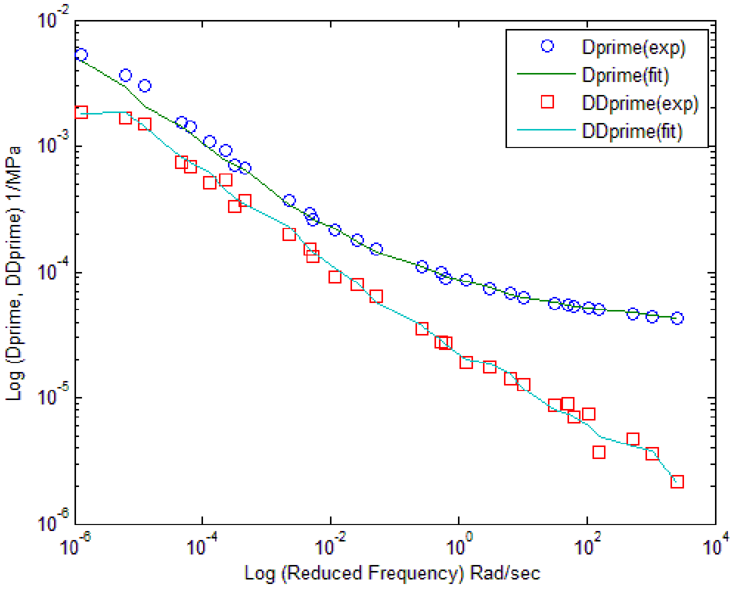

a) Storage and Loss Compliances

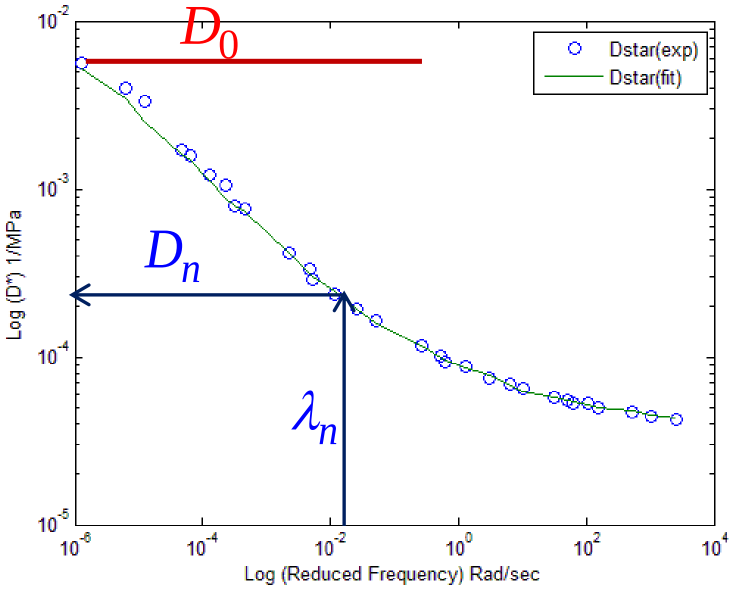

b) Complex Compliance

Figure 4.4 Development of Storage, Loss, and Complex Compliances in Frequency Domain

Once the Prony series coefficients are determined in the frequency domain, as shown in Figure 4.4.b, the compliance in time domain can be formulated, as shown in Equation (4.18) with the same Prony series coefficients.

$$D(t) = D_0 + \sum_{n=1}^{N} D_n \left(1 - \exp\left(\frac{-t}{\tau_n} \right) \right) \tag{4.18}$$

The Prony series coefficients for the DGM, FAM, and CAM are identified based on the aforementioned interconversion relationships between the Prony series coefficients and the loss and storage dynamic moduli using the nonlinear GRG method. These Prony series values are tabulated in Table 4.4.

Table 4.4 Linear Viscoelastic Model Parameters

	DGM		FAM		CAM	
n	$\lambda_n\left(1/\mathrm{s}\right)$	D_n (MPa^{-1})	$\lambda_n\left(1/\mathrm{s}\right)$	D_n (MPa^{-1})	$\lambda_n\left(1/\mathrm{s}\right)$	D_n (MPa^{-1})
D_0		5.16×10^{-5}		6.34×10^{-5}		5.92×10^{-5}
1	2.38×10^{2}	1.20×10^{-5}	3.47×10^{2}	2.65×10^{-5}	3.16×10^{2}	1.11×10^{-5}
2	1.73×10^{1}	2.95×10^{-5}	3.35×10^{1}	4.73×10^{-5}	2.09×10^{1}	2.77×10^{-5}
3	1.25×10^{0}	6.23×10^{-5}	3.22×10^{0}	7.55×10^{-5}	1.39×10^{0}	6.12×10^{-5}
4	9.07×10^{-2}	1.40×10^{-4}	3.11×10^{-1}	1.80×10^{-4}	9.19×10^{-2}	1.53×10^{-4}
5	6.57×10^{-3}	4.82×10^{-4}	3.00×10^{-2}	2.97×10^{-4}	6.09×10^{-3}	4.14×10^{-4}
6	4.76×10^{-4}	7.03×10^{-4}	2.89×10^{-3}	6.47×10^{-4}	4.04×10^{-4}	6.86×10^{-4}
7	3.45×10^{-5}	3.14×10^{-3}	2.78×10^{-4}	8.17×10^{-4}	2.68×10^{-5}	2.49×10^{-3}
8	2.50×10^{-6}	4.79×10^{-3}	2.68×10^{-5}	2.30×10^{-3}	1.77×10^{-6}	3.58×10^{-3}
9			2.59×10^{-6}	1.23×10^{-2}		

4.4.2 Calibration of Nonlinear Viscoelastic PANDA Model Using RCRT-VS

This section outlines the procedure for identifying nonlinear viscoelastic parameters using RCRT-VS data of the DGM, FAM, and CAM. The instantaneous strain response at high temperatures is very small compared to the total viscoelastic strain level. In addition, measuring such small values during the cyclic creep-recovery test is very difficult and depends on several other factors such as date collection rate, loading time, and rest period. The measured value of the instantaneous strain has a high level of variability, making it difficult to assign it a unique value. Thus, g_0 is assumed to be unity, and viscoelastic nonlinearity is captured through the parameters g_1 and g_2. Nonlinear viscoelastic parameters g_1 and g_2 govern the nonlinearity of the transient portion of the strain response (or equivalently, the time-dependent portion of the viscoelastic strain response). During creep (i.e., loading stage), viscoelastic nonlinearity is stemmed through the combined effects of g_1 and g_2. However, g_2 is the parameter controlling the nonlinear response during recovery (i.e., the unloading stage). The time-temperature shift factor captures the response at different temperatures (AASHTO 2008).

To characterize nonlinear viscoelastic responses, irrecoverable strain has to be removed from the strain response. During creep, both recoverable and irrecoverable strains evolve. During recovery, however, viscoplastic strain remains constant and viscoelastic strain recovers. A data reduction method is used to characterize nonlinear viscoelastic parameters using the RCRT-VS. Stress and strain responses during the first loading cycle of the RCRT-VS are schematically presented in Figure 4.5 to show the procedure for identifying nonlinear viscoelastic parameters.

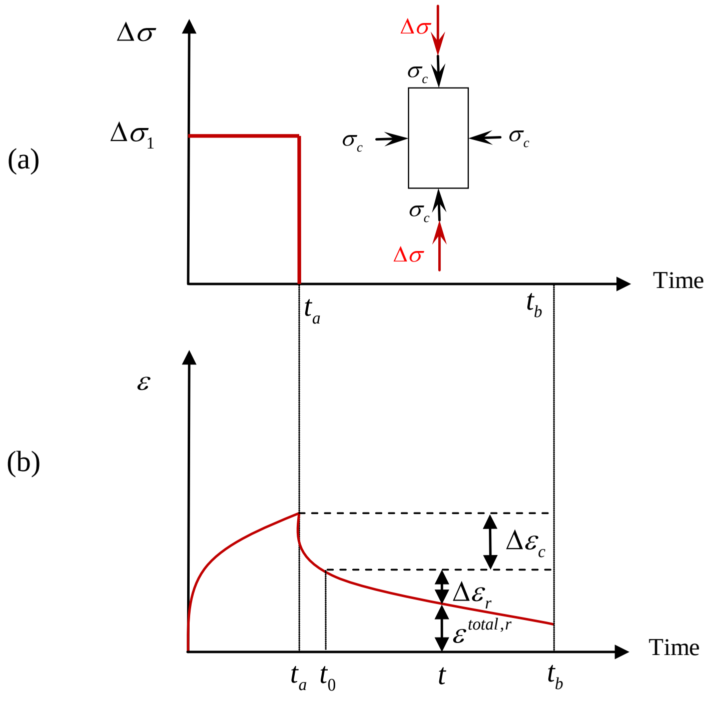

Figure 4.5 Schematic Representation of the Strain Response During a Cycle of RCRT-VS

Parameter g_2 is determined by selecting an arbitrary point during recovery (e.g., t_0). It is recommended to assume t_0 such that $t_0 - t_a$ is $\frac{1}{10}$ of the rest period. Then, the recovered strain, $\Delta\varepsilon_r$ is calculated for every point after t_0 during the rest period. $\Delta\varepsilon_r$ can easily be calculated using experimental data, such that:

$$\Delta\varepsilon_r = \varepsilon^{total,r}\left(t_0\right) - \varepsilon^{total,r}\left(t\right) \tag{4.19}$$

Using Equations (4.5) to (4.9) and assuming the viscoelastic response under pure confinement to be linear yields the following relations for deviatoric and volumetric components of viscoelastic strain during recovery:

$$e_{11}^{r,t} = \frac{1}{2} g_2^a \left(\Delta J\left(\psi^t\right) - \Delta J\left(\psi^t - \psi^{t_a}\right)\right) \frac{2}{3} \Delta\sigma_1 \tag{4.20}$$

$$\varepsilon_{vol}^{r,t} = \frac{1}{3} g_2^a \left(\Delta B\left(\psi^t\right) - \Delta B\left(\psi^t - \psi^{t_a}\right)\right) \Delta\sigma_1 + \frac{1}{3}\left(B_0 + \Delta B\left(\psi^t\right)\right) 3\sigma_c \tag{4.21}$$

where t_a is the time corresponding to the end of loading. Deviatoric and volumetric components of $\Delta\varepsilon_r$ are calculated using Equations. (4.20) to (4.21), such that:

$$\Delta e_{11,r} = e_{11}^{r,t} - e_{11}^{r,t_0}; \qquad \Delta\varepsilon_{vol,r} = \varepsilon_{vol}^{r,t} - \varepsilon_{vol}^{r,t_0} \tag{4.22}$$

Equations (4.20) to (4.22) show that the only unknown to analytically calculate deviatoric and volumetric components of $\Delta\varepsilon_r$ is g_2. g_2 is calculated by minimizing the error between experimentally measured components of $\Delta\varepsilon_r$ (i.e., Eq. (4.19)) and analytically calculated components of $\Delta\varepsilon_r$ (i.e., Eq. (4.21)).

Once the parameter g_2 is defined, g_1 can be calculated. $\Delta\varepsilon_c$ is determined from the experimental measurements. The term $\Delta\varepsilon_c$ is the difference between the total strain at the end of loading and the strain at an arbitrary point during the rest period (i.e., $\Delta\varepsilon_c = \varepsilon^{total}\left(t_a\right) - \varepsilon^{total,r}\left(t\right)$), as shown in Figure 4.3. $\Delta\varepsilon_c$ is calculated using the nonlinear viscoelastic constitutive relationship, such that:

$$\Delta\varepsilon_c = \varepsilon^{nve}\left(t_a\right) - \varepsilon^{nve}\left(t\right) \tag{4.23}$$

g_2 is the only unknown in calculating $\Delta\varepsilon_c$ using Equations (4.20) to (4.21). g_1 is identified by minimizing the error between the experimentally measured and calculated values of $\Delta\varepsilon_c$. If both axial and radial strains are measured, the procedure outlined above is repeated for both volumetric and deviatoric components of $\Delta\varepsilon_c$. The parameter g_1 is the average of the g_1 parameters obtained from deviatoric and volumetric components of $\Delta\varepsilon_c$.

Having the nonlinear parameters on hand for different stress levels during the RCRT-VS (as shown in Figure 4.6) allows the nonlinear viscoelastic behavior of the asphalt mixtures to be characterized. Figure 4.7 shows that the nonlinear viscoelastic parameters predict the recovered strain well. Once the linear and nonlinear viscoelastic parameters are known, the irrecoverable strain response can be obtained by subtracting the viscoelastic behavior from the total measured strain response, as presented in Figure 4.8. Figure 4.9 presents the identified values of the nonlinear parameters for different temperatures, while Figure 4.10 presents the identified values of the nonlinear parameters for different confinement levels.

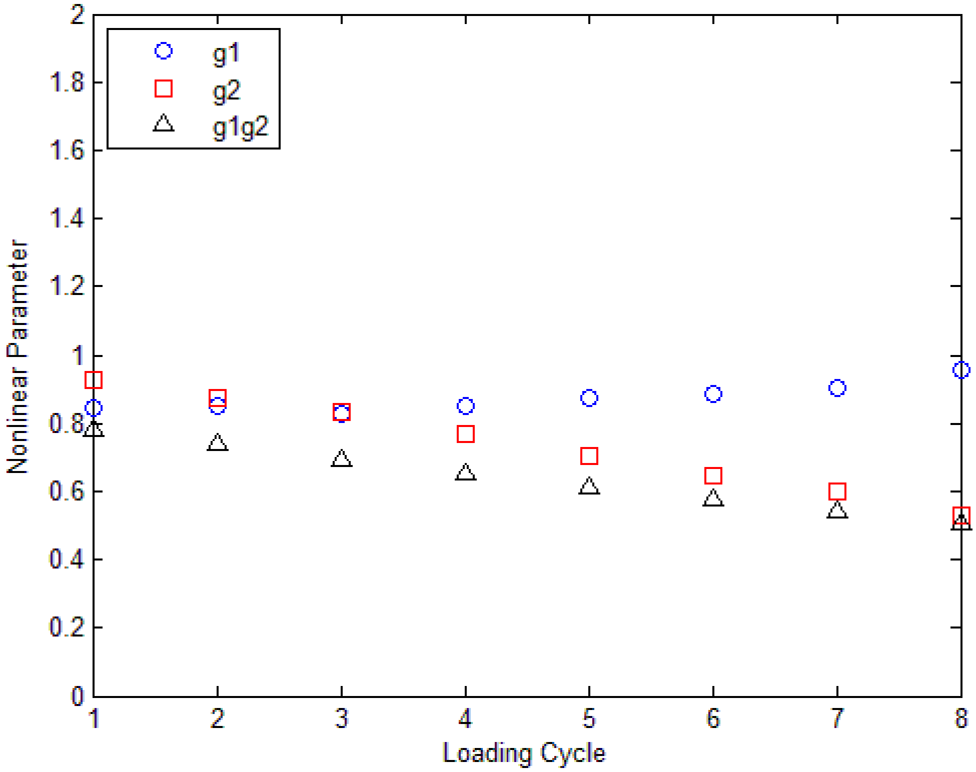

Figure 4.6 Variation in Nonlinear Viscoelastic Parameters with Respect to Loading Cycle

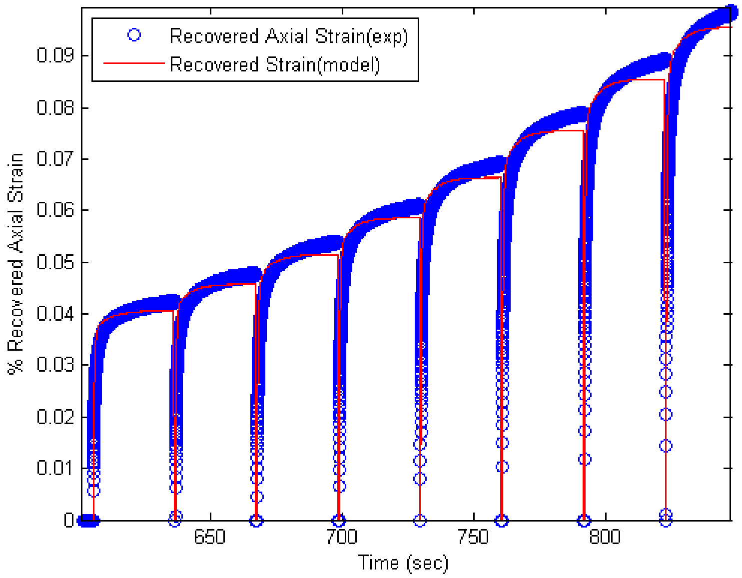

a) Recovered Axial Strain Vs. Time

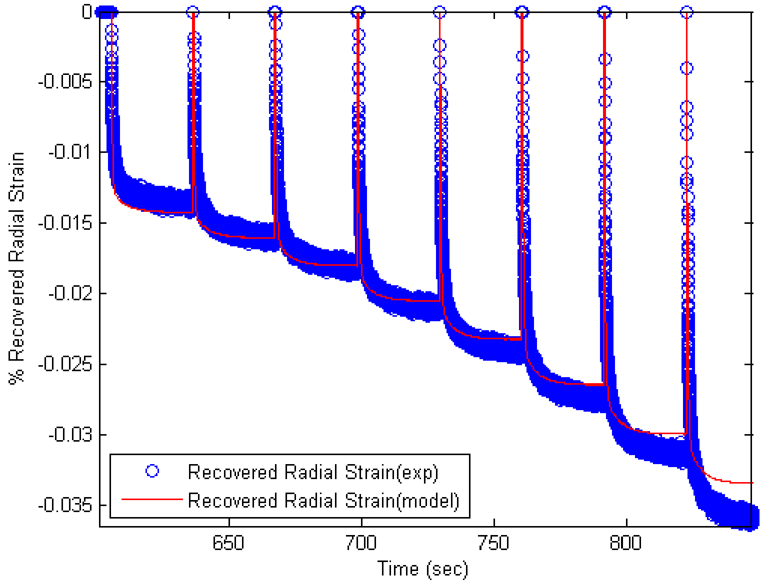

b) Recovered Radial Strain Vs. Time

Figure 4.7 Experimental Measurements and Model Predictions of the Recovered Axial and Radial Strains

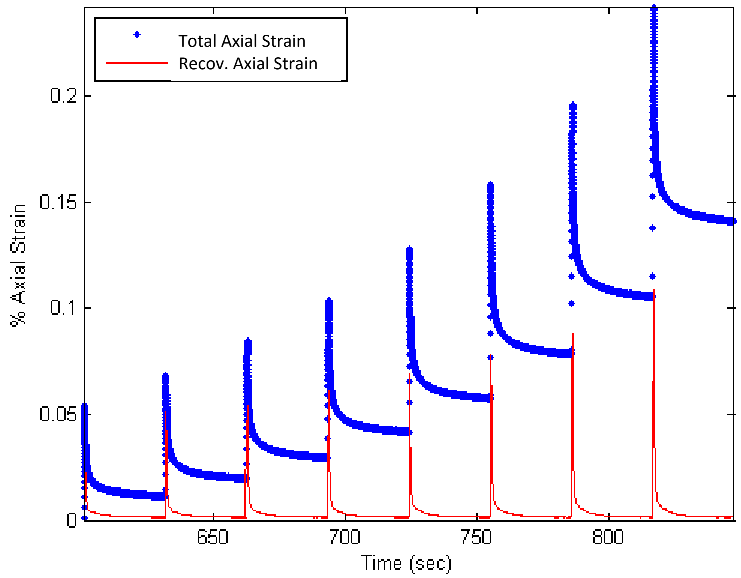

a) Recovered and Total Axial Strain Vs. Time

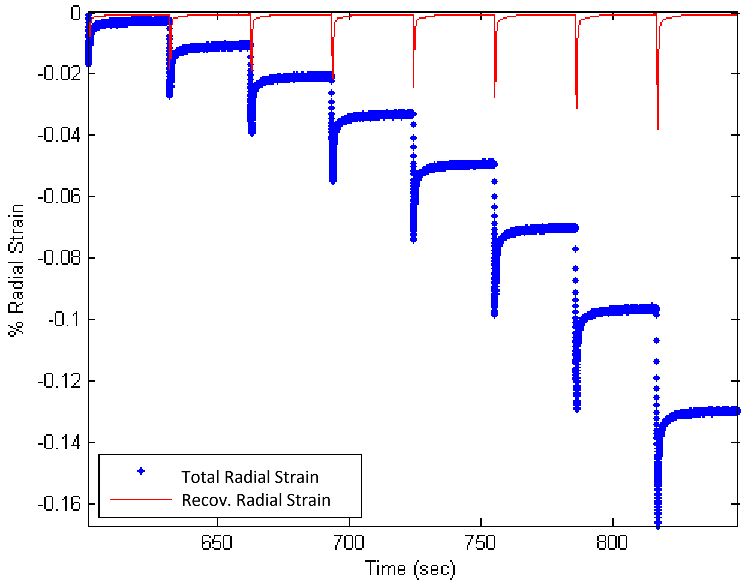

b) Recovered and Total Radial Strain Vs. Time

Figure 4.8 Recovered and Total Axial and Radial Strains

a)

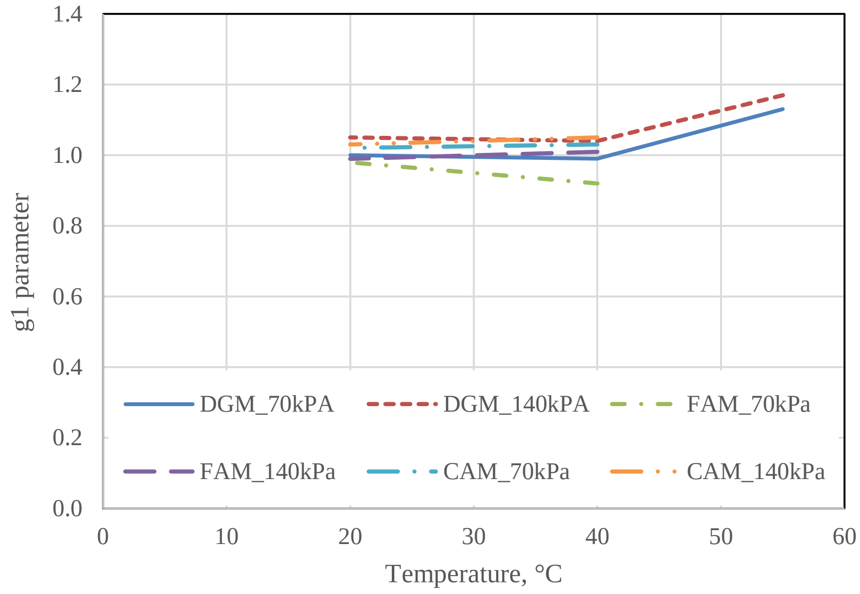

b)

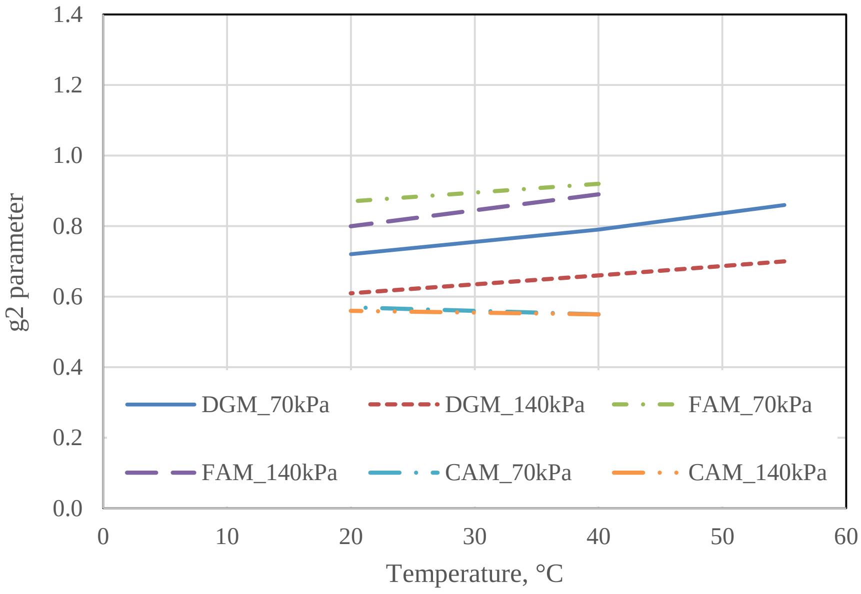

Figure 4.9 Variation in Nonlinear Viscoelastic Parameters with Respect to Temperature

c)

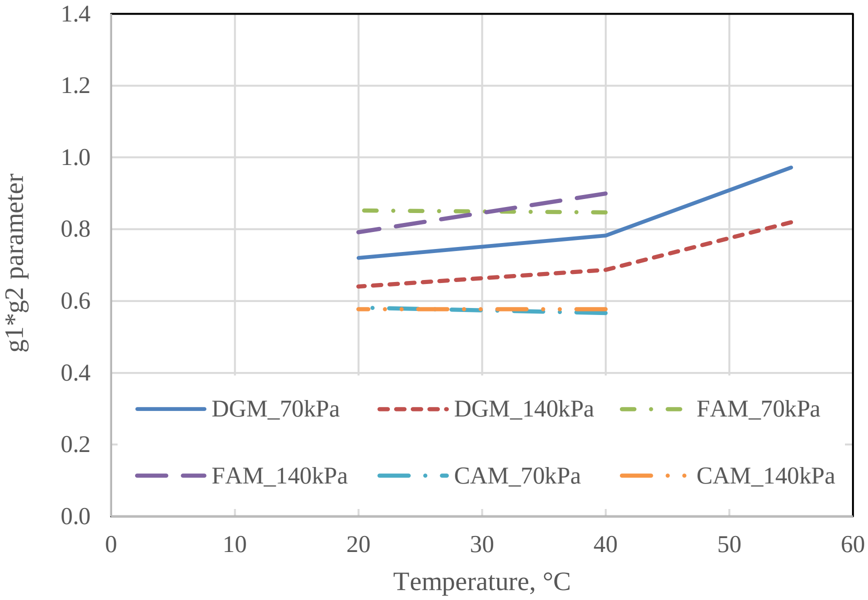

Figure 4.9 Continued

a)

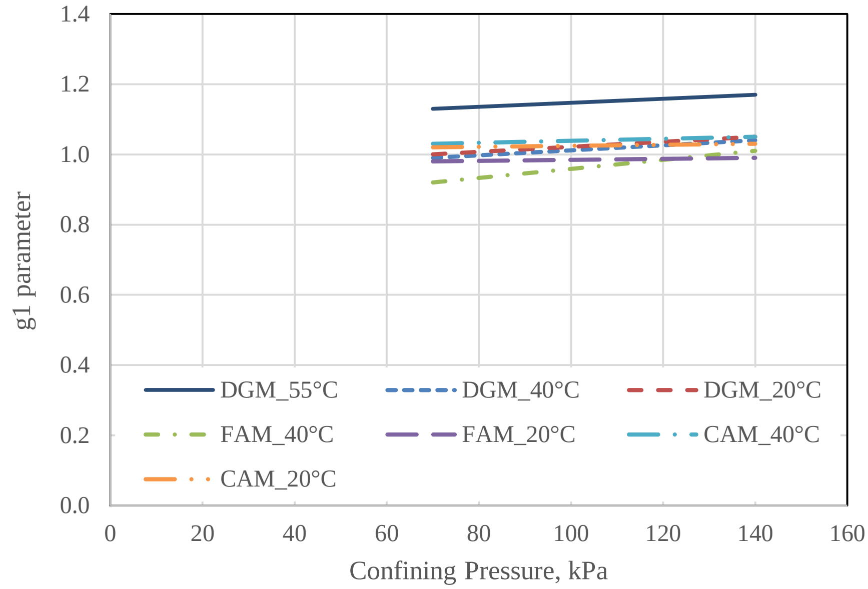

Figure 4.10 Variation in Nonlinear Viscoelastic Parameters with Respect to Confinement Level

b)

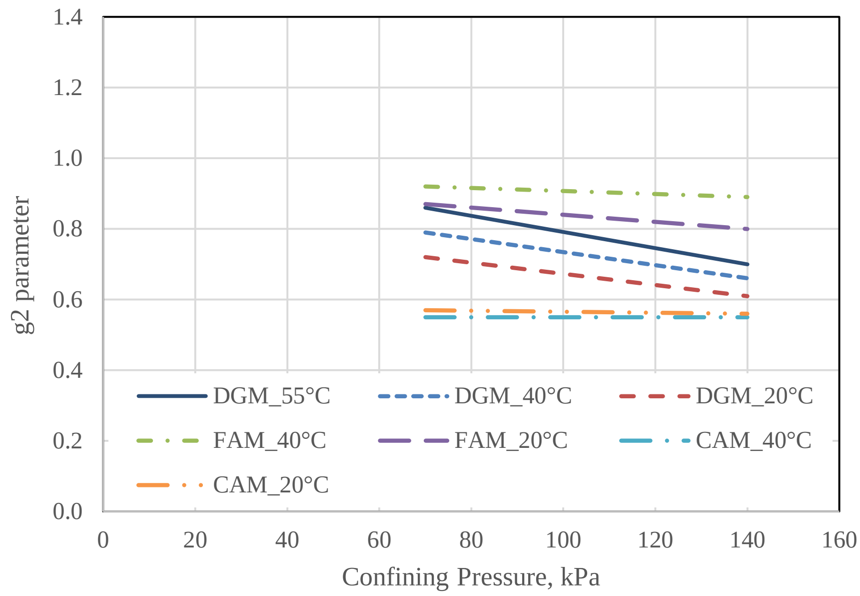

c)

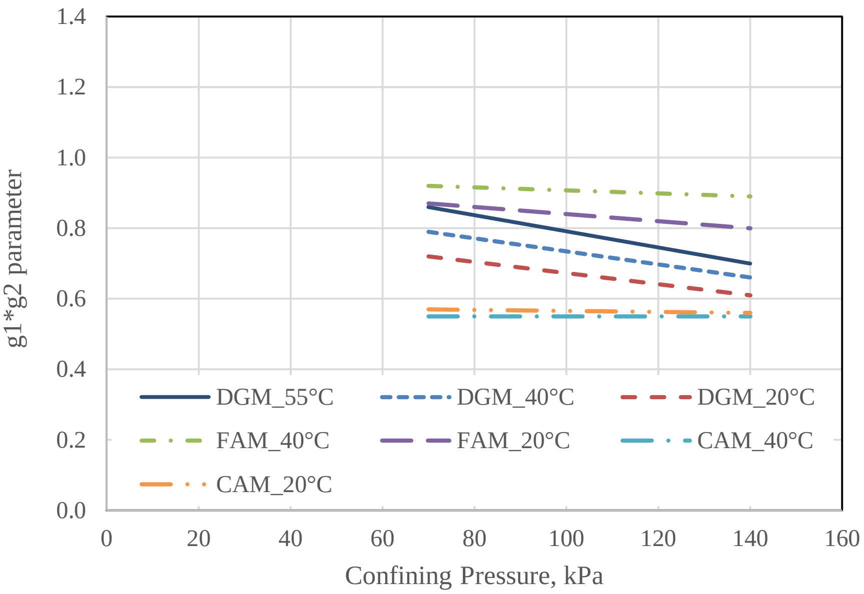

Figure 4.10 Continued

According to Figures 4.9 and 4.10, the $g_1 \times g_2$ parameter, which expresses the transient response, increases as the temperature increases, while the $g_1 \times g_2$ parameter decreases as the confinement level increases. The asphalt materials become more nonlinear as temperature increases. Due to the effect of confinement level, the asphalt materials become more resistant to applied axial stress, producing less strain magnitude. As confinement level increases, slippage and change of the aggregate orientation during deformation decrease, which means that the confinement pressure makes the material stiffer and less time-dependent.

The nonlinear viscoelastic behavior of the FAM is greater than the nonlinear viscoelastic behavior of the DGM, while the nonlinear viscoelastic behavior of the CAM is less than the nonlinear viscoelastic behavior of the DGM. The FAM, which has high asphalt binder content, has more aggregate mobility than the CAM, which has low asphalt binder content. At the same stress level, the nonlinear parameter g_2 values of the CAM are lower those of the FAM, and the nonlinear parameter g_1 values of the CAM are higher than those of the FAM. The CAM is more resistant to applied stress, producing less strain magnitude than the FAM. Especially at high temperatures, a FAM with high binder content (soft material) is more susceptible to nonlinear deformation than a CAM with low binder content (stiff material).

The nonlinear viscoelastic parameters of the DGM, FAM, and CAM at different temperatures and confining levels are summarized in Table 4.5.

Table 4.5 Nonlinear Viscoelastic Model Parameters

Mixture Type	Temperature, °C	Confining Level, kPa	g1	g2	g1 × g2
DGM	55	70	1.13	0.86	0.97
		140	1.17	0.70	0.82
	40	70	0.99	0.79	0.87
		140	1.04	0.66	0.58
	20	70	1.00	0.72	0.72
		140	1.05	0.61	0.64
FAM	40	70	0.92	0.92	0.85
		140	1.01	0.89	0.90
	20	70	0.98	0.87	0.85
		140	0.99	0.80	0.79
CAM	40	70	1.03	0.55	0.57
		140	1.05	0.55	0.58
	20	70	1.02	0.57	0.58
		140	1.03	0.56	0.58

4.4.3 Calibration of Viscoplastic PANDA Model Using RCRT-VS

This section outlines the procedure for identifying viscoplastic parameters using RCRT-VS data. Several viscoplastic parameters are assumed because they do not vary significantly among asphalt mixtures and can be assumed constant with reasonable accuracy.

Equation (4-2) is used to calculate viscoelastic strain response during the loading stage of the RCRT-VS once linear and nonlinear viscoelastic parameters are identified. Viscoelastic strain is subtracted from total strain to obtain viscoplastic strain response during the creep part of RCRT-VS. Figure 4.11 schematically illustrates the extraction of viscoelastic and viscoplastic strain responses from the total measured strain. The viscoplastic parameters are identified by analyzing the extracted viscoplastic strain response.

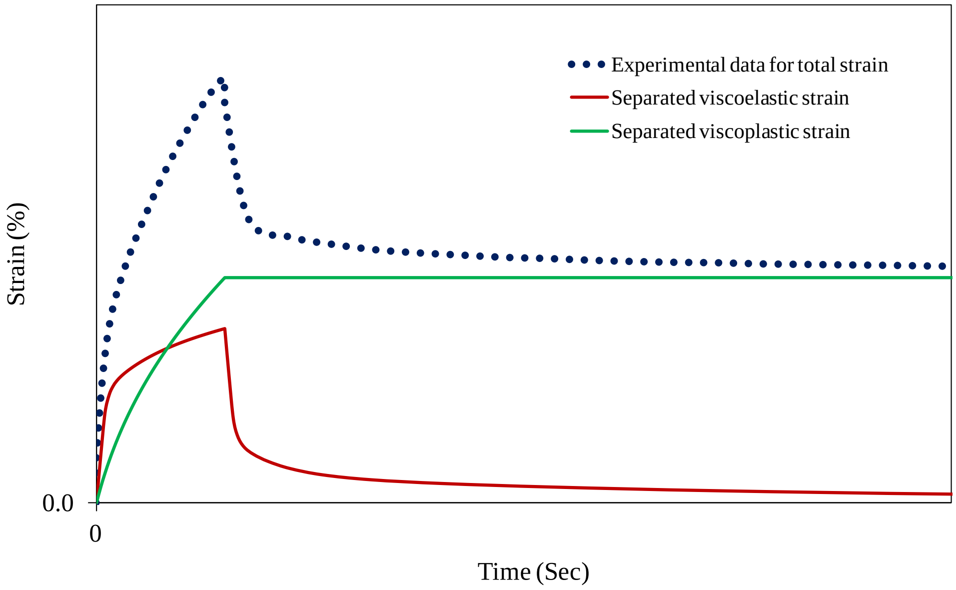

Figure 4.11 Illustrative Schematic of the Extraction of the Viscoelastic and Viscoplastic Components of the Total Strain

The hardening parameter κ_2 is identified by manipulating Equations (4.10) and (4.11), yielding:

$$\frac{\Delta\gamma^{vp}}{\Delta t}=\Gamma\left[\frac{\left\{\tau-\alpha I_1-\left[\kappa_0+\kappa_1\left(1-\exp\left(-\kappa_2 p\right)\right)\right]\right\}}{\sigma_y^0}\right]^N \tag{4.24}$$

$\Delta\gamma^{vp}$ is calculated using the extracted axial viscoplastic strain $\Delta\varepsilon_1^{vp}$, such that:

$$\Delta\gamma^{vp}=\Delta\varepsilon_1^{vp}/\left(1-\beta/3\right) \tag{4.25}$$

The effective viscoplastic strain, p, is calculated using extracted axial and radial viscoplastic strains (ε_1^{vp} and ε_2^{vp}, respectively), such that:

$$p=\left[1+2\left(\frac{0.5+\beta/3}{1-\beta/3}\right)\right]^{-0.5}\sqrt{\left(\varepsilon_1^{vp}\right)^2+2\left(\varepsilon_2^{vp}\right)^2} \tag{4.26}$$

If radial measurements are not available, radial viscoplastic strain is estimated as $\varepsilon_2^{vp}=\left(\frac{0.5+\beta/3}{1-\beta/3}\right)\varepsilon_1^{vp}$. Constant values for $\Delta\gamma^{vp}$ are picked at different stress levels of the RCRT-VS, as shown in Figure 4.5. Then, Equation (4.24) is rearranged such that:

$$\tau-\alpha I_1-\left(A-\kappa_1\right)=\kappa_1\left(1-Exp\left(-\kappa_2 p\right)\right); \qquad A=\sigma_y^0\left(\frac{\Delta\gamma^{vp}}{\Gamma\Delta t}\right)^{1/N}+\kappa_0+\kappa_1 \tag{4.27}$$

$\tau-\alpha I_1-\left(A-\kappa_1\right)$ is plotted (as shown in Figure 4.12) versus p at different stress levels where p, A, κ_1, and $\tau-\alpha I_1$ are known. The parameter κ_2 is identified by minimizing the error between the experiments and calculations using Equation (4.27). Different values for $\Delta\gamma^{vp}$ are picked, and the procedure is repeated to identify κ_2 at different values of $\Delta\gamma^{vp}$. The average κ_2 value is calculated at different $\Delta\gamma^{vp}$.

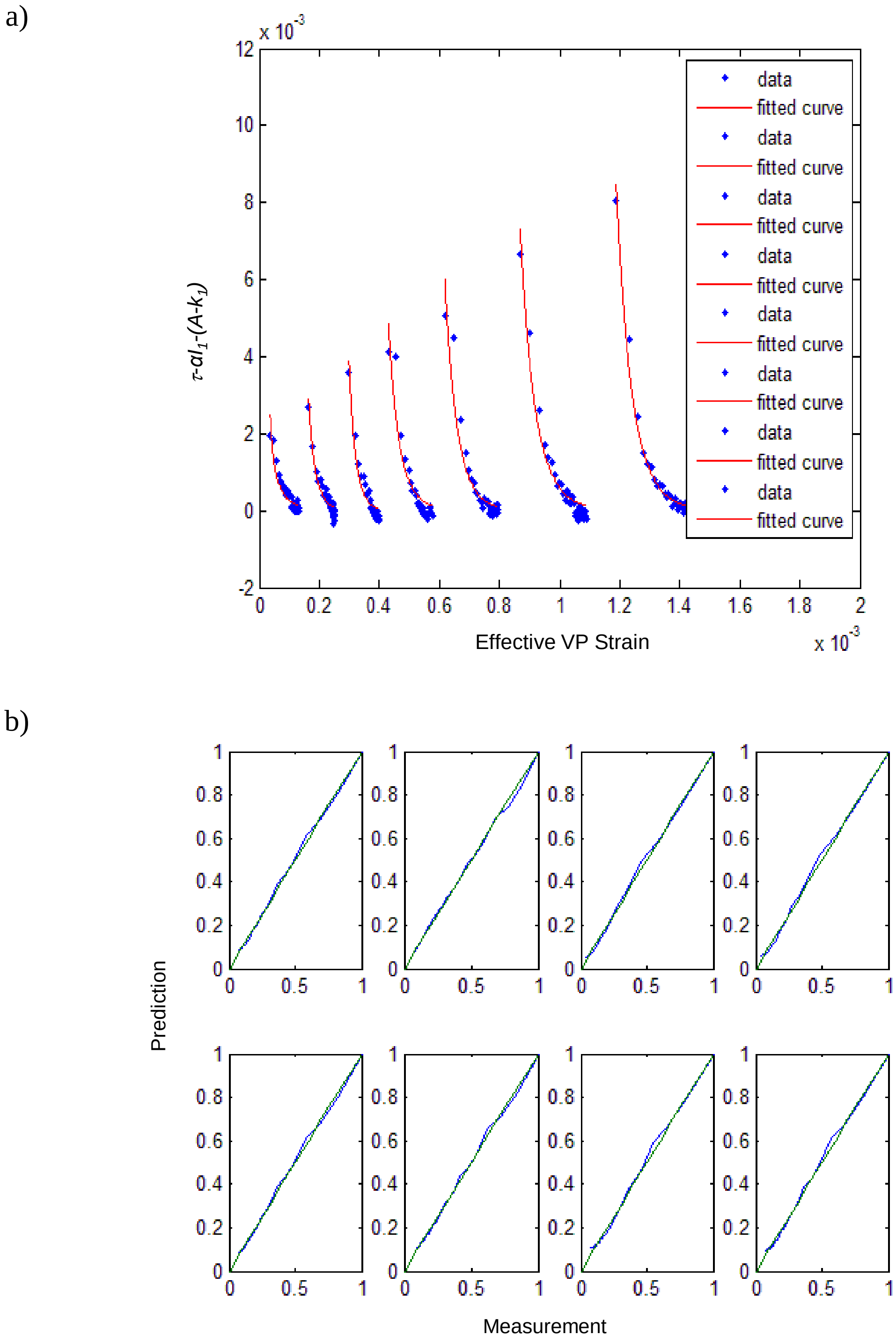

Figure 4.12 Identification of the Parameter κ_2 by Minimizing the Error for Eight Successive Cycles

The rate-sensitivity exponent parameter, N, is identified by calculating $\Delta\gamma^{vp}\left(t\right)$ and p^{t} during the loading stage of the RCRT-VS at different stress levels using Equations (4.25) and (4.26), respectively. $\Delta\gamma^{vp}\left(t_0\right)$ and p^{t_0} are calculated at the beginning of each loading cycle using Equations (4.25) and (4.26), respectively. Rearranging the formulation yields:

$$\frac{\Delta\gamma^{vp}\left(t\right)}{\Delta\gamma^{vp}\left(t_0\right)}=\left[\frac{\tau-\alpha I_1-\left[\kappa_0+\kappa_1\left(1-Exp\left(-\kappa_2\varepsilon_e^{vp,t}\right)\right)\right]}{\tau-\alpha I_1-\left[\kappa_0+\kappa_1\left(1-Exp\left(-\kappa_2\varepsilon_e^{vp,t_0}\right)\right)\right]}\right]^N \tag{4.28}$$

N is identified by minimizing the error between the experimentally measured $\Delta\gamma^{vp}\left(t\right)/\Delta\gamma^{vp}\left(t_0\right)$ and model results using Equation (4.28), as shown in Figure 4.13.

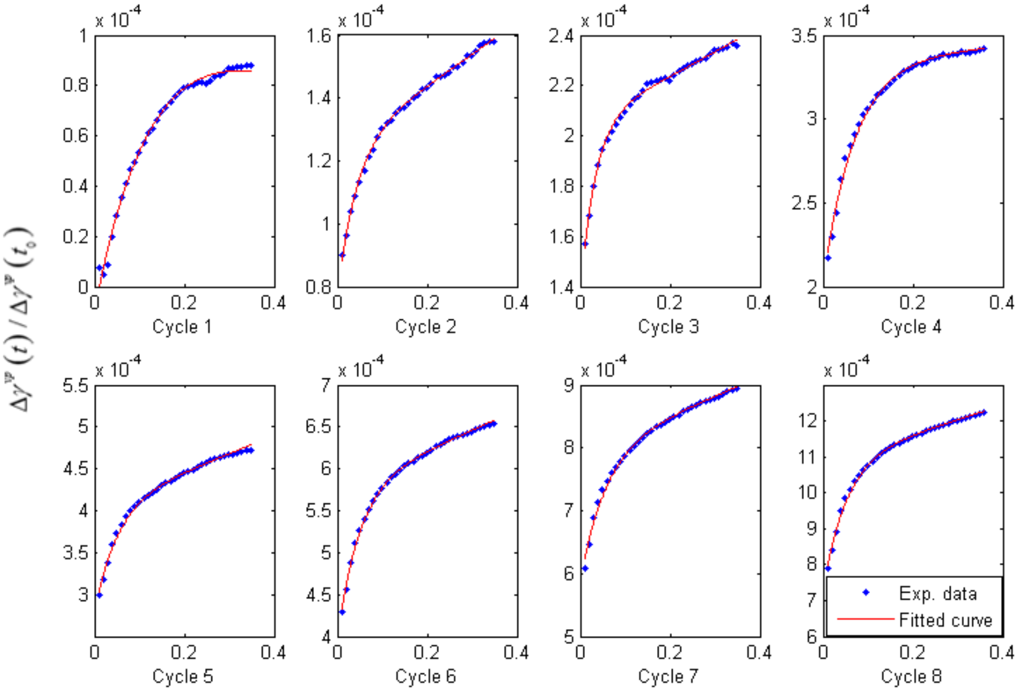

Figure 4.13 Identification of the Rate-Sensitivity Exponent Parameter N from the Relationship Between $\Delta\gamma^{vp}$ and Loading Time for Eight Successive Cycles

Once viscoplastic parameters κ_2 and N are identified, the viscoplasticity parameter Γ^{vp} can be identified by fitting the $\Delta\gamma^{vp}$ in each cycle using Equation (4.24), as shown in Figure 4.14.

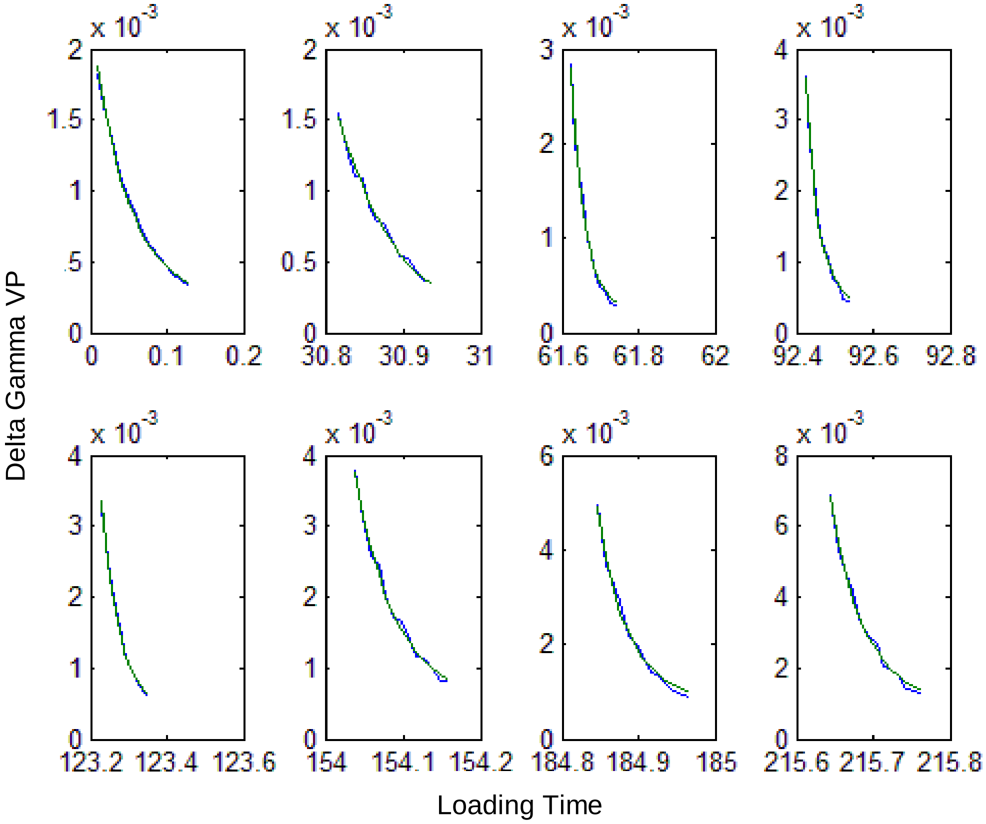

Figure 4.14 Identification of Viscoplasticity Parameter Γ^{vp} from the Relationship Between $\Delta\gamma^{vp}$ and Time for Eight Successive Cycles

By determining the viscoplastic parameters, predicted viscoplastic strain can be compared to the measured one, as shown in Figure 4.15. By adding predicted viscoelastic strain to predicted viscoplastic strain, predicted total strain can be determined and compared to the measured one, as shown in Figure 4.16. The viscoplastic model parameters are summarized in Table 4.6 for the DGM, FAM, and CAM.

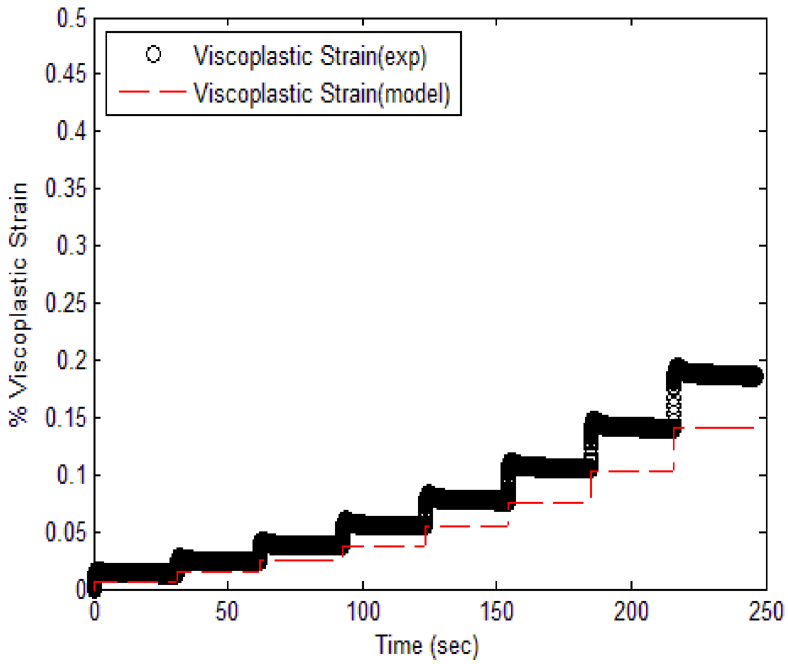

Figure 4.15 Measured and Predicted Viscoplastic Strain

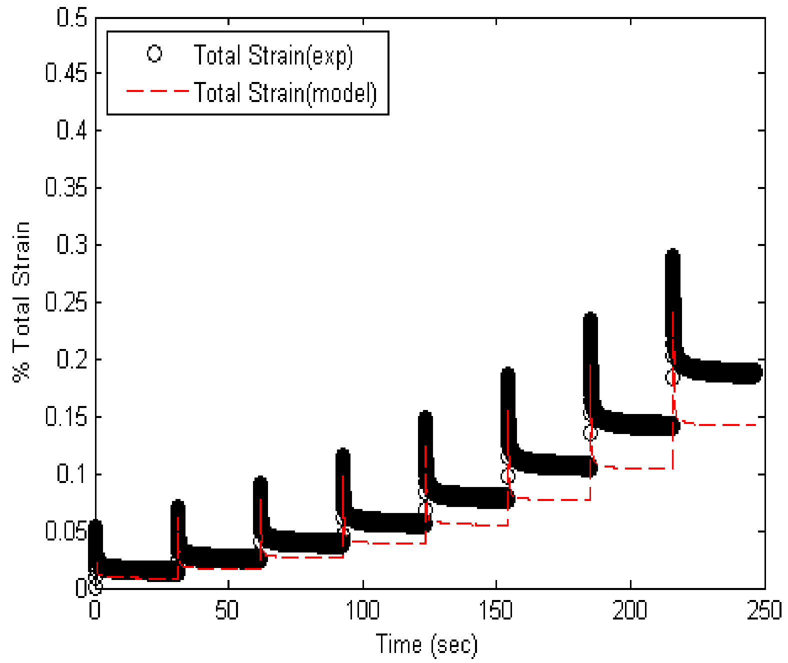

Figure 4.16 Measured and Predicted Total Strain

Table 4.6 Viscoplastic Model Parameters

Mix. Type	Temp. , °C	α	β	d^{vp}	Γ^{vp}	N	k_0	k_1	k_2
DGM	55	0.15	0.080	0.778	1.91E-3	1.54	63	1613	322
	40	0.15	0.040	0.778	3.79E-4	1.07	75	1669	512
	20	0.15	0.001	0.778	1.23E-4	1.53	96	1670	5165
FAM	40	0.10	0.280	0.778	7.85E-4	2.2	38	759	991
	20	0.10	0.040	0.778	1.68E-4	1.5	40	1110	2150
CAM	40	0.12	0.180	0.778	3.02E-4	1.2	30	1033	1350
	20	0.12	0.001	0.778	1.14E-4	2.1	30	1237	4344

The viscoplastic deformation of asphalt materials is nonassociative, which requires assuming the plastic potential function F to be different than the yield function f. By doing so, the direction of the viscoplastic strain increment is not normal to the yield surface, but to the plastic potential surface. In order to obtain nonassociative viscoplasticity, the Drucker-Prager–type function is used, where parameter α is replaced by another parameter, β (Huang 2008, Darabi 2011). Figure 4.17 shows different values of dilation parameter for the DGM, FAM, and CAM. The results show an increase in dilation characteristics for asphalt mixtures with an increase in temperature, which explains why the material expands more at high temperatures. The FAM has a high angle of friction, which is why it dilates more than the CAM and DGM.

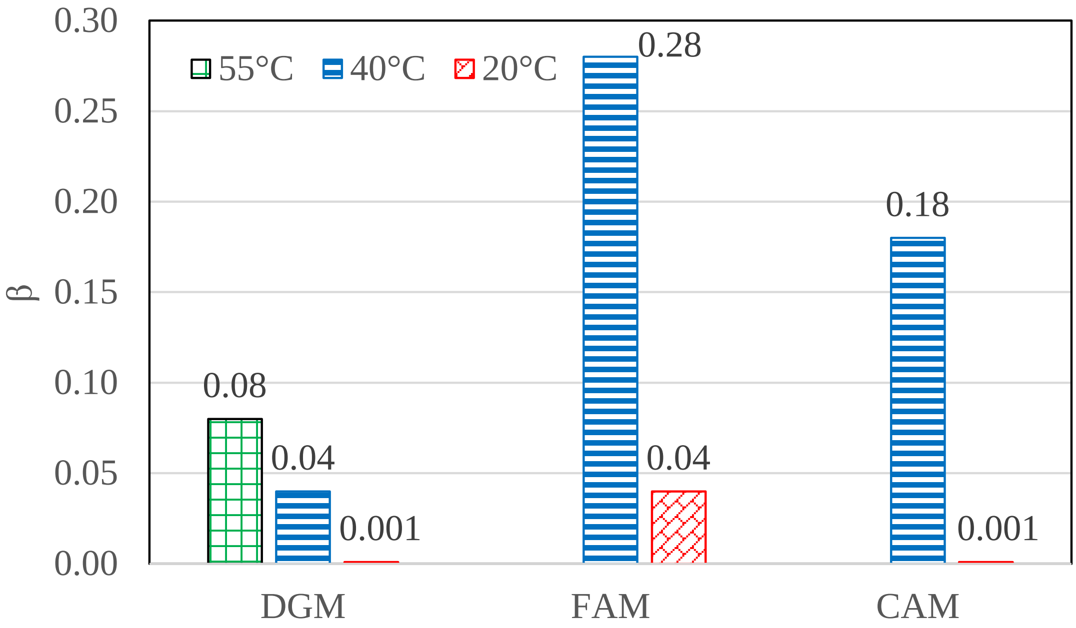

Figure 4.17 Dilation Characteristics of DGM, FAM, and CAM

As the asphalt materials become stiffer at low temperatures, they require more time to relax. Figure 4.18 shows that CAM, which have lower binder content, need more time to relax than FAM, which have higher binder content. FAM act more viscoelastically than CAM. As temperature increases, the difference increases between the orientation and position of the aggregates at the end of loading and during unloading. This is because the binder gets softer and deforms more easily as temperature increases, which provides more mobility for the aggregates. Moreover, because the binder and the residual stresses relax faster during the rest period as temperature increases, the time-dependent residual stresses cause faster rearrangement of the microstructure and, in turn, more recovery at the hardening level.

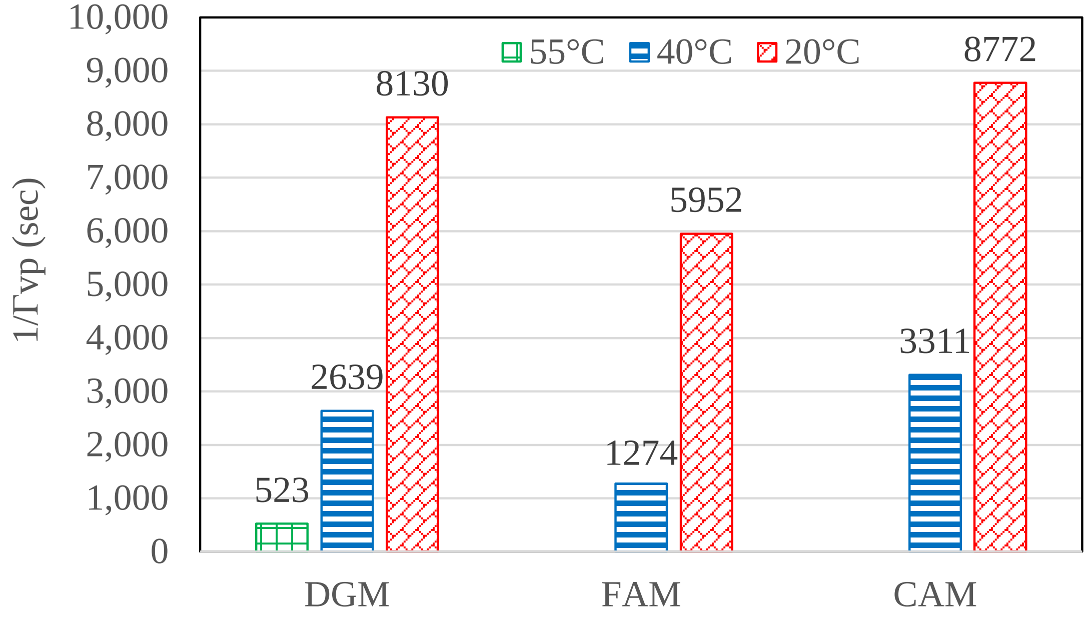

Figure 4.18 Viscoplasticity-Relaxation Time of DGM, FAM, and CAM

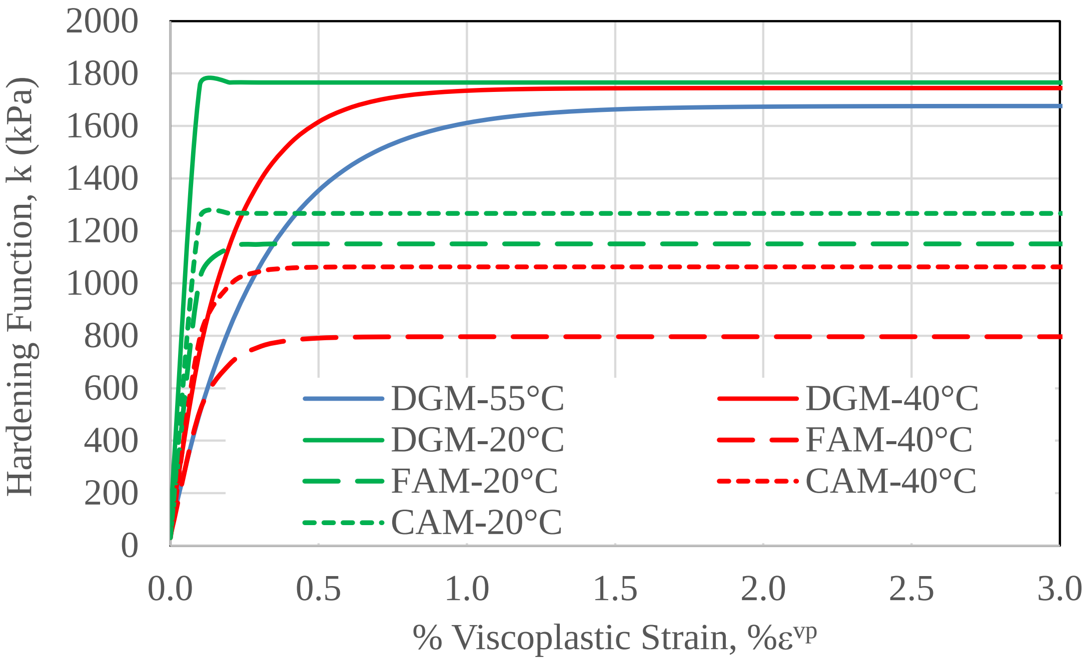

Figure 4.19 Hardening Functions of DGM, FAM, and CAM

Figure 4.19 shows how the hardening function evolves with an increase in effective viscoplastic strain. At low temperatures, asphalt materials hardens faster, meaning that the material becomes harder as a result of plastic deformation, while the strengthening due to strain hardening can be lost at elevated temperatures. Therefore, the DGM gains more strain hardening than the CAM and FAM due to aggregate sizes, aggregate structure, and aggregate interlocking, which add more strength to the material.

4.5 Development of Shear Strength Envelopes During RCRT-VS

Strength parameters are very important in understanding the behavior of asphalt mixtures. There are various functions, or models, to describe failure criteria, such as Tresca criterion, von Mises criterion, Mohr-Coulomb criterion, and Drucker-Prager criterion (Chen & Liu 1990).

In general, the simple one-parameter models of Tresca and von Mises cannot be applied to asphalt concrete because they neglect the major effect of the hydrostatic stress component on strength. Mohr-Coulomb and Drucker-Prager criteria are commonly used for geomaterials. According to the Mohr-Coulomb criterion, shear strength increases with increasing normal stress on the failure plane. It can be represented by the following equation:

$$\tau = C + \sigma \tan \phi \tag{4.29}$$

where τ is the shear stress; σ is the normal stress; C is the cohesive strength; and ϕ is the internal frictional angle. The Mohr-Coulomb failure function, *f*, can be written in terms of the stress invariants (Chen and Baladi 1985), which results in:

$$f = \frac{I_1}{3}\sin\phi + \sqrt{J_2}\sin(\psi + \frac{\pi}{3}) + \frac{\sqrt{J_2}}{\sqrt{3}}\cos(\psi + \frac{\pi}{3})\sin\phi - \mathrm{C}\cos\phi \tag{4.30}$$

where I_1,J_2, J_3 are the first , second, and third stress invariants of deviatoric stress tensor,

ψ is the angle of similarity (lode angle) $\psi = \frac{1}{3}\cos^{-1}\left(\frac{3\sqrt{3}}{2}\frac{J_3}{J_2^{3/2}}\right) = \frac{1}{3}\cos^{-1}\left(\frac{\sqrt{2}J_3}{\tau_{oct}^{\ 3}}\right)$, and

τ_{oct} is the octahedral shear stress $\tau_{oct} = \frac{1}{3}\left[(\sigma_1 - \sigma_2)^2 + (\sigma_2 - \sigma_3)^2 + (\sigma_3 - \sigma_1)^2\right]^{1/2}$.

The Mohr-Coulomb yield surface represents the yield criterion at its simplest; however, the failure surface has sharp corners (singularities) (Meyer and Labuz 2013). Shear strength properties (C and ϕ) have well-defined physical interpretation, and they can easily be determined from experimental testing data.

An approximation of the Mohr-Coulomb criterion is presented as an extended Mohr-Coulomb rule (Drucker and Prager 1952). The material constants in Drucker-Prager criterion can be determined by matching two particular points with those of the Mohr-Coulomb criterion; thus, the two constants α and k can be expressed in terms of the Mohr-Coulomb parameters C and ϕ.

In 3D stress-matching, if the points are selected in such a way that the failure surface circumscribes the Mohr-Coulomb hexagonal pyramid, as shown in Figure 2.8, the material constants are (Chen and Liu 1990, Chen and Mizuno 1990):

$$\alpha = \frac{2\sin\phi}{\sqrt{3}(3 - \sin\phi)}; \qquad k = \frac{6C\cos\phi}{\sqrt{3}(3 - \sin\phi)} \tag{4.31}$$

The traditional method for determining shear strength properties of asphalt materials at the failure stage is determined by analyzing the output of the UCSRCT based on the Mohr-Coulomb yield failure criteria. Equation (4.29) is used to capture the Mohr-Coulomb envelope for the DGM, FAM, and CAM. Figure 4.20 presents the experimental measurements of monotonic tests for unconfined conditions and confinement stress of 140 kPa, strain rate of 0.021 mm/sec, and temperatures of 40 and 55°C. Shear strength parameters *C* and ϕ are determined at failure stage as the intercept and slope of the Mohr-Coulomb envelope, respectively, as shown in Figure 4.21.

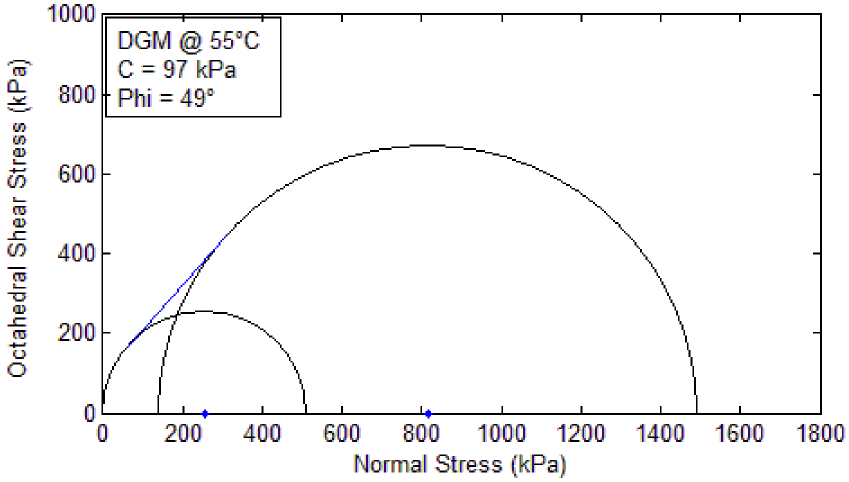

a) Mohr-Coulomb Envelope for DGM at 55°C

Figure 4.20 Monotonic Test Measurements for Unconfinement and Confinement Stress of 140 kPa at a Strain Rate of 0.021 mm/sec and Temperatures of 40 and 55°C

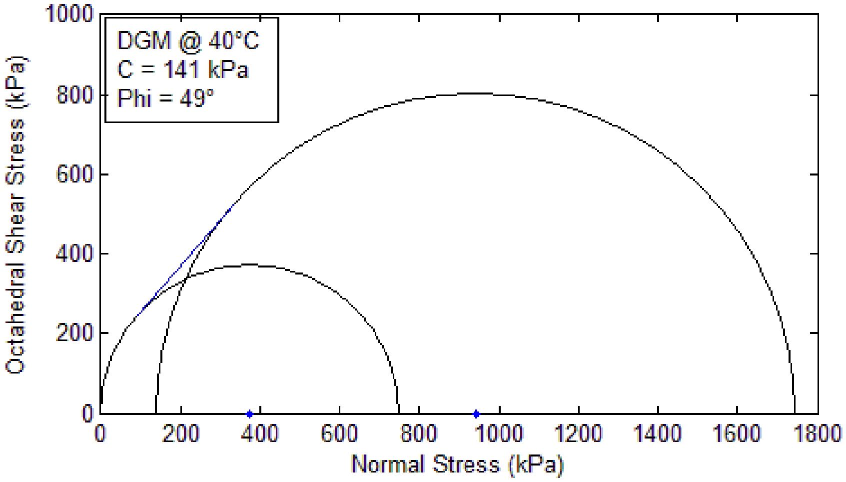

b) Mohr-Coulomb Envelope for DGM at 40°C

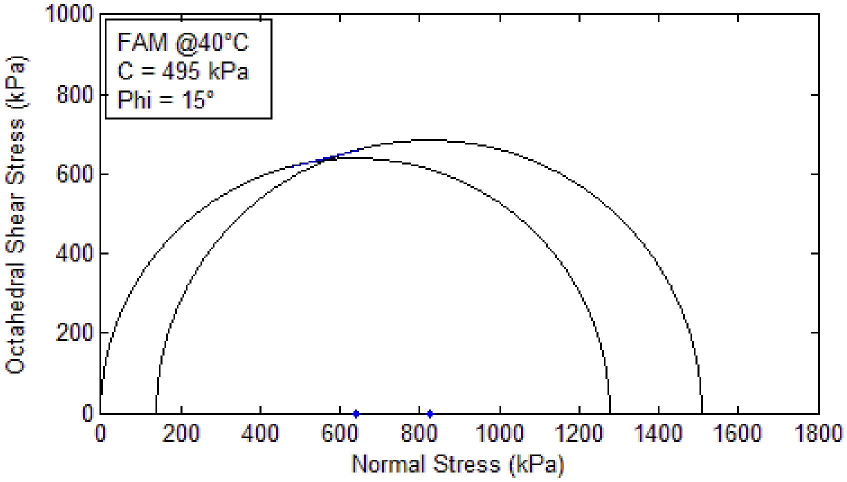

c) Mohr-Coulomb Envelope for FAM at 40°C

Figure 4.20 Continued

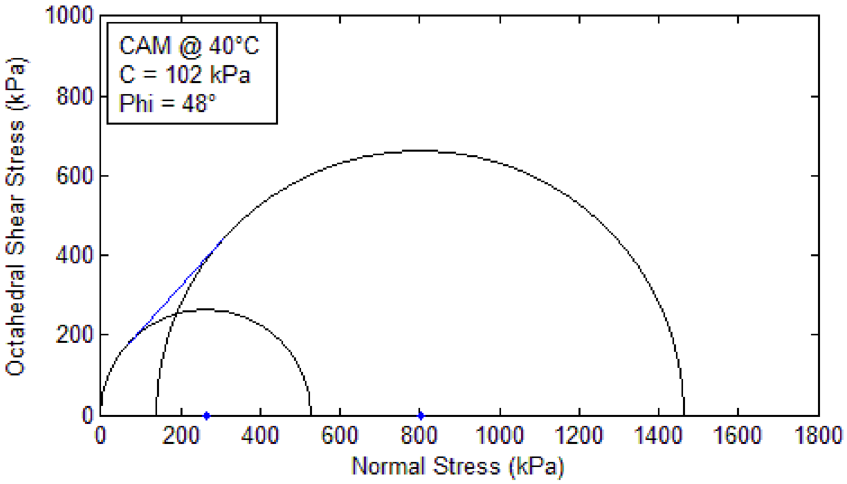

d) Mohr-Coulomb Envelope for CAM at 40°C

Figure 4.20 Continued

A new approach is presented to extract the shear strength parameters of the asphalt materials by analyzing the output of the RCRT-VS based on the modified Drucker-Prager yield surface, which is implemented in PANDA. The new approach evaluates the evolution of shear strength parameters during creep and relaxation behavior, taking into consideration the hardening effect generated during testing.

This section evaluates the validity of the value α by analyzing the RCRT-VS. After separating the viscoelastic response from the total response of the material under the RCRT-VS as described in Section 4.4.2, the viscoplastic response can be plotted with time. Figure 4.21 shows an example of viscoplastic strain versus time for a DGM at unconfined conditions and at a confinement level of 140 kPa. From the experimental data, the first component of the deviatoric stress tensor (S_{11}) can be plotted with viscoplastic strain, as shown in Figure 4.22. In Figures 4.21 and 4.22, S_{11} can be read for both confinement levels at the same time of loading, as shown graphically. Then, the relationships of the first stress invariant (I_1) and the deviatoric effective shear stress (τ_{oct}) can be generated at different times of loading, as shown in Figure 4.23 as an example. It is noticeable that the intercept and slope of the relationship between the first stress invariant and the deviatoric effective shear stress increase with time as testing proceeds.

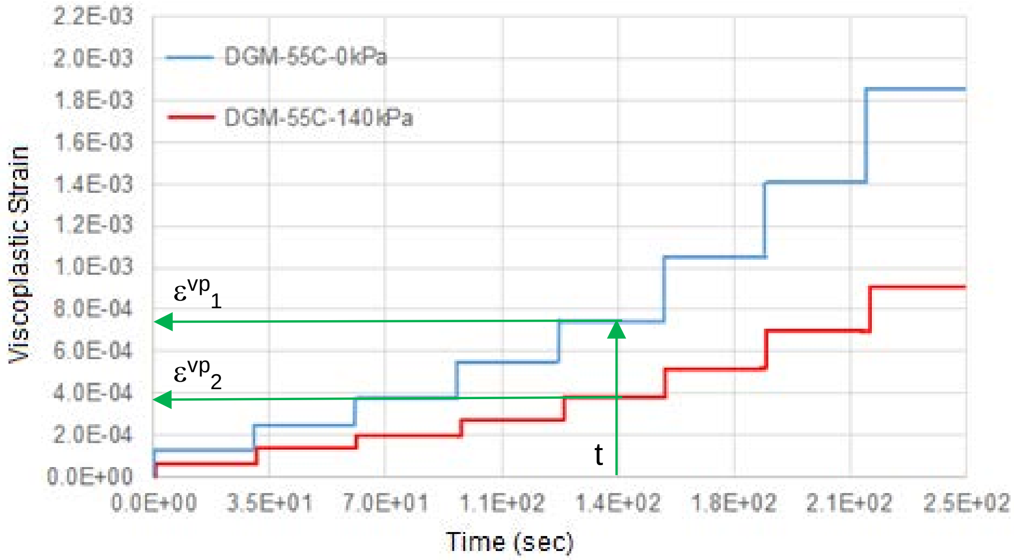

Figure 4.21 Viscoplastic Strain Vs. Time

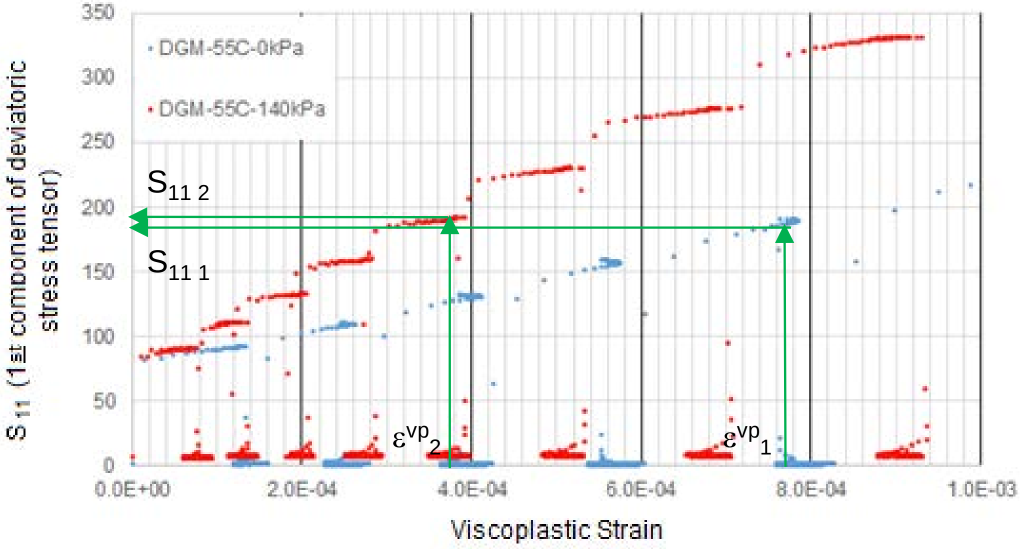

Figure 4.22 First Component of Deviatoric Stress Tensor Vs. Viscoplastic Strain

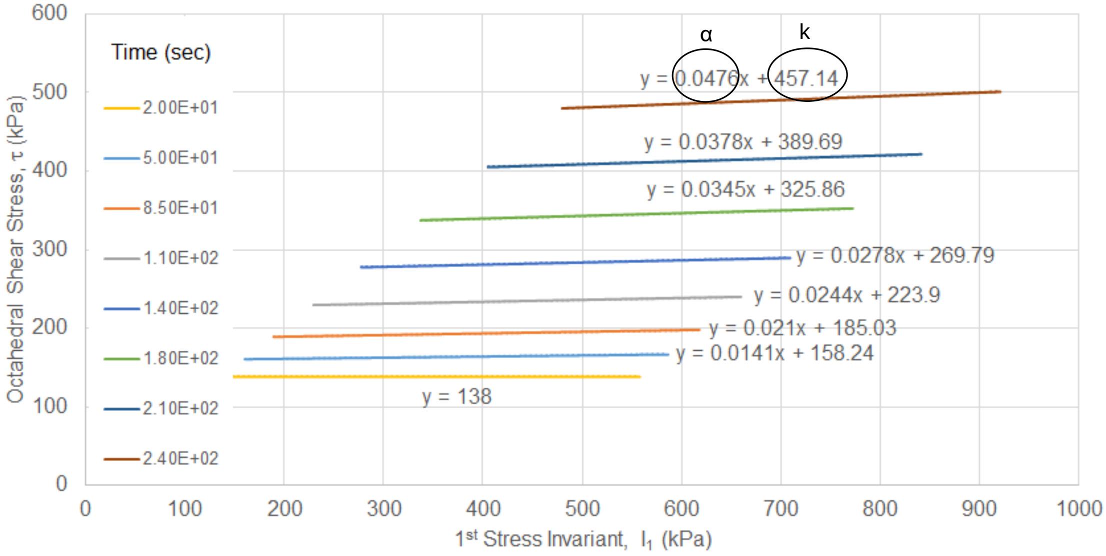

Figure 4.23 Relationship Between Octahedral Shear Stress and First Stress Invariant

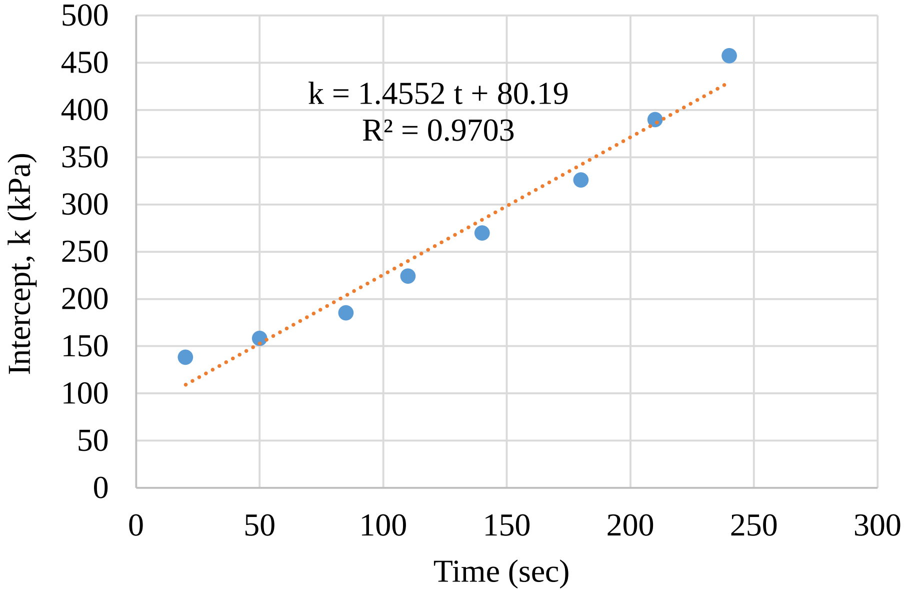

a) Intercept vs. Time

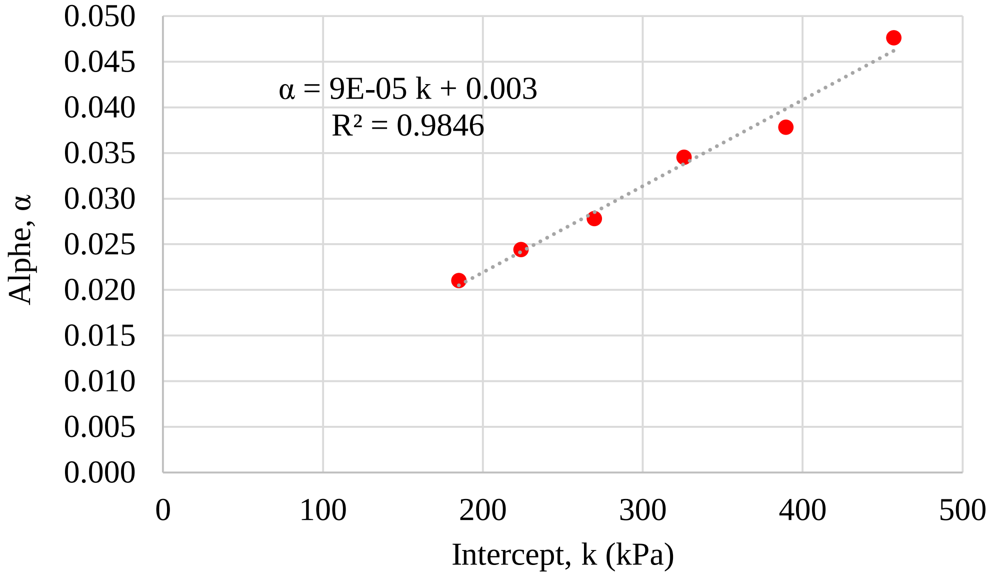

b) Alpha vs. Intercept

Figure 4.24 Evolution of Intercept and Slope During RCRT-VS

Using Equation (4.31), shear strength parameters are determined at each loading cycle. Figure 4.24 presents the evolution of the intercept and slope (i.e., shear strength parameters) during the RCRT-VS. Alpha is not constant during the RCRT-VS; however, its variation may be negligible. The asphalt material shear strength parameters are stress-sensitive and time-dependent.

By comparing the hardening function calculation from Section 4.4.3 and this new approach, for example at a viscoplastic strain of 0.1%, k equals 507 kPa when assuming a constant alpha, while it is 326 kPa when alpha is determined. At a viscoplastic strain of 0.2%, k equals 829 kPa when assuming a constant alpha, while it is 477 kPa when alpha is determined. These values come from measurements of the DGM at 55°C. As a result, assuming alpha overestimates the hardening function.

4.6 Summary

This chapter presents a framework for analyzing linear viscoelastic, nonlinear viscoelastic, and viscoplastic behaviors of different asphalt mixtures at different temperatures and loading conditions. Two different tests are conducted to extract the viscoelastic and viscoplastic parameters. A systemic analysis procedure is developed to identify linear viscoelastic properties, nonlinear viscoelastic parameters, and viscoplastic parameters using the DMT and RCRT-VS. This analysis determines the long-term linear viscoelastic properties and time-temperature shift factors from dynamic modulus. Then, these linear viscoelastic coefficients are employed to decouple the recoverable and irrecoverable response from the RCRT-VS and obtain the nonlinear parameters. The viscoelastic and viscoplastic PANDA models are used in this study to investigate the effect of temperature (20, 40, and 55°C) and asphalt mixture type (DGM, FAM, and CAM) on the response and performance of asphalt mixes. The results demonstrate that this material model has the ability to describe asphalt material behavior under different loading paths, and the results show reasonable correlation with experimental measurements. Pavement engineers can use PANDA to analyze and predict the performance of pavements of various material combinations and, thus, select the best and most cost-effective materials for a proposed project.

The analysis applies only to one asphalt mixture. It is necessary to evaluate the applicability of the analysis method for more asphalt binders and aggregate sources that exhibit different properties from different sources.

CHAPTER V

EFFECT OF AIR VOID CONTENT AND AGING LEVEL ON LINEAR VISCOELASTIC, NONLINEAR VISCOELASTIC, AND VISCOPLASTIC RESPONSES OF ASPHALT MIXTURES

5.1 Introduction

This chapter presents the characterization of linear viscoelastic, nonlinear viscoelastic, and viscoplastic behavior of asphalt mixtures, taking into account the possible interactions among temperature, aging level, and air void content. The analytical procedure described in Chapter IV is followed to determine the viscoelastic and viscoplastic PANDA model parameters for a DGM at three aging levels (0, 3, and 6 months) and various air void contents (4, 7, and 10%). Experimental measurements are obtained from testing the mixture using the DMT and RCRT-VS at two different temperatures (40 and 55°C). The DMT data is used to identify the linear viscoelastic parameters, while the RCRT-VS data is used to identify the nonlinear viscoelastic and viscoplastic parameters of the PANDA model.

5.2 Background

As discussed earlier, asphalt materials are time-dependent materials, which can behave linearly or nonlinearly based on stress/strain level, loading rate, and temperature. The material behaves linearly when its properties are functions of time and temperature, and its response follows superposition and proportionality principles (Ferry 1961). In addition, asphalt materials behave nonlinearly due to slippage and rotation of aggregates and localized high strains in the asphalt binder (Kose et al. 2000).

Aging of asphalt materials causes premature failure, which affects the service life of asphalt pavement at high levels (Bell 1989, Campbell et al. 1962). Previous research studies show that the rate of oxidation of asphalt binder (i.e., oxidation as a function of exposure time) depends on environmental factors such as temperature and relative humidity (Chipperfield 1970). Peterson (1984) summarized the basic factors that control asphalt binder aging as volatilization, oxidation, and steric hardening. Volatilization happens when oily components of the asphalt binder is volatilized or absorbed by porous aggregates. Oxidation is the reaction of asphalt binder with oxygen, resulting in a change in its chemical composition. Steric hardening happens when thixotropic effects are produced due to molecular structuring. Aging phenomenon occurs in both the short and long terms (Bell et al. 1994). Short-term aging happens during the mixing process and the construction phase. Volatilization and oxidation effects cause short-term aging when asphalt mixtures are at elevated temperatures. Long-term aging happens in accordance with short-term aging and during the service life of asphalt pavement, as long as it is exposed to the environment. Oxidation is the main cause of long-term aging. Aging of asphalt binder is influenced by properties and content of asphalt binder, properties and gradation of aggregates, air void content of mixtures, and external factors such as time, temperature, and production-related factors (Xiaohu and Isaccson 2000).

Research studies show that mechanical properties of asphalt materials are highly dependent on air void content. Air voids in the asphalt mix should be small and well scattered so as to not affect the mix coherence. Having too many air voids allows more air and water to access asphalt layers, inducing aging and moisture damage and leading to growth of cracks. Not having enough air voids causes bleeding and promotes more plastic deformations. Tarefdar et al. (2007) studied the influence of air void content on the dynamic modulus and rut potential of asphalt mixtures. They reported that mixtures with high air voids have low dynamic modulus and high rut potential. Permanent deformation is usually associated with an increase in voids filled with asphalt binder.

The objective of this part of the study is to characterize linear viscoelastic, nonlinear viscoelastic, and viscoplastic behaviors of asphalt mixtures that account for the possible interactions among temperature, time of loading (frequency), stress level, aging level, and air void content. Analysis of the linear viscoelastic behavior of investigated cases is done using DMT data; analysis of the nonlinear viscoelastic and viscoplastic behaviors is accomplished using RCRT-VS data.

5.3 Materials and Experimental Testing Matrix

The materials used in this study are designed, compacted, and fabricated following the same procedures described in Chapter III. To obtain uniform air void distribution, specimens are cored and cut to a height of 150 mm with a diameter of 100 mm. The asphalt mixture is designed as a DGM based on Texas Department of Transportation (TxDOT) specifications (TxDOT 2004). An unmodified binder, PG 67-22, is used with 4.4% binder content by asphalt mixture weight. DGM specimens are prepared to investigate three air void contents (4, 7, and 10%) and three aging levels (0, 3, and 6 months). Two different tests are conducted to extract the viscoelastic and viscoplastic PANDA model parameters, as shown in Table 5.1. The first test is the DMT, which is used to identify linear viscoelastic parameters. The second test is the RCRT-VS in compression. This test is conducted at two temperatures (40 and 55°C) and at a 140-kPa confinement level. The RCRT-VS is used to identify viscoplastic parameters, as well as nonlinear viscoelastic parameters.

Table 5.1 Experimental Tests Used for Identification of Linear Viscoelastic, Nonlinear Viscoelastic, and Viscoplastic Parameters

Test	Temperature (°C)	Loading Time/ Rest Period(s)	Confinement Level (kPa)
DMT	–10, 4, 21, 37, 54	-	-
RCRT-VS in compression	40, 55	0.4/30	140

5.4 Linear Viscoelastic Behavior

The DMT is used to identify linear viscoelastic parameters, as well as temperature coupling term parameters (i.e., time-temperature shift factors). AASHTO PP62-09 “Standard Practice for Developing Dynamic Modulus Master Curves for Hot Mix Asphalt (HMA)” is applied to develop the E* master curves for the investigated DGM cases using the following equations (AASHTO, 2016):

$$-\log\left|E^{*}\right| = \delta + \frac{\alpha}{1+\exp\left[\beta+\gamma\log\left(\omega_{r}\right)\right]} \tag{5.1}$$

where |E*| is the dynamic modulus of the mixture in psi; δ, α, β, and γ are fitting parameters; and ω_r is the reduced frequency in Hz. The reduced frequency is computed using time-temperature shift factors based on the second-order polynomial, shown as:

$$\begin{aligned} &\log \omega_r = \log \omega + a_1 \left(T_R - T\right) + a_2 \left(T_R - T\right)^2 ; \\ &\log t_r = -\log \omega_r ; \qquad \log a_T = \log t - \log t_r \end{aligned} \tag{5.2}$$

where, ω_r is the natural circular frequency normalized by the time-temperature shift factor at the reference temperature in Hz; ω is the loading frequency at the test temperature in Hz; t_r is the reduced time in seconds; a_1, a_2 are fitting coefficients; T_R is the reference temperature; T is the test temperature in °F; t is the time in seconds; t_r is the reduced time in seconds; and a_T is the time-temperature shift factor.

The fitting parameters are determined by a numerical optimization using the Solver function in Microsoft Excel. Starting with seed (initial) values for these parameters, the Solver function is used to minimize the sum of the squared errors between the logarithms of the average measured dynamic moduli at each temperature/frequency combination by varying the fitting parameters of the sigmoid function. Figures 5.1 and 5.2 show the E* master curves of the investigated DGM cases at different aging levels and various air void contents.

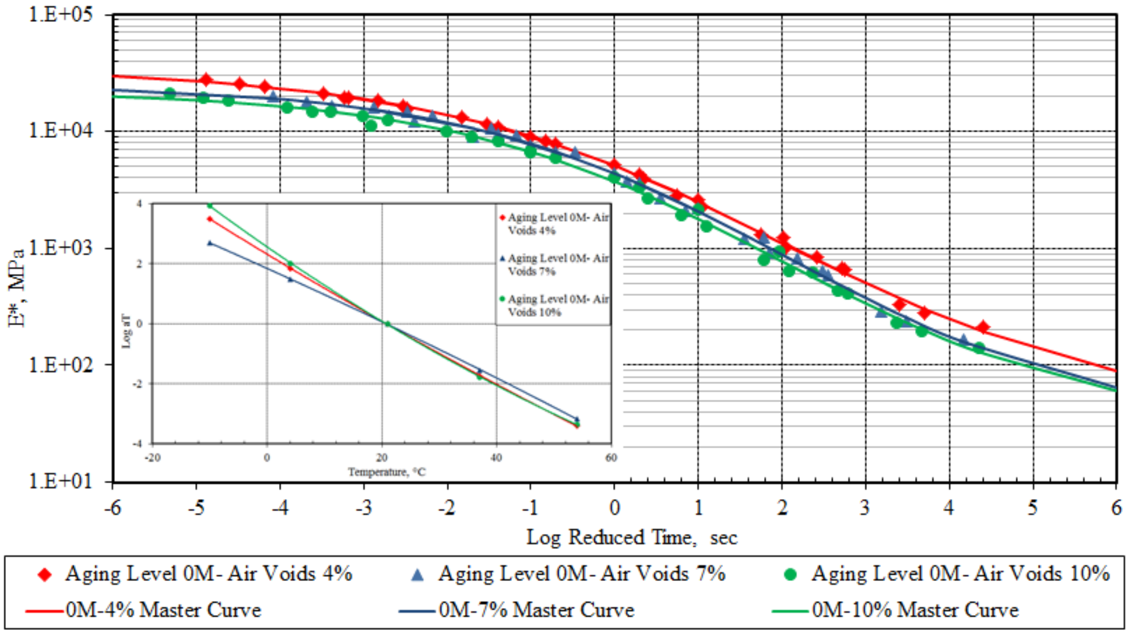

a) Dynamic Modulus Master Curves of DGM at 0-Month Aging Level

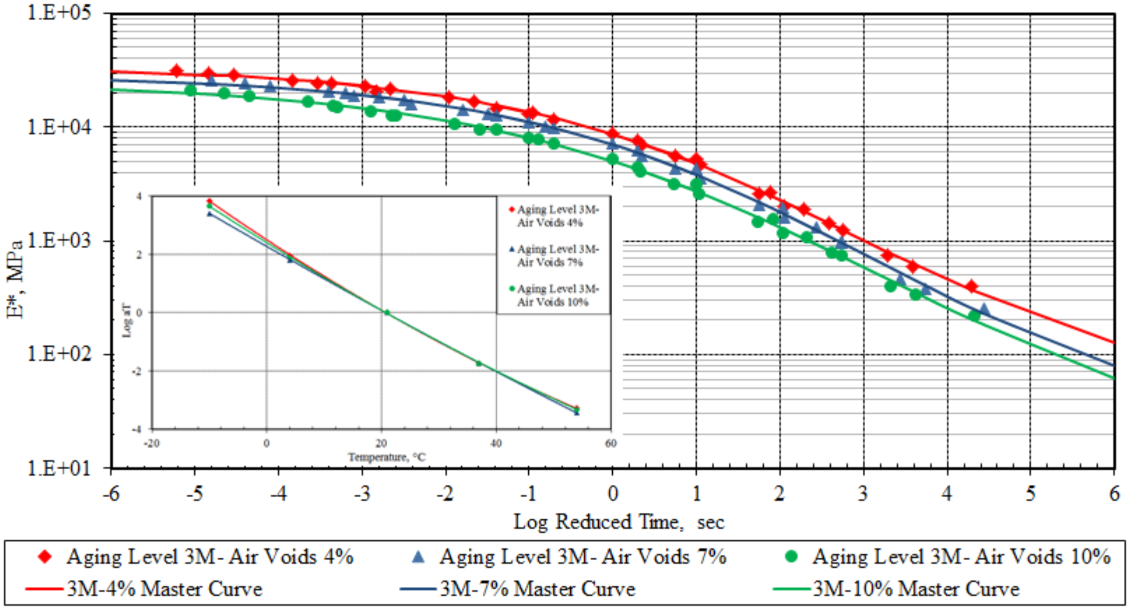

b) Dynamic Modulus Master Curves of DGM at 3-Month Aging Level

Figure 5.1 Effect of Air Void Content on Dynamic Modulus Master Curve

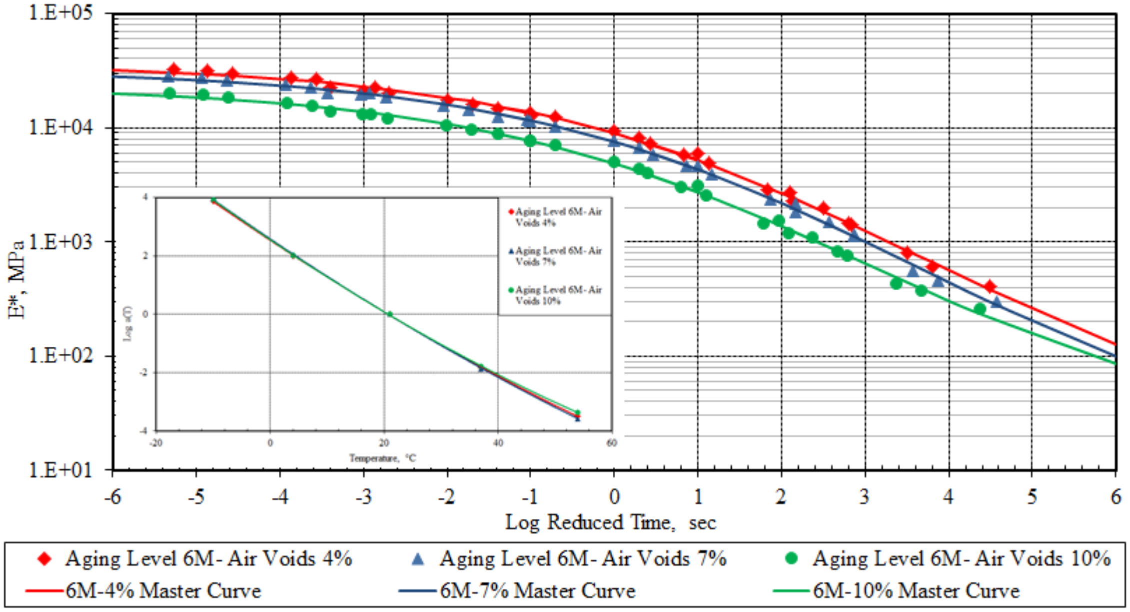

c) Dynamic Modulus Master Curves of DGM at 6-Month Aging Level

Figure 5.1 Continued

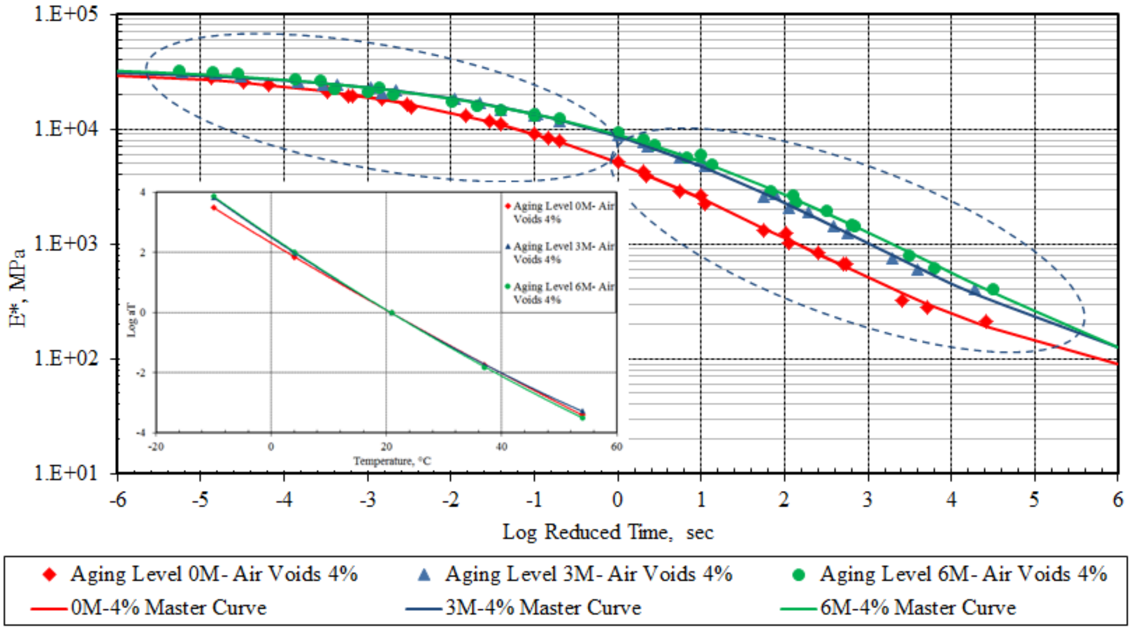

a) Dynamic Modulus Master Curves of DGM at 4% Air Void Content

Figure 5.2 Effect of Aging Level on Dynamic Modulus Master Curve

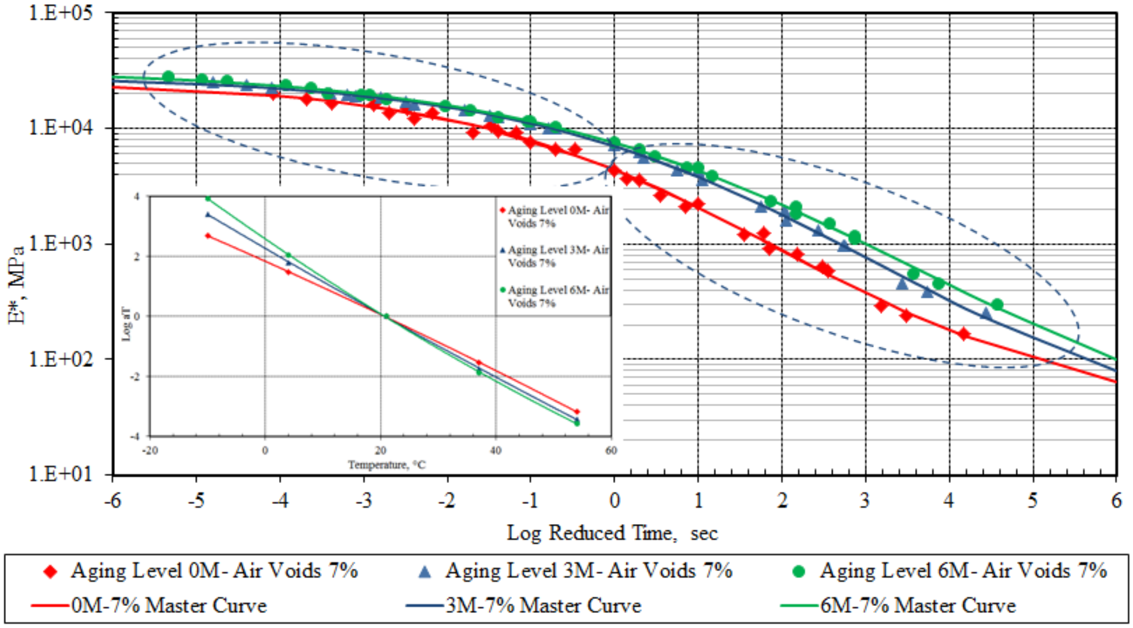

b) Dynamic Modulus Master Curves of DGM at 7% Air Void Content

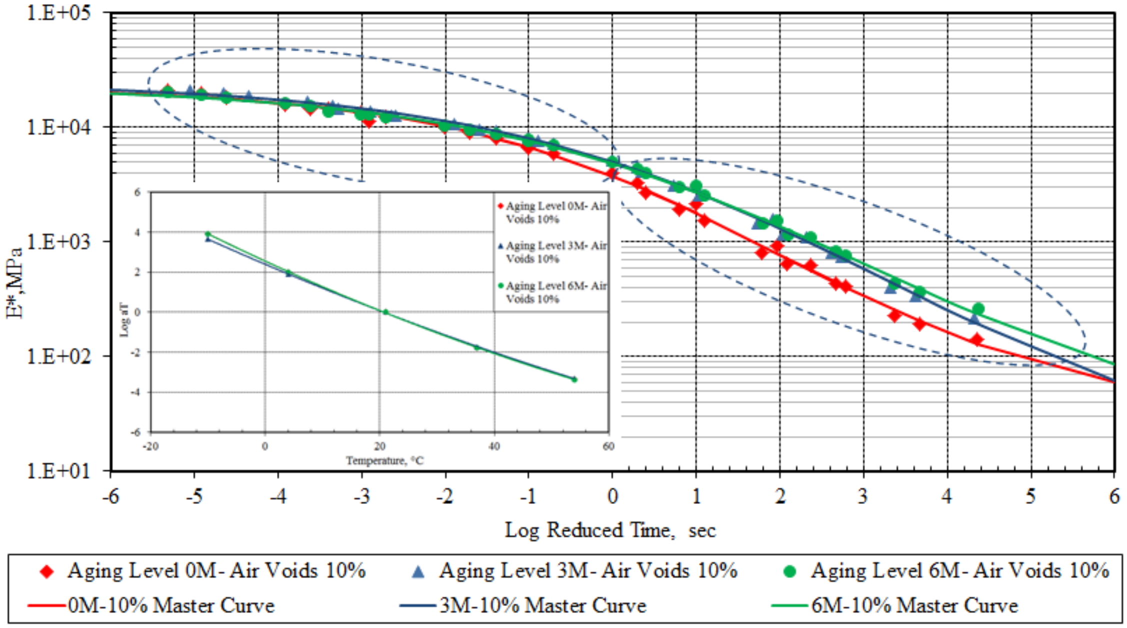

c) Dynamic Modulus Master Curves of DGM at 10% Air Void Content

Figure 5.2 Continued

Figure 5.1.a, Figure 5.1.b, and Figure 5.1.c show the effect of air void content at 0-, 3-, and 6-month aging levels, respectively. The DGM, which has the lowest air void content (4%), has higher dynamic modulus values than the DGM with the highest air void content (10%); i.e., the material gets stiffer with decreasing air void content. At the 0-month aging level, there is no significant difference in the dynamic modulus values for mixtures, which have an air void content of 7 or 10%. This means that the variation in the dynamic modulus trend decreases with an increase in air void content. After 6 months of aging, there is no significant difference in the dynamic modulus values for mixtures, which have an air void content of 4 or 7%. This is because the low air void content reduces oxygen infiltration into the material, which causes less aging.

Figure 5.2.a, Figure 5.2.b, and Figure 5.2.c show aging level effects at 4, 7, and 10% air void contents, respectively. It is noticeable that aging level does not have a uniform effect on the dynamic modulus trend. The dynamic modulus master curve can be divided into two parts: the dynamic modulus trend at high temperatures (lower part of the figure) and the dynamic modulus trend at low temperatures (upper part of the figure). As observed, aging level does not have much effect on the upper part of the curve, as it represents the dynamic modulus trend in cold weather. This is due to the fact that asphalt materials become stiffer and purely elastic at low temperatures. On the other hand, there is a significant effect of aging level on the lower part of the curve, which represents the dynamic modulus trend at high temperatures. At high temperatures, the asphalt material behaves more as a viscoelastic material and depends on aging level. It is also obvious that dynamic modulus values increase with an increase in aging level. However, it is

noticeable that there is not much difference in the dynamic modulus values after 3 months of aging. It is also noticeable that aging effect is not as significant on the 10% air void content mix as it is on the 7% air void content mix.

The standard procedure is used to identify the linear viscoelastic parameters of the creep compliance (Prony series coefficients) and time-temperature shift factors using the complex compliance, D^*, and the phase angle, θ. After constructing the master curves for the dynamic modulus, E^*, from which the time-temperature shift factors are also identified, the next step is to calculate the complex compliance, D^*, the storage compliance, $D' = \|D^*\| \sin\theta$, and the loss compliance, $D'' = \|D^*\| \cos\theta$, versus the reduced frequency, ω_R. The Prony series coefficients (D_n and λ_n) are related to D' and D'' as follows (Park and Schapery 1999):

$$D' = D_0 + \sum_{n=1}^{N} \frac{D_n}{1+\left(\omega/\lambda_n\right)^2}; \qquad D'' = \sum_{n=1}^{N} \left[\frac{1}{\lambda_n} \frac{D_n \omega}{1+\left(\omega/\lambda_n\right)^2} \right] \tag{5.3}$$

where D_n and λ_n can be identified from the above expressions by minimizing the error between the experimental and calculated D' and D'', such that:

$$error = \left(\frac{D'}{D'_{Exp}} - 1 \right)^2 + \left(\frac{D''}{D''_{Exp}} - 1 \right)^2 \tag{5.4}$$

Rahmani (2015) proposed a phenomenological relationship for aged transient compliance of a viscoelastic material. Aged transient compliance is expressed as a function of the aging state variable and unaged transient compliance, such that:

$$\Delta\bar{D}^A = f(\Delta\bar{D}, A) \tag{5.5}$$

where $\Delta\bar{D}^A$ and $\Delta\bar{D}$ are the transient compliance of the unaged and aged material in the effective configuration, respectively. Equation (5.5) allows for the viscoelastic properties of the aged material to be expressed in two different time scales: loading time and aging time. In other words, $\Delta\bar{D}$ is a function defined in a time scale when the mechanical loading is applied, and the aging state variable, A, is expressed in terms of a time when oxidative aging happens. The influence of oxidation on the viscoelastic behavior of the aged asphalt mixtures is captured by the following relationships for parameters of aged transient compliance:

$$D_n^A = \left(1 - A\right)^{k_1} D_n \tag{5.6}$$

$$\lambda_n^A = \left(1 - A\right)^{k_2} \lambda_n \tag{5.7}$$

where D_n^A and λ_n^A are compliance terms and retardation times of the aged material, and k_1 and k_2 are material properties. It is noted that the compliance terms are measures of stiffness, whereas the retardation times are the characteristic properties of viscoelastic materials being inversely related to viscosity of the matter. It is noted that the mechanistic-based relationships, Equations (5.6) and (5.7), imply that the compliance terms and retardation times decrease with aging. Therefore, it is interpreted that the proposed relationship for the aged viscoelasticity ensures that the stiffness and viscosity of the aged material increases by decreasing the compliance terms and retardation times.

The dynamic modulus trend of unaged specimens with 7% air void content is considered as the reference state. For any other air void content, the shift factor (*AV*) is used to account for vertical shift of the compliance of specimens with other percentages of air voids relative to specimens with 7% air voids. Finally, the change in air void content and aged transient compliance of asphalt mixtures can be defined by substituting in Equation (5.5), such that:

$$\Delta\bar{D}^{A,AV} = AV.\sum_{n=1}^{N}(1-A)^{k_1} D_n.\left[1-\exp\left(-(1-A)^{k_2}\lambda_n.\psi^t\right)\right] \tag{5.8}$$

The proposed shifting factors (*AV*, *A*, k_1, and k_2) can be identified from the above expressions by minimizing the error between the experimental and calculated $\Delta\overline{D}^{A,AV}$, such that:

$$error = \left(\Delta\overline{D}^{A,AV} - \Delta\overline{D}^{A,AV}{}_{Exp}\right)^2 \tag{5.9}$$

Table 5.2 Shifting Parameters at Different Air Void Contents and Aging Levels

Shifting Parameters	Air Void Content		
	4%	7%	10%
AV	0.76	1.00	1.03
A_3	0.17	0.17	0.17
A_6	0.22	0.22	0.22
k_1	2.97	2.88	1.79
k_2	0.48	0.56	0.24

Table 5.2 summarizes the shift factors. By evaluating the findings in Table 5.2, it can be concluded that the air void shift factor is mostly a function of the air void content in the asphalt mixture, while the aging shift factor is calculated for each aging level. The material properties k_1 and k_2 depend on air void content.

5.5 Schapery’s Nonlinear Viscoelastic Constitutive Relationship

Schapery’s nonlinear viscoelasticity theory (Schapery 1969a and 1969b) is used to model the viscoelastic response of HMA, as described earlier in Section 4.3.2. Having the nonlinear viscoelastic parameters on hand for different stress levels during the RCRT-VS allows for characterization of nonlinear viscoelastic behavior of the asphalt mixtures. The irrecoverable strain response can be obtained by subtracting the viscoelastic behavior from the total measured strain response. Figure 5.3 presents the identified values of the nonlinear parameters at different temperatures, different aging levels, and different air void contents.

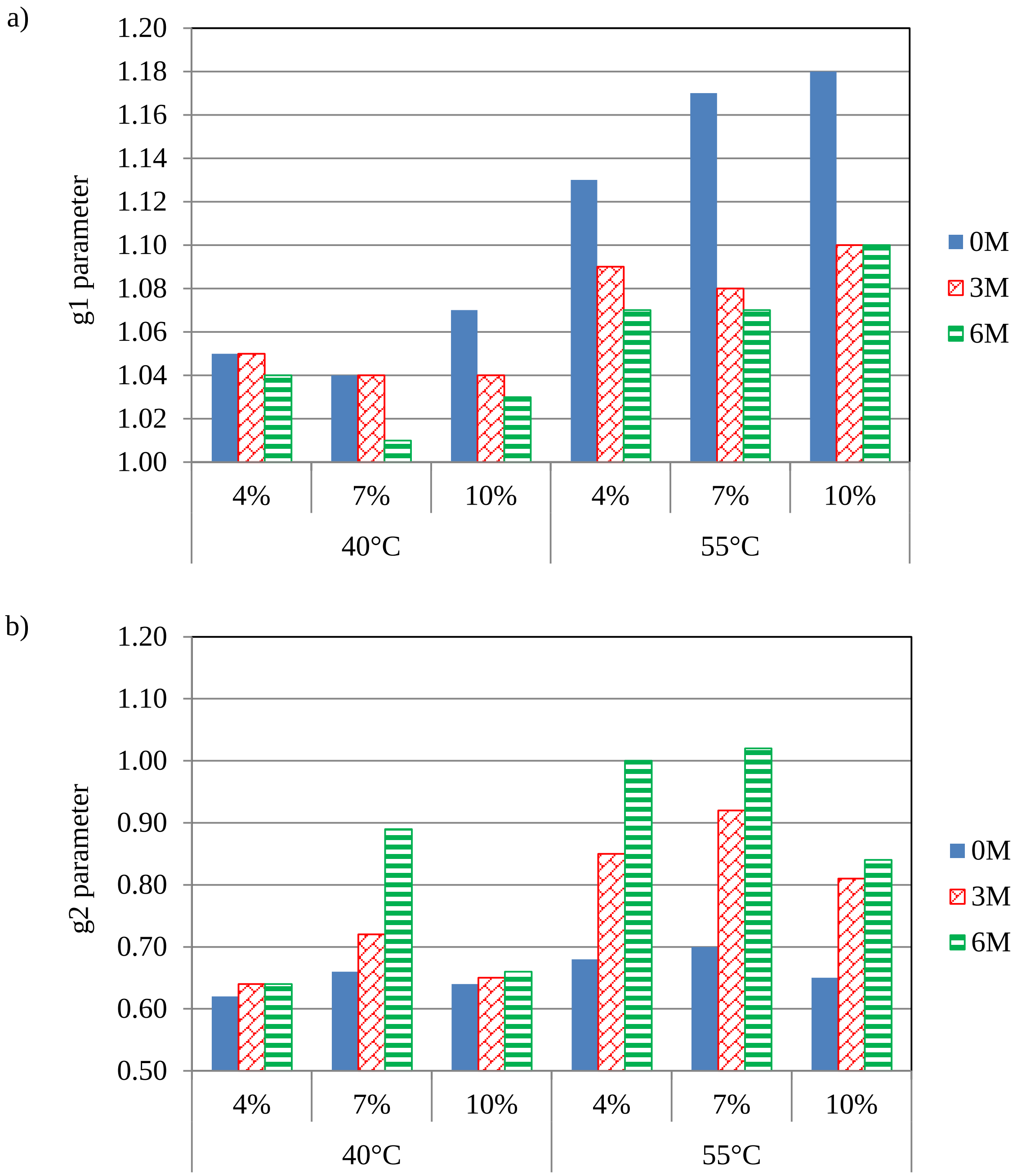

Figure 5.3 Effect of Aging Level and Air Void Content on Nonlinear Viscoelastic Properties

c)

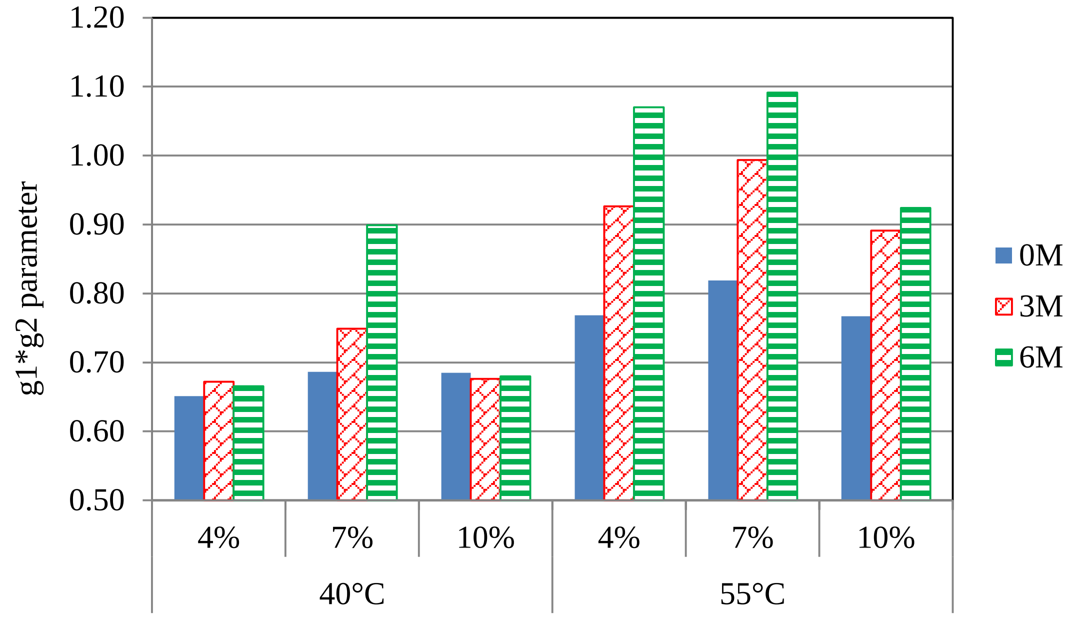

Figure 5.3 Continued

As $g_1 \times g_2$ increases, the nonlinearity in viscoelastic deformation increases. From Figure 5.3, nonlinearity increases with an increase in testing temperature and an increase in aging level. In addition, the nonlinear viscoelastic deformation reaches its maximum at 7% air void content. Linear viscoelastic behavior is the case when the $g_1 \times g_2$ parameter equals 1. However, most of the $g_1 \times g_2$ parameter values are less than unity, which is an indication that the RCRT-VS causes changes in the material structure (or hardening), reducing the viscoelastic response relative to the linear case.

5.6 Perzyna’s Viscoplastic Constitutive Relationship

In order to calculate the viscoplastic deformations in asphalt mixtures, Perzyna-type viscoplasticity constitutive equations (Masad et al. 2005, Tashman et al. 2005a, Huang et al. 2011a, and Huang et al. 2011b), as described earlier in Section 4.3.3, are used. By determining the viscoplastic parameters, the predicted viscoplastic strain can be determined and compared to the measured. The viscoplastic model parameters are summarized in Table 5.3 for different temperatures, aging levels, and air void contents.

The viscoplastic deformation of asphalt materials is nonassociative, which requires assuming the plastic potential function F to be different than the yield function f. By doing so, the direction of the viscoplastic strain increment is normal to the plastic potential surface and not to the yield surface. In order to obtain nonassociative viscoplasticity, the Drucker-Prager-type function is used as the plastic potential function, but using the parameter β instead of α (Huang 2008, Darabi 2011).

Figure 5.4 shows different values of dilation parameter of the investigated cases of asphalt mixtures. Results show an increase in the dilation characteristics for asphalt mixtures with an increase in temperature, which explains why the material expands more at high temperatures. However, the dilation characteristics decrease with an increase in aging level and air void content. As the air void content decreases, the angle of friction increases with an increase in material dilation. In addition, the material gets stiffer when it gets aged, which decreases dilation of the material.

Table 5.3 Viscoplastic Parameters for Different Aging Levels and Air Void Contents

Temp., °C	Air Void Content	Aging Level	α	β	d^{vp}	Γ^{vp}	N	k_0	k_1	k_2
40°C	4%	0 months	0.15	0.07	0.778	0.000507	1.42	27	1384	573
		3 months	0.15	0.05	0.778	0.000400	1.49	53	1523	2389
		6 months	0.15	0.03	0.778	0.000377	1.32	64	1600	2944
	7%	0 months	0.15	0.04	0.778	0.000879	1.07	75	1669	512
		3 months	0.15	0.01	0.778	0.000857	1.12	94	1416	975
		6 months	0.15	0.001	0.778	0.000801	1.70	114	1479	1041
	10%	0 months	0.15	0.03	0.778	0.002935	1.46	55	1365	493
		3 months	0.15	0.009	0.778	0.002495	1.82	92	1388	618
		6 months	0.15	0.001	0.778	0.002054	2.18	129	1411	743

Table 5.3 Continued

Temp., °C	Air Void Content	Aging Level	α	β	d^{vp}	Γ^{vp}	N	k_0	k_1	k_2
55°C	4%	0 months	0.15	0.12	0.778	0.001152	1.22	33	1858	697
		3 months	0.15	0.10	0.778	0.000931	1.57	41	1881	932
		6 months	0.15	0.08	0.778	0.000829	1.41	51	1901	1239
	7%	0 months	0.15	0.08	0.778	0.002010	1.54	63	1613	322
		3 months	0.15	0.06	0.778	0.001911	1.63	71	1829	462
		6 months	0.15	0.05	0.778	0.001720	1.44	85	1877	579
	10%	0 months	0.15	0.05	0.778	0.006300	1.31	70	1363	155
		3 months	0.15	0.04	0.778	0.006079	1.52	81	1417	451
		6 months	0.15	0.03	0.778	0.005507	1.70	89	1504	632

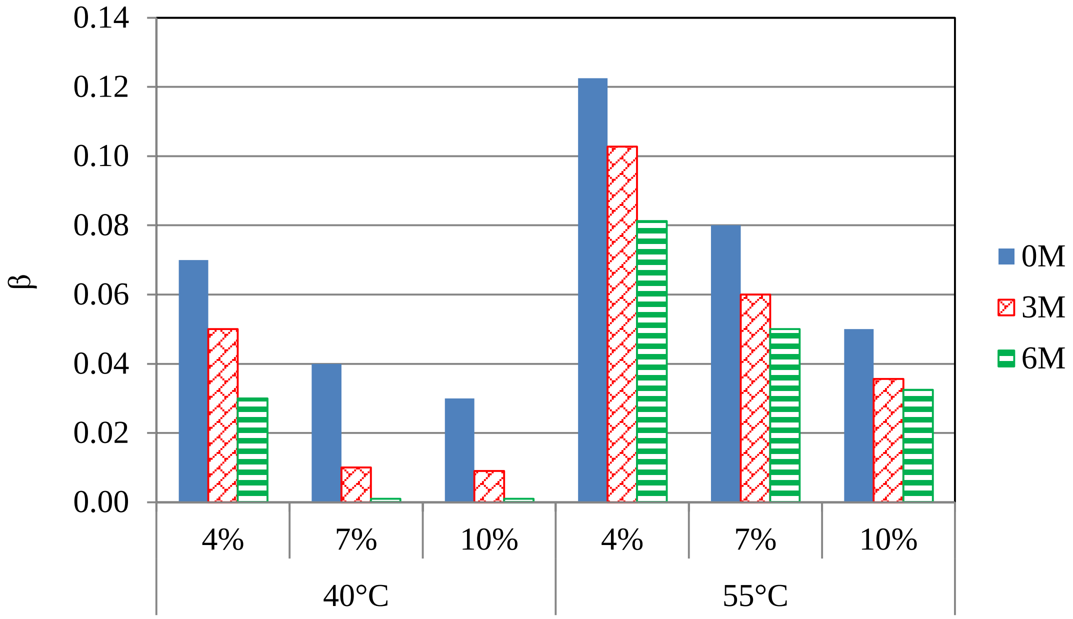

Figure 5.4 Effect of Aging Level and Air Void Content on Dilation Characteristics

Asphalt materials get stiffer as temperatures decreases, as aging level increases, and as air void content decreases. When they get stiffer, viscoplastic potential decreases such that the resistance of the materials to undergo viscoplastic deformation increases. Such increase in resistance can be phenomenologically explained by changes in the viscoplastic fluidity parameter, Γ^{vp}. Figure 5.5 shows that stiff materials need more time to relax.

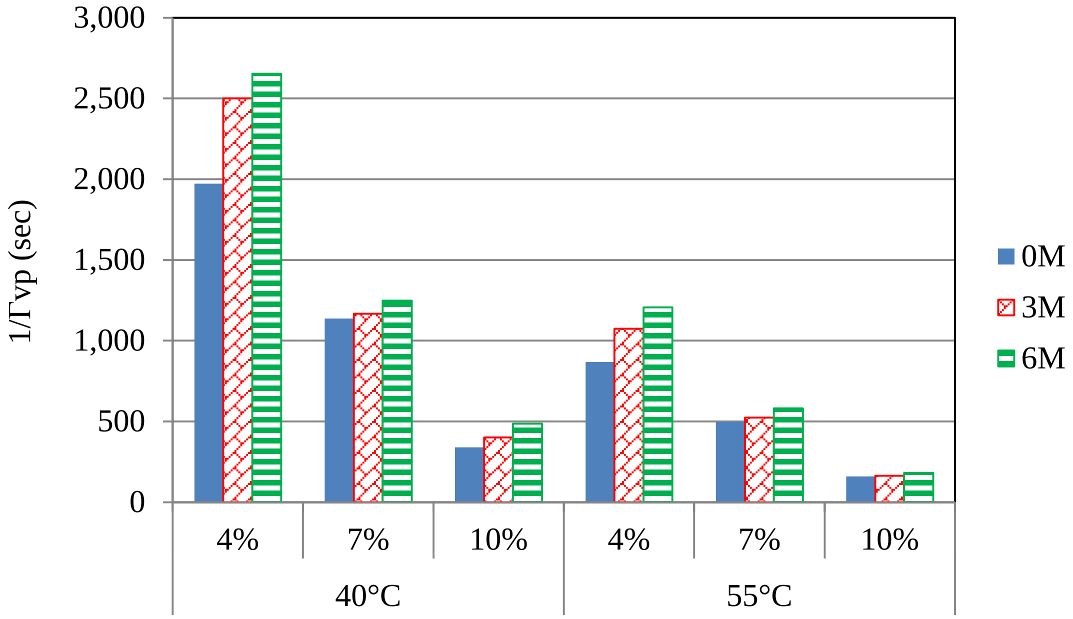

Figure 5.5 Effect of Aging Level and Air Void Content on Viscoplasticity-Relaxation Time

Figure 5.6 shows how the hardening function evolves with an increase in viscoplastic strain for different aging levels and air void contents. The asphalt materials harden faster as aging level increases and air void content decreases.

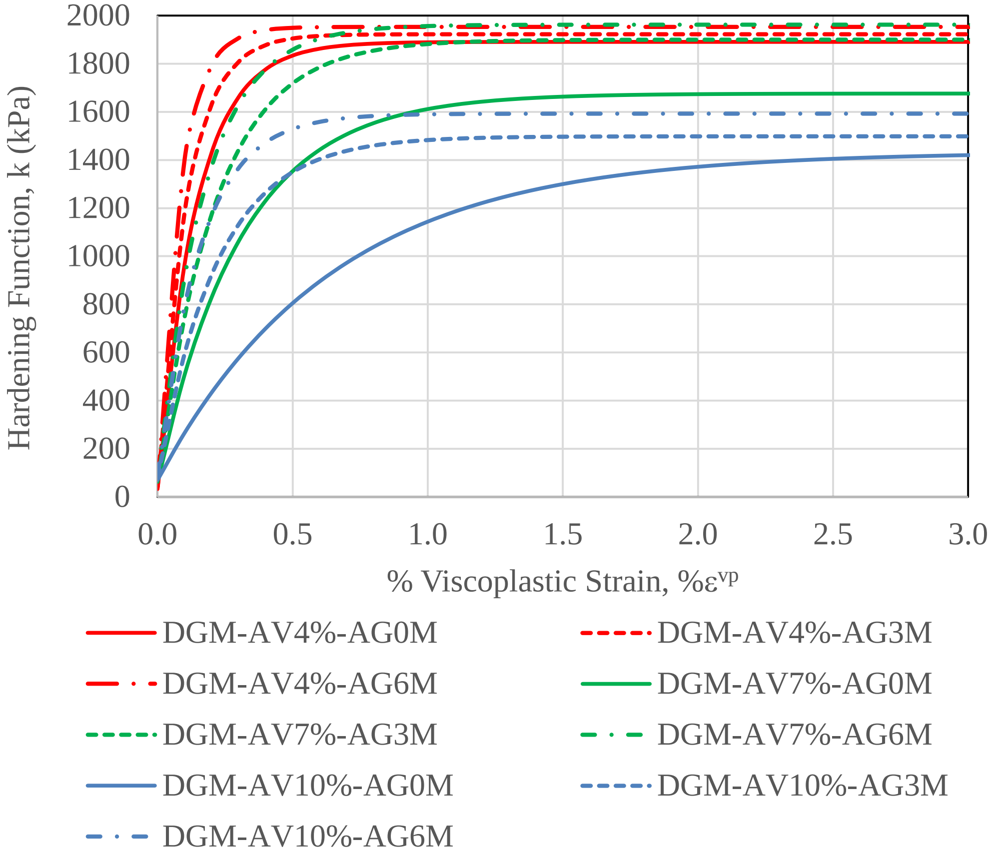

Figure 5.6 Effect of Aging Level and Air Void Content on Hardening Function

5.7 Summary

This chapter presents a framework for the analysis of linear viscoelastic, nonlinear viscoelastic, and viscoplastic behaviors of asphalt mixtures at different temperatures, air void contents, aging levels, and loading conditions. Two different tests are conducted to extract the viscoelastic and viscoplastic PANDA model parameters. The DMT is used to identify the linear viscoelastic parameters, while the RCRT-VS is used to identify the nonlinear viscoelastic and viscoplastic parameters.

The asphalt mixture gets stiffer with a decrease in air void content. While aging effect is small at low temperatures, there is a significant effect of aging level on the dynamic modulus at high temperatures.

The linear viscoelastic data at different temperatures and loading frequencies are shifted horizontally to obtain the long-term response of the asphalt mixture by using the time-temperature shift factor (a_T). The linear viscoelastic response for any air void content or aging level is obtained by vertically shifting the compliance terms and retardation times to the reference trend at an unaged 7% air void content. The nonlinearity term ($g_1 \times g_2$) increases with an increase in testing temperature and aging level.

For the viscoplastic properties, the dilation characteristics decrease with a decrease in temperature, increase in aging level, and increase in air void content. When the asphalt material gets stiffer, its viscoplastic potential decreases such that the resistance of the mixture to undergo viscoplastic deformation increases. The asphalt material hardens faster, meaning that the material becomes harder as a result of plastic deformation, as aging level increases and air void content decreases.

The analysis in this chapter is conducted for only one asphalt mixture. It is necessary to evaluate the applicability of the analysis method for more asphalt binders, aggregate sources, and mixture types that exhibit different properties for asphalt mixtures.

CHAPTER VI

GLOBAL SENSITIVITY ANALYSIS FOR VISCOELASTIC AND VISCOPLASTIC PANDA MODELING OF ASPHALT MIXTURE PERFORMANCE

6.1 Introduction

The ability of the PANDA constitutive models to describe stress/strain relationships with time is dependent on the rational prediction of each model parameters. The sensitivity analysis of the PANDA constitutive models' output is essential in identifying the significance of each model parameter's effect on asphalt mixture response. By displaying the range of possible responses of an asphalt mixture for a range of input values, the pavement engineer can decide which input values are critical for an asphalt mixture to achieve desirable performance. In addition, the outcomes of the sensitivity analysis guide the experimental work to focus on determining the parameters that significantly affect mixture performance. The GSA methods based on FAST and Sobol sequence approaches are implemented in GSAT in MATLAB to evaluate the sensitivity of PANDA constitutive models to their input parameters.

6.2 Background

Several constitutive relationships and mechanistic models are developed for simulating, studying, and predicting the performance of asphalt mixtures under compression. These modeling approaches, including PANDA models, have many parameters that need to be determined experimentally. The uncertainty in model parameters causes uncertainty in the model output prediction (Hornberger and Spear 1981). As shown in Figure 5.1 (Loucks 2006), a highly sensitive model amplifies the uncertainty of the input to the uncertainty of the output. So, identification of the relevancy of the input parameters allows model simplification and reduces the computational cost.

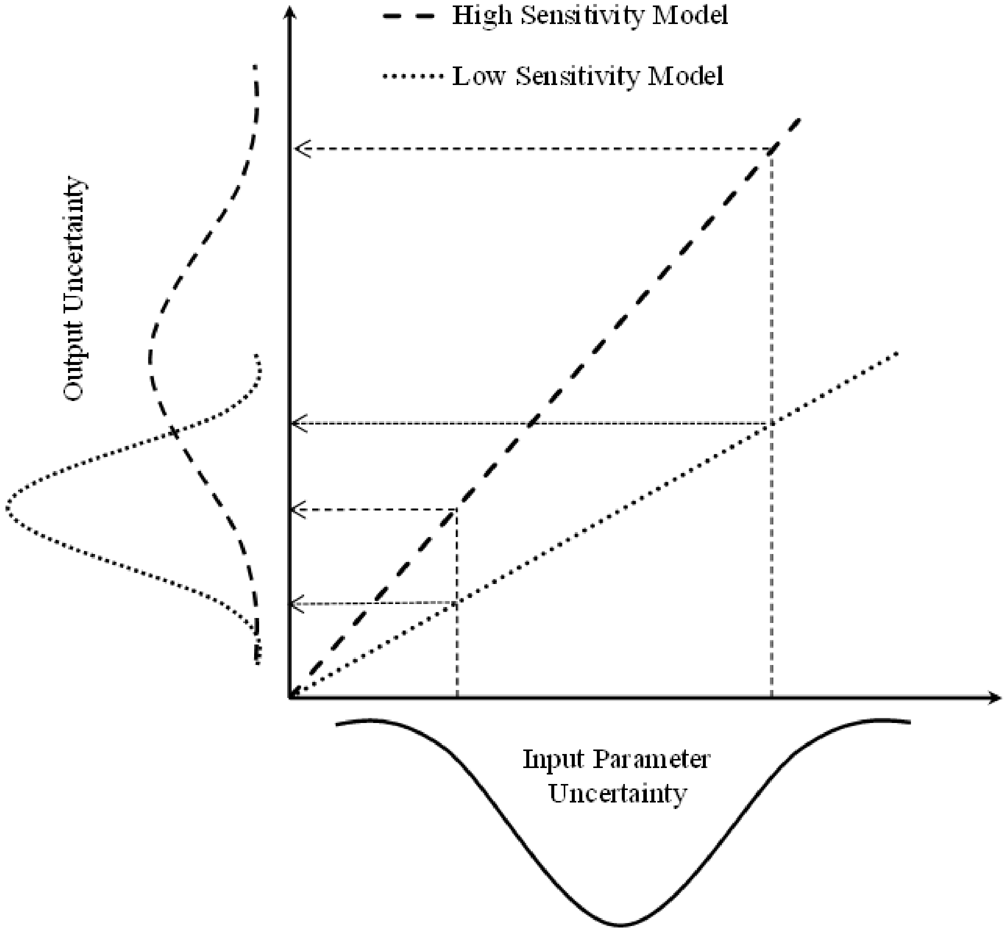

Figure 6.1 Influence of Model Sensitivity on the Relationship Between Input and Output Uncertainties (adapted from Loucks 2006)

6.3 Sensitivity Analysis Methods

Sensitivity analysis allows studying the relationships between input and output uncertainties and identifying the most significant input parameters and the contribution of the variability input interactions (Sobol 1993, Saltelli et al. 2000, Pradlwarter et al. 2005).

Based on the literature of sensitivity analysis, it can be classified into two major branches: local sensitivity and global sensitivity. Local sensitivity is the only analysis performed in practical cases due to the computational costs (Saltelli 2002a). It refers to sensitivity at a certain point in the parameter space (typically at the optimal fit point to the real data). The local response of the model, obtained by varying input factors one at a time, is investigated while the remaining parameters are set to their nominal values. This procedure involves estimating the partial derivatives, possibly normalized by the nominal value of the factor or by its standard deviation (Campolongo et al. 1999).

On the other hand, global sensitivity refers to a consolidated sensitivity over the entire input parameter space. The aim of GSA is to partition the whole output uncertainty to the different sources of uncertainty in the model inputs (Saltelli 2002b). In a complex model with many input parameters, GSA can be useful to simplify the model. So, if the model output is not sensitive to an input parameter, x_i,, the effect of that parameter can be ignored, x_i can be fixed, and the complexity of the model is reduced.

GSA methods are based on estimating the fractional contribution of each input factor to the total variance of the model under investigation (Patelli and Pradlwarter 2010). Too many algorithms are proposed in the literature for GSA. Two vigorous approaches based on analysis of variance (ANOVA) decomposition are implemented and used (Cannavo 2012), namely the FAST method and the Sobol sensitivity, discussed in the following sections.

In this study, a free software tool for GSA (named GSAT) is modified for the research purpose. The proposed approach of sensitivity analysis is tested and applied on the input parameters of both viscoelastic and viscoplastic PANDA models parameters, and their effects are studied on both recoverable and irrecoverable deformation.

6.4 Variance-Based Sensitivity Analysis

Variance-based sensitivity analysis is a form of GSA. Variance-based measures of sensitivity are attractive because they measure sensitivity across the whole input space, deal with nonlinear responses, and measure the effect of interactions in nonadditive systems (Patelli and Pradlwarter 2010). For these reasons, they are widely used when it is feasible to calculate them involving the use of Monte Carlo methods.

Let $y = f(X)$ be the model function, where y is the output and $X = x_i$, where $i = 1$ to n input parameters, each one associated with a probability density function (pdf). In sensitivity analysis, knowing how much variance would disappear is required if one or more input parameters is known and fixed. In other words, in the case of a single input factor, we are interested in the conditional variance of y, given $x_i = \overline{x_i}$, $\operatorname{var}\left\{y \mid \overline{x_i}\right\}$.

Because the true value of x_i is not known in advance, only the variance of the conditional expectation, $E\left[y \mid \overline{x_i}\right]$, for all possible values, x_i, can be calculated. This variance, usually indicated with D_i, is a measure of the importance of input factor x_i on the variance of the output, i.e., the sensitivity of y to x_i. Normalizing D_i by the unconditional variance of y, the following quantity is obtained:

$$S_i = \frac{\operatorname{var}\left\{E\left[y \mid \overline{x_i}\right]\right\}}{\operatorname{var}\left\{y\right\}} \tag{6.1}$$

The measure S_i was referred to by Sobol (1993) as first-order sensitivity index, and it measures the only main contribution of the input x_i on the output variance, neglecting interactions with other input parameters. If an interaction among input parameters occurs, the total effect on the output variance is greater than the sum of their first-order effects, i.e., $S_{ij} \geq S_i + Sj$. Each index, S_i, ranges between 0 and 1 and grows with an increase in input factor importance. The expected value of the output E[y] can be evaluated by the n-dimensional integral.

$$E\left\{y\right\} = \int_{I^n} f\left(x\right)\, dx \tag{6.2}$$

where, without losing generality $f \subseteq I^n$, I^n is the n-dimensional unit hypercube.

In the following sections, first function decomposition is introduced as useful to solve Equation (6.2); then, two methods (FAST and Sobol) are described, which basically use Equation (6.2) to calculate the sensitivity indices; and finally, their MATLAB implementation is discussed.

6.5 ANOVA

If the mathematical model is described by a scalar function $y = f(X)$, where X is the vector of the n-input variables and $f(X)$ is defined and square-integrable in the unit hypercube $[0, 1]^n$, it is always possible to write it as an expansion of terms in the following form:

$$f(x) = f_o + \sum_{s=1}^{n} \sum_{i=1}^{s} f_i(x_i) \tag{6.3}$$

where the second summation is made over all the possible combinations of *s* different input variables, at most 2^n components. Sobol (1990 and 1993) proved that this decomposition is unique and is known as ANOVA, if for all the components of the sum:

$$\int_0^1 f_i(x_i)\ dx_i = 0,\ \text{where i = 1 to s} \tag{6.4}$$

and $f_o = \int_0^1 f(\mathrm{x})\,\mathrm{dx}$ (6.5)

is the expected value of the model for uniformly distributed input variables.

This decomposition has the important property of orthogonality, i.e., for any two subsets of input variables, $\alpha \neq \beta$, an inner product.

$$\int_0^1 f_\alpha f_\beta\ dx = 0 \tag{6.6}$$

6.6 FAST

The FAST has successfully been applied to several linear and nonlinear modeling problems (Cukier et al. 1973, Cukier et al. 1975). The main idea underlying the FAST method is to convert the n-dimensional integral in Equation (6.2) into a one-dimensional (1D) integral using the ergodic theorem (Weyl 1938). Essentially, the function *f(X)* is expressed in a Fourier series:

$$f\left(x\right)=\sum_{k_i=-\infty}^{\infty} C_{k_i} e^{j2\pi\sum k_i x_i},\ \text{where } i=1 \text{ to n} \tag{6.7}$$

with $$C_{k_i}=\int_{I^n} f(x)e^{-j2\pi\sum k_i x_i}dx \tag{6.8}$$

Considering the ANOVA decomposition, the component $f_i(x_i)$,

where i = 1 to s, can be expressed as a Fourier series by taking into account the elements in Equation (5.7) with i = 1 to s, the only non-null indices (i.e., $k_{i1} \ldots k_{is}$).

In this way, the variances result in the sums of the modules of the Fourier coefficients:

$$\operatorname{var}\left\{f_i\right\}=\sum_{k_i=-\infty}^{\infty} | C_{k_i} |,\ \text{where } i=1 \text{ to s} \tag{6.9}$$

Because a multidimensional integral must be evaluated to calculate the Fourier coefficients in Equation (6.8), the idea is to transform the n-dimensional integral into a 1D integral by expressing every input as a function of a new independent variable, s, as recommended by Saltelli et al. (1999).

$$x_i\left(s\right)=\frac{1}{2}+\arcsin\left(\sin\left(\omega_i s\right)\right) \tag{6.10}$$

where the set {ω1, …, ωn} is linearly independent of integer frequencies. The transform in Equation (6.10) defines a search curve in the input space. If the frequencies, ωi, are morphologic, the search curve can pass through every point in the input space as s varies from 0 to ∞, so the multidimensional integral over the input space can accurately be transformed into a 1D integral along the search curve. It is possible to demonstrate that the n-dimensional integral in Equation (6.2) can be estimated by integrating over this parameterized curve (Saltelli et al. 2000). Because the curve is periodic as in Equation (6.10), only the integration over a period of 2π is required:

$$E\left\{y\right\}=\frac{1}{2\pi}\int_{-\pi}^{\pi} f(s)\, ds \tag{6.11}$$

In order to calculate Equation (6.1), the output variance of the first-order functions in ANOVA decomposition, i.e., the ones depending only on an input factor x_i, may be approximated by performing a Fourier analysis:

$$E\left[y\,|\,x_i\right]=\sum_i |\, C_{k_i}\, | \tag{6.12}$$

whose coefficients can be calculated as:

$$C_{k_i}=\frac{1}{2\pi}\int_{-\pi}^{\pi} f(s)e^{-j2\pi k_i\omega_i s}ds \tag{6.13}$$

The approximated Fourier coefficients, C_{ki}, can be computed by numerical integration of Equation (6.13).

6.7 Sobol Sequence Sensitivity

Sobol sequences are classified as quasi-random, low-discrepancy sequences (Sobol 1967). As shown in Figure 6.2, The Sobol sequence covers the space more evenly. These sequences use a base of two to form successively finer uniform partitions of the unit interval and then reorder the coordinates in each dimension.

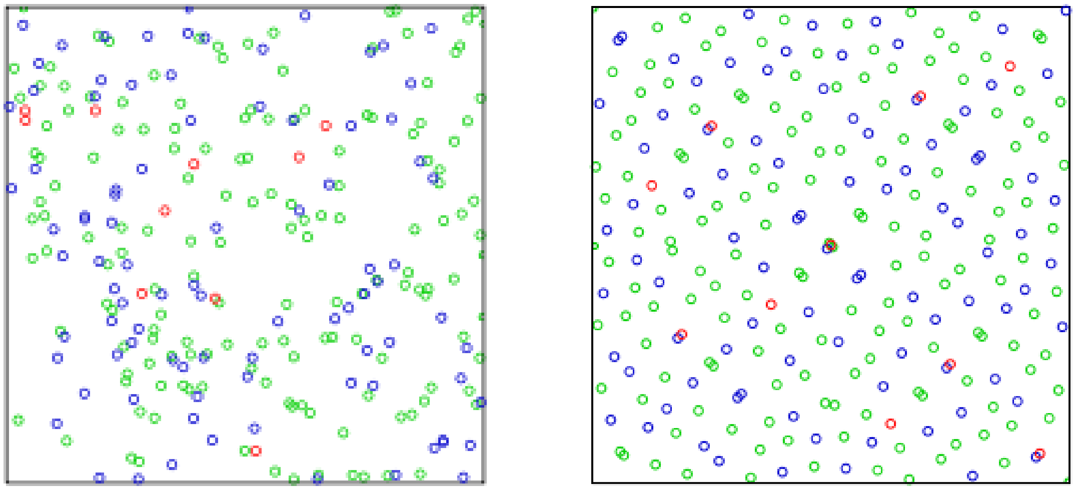

a) Pseudo-Random Sequence b) Sobol (Quasi-Random) Sequence

Figure 6.2 The Difference Between Pseudo-Random and Quasi-Random Sequences (adapted from Jheald 2011)

In 1990, Sobol proposed a new approach to determine sensitivity indices based on ANOVA decomposition and to determine the sensitivity of coupled input parameters. The main concept is to determine variances of the terms in the ANOVA decomposition:

$$D_i = \int_0^1 f_i^2 \ dx_i, \text{ where } x = 1 \text{ to } s \tag{6.14}$$

while the total variance will be:

$$D = \int_0^1 f^2\left(X\right) \ dX - f_o^2 = \sum_{s=1}^{n} \sum_{i=1}^{s} D_i \tag{6.15}$$

Sobol (2001) defined the global sensitivity index as the ratio of variances, and all sensitivity indices are non-negative.

$$S_i = \frac{D_i}{D}, \text{ where } i = 1 \text{ to } s \tag{6.16}$$

$$S_i = 0 \ \Leftrightarrow \ f_i = 0, \text{ and } \sum_{s=1}^{n} \sum_{i=1}^{s} S_i = 1, \text{ where } i = 1 \text{ to } s \tag{6.17}$$

S_i can be seen as a sensitivity measure of a set of variables x_i. It corresponds to a fraction of the total variance given by f_i (x_i). For instance, S_2 is the main effect of the variable x_2; S_{23} is a measure of interactions between the variables x_2 and x_3 (i.e., the total variance due to parameters x_2 and x_3 does not equal the sum of the main effects of parameters x_2 and x_3 alone), and so on. From another standpoint, the first-order indices, S_i, stand for the predicted percentage decrease in variance value, which is obtained when the *i*th parameter has no uncertainty (Borgonovo 2007, Saltelli 2002b). The first-order Sobol sensitivity indices are equivalent to the FAST indices (Chan et al. 2000).

Determining all the sensitivity indices demands the estimation of second integrals. For highly dimensional problems, another approach by Sobol (1990) introduced sensitivity indices for subsets of variables and total sensitivity indices. If the model inputs $x_1, \ldots, x_n$ are assumed as independent random variables, the Sobol approach remains the same. However, the integral functions Equations (6.4) and (6.5) must be multiplied by the respective distribution functions, and the integral intervals must be extended to $\left[-\infty, +\infty\right]$, as reported in Sobol and Kucherenko (2005a).

6.8 Quasi-Monte Carlo Approach

Monte Carlo integration is a method for numerical integration (i.e., numerically computing a definite integral) using random sampling. Contradictory to most algorithms that usually evaluate the integrand on a regular grid, Monte Carlo integration is evaluated at random points (Caflisch 1998). This method is particularly useful for higher-dimensional integrals (Press and Farrar 1990).

The Monte Carlo approach includes generating a sequence of pseudo-randomly distributed points inside the unit hypercube. Practically, replacing random sequences with low-discrepancy sequences is widely known as the Quasi-Monte Carlo method to improve the efficiency of the estimators. Some low-discrepancy sequences commonly used in sensitivity analysis include the Sobol sequence and the Latin hypercube design (Sobol and Kucherenko 2005b).

The applicability of the Sobol GSA is related to the possibility of computing the multidimensional integrals reported in the previous section. The Monte Carlo quadrature formula is based on the probabilistic interpretation of an integral (Kucherenko and Shah 2007). For a random variable that is uniformly distributed in I^n:

$$\int_0^1 f\left(x\right) dx = E\left\{ f\left(x\right)\right\} \tag{6.18}$$

where $E\left\{f\left(x\right)\right\}$ is the mathematical expectation and can be approximated as:

$$\overline{E}\left\{f\left(x\right)\right\} = \frac{1}{N}\sum_{i=1}^{N} f\left(x_i\right) \tag{6.19}$$

where $\left(x_i\right)$ is a sequence of random points in I^n of length N. The approximated Equation (6.19) converges to Equation (6.18) with probability 1 for $N \to \infty$.

For an arbitrary subset of variables $\alpha = \left\{x_i\right\} \subset \left\{x_1, ..., x_m\right\}$ and its complementary $\beta = \left\{x_1, ..., x_n\right\} / \alpha$, two independent random points uniformly distribute in I^n: $\pi_1 = \left[\alpha_1; \beta_1\right]$ and $\pi_2 = \left[\alpha_2; \beta_2\right]$. The model *f(x)* is evaluated in the two points $f\left(\pi_1\right)$ and $f\left(\alpha_1; \beta_2\right)$. For N independent trials at $N \to \infty$, the hypothesis of square-integrability of *f(x)* is as follows:

$$\left.\begin{aligned} &\frac{1}{N}\sum_{k=1}^{N} f\left(\pi_{1k}\right) \to f_o \\ &\frac{1}{N}\sum_{k=1}^{N} f^2\left(\pi_{1k}\right) \to D + f_o^2 \\ &\frac{1}{N}\sum_{k=1}^{N} f\left(\pi_{1k}\right).f\left(\alpha_{1k}; \beta_{2k}\right) \to D_\alpha + f_o^2 \end{aligned}\right\} \tag{6.20}$$

For the set of α, S_α is the sensitivity index, which includes all its partial variances. Each single sensitivity index can be iteratively determined from the following formula:

$$D_i = D_\alpha - \sum_{\alpha-1} D_{\alpha-1} + ...(-1)^{m-r}\sum_{\alpha-r} D_{\alpha-r} + ...(-1)^m f_o^2, \text{ where } i = 1 \text{ to } m \tag{6.21}$$

The summations are over all the permutations of size *m-r* of the indices listed in α. The estimation of D_α is accompanied by an error with 50% confidence as (Homma and Saltelli 1996):

$$\Delta D_\alpha = 0.6745\sqrt{\frac{F-I}{N}} \tag{6.22}$$

where $\begin{cases} I = \dfrac{1}{N}\sum\limits_{k=1}^{N} f\left(\pi_{1k}\right).f\left(\alpha_{1k};\beta_{2k}\right) \\ F = \dfrac{1}{N}\sum\limits_{k=1}^{N} f^2\left(\pi_{1k}\right).f^2\left(\alpha_{1k};\beta_{2k}\right) \end{cases}$

On the other side, the estimation of each D_i, which follows the relation in Equation (6.21), is accompanied by an error of linear combination of the terms in ΔD_α.

The efficiency of Monte Carlo methods is measured by the properties of random numbers. Clustering is a common disadvantage produced by random sampling. For any sampling, there will always be both empty areas and areas with dense points wasted due to clustering, as shown in Figure 6.2.a. In addition, the new points, which are randomly added, will not cover the empty areas precisely. Instead of pseudo-random sequences, using deterministic uniformly distributed sequences (low-discrepancy sequences) can produce a higher rate of convergence. The discrepancy of a sequence is a measure of its uniformity in a given volume of multidimensional space (Kuipers and Niederreiter 2006). The sequence of low-discrepancy (or Quasi-Random) points, as shown in Figure 6.2.b, prescribed in the Quasi-Monte Carlo approach (Sobol 1967), is featured by an enhanced convergence rate compared to the crude Monte Carlo as presented by Sobol (1990) and Homma and Saltelli (1995). For the number of trials, *k*, the selection of one

2n-dimensional quasi-random point, split into two n-dimensional points, reduces the number of samples N.

6.9 GSAT

A MATLAB framework consisting of a main code and a set of subroutines is used to determine the aforementioned sensitivity indices of a generic user-defined model in a toolbox named GSAT. This MATLAB code is an open source containing other features and expandable to any other MATLAB script (Cannavo 2012). Each subroutine included in the MATLAB code is responsible for performing a certain function. The functions are designed in a sequence for performing the desired sensitivity analysis.

The basic steps to analyze the global sensitivity of a model are shown in Figure 6.3. These steps begin with the creation of a new project (pro_Create). Then, for each input variable, x_i, a new input with its characteristics must be added to the project by using the function (pro_AddInput). This function requires the name of the variable and its pdf, which allows the (fnc_SampleInputs) subroutine to know how to sample the input variables. Two pdfs are already implemented: the uniform distribution for an interval and the Sobol one for the Sobol quasi-random distribution. Once the set of input variables is specified, the analysis begins with an initialization step by the subroutine (GSA_Init). This step is required for generating the two sets of quasi-random points used for the quasi-Monte Carlo procedures, as explained in Section 6.8. For this purpose, the MATLAB framework should include the Sobol set code for generating the quasi-random sequences. In this specific subroutine, more samples are required to obtain similar results in convergence, which enhances the quality of the low discrepancy in the supplied sequences. After that, the generic user-defined model is evaluated using the generated set of points, and the results are stored for sensitivity computation. Problem definition and algorithm initialization are followed by determining the sensitivity indices.

GSAT includes a subroutine called (GSA_FAST_GetSi) for performing the FAST analysis to models with up 50 different input parameters (Cukier et al. 1973). The function under consideration is defined as an input parameter, and then the vector of sensitivity indices for all the input parameters is produced. On the other hand, the subroutine (GSA_GetSi) carries out the Sobol analysis by calculating the sensitivity index of a defined input set. The intermediate calculations and partial solutions are saved immediately during code processing to avoid repeating the calculations and to save time by speeding up the successive calculations on other input sets. All time consumed during code processing depends exponentially on the number of input variables. The algorithm is checked and tested using some benchmarks included in the GSAT package.

As GSA's goal is to assess the sensitivity of an output to a given set of input parameters (Saltelli et al. 2009), the implementation of the viscoelastic and viscoplastic PANDA models in GSAT is described in the following section. The sensitivity of the recoverable and irrecoverable permanent deformation is investigated based on the input parameters of the viscoelastic and viscoplastic PANDA models.

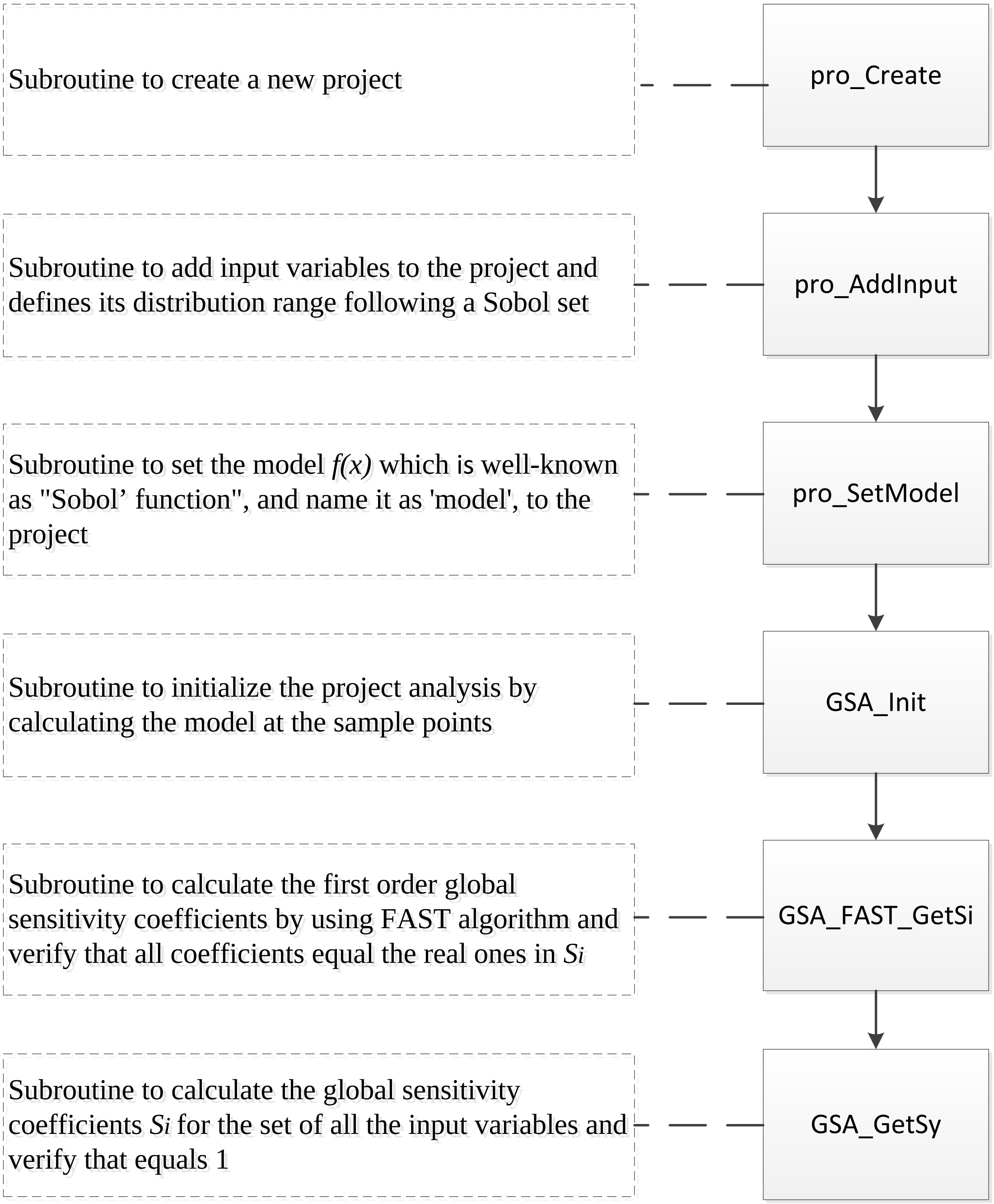

Figure 6.3 Flowchart of the Subroutines Performing the Sensitivity Analysis Steps Included in the GSAT Using a MATLAB Code

6.10 Implementation of Viscoelastic and Viscoplastic PANDA Models in GSAT

The PANDA modeling framework seeks to provide an advanced mechanistic approach to predict rutting (permanent deformation) with consideration to environmental conditions. The responses of asphalt mixes show both recoverable (viscoelastic) and irrecoverable (viscoplastic) components (Perl et al. 1983, Collop et al. 2003, Huang 2008). The recoverable component is usually modeled using the solid-like viscoelasticity constitutive relationships, whereas the irrecoverable component is usually modeled using fluid-like viscoelasticity and/or viscoplasticity constitutive relationships. The viscoelastic and viscoplastic PANDA models couple Schapery's nonlinear viscoelastic model (1969) with Perzyna's viscoplastic model (1971) described by the extended Drucker-Prager yield surface. Schapery's nonlinear viscoelastic and Perzyna's viscoplastic constitutive relationships characterize and decouple the recoverable and irrecoverable strains by analyzing dynamic modulus and repeated creep-recovery experimental tests. More details about the PANDA models were mentioned earlier in Section 4.3.

Three different asphalt mixtures are used to build the database of the PANDA model input parameters: FAM, DGM, and CAM. The investigated asphalt mixtures represent a rational range of commonly used asphalt mixtures in the field. From the input parameters database, the definition of each input parameter distribution range is built.

6.10.1 Sensitivity of Viscoelastic PANDA Model Parameters

Schapery's 1D single-integral viscoelastic model is presented in detail in Sections 4.3.1 and 4.3.2. For a specific asphalt mixture, linear and nonlinear viscoelastic parameters are extracted from the DMT and RCRT-VS. The DGM linear viscoelastic properties are used in the sensitivity analysis process, as shown in Table 6.1. Based on the presented data, the investigated sensitivity of Schapery's model output is based on the effect of the nonlinear viscoelastic properties (g_1 and g_2). The characteristics of the nonlinear viscoelastic input parameters are implemented in the algorithm runs, as presented in Table 6.2, based on the database ranges of the three mixtures.

Results from both FAST and Quasi-Random Monte Carlo sampling are both included in Table 6.3 for comparison. From the FAST results, it is observed that the S_{FAST} for g_1 is relatively small compared to the one for g_2. These observations are consistent with the quasi-random Monte Carlo simulation sampling, with a different number of samples. As long as the sampling number increases, the quality of the low discrepancy gets enhanced. While the summation of the global sensitivity indices equals 1, the sensitivity index of the interaction between the input parameters is also small. The parameter g_2 represents the nonlinear contribution in the viscoelastic response due to the level of stress, while parameter g_1 represents the nonlinear contribution in the transient response. As a result, input parameter g_2 is most significant compared to input parameter g_1.

Table 6.1 Linear Viscoelastic PANDA Model Parameters

n	$\lambda_n\left(1/\mathrm{s}\right)$	D_n (MPa^{-1})
1	2.38×10^{2}	1.20×10^{-5}
2	1.73×10^{1}	2.95×10^{-5}
3	1.25×10^{0}	6.23×10^{-5}
4	9.07×10^{-2}	1.40×10^{-4}
5	6.57×10^{-3}	4.82×10^{-4}
6	4.76×10^{-4}	7.03×10^{-4}
7	3.45×10^{-5}	3.14×10^{-3}
8	2.50×10^{-6}	4.79×10^{-3}
D_0		5.16×10^{-5}

Table 6.2 Characteristics of Nonlinear Viscoelastic PANDA Model Parameters as Sobol pdfs

Definition	Input Variables	
	g_1	g_2
Lower bound	0.6	0.1
Upper bound	1.7	1.2

Table 6.3 Global Sensitivity Indices of Nonlinear Viscoelastic PANDA Model Parameters

GSI			g_1	g_2
S_{FAST}			0.0295	0.9023
S_i	No. of samples for Quasi-Random Monte Carlo simulation	50000	0.0283	0.9031
		100000	0.0282	0.9030
		500000	0.0281	0.9030
		1000000	0.0280	0.9029

A parametric analysis is conducted to capture the total effect of each input parameter using the upper and lower bounds in their definitions at a certain set of input values. Figure 6.4 shows the sensitivity of the viscoelastic strain due to the variation of each input parameter separately. The relative difference of the resulted viscoelastic strain is calculated as follows:

$$Relative\ Difference = \frac{\varepsilon_i^{ve} - \varepsilon_{reference}^{ve}}{\varepsilon_{reference}^{ve}} \tag{6.23}$$

As a result, the total effect of the g_1 parameter produces 1.77% change in the viscoelastic strain value within the lower and upper bounds of 0.6 and 1.7, respectively. On the other hand, the total effect of the g_2 parameter produces 10.01% change in the viscoelastic strain value within the lower and upper bounds of 0.1 and 1.2, respectively. These findings confirm the results of the FAST algorithm and the global sensitivity of Quasi-Monte Carlo simulations.

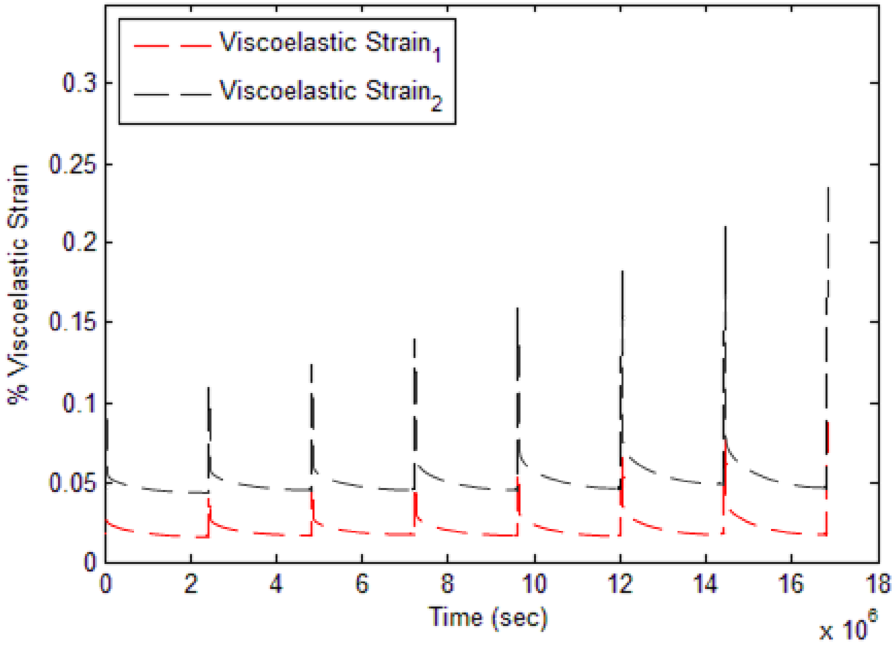

a) The Effect of g_1 Parameter on the Viscoelastic Strain

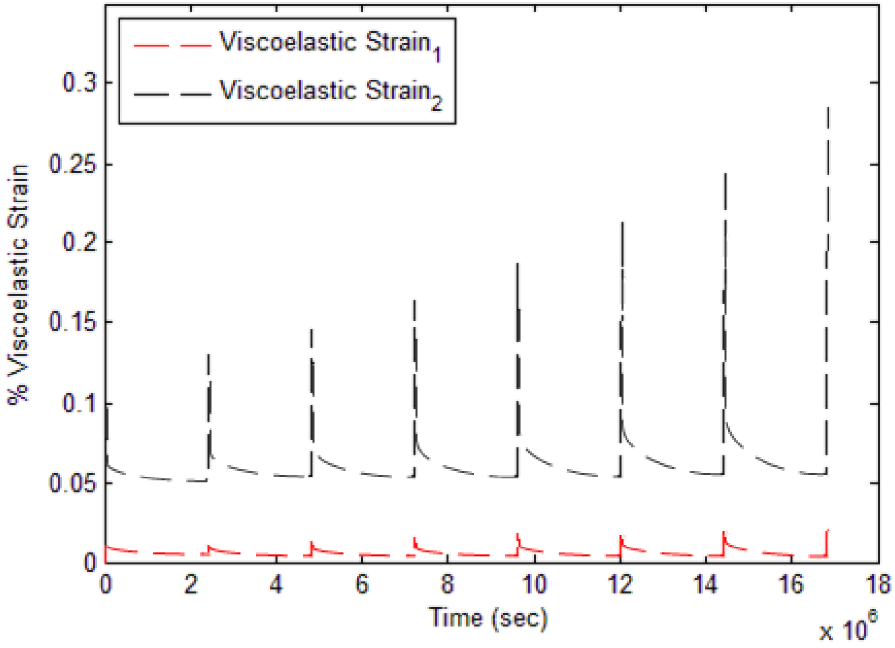

b) The Effect of g_2 Parameter on the Viscoelastic Strain

Figure 6.4 The Total Effects of Nonlinear Viscoelastic PANDA Model Parameters

6.10.2 Sensitivity of Viscoplastic PANDA Model Parameters

Perzyna-type viscoplasticity constitutive equations with modified Drucker-Prager yield surface are used to calculate viscoplastic strain in asphalt mixtures. These constitutive equations are presented in detail in Section 4.3.3. For a specific asphalt mixture, viscoelastic parameters are extracted from the RCRT-VS after separating the viscoelastic strain from the full response. The investigated sensitivity of Perzyna's model output is based on the effect of the viscoplastic properties (α, β, Γ^{vp}, N, k_o, k_1, and k_2). The characteristics of viscoplastic input parameters are implemented in the algorithm runs, as presented in Table 6.4, based on the database ranges of the three mixtures.

Table 6.4 Characteristics of Viscoplastic PANDA Model Parameters as Sobol pdfs

Definition	Input Variables						
	α	β	Γ^{vp}	N	k_o	k_1	k_2
Lower bound	0.15	0.001	0.0004	1.0	10	1000	150
Upper bound	0.30	0.30	0.006	5.0	150	2000	600

Results of sensitivity analysis by the FAST and quasi-Monte Carlo algorithms are presented in Table 6.5 for comparison. From the FAST results, it is observed that the S_{FAST} of k_1 is relatively high, followed by the S_{FAST} of Γ^{vp} and k_2 compared to the S_{FAST} of other parameters. These observations are consistent with the quasi-random Monte Carlo simulation sampling, with a different number of samples. From the observation, increasing the sampling number enhances the quality of the low discrepancy. As the summation of the global sensitivity indices equals 1, the interaction effect among these parameters, which is represented by 121 sensitivity indices, is remarkable. Where the k_1 parameter represents the hardening limit of asphalt mixtures against viscoplastic deformation, the N parameter is an exponent representing the viscoplastic rate sensitivity, the Γ^{vp} parameter represents the inverse of viscoplasticity-relaxation time, and the k_o parameter represents the initial yield strength of the asphalt mixtures. The α parameter is related to the angle of friction of the asphalt mixtures, the β parameter describes the dilation characteristics of asphalt mixtures, and the k_2 parameter is the strain-hardening rate. As a result, the input parameter k_1 is the most significant parameter compared to other input parameters.

Table 6.5 Global Sensitivity Indices of Viscoplastic PANDA Model Parameters

GSI			α	β	Γ^{vp}	N	k_o	k_1	k_2
S_{FAST}			0.0099	0.0116	0.1512	0.0236	0.0120	0.3264	0.1211
S_i	No. of samples for Quasi-Random Monte Carlo simulation	50000	0.0122	0.0117	0.1538	0.0262	0.0138	0.3063	0.1253
		100000	0.0045	0.0117	0.1515	0.0200	0.0116	0.3063	0.1254
		500000	0.0068	0.0116	0.1513	0.0220	0.0118	0.3158	0.1223
		1000000	0.0093	0.0116	0.1512	0.0233	0.0119	0.3260	0.1210

A parametric analysis is conducted to capture the main effect of each input parameter using the upper and lower bounds in their definitions at a certain set of input values. Figure 6.5 show the sensitivity of the viscoplastic strain due to the variation of each input parameter separately. The relative difference of the resulted viscoplastic strain is calculated as follows:

$$Relative\ Difference = \frac{\varepsilon_i^{vp} - \varepsilon_{reference}^{vp}}{\varepsilon_{reference}^{vp}} \tag{6.23}$$

As a result, the main effect of the k_1 parameter produces 103.0% change in the viscoplastic strain value within the lower and upper bounds of 1000 and 2000, respectively. The main effect of the N parameter produces 13.2% change in the viscoplastic strain value within the lower and upper bounds of 1 and 5, respectively. The main effect of the k_2 parameter produces 230.0% change in the viscoplastic strain value within the lower and upper bounds of 150 and 600, respectively. The main effect of the Γ^{vp} parameter produces 77.6% change in the viscoplastic strain value within the lower and upper bounds of 0.0004 and 0.006, respectively. The main effect of the k_o parameter produces 40.3% change in the viscoplastic strain value within the lower and upper bounds of 10 and 150 kPa, respectively. The main effect of the β parameter produces 32.0% change in the viscoplastic strain value within the lower and upper bounds of 0.001 and 0.30, respectively. The main effect of the α parameter produces 12.0% change in the viscoplastic strain value within the lower and upper bounds of 0.15 and 0.30, respectively.

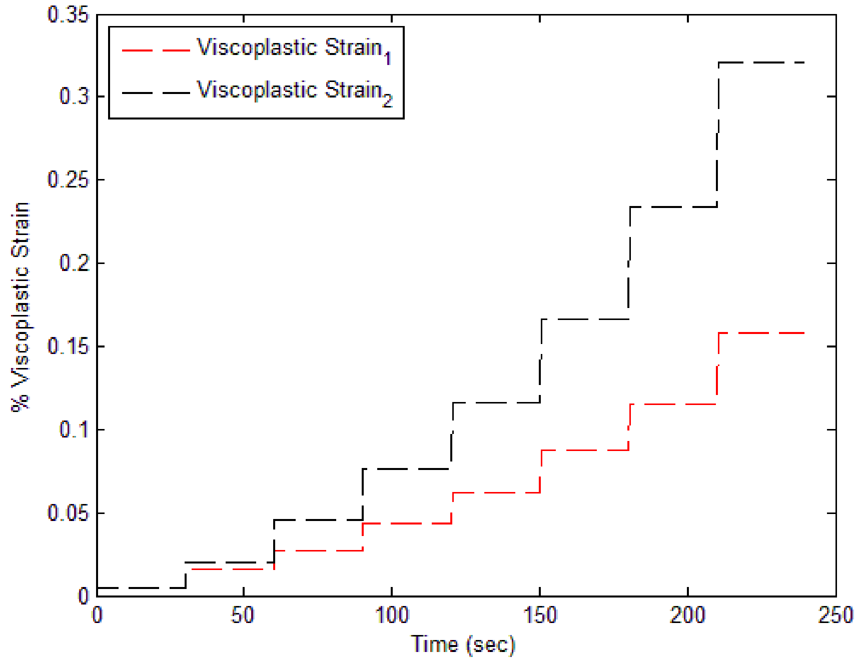

a) The Effect of k_1 Parameter on the Viscoplastic Strain

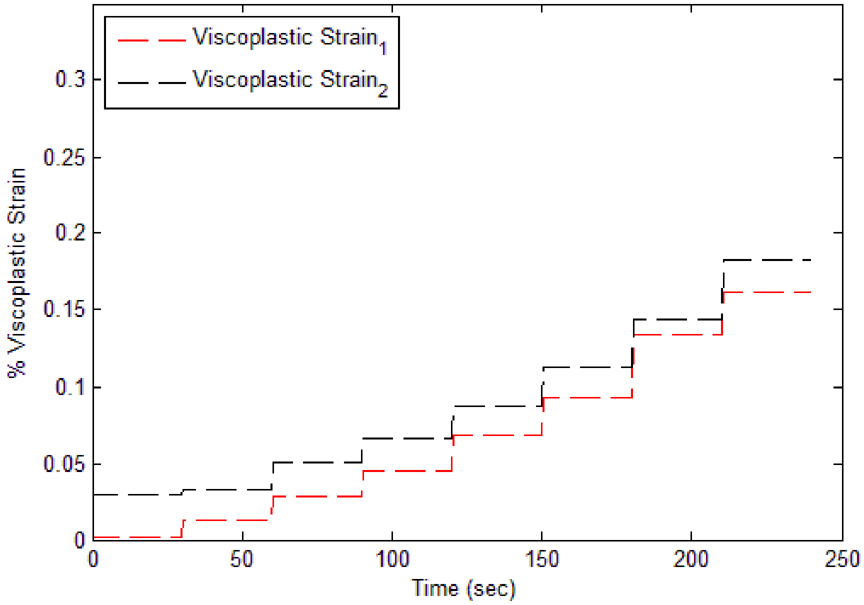

b) The Effect of N Parameter on the Viscoplastic Strain

Figure 6.5 The Total Effects of Viscoplastic PANDA Model Parameters

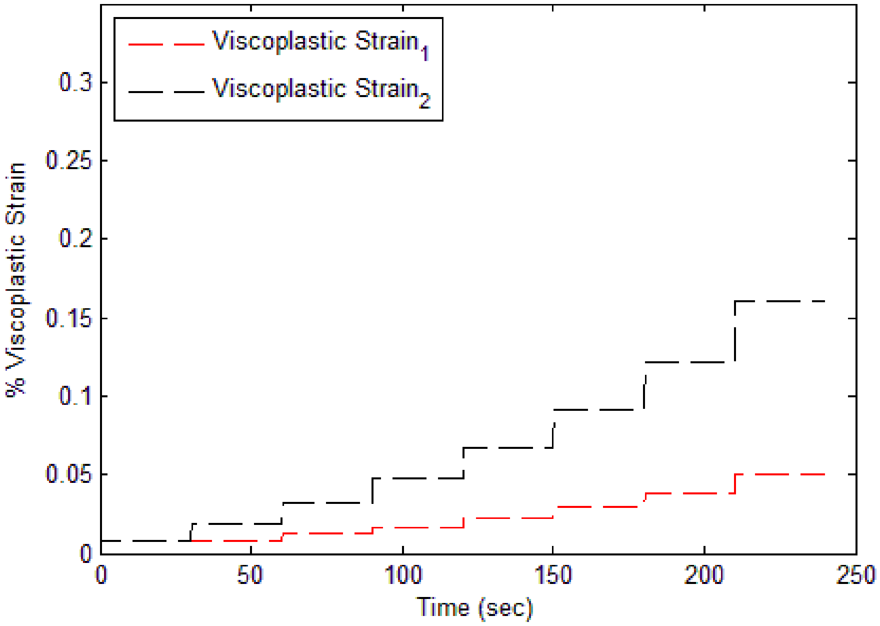

c) The Effect of k_2 Parameter on the Viscoplastic Strain

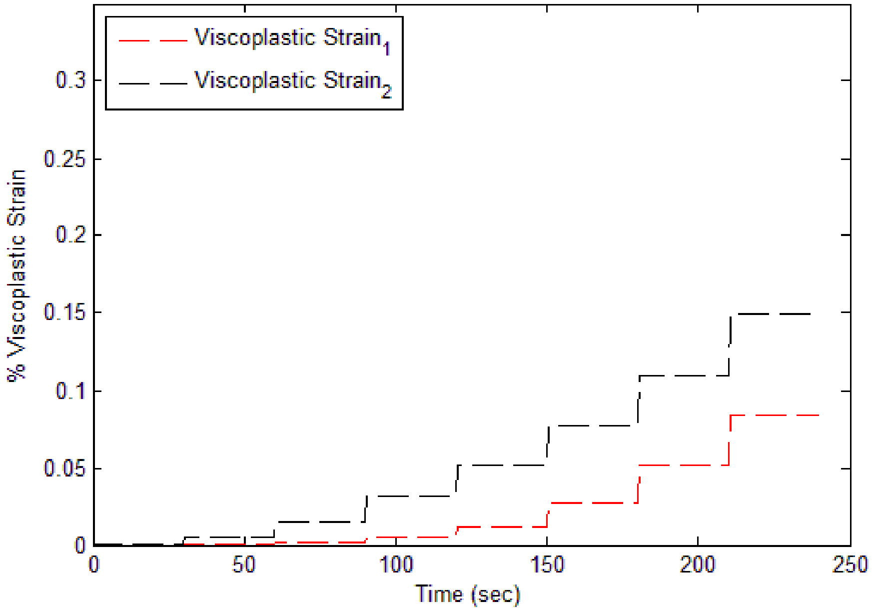

d) The Effect of Γ^{vp} Parameter on the Viscoplastic Strain

Figure 6.5 Continued

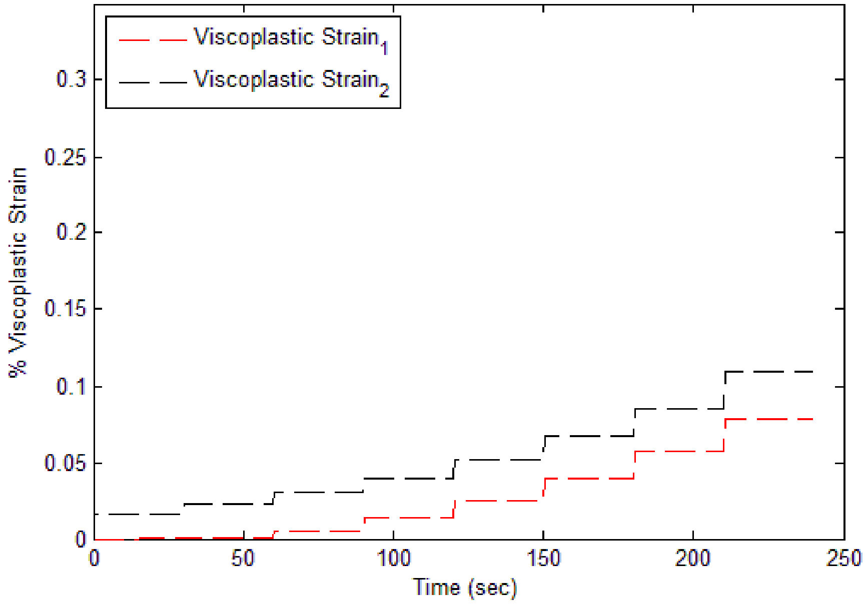

e) The Effect of k_o Parameter on the Viscoplastic Strain

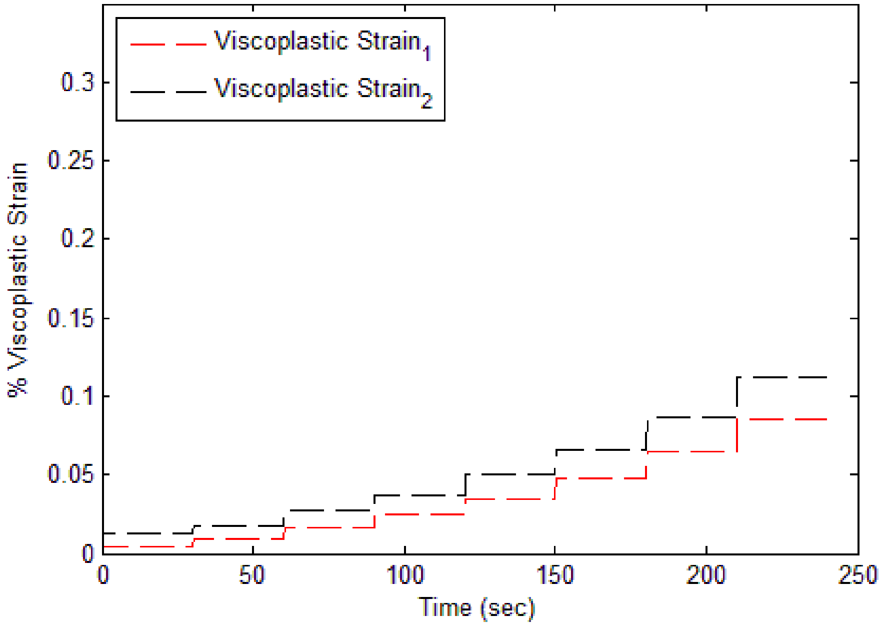

f) The Effect of β Parameter on the Viscoplastic Strain

Figure 6.5 Continued

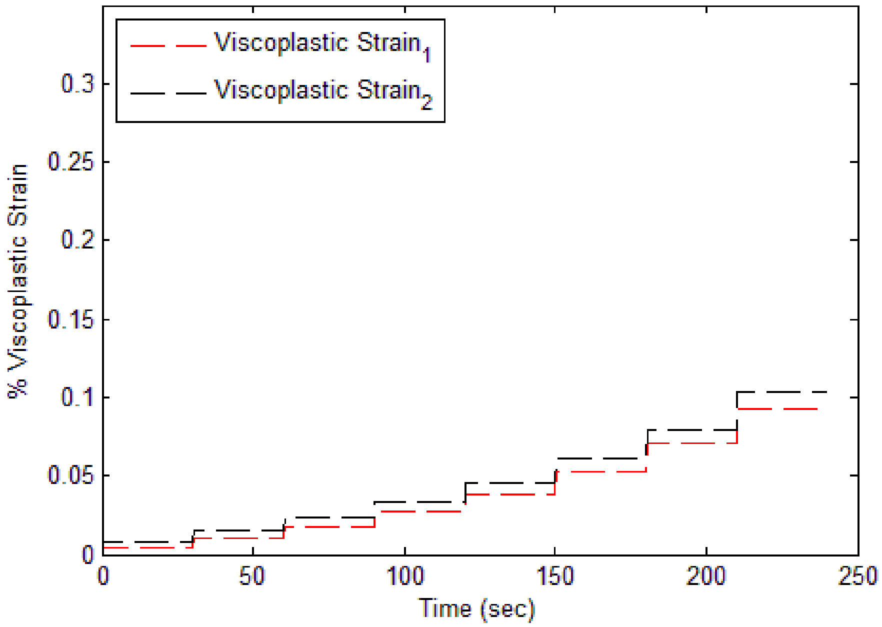

g) The Effect of *α* Parameter on the Viscoplastic Strain

Figure 6.5 Continued

These findings confirm the results of the FAST algorithm and the global sensitivity of quasi-random Monte Carlo simulations. The k_1 parameter is the most significant parameter compared to the others. α, β, and k_0 parameters can be assumed to be 0.15, 0.10, and 80 to 150 kPa, respectively, to reduce the computational cost and simplify the model. The outcomes of the parametric study come in accordance with results from both FAST analysis and using quasi-random Monte Carlo sampling, which are more accurate and consistent.

6.11 Summary

In this chapter, GSA is used for assessing the sensitivity of the viscoelastic and viscoplastic PANDA models to the values of its input parameters. This sensitivity analysis allows computing the significance of model parameters, thus giving the possibility to focus the experimental work to determine parameters truly related to material behavior and significantly affecting the model response. An open-source MATLAB toolbox, namely GSAT, is used to perform the described sensitivity analysis. This toolbox has been tested by various researchers using different types of test functions. In this part of the study, the capabilities of the proposed GSA approach are used to test the robustness of the viscoelastic and viscoplastic PANDA models in order to simplify the models by fixing the values of their input parameters without significant effect on the output. In conclusion, GSAT serves as a flexible design tool for the purpose of this part of the study. Based on the GSAT results, some of the input parameters of the viscoelastic and viscoplastic PANDA models are relatively sensitive to the type of asphalt mixture. These are the nonlinearity parameter (g_2), hardening function parameters (k_1, and k_2), and viscoplasticity-relaxation time ($1/\Gamma^{vp}$). However, some parameters can be assumed as constant values: g_1, α, β, and k_o parameters can be assumed to be 1.0, 0.15, 0.10, and 80 to 150 kPa, respectively, in order to simplify the viscoelastic and viscoplastic modeling behaviors.

CHAPTER VII

FIELD PERFORMANCE SIMULATIONS OF ASPHALT CONCRETE MIXTURES USING VISCOELATIC AND VISCOPLASTIC PANDA MODEL FRAMEWORK

7.1 Introduction

This chapter presents PANDA analysis of the effects of mixture type, air void content, and aging level on performance. The mixtures considered in the analysis are the DGM, FAM, and CAM, discussed earlier in Chapter IV. In addition, the DGM properties are determined at three different air void contents (including 4, 7, and 10%) and three aging levels (including 0, 3, and 6 months). Simulations are conducted using a 2D axisymmetric FE model subjected to pulse wheel loading at intermediate and high temperatures.

7.2 Background

Rutting is the accumulation of permanent deformation that grows gradually with increasing numbers of loading cycles (Collop et al. 1995). Computer simulations of rutting should include structural loading, boundary conditions, and material constitutive behavior. The model should account for the effects of different stress levels, loading rates, and temperatures (Abu Al-Rub et al. 2012).

FE analysis has been used extensively in the analysis of asphalt pavement performance. Lu and Wright (1998) constructed a 2D plane strain FE model to represent a three-layer pavement structure and employed Perzyna’s viscoplastic constitutive relationship to predict permanent deformation under a large number of loading cycles, assuming pulse loading. Pulse loading is commonly used to represent a wheel-moving load. However, the implicit assumption in conducting 2D plane strain FE simulations is that the loading condition is represented as an infinite load strip in the traffic direction. Hunter et al. (2007) conducted 2D plane strain FE simulations of the wheel-tracking test in order to predict rutting performance assuming pulse loading. However, Hunter et al. (2007) used a power law viscoplasticity constitutive relationship and neglected viscoelasticity and damage evolution. Their simulations show that the shape of rutting is significantly different than that obtained experimentally. Kettil et al. (2007) conducted 2D axisymmetric FE simulations and compared two different loading assumptions: pulse loading and equivalent loading. The equivalent loading assumption, which is another commonly adapted loading assumption to represent a wheel-moving load, applies wheel loading over the respective accumulative loading time, neglecting the unloading time periods. Results from this study show that the equivalent loading assumption gives comparable rutting performance predictions from the pulse loading assumption, such that by assuming an equivalent loading, one can save a significant amount of computational time. However, this conclusion is based on assuming an elasto-viscoplastic material behavior, neglecting the viscoelastic and damage behavior of asphalt materials. Cho et al. (1996) compared rutting predictions from 2D plane strain, 2D axisymmetric, and 3D FE simulations assuming a linear elastic behavior of asphalt materials. Results show that rutting values are similar for 2D and 3D cases when material is assumed to be linear elastic. Huang et al. (2001) conducted 2D and 3D axisymmetric simulations of asphalt pavement sections using an elasto-viscoplastic constitutive relationship. Results of this research show that 3D FE analysis gives more accurate predictions as compared to field measurements. Huang (1995) proposed a step-loading function to simulate a large number of loading cycles of a moving load in 3D FE simulations. This loading function accumulates each wheel pass time to produce a total cumulative loading time and then applies a single load step to a set of elements in the middle of the whole wheel path. Hua (2000) improved the cumulative loading time approach of Huang (1995). The improved approach also accumulates each single loading time and then applies a single load step on the whole wheel path to represent the moving wheel loading in 3D simulations. However, in both Huang’s (1995) and Hua’s (2000) work, an elasto-viscoplastic constitutive relationship is used for validating the proposed loading models. Park et al. (2005), Hua and White (2002), and Huang et al. (2001) used an elasto-viscoplastic model along with the cumulative loading time approach to represent a large number of loading cycles. Saleeb et al. (2005) used a visco-elasto-plastic constitutive relationship to conduct a 3D FE simulation with a moving loading model by applying the loading on one set of elements and then moving forward to the next set of elements. However, most of the aforementioned FE simulations focus on the effect of loading modes. Rushing et al. (2015) used full-scale test sections subjected to heavy aircraft loadings at different temperatures to validate viscoelastic, viscoplastic, and hardening-relaxation constitutive relationships implemented in PANDA by conducting 2D FE simulations. PANDA simulations successfully evaluate the existing pavement structure, as well as predict the critical locations of tensile and compressive stresses within the pavement structure.

7.3 FE Model

A 2D axisymmetric FE model is used in rutting simulation of a pavement structure. The 2D model consists of four layers: asphalt layer of 100-mm thickness, base layer of 160-mm thickness, sub-base layer of 400-mm thickness, and subgrade layer of 300-mm thickness, as shown in Figure 7.1. A pulse wheel load of 44 kN and tire pressure of 780 kPa are applied to simulate traffic on the top of an asphalt concrete pavement surface. The wheel moves with a speed of 100 passes/min, consisting of 0.2 seconds of loading time and 0.4 seconds of unloading time. The wheel loading area is assumed to have a circular shape with an area of 56400 mm^2. The simulated total loading-unloading cycles are 10000 load pulses to represent the number of simulated wheel passes. The employed asphalt pavement layer thicknesses, loading area dimensions, and 2D pulse wheel loading characteristics are representative of those used in field testing. Because of the symmetric nature of the wheel loading condition and the slab geometry, the FE model can be reduced to half of the slab by constraining the horizontal direction on the vertical edge of the model to represent the middle of the slab.

The boundary conditions in the 2D FE model are imposed such that the horizontal direction on the opposite side of the symmetric boundary is fixed, while the bottom of the pavement structure model is fixed in the vertical direction. Axisymmetric four-node elements with reduced integration (CAX4R) are used for axisymmetric analysis (Abaqus 2010). A maximum element aspect ratio of 2 is used for the 2D elements. According to the performed convergence studies for the 2D simulations, 2.5 × 2.5 mm^2 elements (fine mesh) are used under and close to the loads where stress and strain levels are relatively high, whereas a maximum element size of 5 × 5 mm^2 is used for the area far from the loading area. Infinite elements are used to eliminate the impact of boundaries on simulation results. Moreover, frictional and tangential loadings from the contact of the wheel with the asphalt top surface are neglected.

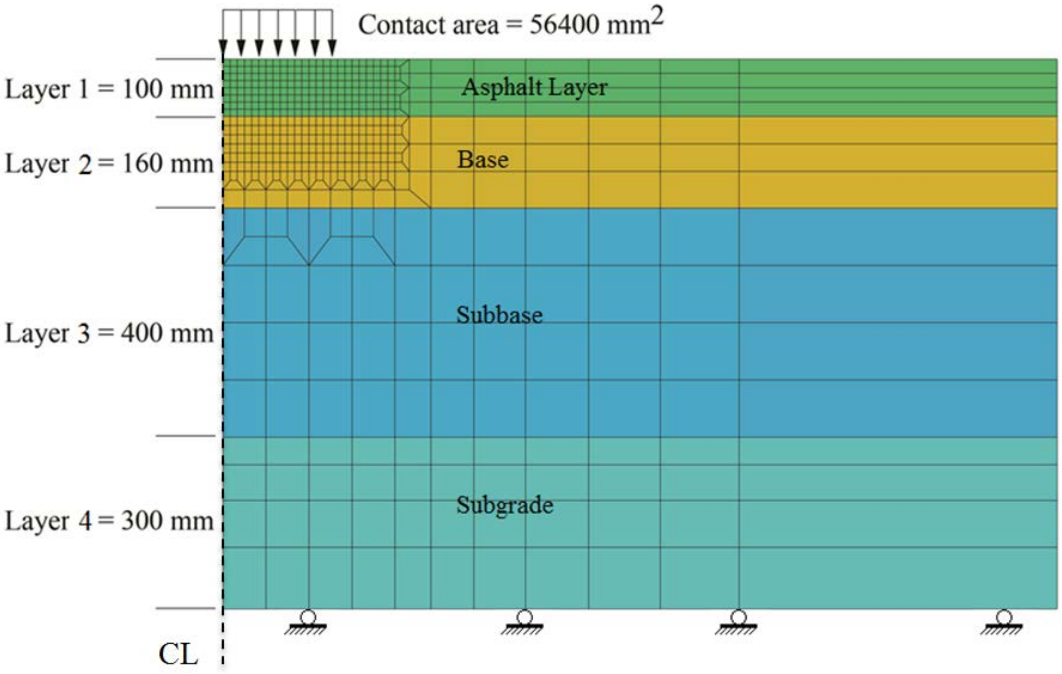

Figure 7.1 2D Axisymmetric FE Model

Nonlinear viscoelastic and viscoplastic behaviors are used in this analysis. Thus, viscodamage (due to stiffness loss), moisture damage, and oxidative aging constitutive relationships in the PANDA modeling framework are turned off and not used for the purpose of this analysis.

The toolkit PUI is used to create ABAQUS input files for simulations of pulse wheel loading applied to an asphalt concrete pavement surface. Appendix C presents a detailed description of PUI. Pavement structure and material properties are selected to represent a full-scale pavement section, as shown in Table 7.1. Asphalt concrete material properties are extracted from the laboratory RCRT-VS of plant-produced mixtures at the target test temperatures (40 and 55°C).

Table 7.1 Material Properties of Asphalt Pavement Structure

Layer	Young's Modulus (MPa)	Poisson's Ratio
1	From experimental testing based on the type of asphalt mixture	0.35
2	150.0	0.40
3	150.0	0.40
4	100.0	0.45

Because permanent (viscoplastic) displacement is not considered as a degree of freedom at the element's nodes in the classical FE method, it is impossible to directly calculate permanent surface deformation (rutting). However, the magnitude of rutting can be calculated numerically by integrating the magnitude of viscoplastic deformation through the pavement's thickness. This can be achieved by dividing the thickness of the asphalt layer into a number of sublayers, such that the rutting depth can be calculated as follows:

$$z_{rutting} = \sum_{i=1}^{k} \varepsilon^{vp(i)} h^{(i)} \tag{7.1}$$

where $z_{rutting}$ is the permanent displacement (rutting), $\varepsilon^{vp(i)}$ is the vertical viscoplastic strain at the i^{th} layer through the depth of the asphalt layer, and $h^{(i)}$ is the i^{th} layer thickness. In the following, rutting is calculated at the center of the pavement structure and for the asphalt layer, only for the purpose of conducting numerical comparisons.

The rutting simulations of this chapter are conducted for up to 10000 loading cycles, which is much lower than the actual number of loading cycles in the wheel-tracking tests. Hence, it is not a surprise that the predicted values for the surface rutting are lower than the actual rutting values in the wheel-tracking tests, which are conducted for a huge number of cycles. However, the main purpose of these simulations is obtaining qualitative comparisons of rutting values from different simplified assumptions.

7.4 First Case Study: Effect of Asphalt Mixture Type on Rutting Performance

In this study, the DGM, FAM, and CAM are simulated as the top asphalt layer in the aforementioned asphalt pavement structure in Figure 7.1. All simulations are performed using PANDA capabilities with asphalt layers represented using linear viscoelastic, nonlinear viscoelastic, and viscoplastic properties (Darabi et al. 2011a, 2011b, 2012a, 2012b, 2012c, and 2013). Three different mixture types (DGM, FAM, and

CAM) are simulated by changing the viscoelastic and viscoplastic properties of the asphalt mix layer at 40°C to represent laboratory measurements. The resultant vertical viscoplastic strains are integrated along the depth of asphalt layer only to determine permanent deformation at the center of the loading pattern. The resultant rutting in pavement sublayers is not included in the calculations of permanent deformation. Figure 7.2 shows the rutting performance of the DGM, FAM, and CAM as asphalt concrete layers at 40°C. The predicted permanent deformation after 10000 passes of DGM as an asphalt layer is 0.85 mm, while that of the FAM and CAM as asphalt layers are 1.0 and 0.4 mm, respectively. These values are presented to show the capability of PANDA to simulate the rutting of different mixtures. Recall that the FAM and CAM are derivatives of a DGM and are not practical mixtures for road construction.

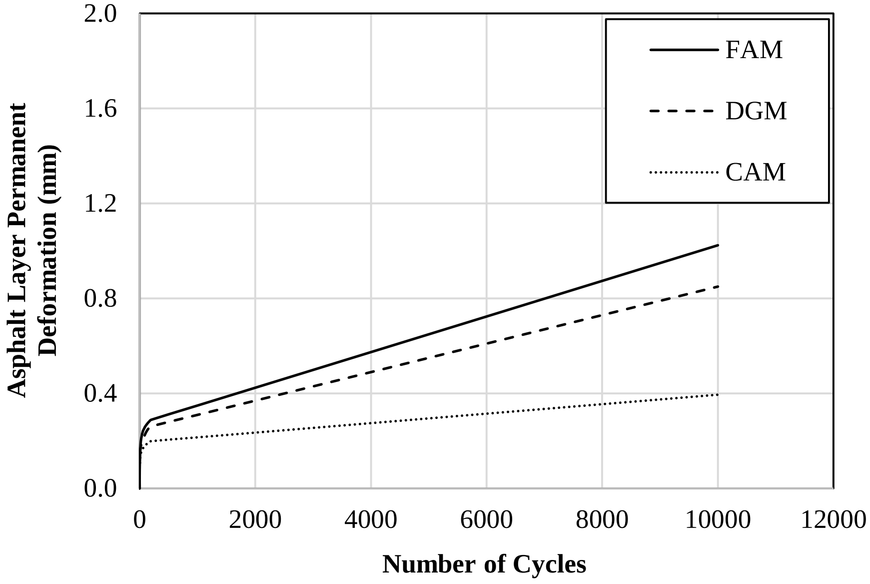

Figure 7.2 Comparison of Rutting Performance of Different Asphalt Concrete Layers (DGM, FAM, and CAM) at 40°C

Figure 7.3 represents vertical viscoplastic strains within the investigated asphalt layers after 10000 cycles of loading at 40°C. The magnitude of viscoplastic strain is shown on the scale beside the figure. Compression strains are positive values, while tension strains are negative values. Computational results show that the highest magnitude of vertical viscoplastic compressive strain is located along the centerline of the loading area and decreases in magnitude toward the edge of the loading area, as shown in Figure 7.3. The magnitude of vertical viscoplastic compressive strains resulting in the DGM layer is higher than those in the FAM and CAM layers. The CAM has the highest resistance to rutting because of its low asphalt binder content. Moreover, DGM and CAM layers do not show gradual distribution of viscoplastic strains through the layer thickness compared to the nearly uniform distribution of viscoplastic strains through most of the FAM layer thickness in the early stages of pavement life. This can be attributed to the homogeneity of the FAM internal structure compared to the DGM and CAM.

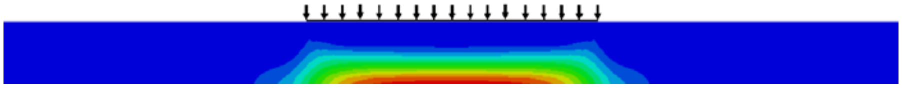

a) DGM Layer

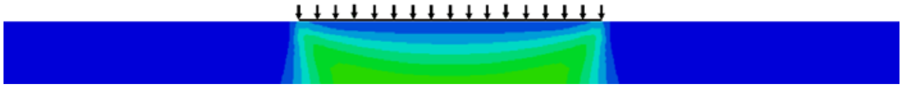

b) FAM Layer

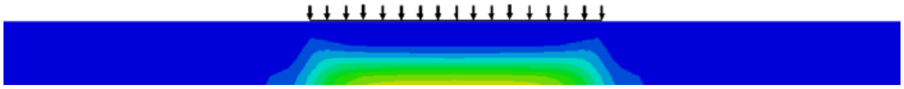

c) CAM Layer

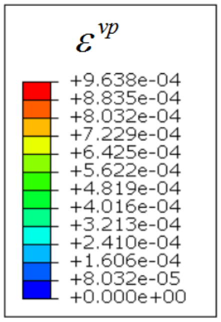

Figure 7.3 Comparison of Vertical Viscoplastic Strain Contours of First Case Study at 40°C

Figure 7.4 shows vertical viscoelastic strains within asphalt layers after 10000 cycles of loading at 40°C. The highest magnitude of vertical viscoelastic strains is located along the centerline of the asphalt concrete layer and decreases in magnitude toward the edge of the loading area, as shown in Figure 7.4. Vertical viscoelastic compressive strains are generated at the top of the layer and decrease with depth. Vertical viscoelastic tensile strains are generated at the bottom of the layer.

The magnitude of vertical viscoelastic strains resulting in the CAM layer is lower than those experienced in the FAM layer. This is because the CAM layer has less asphalt binder and fines contents than the FAM layer. The increase in compressive viscoelastic strains causes the asphalt material to reach the yielding point faster, leading to the development of compressive viscoplastic strains, which are shown in Figure 7.3.

It is observed that the recoverable viscoelastic strains of the FAM layer, compared to other layers, have the highest contribution to total strain generated under the loading area. However, the magnitude of viscoplastic strains in the DGM layer is the highest due to the wide range of aggregate size distribution in its mix design compared to the other asphalt mixtures considered in this study.

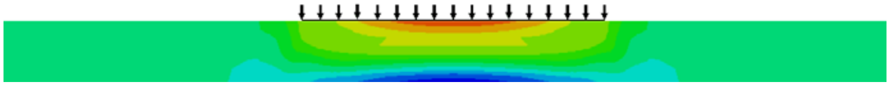

a) DGM Layer

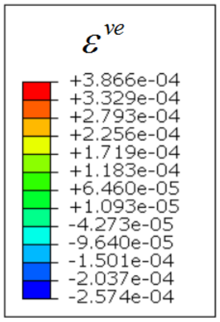

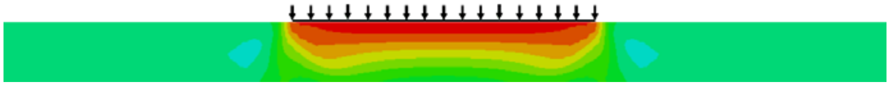

b) FAM Layer

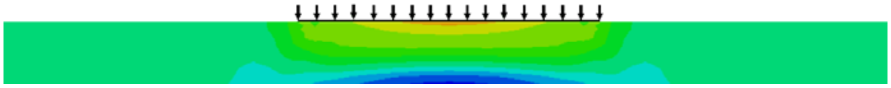

c) CAM Layer

Figure 7.4 Comparison of Vertical Viscoelastic Strain Contours of First Case Study at 40°C

7.5 Second Case Study: Effect of Air Void Content on Rutting Performance

In this part of the study, the DGM is simulated as the top asphalt layer in the aforementioned asphalt pavement structure in Figure 7.1, with different air void contents (4, 7, and 10%) presenting three different scenarios of viscoelastic and viscoplastic PANDA simulations. The resultant viscoplastic strains are integrated along the depth of asphalt layer only to determine permanent deformation at the center of the loading pattern. As mentioned earlier, the resultant rutting in the pavement sublayers is not included in calculations of permanent deformation. Figure 7.5 shows the rutting performance of the DGM with different air void contents at 55°C. Accordingly, the predicted permanent deformation after 10000 passes is 3.0, 1.65, and 1.25 mm in an asphalt layer with air void percentages of 10, 7, and 4%, respectively. The increase in air void content significantly increases the accumulated permanent deformation of the DGM, as shown in Figure 7.5.

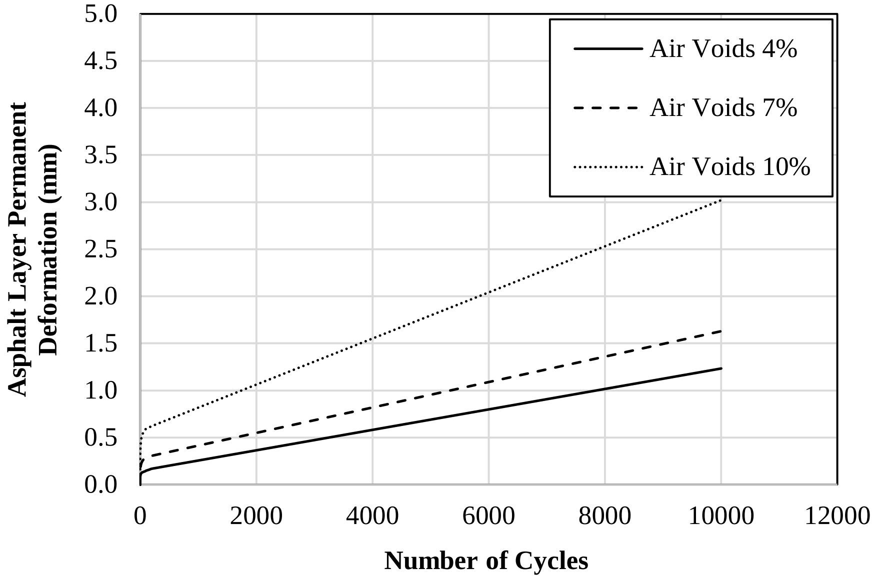

Figure 7.5 Comparison of Rutting Performance of Asphalt Concrete Layers with Different Air Void Contents at 55°C

Figure 7.6 represents the vertical viscoplastic compressive strains within the DGM layer with different air void contents (4, 7, and 10%) after 10000 cycles of loading at 55°C. Computational results show that the vertical viscoplastic compressive strains evolve beneath the loaded area. Simulation results in Figure 7.6 confirm that the magnitudes of vertical viscoplastic compressive strains in the DGM increase with an increase in air void content.

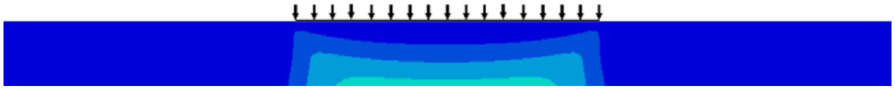

a) DGM Layer with 4% Air Void Content

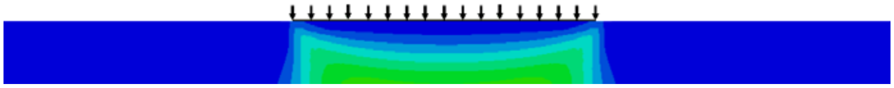

b) DGM Layer with 7% Air Void Content

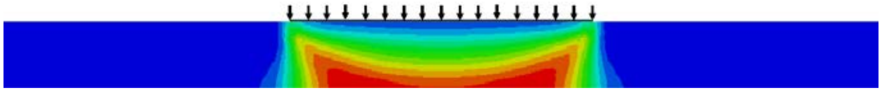

c) DGM Layer with 10% Air Void Content

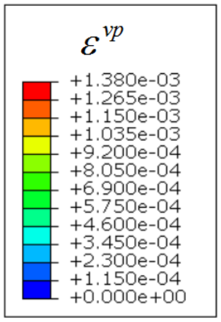

Figure 7.6 Comparison of Vertical Viscoplastic Strain Contours of Second Case Study at 55°C

Figure 7.7 shows vertical viscoelastic strains within asphalt layers with different air void contents (4, 7, and 10%) after 10000 cycles of loading at 55°C. The highest magnitudes of vertical viscoelastic strains are located along the centerline of the asphalt layer and decrease in magnitude toward the edge of the loading area, as shown in Figure 7.7.

However, the magnitudes of vertical viscoplastic strains in the DGM layer with an air void content of 10% are the highest, and the magnitudes of vertical viscoelastic strains resulting in the DGM layer with an air void content of 7% are the highest. This could explain why an air void content of 7% is desirable in the field, as the recoverable viscoelastic strains have the largest contribution to the total strain generated under the loading area.

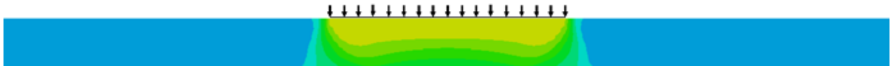

a) DGM Layer with 4% Air Void Content

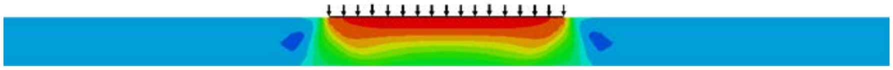

b) DGM Layer with 7% Air Void Content

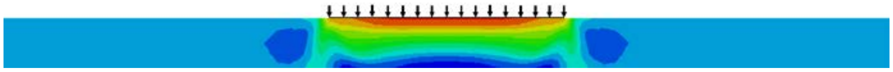

c) DGM Layer with 10% Air Void Content

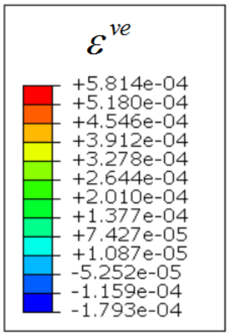

Figure 7.7 Comparison of Vertical Viscoelastic Strain Contours of Second Case Study at 55°C

7.6 Third Case Study: Effect of Aging Level on Rutting Performance

In this study, the DGM is simulated as the top asphalt layer in the aforementioned asphalt pavement structure in Figure 7.1, with different aging levels (0, 3, and 6 months) presenting three different scenarios of viscoelastic and viscoplastic PANDA simulations. Figure 7.8 shows rutting performance at different aging levels and a temperature of 55°C. The predicted permanent deformation after 10000 passes of the DGM as an asphalt layer with an aging level of 0 months is 1.65 mm; however, rutting is 1.1 and 0.85 mm at aging levels of 3 and 6 months, respectively. Permanent deformation accumulation decreases with an increase in aging level, as shown in Figure 7.8. The accumulated permanent deformation decreases by 33% by comparing the performance of the unaged layer to the performance of the 3-month aged layer, while the accumulated permanent deformation decreases by 48.5% by comparing the performance of the unaged layer to the performance of the 6-month aged layer after simulating 10000 loading cycles.

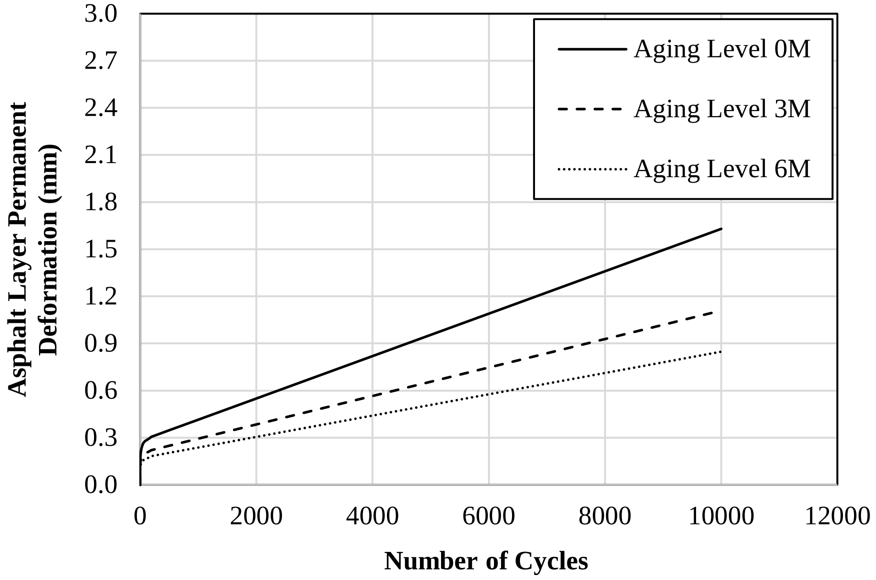

Figure 7.8 Comparison of Rutting Performance of Asphalt Concrete Layers with Different Aging Levels at 55°C

Figure 7.9 represents vertical viscoplastic strains within the DGM layer with different aging levels (0, 3, and 6 months) after 10000 cycles of loading at 55°C. Simulation results in Figure 7.9 show that the magnitudes of vertical viscoplastic compressive strains in the DGM as an asphalt layer increase as the aging level of the asphalt layer decreases.

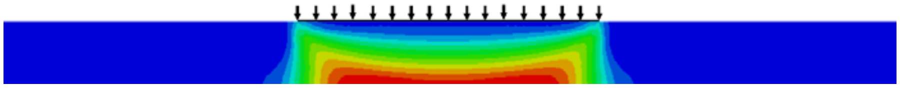

a) DGM Layer with 0-Month Aging Level

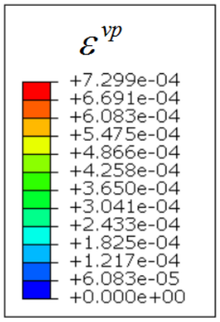

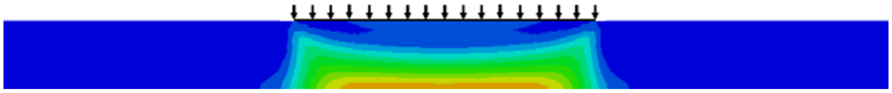

b) DGM Layer with 3-Month Aging Level

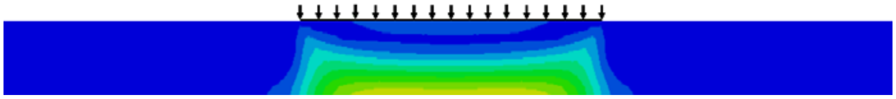

c) DGM Layer with 6-Month Aging Level

Figure 7.9 Comparison of Vertical Viscoplastic Strain Contours of Third Case Study at 55°C

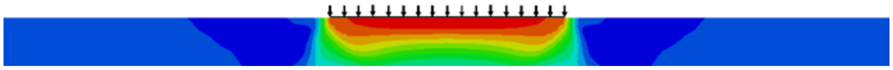

a) DGM Layer with 0-Month Aging Level

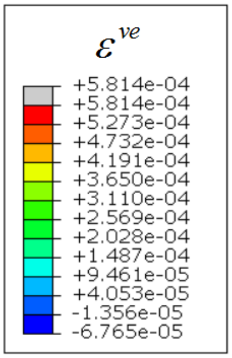

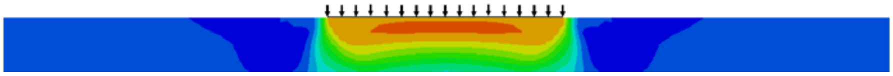

b) DGM Layer with 3-Month Aging Level

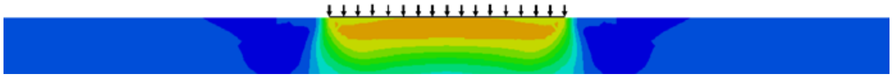

c) DGM Layer with 6-Month Aging Level

Figure 7.10 Comparison of Vertical Viscoelastic Strain Contours of Third Case Study at 55°C

Figure 7.10 shows vertical viscoelastic strains within asphalt layers with different aging levels (0, 3, and 6 months) after 10000 cycles of loading at 55°C. The highest magnitude of vertical viscoelastic strains is located along the centerline of the asphalt concrete layer and decreases in magnitude toward the edge of the loading area, as shown in Figure 7.10.

7.7 Summary

PANDA FE simulations can be used to compare the performance of different asphalt pavements that incorporate different materials and mixture designs. This chapter presents simulations of the response of different mixtures (i.e., different mixture designs, air voids, and aging levels). PANDA results show that the maximum compressive strains are located along the center of the loading area, whereas the maximum tensile strains are located at the edge of the traffic wheel outside the loading area.

As illustrated, the rutting performance of asphalt concrete varies extensively depending, first of all, on the internal structure of the asphalt layer. Based on the information provided in Chapters IV, V, and VI, FAM exhibits the lowest values for hardening function parameters and viscoplasticity-relaxation time compared to DGM and CAM. This means that more permanent deformation takes place in FAM in comparison with DGM and CAM.

Air void content and aging condition significantly influence the behavior of asphalt materials in resisting rutting. As temperature increases, the material becomes softer, resulting in lower yield strength and more susceptibility to permanent deformation. Hardening function parameters and viscoplasticity-relaxation time increase significantly with reducing the air void content or increasing the level of aging condition.

CHAPTER VIII

CONCLUSIONS AND RECOMMENDATIONS

8.1 Conclusions

This dissertation addresses the need in the asphalt pavement community to better understand and characterize the performance of asphalt mixtures due to the combined effects of traffic loading and environmental factors. The primary objectives of this research include the following: (1) to develop a robust experimental testing procedure to characterize the material resistance of asphalt mixtures to permanent deformation; (2) to develop an approach for determining PANDA model parameters for different types of asphalt mixtures and at different temperatures and aging levels; (3) to analyze the sensitivity of asphalt mixture performance to PANDA model parameters in order to reduce output uncertainty and simplify the experimental testing matrix and constitutive model; and (4) to use PANDA constitutive modeling to efficiently simulate and predict the response of asphalt pavements.

A robust experimental approach is developed to measure asphalt mixture responses. The experimental setup controls temperature, confinement level, loading stress, and loading rate. Two experimental tests are conducted to extract the PANDA viscoelastic and viscoplastic parameters following a systemic analysis procedure. This analysis obtains the long-term linear viscoelastic properties and time-temperature shift factors from the DMT. Then, these linear viscoelastic coefficients are employed to decouple the recoverable and irrecoverable response from the RCRT-VS and obtain the nonlinear viscoelastic and viscoplastic parameters.

A new approach is presented to extract shear strength parameters of asphalt materials by analyzing the output of the RCRT-VS based on the modified Drucker-Prager yield surface. The new approach evaluates the evolution of shear strength parameters during creep and relaxation behavior, taking into consideration the hardening effect generated during testing. Results show that assuming alpha-parameter overestimates the hardening function; however, the overestimation is within permissible limits.

Two different scales of asphalt mixture performance are considered in calibrating the PANDA constitutive model: macro-scale (DGM) and meso-scale (FAM and CAM). These asphalt mixtures are selected in order to correlate the model parameters with asphalt mixture components and to evaluate the sensitivity of model parameters for a wide range of mixtures. The viscoelastic response of asphalt mixtures, which becomes more dominant as temperature decreases, is mainly controlled by the FAM properties. Conversely, aggregate structure and interaction, which are clearly represented in the CAM, mainly control the viscoplastic response of asphalt concrete. Therefore, the viscoplastic properties of asphalt mixtures are strongly related to their microstructure. The overall mechanical response of asphalt mixtures is not affected only by the individual responses of its constituents but the complex interactions between these constituents have a great effect.

PANDA models are used to analyze the performance of asphalt mixtures under various conditions of temperature, confinement level, stress level, air void content, and aging level. The asphalt mixtures behave as a viscoelastic material at low temperatures and become more viscous at high temperatures. An increase in confinement level makes asphalt mixtures more resistant to applied axial stress, producing less strain magnitude. In addition, air void content strongly affects the mechanical properties of asphalt mixtures. Air voids in the asphalt mixtures should be small and well distributed so as not to affect the coherence of the mixture. Having too many air voids allows more access to air and water into asphalt layers, which accelerates aging and moisture damage. Not having enough air voids causes bleeding and promotes more rutting. Nonlinearity increases with an increase in testing temperature, as well as an increase in aging level. Asphalt mixtures get stiffer as aging level increases and air void content decreases. When they get stiffer, they become more brittle as the resistance of the materials to undergo viscoplastic deformation increases.

A phenomenological relationship for aged transient compliance of a viscoelastic material (proposed by Rahmani 2015) is modified to consider the effect of air void content and oxidative aging on the linear viscoelastic response of asphalt mixtures. Shift factors are used to vertically shift the compliance function at different aging levels and air void percentages to the referenced linear viscoelastic response at 7% air void content in unaged condition.

In order to effectively and efficiently predict the asphalt pavement performance under general loading and environmental conditions, GSA is performed to identify the significance of each model parameter on asphalt mixture response. GSA determines which model input parameters are sensitive in order to simplify the experimental testing matrix so that asphalt concrete performance can be predicted using a more practical, simpler, and sensitive model. GSA methods based on FAST and Sobol sequence approaches are implemented in GSAT in MATLAB to measure the sensitivity of PANDA constitutive model input parameters. Some of the model input parameters are relatively sensitive to asphalt mixture type. The output of the model is sensitive to the nonlinearity parameter (g_2), hardening function parameters (k_1, and k_2), and viscoplasticity-relaxation time ($1/\Gamma^{vp}$). However, g_1, α, β, and k_o parameters can be assumed to be consistent for a wide range of mixtures.

The capabilities of the PANDA constitutive modeling framework to simulate rutting performance of asphalt concrete layers is investigated by 2D axisymmetric FE simulations performed on the pavement structure. Pulse wheel loading, up to 10000 cycles, is applied in different case studies to investigate the effect of asphalt mixture type, air void content, and aging level on rutting potential. The computational results show that the maximum compressive strains are located along the center of the loading area, whereas the maximum tensile strains are located at the edge of the traffic wheel outside the loading area. FAM shows the lowest values for hardening function parameters (k_1, and k_2) and viscoplasticity-relaxation time ($1/\Gamma^{vp}$) compared to DGM and CAM. The hardening function parameters and the viscoplasticity-relaxation time increase significantly with a decrease in air void content or an increase in the level of aging condition.

8.2 Recommendations and Future Research Areas

The following are the main recommendations for future studies:

- Extend the calibration of PANDA constitutive modeling: Viscoelasticity and viscoplasticity are the only components of the PANDA model investigated in this study, and the sensitivity of the model output to its input parameters is assessed in this dissertation. Additional research is recommended to include other model components, such as viscodamage, moisture damage, and aging components.
- Expand the material database: The analysis conducted in this dissertation is limited to one asphalt mixture source. Validating the applicability of the developed analysis method for more asphalt binders and aggregate sources, that exhibit different properties and responses, is also necessary.
- Enhance PANDA capabilities: PANDA is calibrated using typical types of mixtures. However, its model parameters should be calibrated using other asphalt mixture technologies, such as warm-mix asphalt (WMA), recycled asphalt pavement (RAP), cold asphalt mixtures, etc.

REFERENCES

AASHTO (2008). “Mechanistic-Empirical Pavement Design Guide: a Manual of Practice. Interim Edition.” American Association of State Highway and Transportation Officials, Washington, D.C.

AASHTO (2016). “Standard Specifications for Transportation Materials and Methods of Sampling and Testing, and AASHTO Provisional Standards.” American Association of State Highway and Transportation Officials, Washington, D.C.

Abaqus (2010). “User's and Theory Manuals.” Hibbit, Karlsson & Sorensen Inc., Pawtucket, Rhode Island.

Abu Al-Rub, R., Darabi, M., Huang, C., Masad, E., and Little, D. (2012). “Comparing Finite Element and Constitutive Modelling Techniques for Predicting Rutting of Asphalt Pavements.” International Journal of Pavement Engineering 13(4), 322-338.

Abu Al-Rub, R., Darabi, M., Little, D., and Masad, E. (2010). "A Micro-Damage Healing Model That Improves Prediction of Fatigue Life in Asphalt Mixes." International Journal of Engineering Science 48(11), 966-990.

Abu Al-Rub, R., Masad, E., and Huang, C. (2009). “Improving the Sustainability of Asphalt Pavements through Developing a Predictive Model with Fundamental Material Properties.” Southwest University Transportation Center, Texas A&M Transportation Institute, College Station, TX, 1-45.

Argyris, J., Faust, G., Szimmat, J., Warnke, E., and Willam, K. (1974). "Recent Developments in the Finite Element Analysis of Prestressed Concrete Reactor Vessels." Journal of Nuclear Engineering and Design 28(1), 42-75.

ASTM (2015). “Annual Book of ASTM Standards. Standard Designation E 4: Standard Practices for Force Verification of Testing Machines.” American Society for Testing and Materials, West Conshohocken, PA.

Bahuguna, S., Panoskaltsis, V., and Papoulia, K. (2006). "Identification and Modeling of Permanent Deformations of Asphalt Concrete." Journal of Engineering Mechanics 132(3), 231-239.

Bardet, J. (1990). "Lode Dependences for Isotropic Pressure-Sensitive Elastoplastic Materials." Journal of Applied Mechanics 57(3), 498-506.

Bell, C. (1989). “Summary Report on Aging of Asphalt-Aggregate Systems.” Strategic Highway Research Program, National Research Council, Washington, D.C.

Bell, C., Felling, M., and Wieder, A. (1994). “Field Validation of Laboratory Aging Procedures for Asphalt Aggregate Mixtures.” Journal of the Association of Asphalt Paving Technologists (AAPT) 63, 45-80.

Bonaquist, R., and Witczak, M. (1996). "Plasticity Modeling Applied to the Permanent Deformation Response of Granular Materials in Flexible Pavement Systems." Transportation Research Record, Journal of the Transportation Research Board 1540, 7-14.

Borgonovo, E. (2007). “A New Uncertainty Importance Measure.” Reliability Engineering & System Safety 92(6), 771–784.

Brown, E.; Kandhal, P., and Zhang, J. (2001). “Performance Testing for Hot Mix Asphalt.” NCAT Report No. 01-05. National Center for Asphalt Technology. Auburn, AL.

Caflisch, R. (1998). “Monte Carlo and Quasi-Monte Carlo Methods.” Acta Numerica 7, 1–49.

Campbell, P., Wrigth, J., and Bowman, P. (1962). “The Effect of Temperature and Humidity on the Oxidation of Air Blown Asphalts.” Materials Research Standards 2(12), 988-995.

Campolongo, F., Tarantola, S., and Saltelli, A. (1999). “Tackling Quantitatively Large Dimensionality Problems.” Computer Physics Communications 117, 75–85.

Cannavo, F. (2012). “Sensitivity Analysis for Volcanic Source Modeling Quality Assessment and Model Selection.” Computers and Geosciences 44, 52-59.

Chan, K., Tarantola, S., Saltelli, A., and Sobol, I. (2000). “Variance Based Methods.” In: “Sensitivity Analysis.” (Eds. Saltelli, A., Chan, K., and Scott, M.), John Wiley & Sons Publishers, Probability and Statistics Series, 167–197.

Chen, W., and Baladi, G. (1985). “Soil Plasticity: Theory and Implementation.” Elsevier Science Publishing Co. Inc., New York, NY.

Chen, W., and Liu, X. (1990). “Limit Analysis in Soil Mechanics.” Elsevier Science Publishing Co. Inc., New York, NY.

Chen, W., and Mizuno, E. (1990). “Nonlinear Analysis in Soil Mechanics, Theory and Implementation.” Elsevier Science Publishing Co. Inc., New York, NY.

Chipperfield, E. (1970). “Asphalt Characteristics in Relation to Road Performance.” Journal of the Association of Asphalt Paving Technologists (AAPT) 39, 79-88.

Cho, Y., McCullough, B., and Weissmann, J. (1996). “Considerations on Finite-Element Method Application in Pavement Structural Analysis.” Transportation Research Record, Journal of the Transportation Research Board 1539, 96-101.

Collop, A., Cebon, D., and Hardy, M. (1995). “Viscoelastic Approach to Rutting in Flexible Pavements.” ASCE, Journal of Transportation Engineering 121(1): 82–92.

Collop, A., Scarpas, A., Kasbergen, C., and de Bondt, A. (2003). “Development and Finite Element Implementation of Stress-Dependent Elastoviscoplastic Constitutive Model with Damage for Asphalt.” Transportation Research Record, Journal of the Transportation Research Board 1832, 96-104.

Cukier, R., Fortuin, C., Shuler, K., Petschek, A., and Schaibly, J. (1973). “Study of the Sensitivity of Coupled Reaction Systems to Uncertainties in Rate Coefficients I: Theory.” The Journal of Chemical Physics 59(8), 3873–3878.

Cukier, R., Schaibly, J., and Shuler, K. (1975). “Study of the Sensitivity of Coupled Reaction Systems to Uncertainties in Rate Coefficients III: Analysis of the Approximations.” The Journal of Chemical Physics 63(3), 1140–1149.

Darabi, M. (2011). “Thermo-Viscoelastic-Viscoplastic-Viscodamage-Healing Modeling of Bituminous Materials: Theory and Computation.” Ph.D. Dissertation, Texas A&M University, College Station, TX.

Darabi, M., Abu Al-Rub, R., and Little, D. (2012a). “A Continuum Damage Mechanics Framework for Modeling Micro-Damage Healing.” International Journal of Solids and Structures 49, 492–513.

Darabi, M., Abu Al-Rub, R., Masad, E., Huang, C., and Little, D. (2011a). “A Thermo-Viscoelastic–Viscoplastic–Viscodamage Constitutive Model for Asphaltic Materials.” International Journal of Solids and Structures 48, 191–207.

Darabi, M., Abu Al-Rub, R., Masad, E., Huang, C., and Little, D. (2012c). “A Modified Viscoplastic Model to Predict the Permanent Deformation of Asphaltic Materials under Cyclic-Compression Loading at High Temperatures.” International Journal of Plasticity 35, 100-134.

Darabi, M., Abu Al-Rub, R., Masad, E., and Little, D. (2011b). “Thermodynamic Based Model for Coupling Temperature-Dependent Viscoelastic, Viscoplastic, and Viscodamage Constitutive Behavior of Bituminous Materials.” International Journal for Numerical and Analytical Methods in Geomechanics 36, 817-854.

Darabi, M., Abu Al-Rub, R., Masad, E., and Little, D. (2012b). “A Thermodynamic Framework for Constitutive Modeling of Time- and Rate-Dependent Materials, Part II: Numerical Aspects and Application to Asphalt Concrete.” International Journal of Plasticity 35, 67-99.

Darabi, M., Abu Al-Rub, R., Masad, E., and Little, D. (2013). “Constitutive Modeling of Cyclic Viscoplastic Response of Asphalt Concrete.” Transportation Research Record, Journal of the Transportation Research Board 2373, 22-33.

Desai, C. S., Somasundaram, S., and Frantziskonis, G. (1986). "A Hierarchical Approach for Constitutive Modelling of Geologic Materials." International Journal for Numerical and Analytical Methods in Geomechanics 10(3), 225-257.

Dessouky, S. (2005). "Multiscale Approach for Modeling Hot Mix Asphalt." Ph.D. Dissertation, Texas A&M University, College Station, TX.

Dessouky, S., and Masad, E. (2006). "The Development of a Microstructural-Based Continuum Model for Hot Mix Asphalt." Proc. of Asphalt Concrete: Simulation, Modeling, and Experimental Characterization, Baton Rouge, LA, 44-52.

Di Benedetto, H., Mondher, N., Sauzéat, C., and Olard, F. (2007). "Three-Dimensional Thermo-Viscoplastic Behavior of Bituminous Materials: The DBN model." Road Materials and Pavement Design 8(2), 285-315.

Drucker, D., and Prager, W. (1952). “Soil Mechanics and Plastic Analysis for Limit Design.” Quarterly of Applied Mathematics 10(2), 157–165.

Feng, H., Pettinari, M., and Stang, H. (2015). “Three Different Ways of Calibrating Burger’s Contact Model for Viscoelastic Model of Asphalt Mixtures by Discrete Element Method.” 8th RILEM International Symposium on Testing and Characterization of Sustainable and Innovative Bituminous Materials 11, 423-433.

Ferry, J. (1961). “Viscoelastic Properties of Polymers.” Wiley, New York, NY.

Findley, W., and Davis, F. (2013). “Creep and Relaxation of Nonlinear Viscoelastic Materials.” Courier Corporation, North Chelmsford, MA.

Fwa, T., Tan, S., and Zhu, L. (2004). "Rutting Prediction of Asphalt Pavement Layer Using C-Phi Model." ASCE, Journal of Transportation Engineering 130(5), 675-683.

Haddad, Y. (1995). “Viscoelasticity of Engineering Materials.” Springer Science+Business Media, Dordrecht, Netherlands.

Haythornthwaite, R. (1985). "A Family of Smooth Yield Surfaces." Mechanics Research Communications 12(2), 87-91.

Homma, T., and Saltelli, A. (1995). “Use of Sobol’s Quasirandom Sequence Generator for Integration of Modified Uncertainty Importance Measure.” Journal of Nuclear Science and Technology 32(11), 1164–1173.

Homma, T., and Saltelli, A. (1996). “Importance Measures in Global Sensitivity Analysis of Nonlinear Models.” Reliability Engineering & System Safety 52(1), 1–17.

Hornberger, R., and Spear, G. (1981). “An Approach to the Preliminary Analysis of Environmental Systems.” Journal of Environmental Management 12, 7–18.

Hua, J. (2000). “Finite Element Modeling and Analysis of Accelerated Pavement Testing Devices and Rutting Phenomenon.” Ph.D. Dissertation, Purdue University, West Lafayette, IN.

Hua, J., and White, T. (2002). “A Study of Nonlinear Tire Contact Pressure Effects on HMA Rutting.” International Journal of Geomechanics 2(3), 353-376.

Huang, B., Mohammad, L., and Rasoulian, M. (2001). “Three-Dimensional Numerical Simulation of Asphalt Pavement at Louisiana Accelerated Loading Facility.”

Transp-ortation Research Record, Journal of the Transportation Research Board 1764, 44-58.

Huang, C. (2008). “Development and Numerical Implementation of Nonlinear Viscoelastic-Viscoplastic Model for Asphalt Materials.” Ph.D. Dissertation, Texas A&M University, College Station, TX.

Huang, C., Abu Al Rub, R., Masad, E., Little, D., and Airey, G. (2011b). “Numerical Implementation and Validation of a Nonlinear-Viscoelastic and Viscoplastic Model for Asphalt Concrete Mixes.” International Journal of Pavement Engineering 12, 433–447.

Huang, C., Abu Al-Rub, R., Masad, E., and Little, D. (2011a). “Three Dimensional Simulations of Asphalt Pavement Performance Using a Nonlinear Viscoelastic–Viscoplastic Model.” ASCE Journal of Materials in Civil Engineering 23, 56–68.

Huang, C., Masad, E., Muliana, A., and Bahia, H. (2007). “Nonlinear Viscoelastic Analysis of Asphalt Mixes Subjected to Shear Loading.” Journal of Mechanics of Time-Dependent Materials 11, 91–110.

Huang, H. (1995). “Analysis of Accelerated Pavement Tests and Finite Element Modeling of Rutting Phenomenon.” Ph.D. Dissertation, Purdue University, West Lafayette, IN.

Hunter, A., Airey, G., and Harireche, O. (2007). “Numerical Modeling of Asphalt Mixture Wheel Tracking Experiments.” International Journal of Pavement Engineering and Asphalt Technology 8, 52-71.

Im, S. (2012). “Characterization of Viscoelastic and Fracture Properties of Asphaltic Materials in Multiple Length Scales.” Ph.D. Dissertation, University of Nebraska-Lincoln, Lincoln, NE.

Jheald (2011). “Sobol Sequence.” In Wikipedia, The Free Encyclopedia. Retrieved from https://en.wikipedia.org/w/index.php?title=Sobol_sequence&oldid=719680813.

Junisbekov, T., Kestelman, V., and Malinin, N. (2003). “Stress Relaxation in Viscoelastic Materials.” Science Publishers, New York, NY

Kettil, P., Lenhof, B., Runesson, K., and Wiberg, N. (2007). “Simulation of Inelastic Deformation in Road Structures due to Cyclic Mechanical and Thermal Loads.” Computers & Structures 85(1-2), 59-70.

Kim, Y., Guddati, M., Underwood, S., Yun, T., Subramanian, V., and Savadatti, S. (2009). “Development of a Multiaxial Viscoelastoplastic Continuum Damage Model for Asphalt Mixtures.” FHWA-HRT-08-073, Federal Highway Administration, Research, Development and Technology, Turner-Fairbank Highway Research Center, McLean, VA.

Kose, S., Guler, M., Bahia, H., and Masad, E. (2000). “Distribution of Strains within Hot-Mix Asphalt Binders.” Journal of Transportation Research Forum 1728, 21-27.

Kucherenko, S., and Shah, N. (2007). “The Importance of Being Global. Application of Global Sensitivity Analysis in Monte Carlo Option Pricing.” Wilmott Magazine 4, 2-10.

Kuipers, L., and Niederreiter, H. (2006). “Uniform Distribution of Sequences.” Dover Books on Mathematics. Dover Publications Inc., Mineola, NY.

Lakes, R. (2009). “Viscoelastic Materials.” Cambridge University Press, Cambridge, NY.

Lemaître, J. (2001). “Handbook of Materials Behavior Models.” Academic Press, San Diego, CA.

Lin, F., and Bazant, Z. (1986). "Convexity of Smooth Yield Surface of Frictional Material." Journal of Engineering Mechanics 112(11), 1259-1262.

Liu, C., Pineda, E., and Crespo, D. (2015). “Mechanical Relaxation of Metallic Glasses: An Overview of Experimental Data and Theoretical Models.” Journal of Metals 5(2), 1073-1111.

Loucks, D. (2006). “Water Resources Systems Planning and Management: Studies and Reports in Hydrology.” United Nations Educational.

Lu, Y. and Wright, P. (1998). “Numerical Approach of Visco-Elastoplastic Analysis for Asphalt Mixtures.” Computers & Structures 69(2), 139-147.

Maiolino, S. (2005). "Proposition of a General Yield Function in Geomechanics." Comptes Rendus Mecanique 333(3), 279-284.

Maiolino, S., and Luong, M. (2009). "Measuring Discrepancies between Coulomb and Other Geotechnical Criteria: Drucker-Prager and Matsuoka-Nakai." Proc. of 7th Euromech Solid Mechanics Conference, Lisbon, Portugal, 1-12.

Masad, E., Dessouky, S., and Little, D. (2007). “Development of an Elastoviscoplastic Microstructural-Based Continuum Model to Predict Permanent Deformation in Hot Mix Asphalt.” International Journal of Geomechanics 7, 119–130.

Masad, E., Huang, C., Airey, G., and Muliana, A. (2008). “Nonlinear Viscoelastic Analysis of Unaged and Aged Asphalt Binders.” Journal of Construction and Building Materials 22, 2170–2179.

Masad, E., Huang, C., D’Angelo, J. and Little, D. (2009). “Characterization of Asphalt Binder Resistance to Permanent Deformation Based on Nonlinear Viscoelastic Analysis of Multiple Stress Creep Recovery (MSCR) Test.” Journal of the Association of Asphalt Paving Technologists (AAPT) 78, 471–501.

Masad, E., Tashman, L., Little, D., and Zbib, H. (2005). “Viscoplastic Modeling of Asphalt Mixes with the Effects of Anisotropy, Damage and Aggregate Characteristics.” Mechanics of Materials 37, 1242–1256.

Matsuoka, H., and Nakai, T. (1974). "Stress-Deformation and Strength Characteristics of Soil under Three Different Principal Stresses." Proc. of Japan Society of Civil Engineers, 59-70.

Matsuoka, H., and Nakai, T. (1985). "Relationship among Tresca, Mises, Mohr-Coulomb and Matsuoka-Nakai Failure Criteria." Soils and Foundations 25(4), 123-128.

Meyer, J., and Labuz, J. (2013). “Linear Failure Criteria with Three Principal Stresses.” International Journal of Rock Mechanics and Mining Sciences 60, 180-187.

Mortara, G. (2008). "A New Yield and Failure Criterion for Geomaterials." Geotechnique 58(2), 125-132.

Muraya, P., Molenaar, A., and van de Ven, M.(2009). "Contribution of Asphalt Mix Components to Permanent Deformation Resistance." Proc. of 8th International Conference on the Bearing Capacity of Roads, Railways and Airfields, Champaign, IL, 259-268.

Nguyen, Q., Di Benedetto, H., and Sauzéat, C. (2015). “Linear and Nonlinear Viscoelastic Behavior of Bituminous Mixtures.” Journal of Materials and Structures 48(7), 2339-2351.

Parente Jr, E., Nogueira, G., Meireles Neto, M., and Moreira, L. (2014). “Material and Geometric Nonlinear Analysis of Reinforced Concrete Frames.” Revista IBRACON de Estruturas e Materiais, 7(5), 879-904.

Park, D., Martin, A., and Masad, E. (2005). “Effects of Nonuniform Tire Contact Stresses on Pavement Response.” ASCE, Journal of Transportation Engineering 131(11), 873-879.

Park, D., Martin, A., Lee, H., and Masad, E. (2005). "Characterization of Permanent Deformation of an Asphalt Mixture Using a Mechanistic Approach." KSCE Journal of Civil Engineering 9(3), 213-218.

Park, S., and Schapery, R. (1999). “Methods of Interconversion between Linear Viscoelastic Material Functions: Part I - A Numerical Method based on Prony Series.” International Journal of Solids and Structures 36(11), 1653-1675.

Patelli, E., and Pradlwarter, H. (2010). “Monte Carlo Gradient Estimation in High Dimensions.” International Journal for Numerical Methods in Engineering 81(2), 172–188.

Perl, M., Uzan, J., and Sides, A. (1983). “Visco-Elasto-Plastic Constitutive Law for a Bituminous Mixture under Repeated Loading.” Transportation Research Record, Journal of the Transportation Research Board 911, 20-27.

Perzyna, P. (1971). “Thermodynamic Theory of Viscoplastcity.” Advances in Applied Mechanics 11, 313–354.

Petersen, J. (1984). “Chemical Composition of Asphalt as Related to Asphalt Durability: State of Art.” Transportation Research Record, Journal of the Transportation Research Board 999, 13-30.

Pradlwarter, H., Pellissetti, M., and Schuëller, G. (2005). “Sensitivity and Uncertainty in Complex FE-Models.” Proceedings of the 9th International Conference on Structural Safety and Reliability (ICOSSAR’05; CD-ROM), Millpress, Rotterdam, Rome, Italy.

Press, W., and Farrar, G. (1990). “Recursive Stratified Sampling for Multidimensional Monte Carlo Integration.” Computers in Physics 4(2), 190–195.

Rahmani, E. (2015). “Continuum-Based Constitutive Modeling of Coupled Oxidative Aging-Mechanical Response of Asphalt Concrete.” Ph.D. Dissertation, Texas A&M University, College Station, TX.

Rahmani, E., Darabi, M., Abu Al-Rub, R., Kassem, E., Masad, E., and Little, D. (2013). “Effect of Confinement Pressure on the Nonlinear Viscoelastic Response of

Asphalt Concrete at High Temperatures." Construction and Building Materials 47, 779-788.

Roque, R., Zou, J., Kim, Y., Baek, C., Thirunavukkarasu, S., Underwood, S., and Guddati, M. (2010). "NCHRP Web-Only Document 162: Top-Down Cracking of Hot-Mix Asphalt Layers: Models for Initiation and Propagation." NCHRP Project 1-42A Final Report, Transportation Research Board of the National Academies, Washington, D.C.

Rushing, J., Darabi, M., Rahmani, E., and Little, D. (2015). "Comparing Rutting of Airfield Pavements to Simulations Using Pavement Analysis Using Nonlinear Damage Approach (PANDA)." International Journal of Pavement Engineering, 1-22.

Saadeh, S. (2005). "Characterization of Asphalt Concrete Using Anisotropic Damage Viscoelastic-Viscoplastic Model." Ph.D. Dissertation, Texas A&M University, College Station, TX.

Saadeh, S., Masad, E., and Little, D. (2007). "Characterization of Asphalt Mix Response under Repeated Loading Using Anisotropic Nonlinear Viscoelastic–Viscoplastic Model." ASCE Journal of Materials in Civil Engineering 19, 912–924.

Saleeb, A., Liang, R., Al Qablan, H., and Powers, D. (2005). "Numerical Simulation Techniques for HMA Rutting under Loaded Wheel Tester." International Journal of Pavement Engineering 6(1), 57-66.

Saltelli, A. (2002a). "Making Best Use of Model Valuations to Compute Sensitivity Indices." Computer Physics Communication 145, 280–297.

Saltelli, A. (2002b). “Sensitivity Analysis for Importance Assessment.” Risk Analysis 22 (3), 579–590.

Saltelli, A., Chan, K., and Scott, E. (2000). “Sensitivity Analysis” Wiley Series in Probability and Statistics, John Wiley & Sons Publishers, Chichester, NY.

Saltelli, A., Ratto, M., Andres, T., Campolongo, F., Cariboni, J., Gatelli, D., Saisana, M., and Tarantola, S. (2009). “Global Sensitivity Analysis: The Primer.” Biometrics 65(4), 1311–1312.

Saltelli, A., Tarantola, S., and Chan, K. (1999). “A Quantitative Model-Independent Method for Global Sensitivity Analysis of Model Output.” Technometrics 41(1), 39-56.

Schapery, R. (1969a). “Further Development of a Thermodynamic Constitutive Theory: Stress Formulation.” Purdue University, Purdue Resarch Foundation, Lafayette, IN.

Schapery, R. (1969b). “On the Characterization of Nonlinear Viscoelastic Materials.” Polymer Engineering & Science 9, 295–310.

Schwartz, C., and Carvalho, R. (2007). “Implementation of the NCHRP 1-37A Design Guide Final Report Volume 2: Evaluation of Mechanistic-Empirical Design Procedure.” MDSHA No. SP0077B41, Maryland State Highway Administration, Lutherville, MD.

Seibi, A., Sharma, M., Ali, G., Kenis, W. (2001). “Constitutive Relations for Asphalt Concrete under High Rates of Loading.” Transportation Research Record, Journal of the Transportation Research Board 1767, 111–119.

Shakiba, M. (2013). “A Continuum Coupled Moisture-Mechanical Constitutive Model for Asphalt Concrete.” Ph.D. Dissertation, Texas A&M University, College Station, TX.

Sobol, I. (1967). “The Distribution of Points in a Cube and the Approximate Evaluation of Integrals.” USSR Computational Mathematics and Mathematical Physics 7(4), 86–112.

Sobol, I. (1990). “Quasi-Monte Carlo Methods.” Progress in Nuclear Energy 24(1–3), 55–61.

Sobol, I. (1993). “Sensitivity Estimates for Nonlinear Mathematical Models.” Mathematical Modeling and Computational Experiment 1, 407–414.

Sobol, I., and Kucherenko, S. (2005a). “Global Sensitivity Indices for Nonlinear Mathematical Models: Review.” Wilmott Magazine 1, 56-61.

Sobol, I., and Kucherenko, S. (2005b). “On Global Sensitivity Analysis of Quasi-Monte Carlo Algorithms.” Monte Carlo Methods and Applications 11(1), 1–9.

Sousa, P., Kassem, E., Masad, E., and Little, D. (2013). “New Design Method of Fine Aggregates Mixtures and Automated Method for Analysis of Dynamic Mechanical Characterization Data.” Journal of Construction and Building Materials 41, 216-223.

Starodubsky, S., Blechman, I., and Livneh, M. (1994). "Stress-Strain Relationship for Asphalt Concrete in Compression." Journal of Materials and Structures 27(8), 474-482.

Tan, S., Low, B., and Fwa, T. (1994). "Behavior of Asphalt Concrete Mixtures in Triaxial Compression." Journal of Testing and Evaluation 22(3), 195-203.

Tanaka, E., and van Eijden, T. (2003). “Biomechanical Behavior of the Temporomandibular Joint Disc.” Critical Reviews in Oral Biology and Medicine 14(2), 138-150.

Tarefdar, R., Stormont, J., and Zaman, M. (2007). “Evaluating Laboratory Modulus and Rutting Potential of Asphalt Concrete.” 86th Annual Meeting of the Transportation Research Board (No. 07-1889), Washington, D.C.

Tashman, L. (2003). “Microstructural Viscoplastic Continuum Model for Asphalt Concrete.” Ph.D. Dissertation, Texas A&M University, College Station, TX.

Tashman, L., Masad, E., Little, D., and Zbib, H. (2005a). “A Microstructure-Based Viscoplastic Model for Asphalt Concrete.” International Journal of Plasticity 21, 1659–1685.

Tashman, L., Masad, E., Zbib, H., Little, D., and Kaloush, K. (2004). "Anisotropic Viscoplastic Continuum Damage Model for Asphalt Mixes." Proc. of Recent Advances in Materials Characterization and Modeling of Pavement Systems in the 15th Engineering Mechanics Division Conference, New York, NY, 111-125.

Tashman, L., Masad, E., Zbib, H., Little, D., and Kaloush, K. (2005b). "Microstructural Viscoplastic Continuum Model for Permanent Deformation in Asphalt Pavements." ASCE, Journal of Engineering Mechanics 131, 48-57.

TxDOT (2004). “Standard Specifications for Construction and Maintenance of Highways, Streets, and Bridges.” Texas Department of Transportation, Austin, TX.

Van Eekelen, H. (1980). "Isotropic Yield Surfaces in Three Dimensions for Use in Soil Mechanics." International Journal for Numerical and Analytical Methods in Geomechanics 4(1), 89-101.

Weyl, H. (1938). “Mean Motion.” American Journal of Mathematics 60(4), 889–896.

Xiaohu, L., and Isaccson, U. (2000). “Artificial Aging of Polymer Modified Bitumens.” Journal of Applied Polymer Science 76(12), 1811-1824.

You, T. (2013). “Two- and Three-Dimensional Microstructural Modeling of Asphalt Particulate Composite Materials Using a Unified Viscoelastic-Viscoplastic-Viscodamage Constitutive Model.” Ph.D. Dissertation, Texas A&M University, College Station, TX.

APPENDIX A

DESIGN OF A FAM AND CAM AS DERIVATIVES OF A DGM

Required conditions to follow for designing FAM and CAM out of DGM:

1. The gradation design of the CAM follows the same gradation design of the DGM. It is designed to represent the portion of aggregate that is retained on sieve #16 only, while the gradation design of the FAM follows the same gradation design of the DGM. It is designed to represent the remaining portion of aggregate that passes sieve #16.
2. The binder content percent (by aggregate weight) in the FAM is the same as the binder content by weight percent of the aggregate passing sieve #16 in the DGM, while the binder content by weight percent of the aggregate retained on sieve #16 in the DGM is the binder content percent (by aggregate weight) in the CAM.

The following example illustrates the procedure used to design FAM and CAM mixtures as a derivative of a typical DGM:

A C-type mixture is selected to serve as a DGM basis for designing the FAM and CAM:

Table A.1 Mix Design for DGM

Sieve Size	Sieve Size (mm)	Cum. % Passing
1 in	25.000	100.0
¾ in	19.000	99.6
3/8 in	9.500	73.9
No. 4	4.750	58.1
No. 8	2.360	37.3
No. 16	1.180	25.5
No. 30	0.600	19.6
No. 50	0.300	8.1
No. 200	0.075	2.7
Binder	PG 67-22	4.4

The following information is determined from the DGM design:

- Total weight of aggregates: W_s = 14000 g
- Percentage of aggregates retained on #16: $P_{s\text{-}R16}$ = 74.5% (10430 g)
- Percentage of aggregates passing #16: $P_{s\text{-}R16}$ = 25.5% (3570 g)
- Percentage of binder (by DGM weight): $P_{b\text{-}DGM}$ = 4.4% (644 g)
- AASHTO T84 is used to determine the specific gravity of fine aggregates: $G_{sb\text{-}P16}$ = 2.541
- AASHTO T85 is used to determine the specific gravity of coarse aggregates: $G_{sb\text{-}R16}$ = 2.571
- Bulk specific gravity of DGM aggregates is determined to be 2.563 by the following equation:

$$G_{sb-DGM} = \frac{100}{\frac{P_{s-R16}}{G_{sb-R16}} + \frac{P_{s-P16}}{G_{sb-P16}}} \tag{A.1}$$

- AASHTO T209 is used to determine the theoretical maximum specific gravity of HMA paving mixtures: $G_{mm\text{-}DGM} = 2.465$
- Effective specific gravity of aggregates is determined to be 2.634 using the following equation:

$$G_{se-DGM} = \frac{100 - P_{b-DGM}}{\frac{100}{G_{mm-DGM}} - \frac{P_{b-DGM}}{G_b}} \tag{A.2}$$

- Percentage of absorbed binder into aggregates (by aggregate weight) is determined to be 1.08% (151 g) by the following equation:

$$P_{ba-DGM} = \frac{(100 * G_b)(G_{se-DGM} - G_{sb-DGM})}{(G_{se-DGM} * G_{sb-DGM})} \tag{A.3}$$

- The amount of effective binder subjected to aggregates is determined to be 493 g.

The following method for determining binder content relies on experimentally separating the fine portion of the mixture (passing sieve #16) from the coarse portion (retained on #16) and determining the asphalt content of the fine portion. This asphalt content is then used to mix and compact FAM specimens in the SGC. This method, developed by Sousa et al. (2011), takes advantage of the procedures described in AASHTO standards T 209 and T 308 for determining the theoretical maximum specific gravity and binder content in asphalt mixtures, respectively. The following information is determined for FAM design:

- Percentage of binder (by FAM weight): $P_{b\text{-}FAM}$ = 8.0% (310 g)
- AASHTO T209 is used to determine the theoretical maximum specific gravity of HMA paving mixtures: $G_{mm\text{-}FAM}$ = 2.374
- Effective specific gravity of aggregates passing #16 is determined to be 2.678 using the following equation:

$$G_{se-P16} = \frac{100-P_{b-FAM}}{\frac{100}{G_{mm-FAM}}-\frac{P_{b-FAM}}{G_b}} \tag{A.4}$$

- Percentage of absorbed binder into aggregates (by aggregate weight) passing #16 is determined to be 2.07% (74 g) by the following equation:

$$P_{ba-P16} = \frac{(100*G_b)(G_{se-p16}-G_{sb-P16})}{(G_{se-P16}*G_{sb-P16})} \tag{A.5}$$

- Amount of effective binder subjected to aggregates passing #16 is determined to be 237 g.

Table A.2 Mix Design for FAM

Sieve Size	Sieve Size (mm)	Cum. % Passing
No. 16	1.180	100.0
No. 30	0.600	77.1
No. 50	0.300	31.6
No. 200	0.075	10.6
Binder	PG 67-22	8.0

DGM design integrates FAM and CAM designs based on the previous method of dividing the fine and coarse portions of the DGM. So, the information for the CAM design is extracted as follows:

- Percentage of binder (by CAM weight): $P_{b\text{-}CAM}$ = 3.4% (334 g)
- AASHTO T209 is used to determine the theoretical maximum specific gravity of HMA paving mixtures: $G_{mm\text{-}CAM}$ = 2.489
- Effective specific gravity of aggregates retained on #16 is determined to be 2.620 using the following equation:

$$G_{se-R16} = \frac{100-P_{b-CAM}}{\frac{100}{G_{mm-CAM}}-\frac{P_{b-CAM}}{G_b}} \tag{A.6}$$

- Percentage of absorbed binder into aggregates (by aggregate weight) retained on #16 is determined to be 0.74% (77 g) by the following equation:

$$P_{ba-R16} = \frac{(100*G_b)(G_{se-R16}-G_{sb-R16})}{(G_{se-R16}*G_{sb-R16})} \tag{A.7}$$

- Amount of effective binder subjected to aggregates retained on #16 is determined to be 256 g.

Table A.3 Mix Design for CAM

Sieve Size	Sieve Size (mm)	Cum. % Passing
1 in	25.000	100
¾ in	19.000	99.5
3/8 in	9.500	65.0
No. 4	4.750	43.8
No. 8	2.360	15.9
No. 16	1.180	0.0
Binder	PG 67-22	3.4

APPENDIX B

STANDARD METHODS AND REQUIRED TESTS FOR CALIBRATING PANDA CONSTITUTIVE RELATIONSHIPS

This protocol is prepared in an AASHTO standard format

1. SCOPE

1.1. This standard covers the test methods required to determine the material parameters for the Pavement Analysis using Nonlinear Damage Approach (PANDA) constitutive relationships.

1.2. *This standard may involve hazardous material, operations, and equipment. This standard does not support to address all of the safety concerns associated with its use. It is the responsibility of the user of this procedure to establish appropriate safety and health practices and determine the applicability of regulatory limitations prior use.*

---

2. REFERENCED DOCUMENTS

2.1. AASHTO Standards:

- TP 62, Determining Dynamic Modulus of Hot Mix Asphalt
- T 166, Bulk Specific Gravity of Compacted Hot Mix Asphalt Using Saturated Surface-Dry Specimens
- T 209, Theoretical Maximum Specific Gravity and Density of Bituminous Paving Mixtures
- T 269, Percent Air Voids in Compacted Dense and Open Asphalt Mixtures
- T 307, Determining the Resilient Modulus of Soils and Aggregate Materials
- T 312, Preparing and Determining the Density of the Hot Mix Asphalt (HMA) Specimens by Means of the Superpave Gyratory Compactor

2.2. ASTM Standards:

- E 4, Standard Practices for Force Verification of Testing Machines

---

3. SIGNIFICANCE AND USE

3.1. The material parameters or constants determined using this standard are used in the constitutive relationships of Pavement Analysis using Nonlinear Damage Approach (PANDA) in order to predict the performance of asphalt pavements. PANDA incorporates several material constitutive relationships to define the behavior (viscoelastic, viscoplastic, mechanical damage, fatigue damage, and fracture) of an asphalt mixture.

3.2. PANDA is used in asphalt pavement performance analysis.

4. SUMMARY OF TEST METHODS

4.1. This standard consists of several test methods required to determine the material parameters needed for the calibration of different components of PANDA. The dynamic modulus test is used to identify the linear viscoelastic parameters and the time-temperature shift factors. The repeated creep-recovery test at variable stress level (RCRT-VS) conducted at 55°C is used to identify the viscoplastic parameters. The repeated creep-recovery test at constant loading and rest times (RCRT-CLR) is used to identify the hardening-relaxation viscoplastic parameters. The uniaxial constant strain rate test in both compression and tension is used to determine the viscodamage parameters. Table 1 summarizes the test methods required to determine parameters associated with PANDA constitutive relationships.

Table B.1 Summary of the Test Methods Required for Calibration of PANDA Constitutive Relationships.

Test Mode	***Total No. of Specimens***	***Test Method***	***Temperature (°C)***	***Level***	***Loading Time/Resting Time (sec)***	***Confining Pressure (kPa)***
Compression	2	TP-62	Varies	80-110 με	N/A	0
	2	RCRT-VS	55	Varies	0.4/5	140
	6	RCRT-CLR	55	840 kPa	0.4/0.4, 1, 5	140
	4	Uniaxial Constant Strain Rate	55	0.021 mm/sec	N/A	140, 380
Tension	6	Uniaxial Constant Strain Rate	5	5×10^{-6}, 1×10^{-5}, 5×10^{-5} 1/sec	N/A	0

5. APPARATUS

5.1. *Dynamic Modulus Test System*—The system should be capable of conducting the Dynamic Modulus Test at specified temperatures and frequencies in accordance with AASHTO Standard TP 62.

5.2. *Universal Materials Testing System*—The machine should be capable of producing controlled load in both compression and tension. It shall be equipped with ±22 kN (5,000 lb) load cell. The load cell should be calibrated in accordance with ASTM E 4. The system shall be fully computer controlled capable of measuring and recording the time, load, deformation, and confining pressure.

5.3. *Environmental Chamber*—The chamber is required to control the temperature of the test specimens at the desired temperatures. It should be capable of controlling the temperature of the test specimens over a temperature range of -10°C to 55°C. The chamber should accommodate the triaxial cell, which is shown schematically in Figure 1.

5.4. *Triaxial Cell*—A triaxial is required for applying a confining pressure on the test specimens. The cell should stand a working pressure up to 400 kPa (air). The cell should accommodate test specimens, with each has the dimensions of 101.6 mm diameter by 152.4 mm height. The cell shall facilitate up to three “through-the-wall” radial strain transducers. Figure 1 shows a schematic for a triaxial.

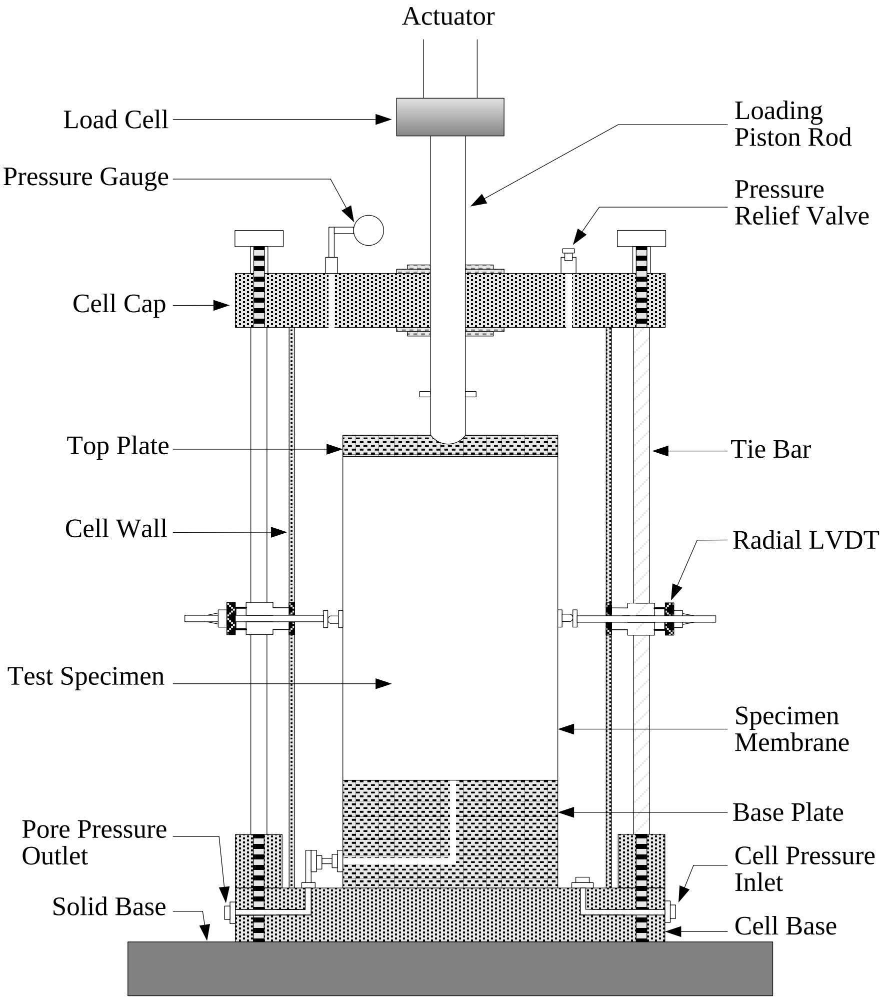

Figure B.1 Schematic View of Typical Triaxial Cell with through-the-wall Radial LVDTs

5.5. *Pressure gauge*—The pressure inside the triaxial cell shall be monitored using a conventional pressure gauge with working pressure of up to 600 kPa and minimum accuracy of 0.7kPa.

5.6. *Strain Transducers*—The axial and radial deformations shall be measured using linear variable differential transformers (LVDTs). Three axial LVDTs shall be used to measure axial deformation. The LVDTs shall be placed on the test specimens at 120 degree apart. A schematic view of the test setup with mounted axial LVDTs is given in Figure 2. Three LVDTs shall be used to measure the radial deformation at the center of the test specimens. Figure 1 shows a tri-axial with “through-the-wall” radial

LVDTs. The LVDTs shall have a linear range of ±2.50 mm and meet the following minimum specifications: linearity, ±0.15 percent of full scale; sensitivity, 156.43mV/V/mm; and repeatability, ±1 percent of full scale.
Note 1—The specifications of the LVDTs used in the dynamic modulus test shall comply with the TP 62 specifications.

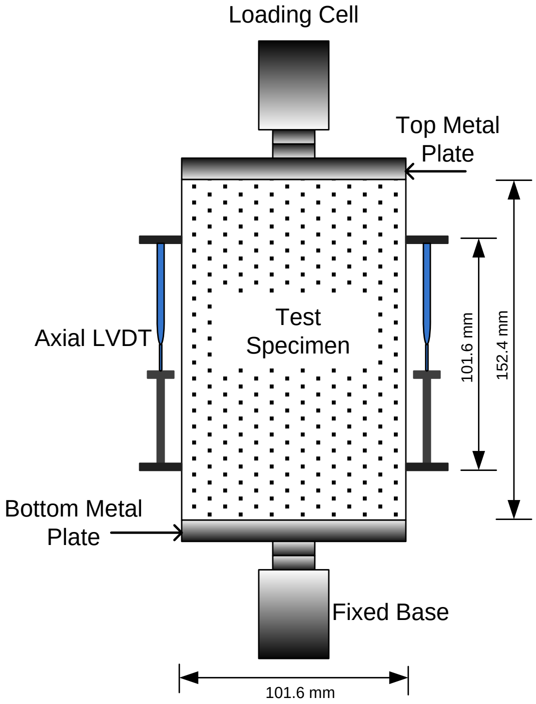

Figure B.2 Schematic View of Test Setup with Mounted Axial LVDTs

5.7. *Loading platens*—The loading platens should be made of stainless steel or high-strength aluminum. The size of the loading platens (104.5±0.5 mm) should be slightly larger than diameter of the test specimens.

5.8. Pressurized air supply—A compressed air supply that is capable of supplying clean, dry, oil-free air up to 400 kPa

5.9. *Calipers*—Digital or analog calipers with an accuracy of ±0.01 mm.

5.10. Glue—must be able to withstand force applied to the sample by a machine and must bond well to the test specimen and loading platens.

5.11. *Superpave Gyratory Compactor*—A compactor and associated equipment needed to compact 152.4-mm diameter and 170-mm height specimens in accordance with the AASHTO T 312 Standard.

5.12. *Core Drill*—A coring machine with a diamond coring bit should be able to cut 101.6-mm diameter specimens out of 152.4-mm diameter SGC specimens.

5.13. *Saw*—Single or double saw with diamond cutting edge should be capable of trimming 170-mm height SGC specimens to 152.4-mm height specimens.

5.14. *Balance*—A balance shall meet the requirements of AASHTO M 231 Standard.

5.15. *Thermometers*—A thermometer should be able to measure the temperature of test specimens over the range of -10^o C to 55^o C.

5.16. *Latex Membrane*—71.1 mm diameter by 0.3mm thick rubber membrane is used when confining pressure is required.

5.17. *End-Friction Reducer*—Greased double latex is placed between the specimen and loading platen.

5.18. *Other apparatus*—other apparatus required to perform the procedures described in this document include a recipient for the applied vacuum saturation.

6. HAZARDS

6.1. Observe and practice standard laboratory safety precautions when preparing, handling, and testing hot mix asphalt (HMA) specimens. Caution should be taken when applying confining pressure on test specimens. The confining pressure must not exceed the limit specified by the manufacturer of the tri-axial cell.

7. TEST SPECIMENS FABRICATION AND INSTRUMENTATION

7.1. HMA specimens are prepared in accordance with T 312. A SGC is used to compact cylindrical 170±1-mm tall and 152.4±1-mm diameter specimens.

7.2. The SGC specimens are cored to 101.6±1-mm diameter, and trimmed using a double or single saw cut to 152.4±1-mm tall. The sides and ends of test specimens shall be smooth and parallel.

7.3. The ends of the test specimens should be perpendicular to axis of the specimens. Each specimen shall be checked using a machinist's square.

7.4. The air void content of test specimens shall be determined in accordance with T 269. A tolerance of 0.5 percent from the target percent air voids is allowed. Any specimen that exceeds this tolerance shall be discarded.

7.5. At least two specimens shall be tested at each test condition.

7.6. Three axial LVDTs shall be mounted to the sides of the test specimens at 120 degree apart. Figure 2 presents a schematic view of the test setup with mounted axial LVDTs. The gauge length of the axial LVDTs shall be 101.6±1 mm. The metal studs are mounted at a distance of 25.4 mm from the top and bottom of the test specimens. The mounting studs for axial LVDTS should be glued directly to test specimens.

Note 2—Quick setting epoxy and glue accelerator such as E-Z BOND and MAXI-CURE exhibit satisfactory performance.

7.7. Three metal studs for the radial LVDTs shall be mounted in the center of the test specimens at 120 degree apart and 60 degree from the axial LVDTs. The gauge length of the radial LVDTs shall be equal to the radius of the test specimens (50.8±0.5 mm). The mounting studs for radial LVDTS should be glued directly to test specimens.

7.8. When confining pressure is required, a latex membrane should be stretched over the test specimen. O-rings should are used to seal the membrane to the top and bottom plates.

---

8. TEST PROTOCOLS

8.1. Dynamic Modulus Test According to AASHTO TP-62

The dynamic modulus test is used to identify the linear viscoelastic parameters and time-temperature shift factors. This test is conducted in accordance with the AASHTO TP 62. This test is conducted at five different temperatures (−10 °C, 4.4 °C, 21.1 °C, 37.8 °C, and 54.4 °C) and six loading frequencies (0.1, 0.5, 1.0, 5, 10, and 25 Hz) at each temperature. A sinusoidal loading is applied and adjusted to obtain axial strain between 80 to 110 microstrain. Testing starts from the lowest to highest temperature and from highest to lowest frequency. The applied stress and recorded strain are used to calculate the dynamic modulus and phase angle.

8.2. *Repeated Creep-*Recovery *Test at Variable Stress Levels (RCRT-VS)*

The repeated creep-recovery test at variable stress level (RCRT-VS) is conducted at 55°C to identify the viscoplastic parameters. The test includes six loading blocks. Each loading block consists of eight creep-recovery cycles with increasing applied deviatoric stress level. The loading and unloading times of each loading cycle remain constant through the entire test. The loading time is 0.4 sec while the unloading time is 30 sec. The deviatoric stress of the first loading cycle of the first loading block is 140 kPa and it increases by a factor of $1.2^{(n-1)}$; where n is the number of loading cycle in a specific loading block; for the next loading cycles until the 8th loading cycle. The first deviatoric stress of the subsequent loading blocks equals to the third stress level in the previous loading block, and it increases by the same factor of $1.2^{(n-1)}$ for the next loading cycles until the 8th loading cycle of that loading block. A confining pressure of 140 kPa is maintained during the entire test. Figure 3 shows an example of the first three loading blocks of the RCRT-VS.

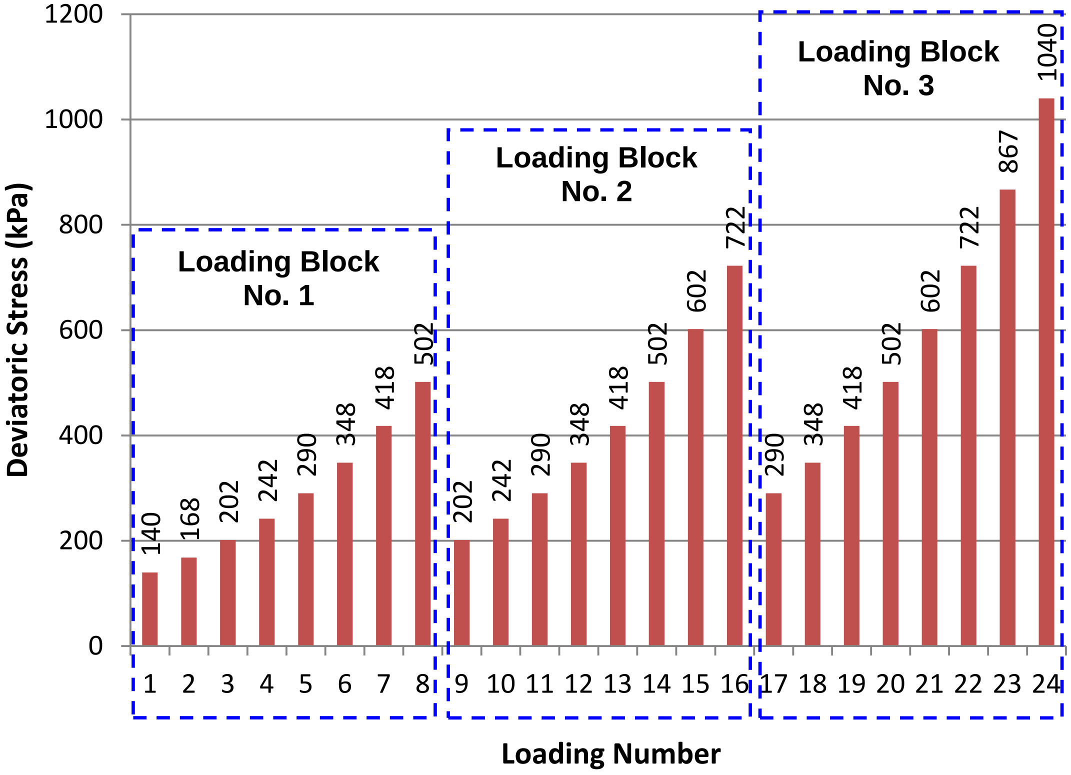

Figure B.3 Applied Deviatoric Stress in the First Three Loading Blocks of the RCRT-VS

8.3. *Repeated Creep-Recovery Test at Constant Loading and Rest Times (RCRT-CLR)*

The creep-recovery test at constant loading and rest times (RCRT-CLR) is performed to identify the hardening-relaxation viscoplastic parameters. The RCRT-CLR consists of repeated creep-recovery loading cycles. The applied confinement and deviatoric stresses in the RCRT-CLR test are 140 kPa and 840 kPa, respectively. The loading time and rest period of all loading cycles are maintained constant throughout the test. A loading time of 0.4 sec and rest periods of 0.4, 1, and 5 sec are used. Two specimens are tested at each rest period as given in Table 1. Figure 4 illustrates a schematic for the RCRT-CLR test.

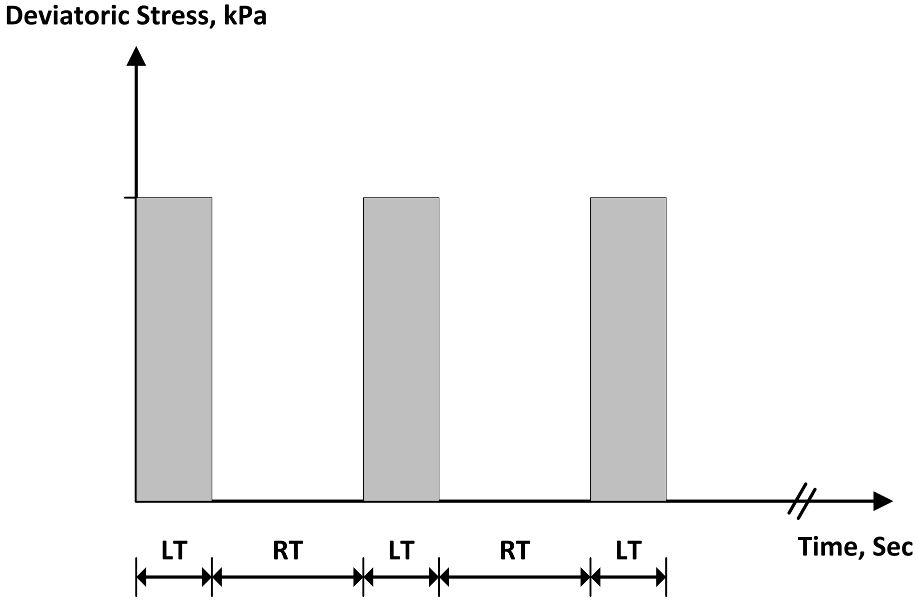

Figure B.4 Schematic for loading cycles of the RCRT-CLR
Note: LT is loading time and RT is rest time

8.4. *Uniaxial Constant Strain Rate Compression Test*

A constant uniaxial strain rate of 0.021 mm/sec is applied on test specimens in compression until failure. This test is conducted at 55°C and two levels of confining pressure; 140 kPa and 380 kPa are required. Two specimens are tested at each confining level as given in Table 1.

8.5. *Uniaxial Constant Strain Rate Tension Test*

This test is conducted in tension at 5°C to determine the viscodamage parameter. The test is performed without confining pressure at three different constant strain rates of 5×10^{-6}, 1×10^{-5}, and 5×10^{-5}/sec until failure. Two specimens are tested at each strain rate as given in Table 1.

Note 3: The uniaxial constant strain rate in tension can be performed without using the tri-axial cell since no confining pressure is required. In this test the test specimen must be glued to the top and bottom plates. The used glue shall be able to withstand force applied to the sample by a machine and must bond well to the test specimen and loading platens. The J-B WELD steel reinforced epoxy is found to provide satisfied adhesion between specimen surface and end plates, and it stands the tensile force. A schematic of the test specimen for the uniaxial constant strain rate in tension is illustrated in Figure 2.

9. TEST PROCEDURE

9.1. Attach the mounting metal studs of the radial and axial LVDTs to the test specimens as described in Sections 7.6, and 7.7.

9.2. Stretch the rubber membrane over the test specimen described in Section 7.8., and fix the fixtures of the LVDTs.

9.3. Place friction reducers between the test specimen and loading platens, and seal the rubber membrane to the top and bottom platens using O-rings as discussed in Section 7.8. When applying confining pressure, the bottom friction reducer should have a hole to allow a passage for specimen's entrapped air to pass to the atmospheric pressure through the base plate as shown in Figure 1.

9.4. Set the temperature of the environmental chamber to the desired test temperature.

9.5. Place the test specimen inside the triaxial cell and adjust the position of the specimen so that the loading piston rod is right in the middle of the top loading platen as shown in Figure 1.

9.6. Install the axial LVDTs, and ensure that the deformation of each axial LVDT is within the calibrated linear range.

9.7. Close the triaxial test and tighten the tie bars.

9.8. Adjust the through-the-wall radial LVDTs and ensure that the deformation of each radial LVDT is within the calibrated linear range.

9.9. Open the pore pressure outlet valve of the triaxial cell (Figure 1).

9.10. Place a dummy specimen inside the environmental chamber and monitor the temperature of this specimen.

9.11. Open the software select pre-programmed testing protocol as described in details in Section 8.

Note 4: The dynamic modulus test should be conducted in accordance AASHTO TP 62.

9.12. Start the test when the temperature of the dummy specimen reaches the desired value. When applying confining pressure, a conditioning period of 2 hours is required after applying the required confining pressure and before loading. This conditioning time is found sufficient to ensure that the bulk creep occurred before loading.

9.13. The RCRT tests are performed until a test specimen fails.

9.14. Perform data quality check on axial deformation measurements. Ensure that the average coefficient of variation of the three axial LVDTs readings, throughout the test and before test specimen fails, is less than 20 percent.

---

10. CALIBRATION PROTOCOL FOR PANDA CONSTITUTIVE RELATIONSHIPS

10.1. Calibration of Linear Viscoelastic Constitutive Relationship using Dynamic Modulus Test

This section presents a systematic procedure to identify time-temperature shift factors as well as the linear viscoelastic parameters based on dynamic modulus test data.

10.1.1 Linear viscoelastic constitutive relationship and its associated parameters

Schapery's (1969) nonlinear viscoelasticity is implemented in PANDA. The nonlinear viscoelastic constitutive relationship can be written as follows:

$$\varepsilon_{ij}^{ve} = g_0 D_0 \bar{\sigma}_{ij}^{t} + g_1 \int_0^t \Delta D^{\left(\psi^t - \psi^\tau\right)} \frac{d\left(g_2 \bar{\sigma}_{ij}^{\tau}\right)}{d\tau} d\tau \tag{1}$$

where

$$D^{\psi^t} = \sum_{n=1}^{N} D_n \left[1 - \exp\left(-\lambda_n \psi^t\right)\right]; \qquad \psi^t = \int_0^t \frac{d\xi}{a_T} \tag{2}$$

where ε_{ij}^{ve} is the viscoelastic strain tensor; $\bar{\sigma}_{ij}$ is the stress tensor; D_0 is the instantaneous compliance; ΔD is the transient compliance; D_n and λ_n are the Prony series coefficients; N is the number of Prony series; a_T is the time-temperature shift factor; and g_0, g_1, and g_2 are the nonlinear viscoelastic parameters. For the linear viscoelasticity $g_0 = g_1 = g_2 = 1$ is assumed. The procedure for identification of nonlinear parameters will be presented in the next section. Table 2 lists the parameters associated with the linear viscoelastic constitutive relationship and their physical significance.

Table B.2 List of linear viscoelastic parameters and their physical significance

Parameter	Physical meaning
a_T	Time-temperature shift factor. Captures the response at different temperatures.
D_0	Instantaneous compliance. Related to the instantaneous viscoelastic response.
D_n	n^{th} Prony series coefficient related to transient compliance.
λ_n	n^{th} Retardation time associated with the n^{th} transient compliance D_n .
N	Number of Prony series to acquire desired accuracy. $N=9$ is recommended. No need to be determined. It should be assumed.

10.1.2 Obtaining time-temperature shift factor

- Dynamic modulus $\left|E^*\right|$ and the phase angle θ at each frequency and temperature are the outputs of the dynamic modulus test. Values of dynamic compliance $\left|D^*\right|$ is determined, such that:

$$\log\left|D^*\right| = -\log\left|E^*\right| \tag{3}$$

- A sigmoidal-type function is used to fit the experimental data and to obtain the time-temperature shift factors. The sigmoidal function for the complex compliance can be written as:

$$-\log\left|D^*\right| = \delta + \frac{\alpha}{1+\exp\left[\beta+\gamma\log\left(\omega_r\right)\right]} \tag{4}$$

where ω_r is the reduced frequency, δ is the maximum value of the dynamic compliance, $\delta+\alpha$ is the minimum value of the dynamic compliance, and β and γ are parameters describing the shape of the sigmoidal function. Time-temperature shift factor is defined as:

$$a_T = \frac{\omega_r}{\omega} \tag{5}$$

where ω is the angular frequency. The term a_T is the time-temperature shift factor at each temperature. Eqs. (4) and (5) introduce $4+(n_T-1)$ unknowns which should be determined ($\alpha,\beta,\delta,\gamma,a_T\left(n_1\right),a_T\left(n_2\right)\ldots a_T\left(n_T-1\right)$); n_T is the number of temperatures at which the test is conducted. It should be noted that number of unknown time-temperature shift factors are (n_T-1) since a_T is known at the selected reference temperature T_r (i.e. $a_T\left(T_r\right)=1$).

- The error function is defined as:

$$R^2 = 1 - \frac{SSE}{SST} \tag{6}$$

where

$$SSE = \sum_{i=1}^{M}\left(\log D_{\exp} - \log D_{fit}\right)^2 \tag{7}$$

$$SST = \sum_{i=1}^{M}\left(\log D_{\exp} - \overline{\log D}\right)^2 \tag{8}$$

where M is the number of data points obtained from dynamic modulus test, $\log D_{\exp}$ is the experimentally measured compliance, $\log D_{fit}$ is the compliance fitted using Eq. (4), $\overline{\log D}$ is the mean value of the measured compliance.

- The $4+(n_T-1)$ unknown variables are determined by minimizing the error function R^2 using Generalized Reduced Gradient (GRG) algorithm which is also available in the excel solver. Initial values for the unknown variables will be set in Excel solver by selecting the corresponding cells for each variable. The objective cell would be the calculated value of R^2. The sigmoidal function parameters and the time-temperature shift factors will be identified by minimizing R^2.
- Excel solver or other optimization algorithms available in other software such as Matlab can be used to obtain the $4+(n_T-1)$ parameters.

10.1.3 Identification of Linear Viscoelastic Parameters of PANDA

- Once the time-temperature shift factors are identified, the linear viscoelastic parameters can be identified.
- Using the experimental data, storage compliance D' and loss compliance D'' can be calculated using the values of the complex compliance and phase angle, such that:

$$D' = \left|D^*\right|\cos\theta; \qquad D'' = \left|D^*\right|\sin\theta \tag{9}$$

- The loss and storage compliances are related to the Prony series coefficients and angular frequencies, such that:

$$D'(\omega) = D_0 + \sum_{i=1}^{N}\frac{D_i}{\omega^2/\lambda_i^2+1}; \qquad D''(\omega) = \sum_{i=1}^{N}\frac{\omega/(\lambda_i D_i)}{\omega^2/\lambda_i^2+1} \tag{10}$$

where N is the number of Prony series coefficients, D_0 is the instantaneous compliance, D_i is the i^{th} transient compliance associated with the i^{th} retardation time λ_i.

- The error function is defined as:

$$error = \frac{1}{M}\sum_{i=1}^{N}\left[\left(\frac{D'_{fit}}{D'_{\exp}}-1\right)^2+\left(\frac{D''_{fit}}{D''_{\exp}}-1\right)^2\right] \qquad (11)$$

where M is the number of data points. D'_{fit} and D''_{fit} are based on Eq. (10) while $D'_{\exp}$ and $D''_{\exp}$ are calculated experimentally.

- The linear viscoelastic PANDA model parameters (i.e. Prony series coefficients) will be identified by minimizing the error function presented in Eq. (11). Eq. (11) can be minimized using excel solver or using other commercial software such as Matlab.
- There is no need to identify N. Based on the desired accuracy, N can be assumed between 5 and 9. $N = 9$ is recommended.

10.2. Calibration of Nonlinear Viscoelastic PANDA Model Parameters using Repeated Creep-Recovery Test at Various Stress levels (RCRT-VS)

This section outlines the procedure for identification of the nonlinear viscoelastic parameters using repeated creep-recovery test at various stress levels (RCRT-VS), refer to Masad et al. (2008) and Rahmani et al. (2013) for more details on identification of nonlinear viscoelastic parameters. To accurately represent the stress states in the pavements, it is recommended to conduct this test at a confinement level of 140-250 kPa. Based on RCRT-VS, three nonlinear parameters g_0, g_1, and g_2 should be determined. It is assumed that $g_0 = 1$. The viscoelastic nonlinearity will be captured through parameters g_1 and g_2. Tables 3 and 4 list the parameters that are fixed and the parameters that should be identified along with their physical significances.

Table B.3 List of nonlinear viscoelastic parameters that are fixed and can be assumed. No need to identify these parameters.

Parameter	Recommended value	Physical significance
g_0	1.0	Affects the instantaneous response. It is recommended to assume $g_0 = 1$ since it is very difficult to measure the instantaneous response of asphalt mixtures. The nonlinear viscoelastic response will be captured through nonlinear parameters g_1 and g_2 Time-temperature shift factor. Captures the response at different temperatures

Table B.4 List of nonlinear viscoelastic parameters that should be identified.

Parameter	Physical meaning
g_1	Controls the nonlinearity in the transient compliance. Affects the viscoelastic nonlinearity mostly during the loading stages.
g_2	Controls the nonlinear response during the recovery and at different loading rates.

10.2.1 Viscoelastic strain decomposition

- To capture the effect of multi-axial state of stresses on nonlinear viscoelastic response of asphalt mixes, the total nonlinear viscoelastic strain tensor ε_{ij}^{nve} is decomposed into deviatoric strain tensor e_{ij}^{nve} and volumetric component ε_{kk}^{nve}, such that:

$$\varepsilon_{ij}^{nve} = e_{ij}^{nve} + \frac{1}{3}\varepsilon_{kk}^{nve}\delta_{ij} \tag{12}$$

- Deviatoric and volumetric components of the viscoelastic strain can be expressed as:

$$e_{ij}^{nve,t} = \frac{1}{2}g_0 J_0 \bar{S}_{ij}^t + \frac{1}{2}g_1\int_0^t \Delta J\left(\psi^t - \psi^\tau\right)\frac{d\left(g_2\bar{S}_{ij}^\tau\right)}{d\tau}d\tau \tag{13}$$

$$\varepsilon_{kk}^t = \frac{1}{3}g_0 B_0 \bar{\sigma}_{kk}^t + \frac{1}{3}g_1\int_0^t \Delta B\left(\psi^t - \psi^\tau\right)\frac{d\left(g_2\bar{\sigma}_{kk}^\tau\right)}{d\tau}d\tau \tag{14}$$

  where $\bar{S}_{ij}$ are the components of the deviatoric stress tensor and $\bar{\sigma}_{kk}$ is the volumetric stress.

- Shear and bulk instantaneous (i.e. J_0 and B_0) and transient (i.e. ΔJ and ΔB) compliances are calculated based on the identified linear viscoelastic parameters and using the following equations:

$$J_0 = 2(1+\nu)D_0; \qquad \Delta J(\psi) = 2(1+\nu)\Delta D(\psi) \tag{15}$$

$$B_0 = 3(1-2\nu)D_0; \qquad \Delta B(\psi) = 3(1-2\nu)\Delta D(\psi) \tag{16}$$

- Assume the Poisson's ratio to be 0.35, $\nu = 0.35$.
- Deviatoric and volumetric components of the stress for RCRT-VS under confinement stress $\bar{\sigma}_c$ and additional axial stress of $\Delta\bar{\sigma}$ are calculated as follows:

$$\frac{1}{3}\bar{\sigma}_{kk}\delta_{ij}=\left(\sigma_c+\frac{\Delta\sigma}{3}\right)\delta_{ij}\quad,\ \bar{S}_{ij}=\begin{bmatrix}\frac{2}{3}\Delta\sigma & 0 & 0\\ 0 & -\frac{1}{3}\Delta\sigma & 0\\ 0 & 0 & -\frac{1}{3}\Delta\sigma\end{bmatrix}\tag{17}$$

10.2.2 Parameter g_0

- Assume nonlinear parameter g_0 to be unity, $g_0 = 1.0$.

10.2.3 Parameter g_2

Figure 5 schematically represents the strain response during a cycle of RCRT-VS test.

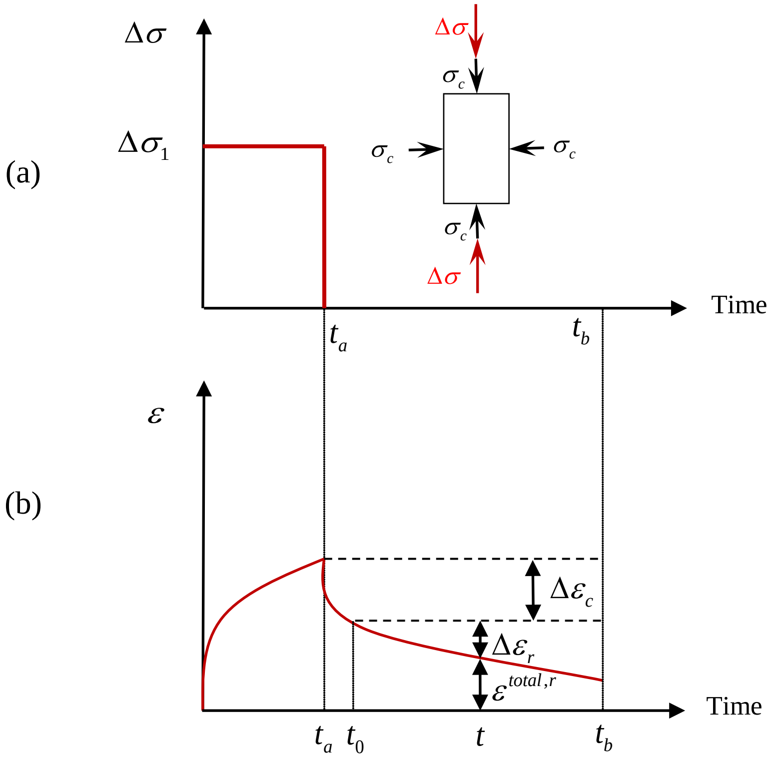

Figure B.5 Schematic representation of the strain response during a cycle of RCRT-VS test.

- Select an arbitrary point during the recovery (e.g. t_0). It is recommended to assume t_0 such that $t_0 - t_a$ is $\frac{1}{10}$ of the rest period.

- Calculate the recovered strain $\Delta\varepsilon_r$ for every point after t_0 during the rest period. $\Delta\varepsilon_r$ can easily be calculated using experimental data, such that:

$$\Delta\varepsilon_r = \varepsilon^{total,r}\left(t_0\right) - \varepsilon^{total,r}\left(t\right) \tag{18}$$

- Using Eqs. (13)-(17) and assuming that the viscoelastic response under pure confinement to be linear yields the following relations for deviatoric and volumetric components of viscoelastic strain during the recovery:

$$e_{11}^{r,t} = \frac{1}{2} g_2^a \left(\Delta J\left(\psi^t\right) - \Delta J\left(\psi^t - \psi^{t_a}\right)\right)\frac{2}{3}\Delta\sigma_1 \tag{19}$$

$$\varepsilon_{vol}^{r,t} = \frac{1}{3} g_2^a \left(\Delta B\left(\psi^t\right) - \Delta B\left(\psi^t - \psi^{t_a}\right)\right)\Delta\sigma_1 + \frac{1}{3}\left(B_0 + \Delta B\left(\psi^t\right)\right)3\sigma_c \tag{20}$$

where t_a is the time corresponding to the end of loading.

- Deviatoric and volumetric components of $\Delta\varepsilon_r$ are calculated using Eqs. (19)-(20), such that:

$$\Delta e_{11,r} = e_{11}^{r,t} - e_{11}^{r,t_0}; \qquad \Delta\varepsilon_{vol,r} = \varepsilon_{vol}^{r,t} - \varepsilon_{vol}^{r,t_0} \tag{21}$$

  Eqs. (19)-(21) show that the only unknown to analytically calculate deviatoric and volumetric components of $\Delta\varepsilon_r$ is g_2.

- Calculate g_2 by minimizing the error between experimentally measured components of $\Delta\varepsilon_r$ (i.e. Eq. (18)) and analytically calculated components of $\Delta\varepsilon_r$ (i.e. Eq. (21)).

10.2.4 Parameter g_1

Once the parameter g_2 is defined, the parameter g_1 can be identified as follows:

- Calculate $\Delta\varepsilon_c$ based on the experimental measurements. The term $\Delta\varepsilon_c$ is the difference between the total strain at the end of the loading and the strain at an arbitrary point during the rest period (i.e. $\Delta\varepsilon_c = \varepsilon^{total}\left(t_a\right) - \varepsilon^{total,r}\left(t\right)$), see Figure 5.
- Calculate $\Delta\varepsilon_c$ using the nonlinear viscoelastic constitutive relationship, such that:

$$\Delta\varepsilon_c = \varepsilon^{nve}\left(t_a\right) - \varepsilon^{nve}\left(t\right) \tag{22}$$

- Using Eqs. (19) and (20), the only unknown in calculating $\Delta\varepsilon_c$ is the g_2 parameter.

- Identify g_1 by minimizing the error between the experimentally measured and calculated values of $\Delta\varepsilon_c$.
- If both axial and radial strains are measured, repeat the procedure outlined above for both volumetric and deviatoric components of $\Delta\varepsilon_c$. The parameter g_1 will be the average of the g_1 parameters obtained from deviatoric and volumetric components of $\Delta\varepsilon_c$.

10.3. Calibration of Viscoplastic PANDA Model using Repeated Creep-Recovery Test at Various Stress levels (RCRT-VS)

10.3.1 Viscoplastic constitutive relationship and its associated parameters

Perzyna's (1971) viscoplastic constitutive relationship with modified Drucker-Prager yield surface has been implemented in PANDA. The viscoplastic flow rule can be written as:

$$\dot{\varepsilon}_{ij}^{vp} = \dot{\gamma}^{vp} \frac{\partial F}{\partial \bar{\sigma}_{ij}}; \quad \dot{\gamma}^{vp} = \Gamma^{vp} \left\langle \frac{f}{\sigma_y^o} \right\rangle^N \tag{23}$$

where ε_{ij}^{vp} is the viscoplastic strain tensor, $\dot{\gamma}^{vp}$ is the viscoplastic multiplier, N is the viscoplastic rate-sensitivity exponent parameter, $\langle \; \rangle$ is the Macaulay brackets defined by $\langle \mathrm{X} \rangle = \left(\mathrm{X} + |\mathrm{X}| \right) / 2$, and σ_y^0 is a yield stress quantity which is used to normalized the yield surface and can be assumed as unity. Functions f and F are yield surface and plastic potential functions, respectively, such that:

$$f = \tau - \alpha I_1 - \kappa(p); \qquad F = \tau - \beta I_1;$$

$$\tau = \frac{\sqrt{3J_2}}{2} \left[1 + \frac{1}{d^{vp}} + \left(1 - \frac{1}{d^{vp}} \right) \frac{3J_3}{\sqrt{3J_2^3}} \right] \tag{24}$$

where α and β are the pressure-sensitivity material parameters; $I_1 = \bar{\sigma}_{kk}$ is the first stress invariant; τ is the deviatoric effective shear stress; $J_2 = \frac{1}{2} \bar{S}_{ij} \bar{S}_{ij}$ and $J_3 = \frac{1}{2} \bar{S}_{ij} \bar{S}_{jk} \bar{S}_{ki}$ are second and third deviatoric stress invariants, respectively; d^{vp} is the parameter that distinguishes the viscoplastic responses during extension and contraction mode of loadings; and κ is the hardening function expressed as:

$$\kappa(p) = \kappa_o + \kappa_1 \left[1 - \exp(-\kappa_2 p) \right];$$

$$\dot{p} = \left[1 + 2 \left(\frac{0.5 + \beta / 3}{1 - \beta / 3} \right) \right]^{-0.5} \sqrt{\dot{\varepsilon}_{ij}^{vp} \, \dot{\varepsilon}_{ij}^{vp}} \tag{25}$$

where p is the effective viscoplastic strain.

10.3.2 Assumed Viscoplastic parameters

Several of viscoplastic parameters are assumed because they do not vary significantly from one asphalt mixture to the other and can be assumed constant with reasonable accuracy. These parameters, their physical meaning and the recommended values are listed in Table 5, please refer to Huang (2008), Abu Al-Rub et al. (2009), and Darabi et al. (2012a) for more details on the identification of viscoplastic parameters.

Table B.5 List of viscoplastic parameters that are fixed and can be assumed. No need to identify these parameters.

Parameter	Recommended value	Physical significance
α	0.15-0.3	Related to the angle of friction of the asphalt mixtures.
β	$\alpha - 0.05$	Related to the angle of friction and the dilation characteristics of asphalt mixtures.
d^{vp}	0.78	Ratio of yield strength in tension to that in compression. Fixed for most asphalt mixes.
κ_0	50-150 kPa	Initial yield strength. It has a very low value at high temperatures. Does not affect the results very much and can be assumed to have a small value between 50-150kPa for most asphalt mixtures.
κ_1	Compressive strength of asphalt mixture at 40°C	The hardening limit of asphalt mixtures against viscoplastic deformation. Is in the order of compressive strength of asphalt mixtures at 40°C

10.3.3 Extraction of viscoplastic strain during the creep part of RCRT-VS

- Use Eq. (1) to calculate the viscoelastic strain response during the loading stage of RCRT-VS once linear and nonlinear viscoelastic parameters are identified.
- Subtract the viscoelastic strain from the total strain to obtain the viscoplastic strain response during the creep part of RCRT-VS.
- Figure 6 schematically illustrates the extraction of the viscoelastic and viscoplastic strain responses from the total measured strain. The viscoplastic parameters will be identified by analyzing the extracted viscoplastic strain response.

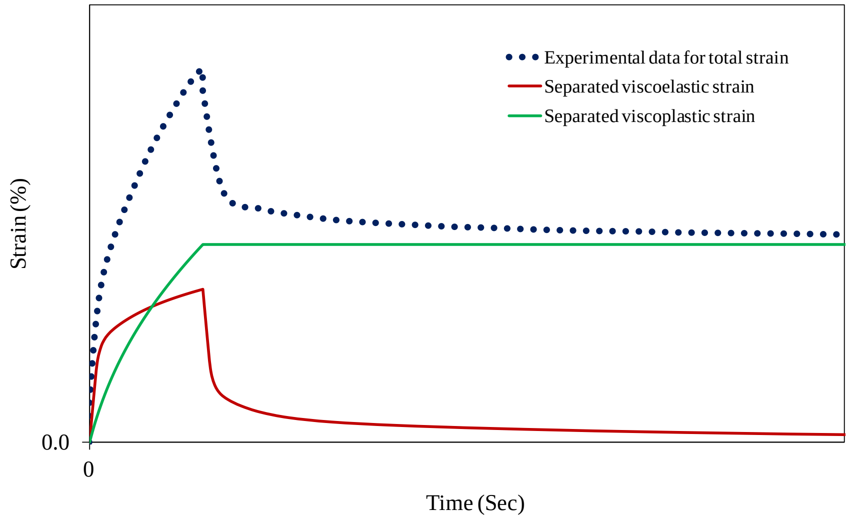

Figure B.6 Schematic illustration of the extraction of the viscoelastic and viscoplastic components of the strain.

10.3.4 Identification of hardening parameter κ_2

- Manipulating Eqs. (23)-(24) yields:

$$\frac{\Delta\gamma^{vp}}{\Delta t}=\Gamma\left[\frac{\left\{\tau-\alpha I_1-\left[\kappa_0+\kappa_1\left(1-\exp\left(-\kappa_2 p\right)\right)\right]\right\}}{\sigma_y^0}\right]^N \tag{26}$$

- Calculate $\Delta\gamma^{vp}$ using the extracted axial viscoplastic strain $\Delta\varepsilon_1^{vp}$, such that:

$$\Delta\gamma^{vp}=\Delta\varepsilon_1^{vp}/\left(1-\beta/3\right) \tag{27}$$

- Calculate effective viscoplastic strain p using extracted axial and radial viscoplastic strains (i.e. ε_1^{vp} and ε_2^{vp}, respectively) , such that:

$$p=\left[1+2\left(\frac{0.5+\beta/3}{1-\beta/3}\right)\right]^{-0.5}\sqrt{\left(\varepsilon_1^{vp}\right)^2+2\left(\varepsilon_2^{vp}\right)^2} \tag{28}$$

- Estimate radial viscoplastic strain as $\varepsilon_2^{vp}=\left(\frac{0.5+\beta/3}{1-\beta/3}\right)\varepsilon_1^{vp}$ if radial measurements are not available.
- Pick constant values for $\Delta\gamma^{vp}$ at different stress levels of RCRT-VS test.
- Rearrange Eq. (26), such that:

$$\tau - \alpha I_1 - \left(A - \kappa_1\right) = \kappa_1\left(1 - Exp\left(-\kappa_2 p\right)\right);$$
$$A = \sigma_y^0 \left(\frac{\Delta\gamma^{vp}}{\Gamma\Delta t}\right)^{1/N} + \kappa_0 + \kappa_1 \tag{29}$$

- Plot $\tau - \alpha I_1 - \left(A - \kappa_1\right)$ versus p at different stress levels. Note that p, A, κ_1, and $\tau - \alpha I_1$ are known.
- Identify the parameter κ_2 by minimizing the error between the experiments and calculations using Eq. (29).
- Pick different values for $\Delta\gamma^{vp}$ and repeat the procedure to identify κ_2 at different values of $\Delta\gamma^{vp}$.
- Calculate the average κ_2 value at different $\Delta\gamma^{vp}$.

10.3.5 Identification of rate-sensitivity exponent parameter N

- Calculate $\Delta\gamma^{vp}\left(t\right)$ and p^t during the loading stage of RCRT-VS at different stress levels using Eqs. (27) and (28), respectively.

- Calculate $\Delta\gamma^{vp}\left(t_0\right)$ and p^{t_0} at the beginning of each loading cycle using Eqs. (27) and (28), respectively.
- Rearranging the formulation yields:

$$\frac{\Delta\gamma^{vp}\left(t\right)}{\Delta\gamma^{vp}\left(t_0\right)} = \left[\frac{\tau - \alpha I_1 - \left[\kappa_0 + \kappa_1\left(1 - Exp\left(-\kappa_2 \varepsilon_e^{vp,t}\right)\right)\right]}{\tau - \alpha I_1 - \left[\kappa_0 + \kappa_1\left(1 - Exp\left(-\kappa_2 \varepsilon_e^{vp,t_0}\right)\right)\right]}\right]^N \tag{30}$$

- Identify N by minimizing the error between the experimentally measured $\Delta\gamma^{vp}\left(t\right)/\Delta\gamma^{vp}\left(t_0\right)$ and the model results using Eq. (30).

10.3.6 Identification of viscoplastic viscosity parameter Γ^{vp}

Once viscoplastic parameters κ_2 and N are identified, the viscoplasticity parameter Γ^{vp} can be identified by fitting the $\Delta\gamma^{vp}$ in each cycle using Eq. (26).

10.4. Calibration of Hardening-Relaxation Viscoplastic PANDA Model using Repeated Creep-Recovery Test at Constant Loading and Rest times (RCRT-CLR)

10.4.1. Hardening-relaxation constitutive relationship and its associated parameters

When subjected to cyclic creep loading with rest periods between the loading cycles, the viscoplastic behavior of asphalt concrete materials changes such that the rate of accumulation of the viscoplastic strain at the beginning of a loading cycle increases comparing to that at the end of the preceding loading cycle. This phenomenon is referred to as the *hardening-relaxation* and is a key element in predicting the permanent deformation (rutting) of asphalt pavements. The hardening relaxation phenomenon is modeled using the hardening-relaxation memory concept (Darabi et al., 2012b). To model the hardening-relaxation, static and dynamic hardening-relaxation memory surfaces are defines as:

$$f^{h-r} = p - q^{vp} \leq 0 \,; \qquad \chi^{h-r} = p - q^{vp} - \left(\frac{\dot{q}^{vp}}{\Gamma^{h-r}} \right)^{\frac{1}{S_1}} \leq 0 \tag{31}$$

where f^{h-r} and χ^{h-r} are static and dynamic hardening-relaxation memory surfaces, respectively. The term q^{vp} is the hardening-relaxation internal state variable that memorizes the maximum experienced viscoplastic strain for which the hardening-relaxation has occurred while p is the effective viscoplastic strain. Parameters Γ^{h-r} and S_1 are hardening-relaxation parameters. The rate of relaxation in the hardening parameter is calculated, such that:

$$\dot{\kappa}_1^{vp} = -S_2 \, \dot{q}^{vp} \tag{32}$$

where S_2 is another parameter associated with the hardening-relaxation constitutive relationship. Table 6 lists the parameters associated with the hardening-relaxation constitutive relationship and their physical significance. Repeated creep-recovery test at constant loading and rest times (RCRT-CLR) will be used to identify the hardening-relaxation parameters.

Table B.6 List of hardening-relaxation viscoplastic parameters.

Parameter	**Physical meaning**
Γ^{h-r}	Hardening-relaxation fluidity parameter controlling the rate of evolution of the hardening-relaxation state variable.
S_1	Hardening-relaxation exponent controlling the time-dependency of the hardening-relaxation state variable.
S_2	Hardening-relaxation parameter controlling the rate at which the hardening parameter relaxes.

10.4.2. Calculation of hardening parameter κ_1

Figure 7 schematically shows the evolution of the effective viscoplastic strain p and the hardening-relaxation state variable q^{vp} during a cycle of RCRT-CLR.

- From the experimental measurements, calculate the rate of the effective viscoplastic strain at the end of the loading and at the beginning of the following loading cycles: (i.e. times t_1 and t_2, respectively).
- Apply Eq. (23) and (25) to times t_1 and t_2, such that:

$$\dot{p}(t_1)=\Gamma^{vp}\left[A-\kappa_1(t_1)B(t_1)\right]^N;\qquad \dot{p}(t_2)=\Gamma^{vp}\left[A-\kappa_1(t_2)B(t_1)\right]^N \qquad (33)$$

where $A=\dfrac{\tau-\alpha I_1-\kappa_0}{\sigma_y^0}$ and $B(t_1)=\dfrac{1-\exp\left(-\kappa_2 p(t_1)\right)}{\sigma_y^0}$.

- Calculate the hardening parameter κ_1 at the end of loading and at the end of the rest period, such that:

$$\kappa_1(t_1)=\frac{1}{B(t_1)}\left[A-\left(\frac{\dot{p}(t_1)}{\Gamma^{vp}}\right)^{1/N}\right];\qquad \kappa_1(t_2)=\frac{1}{B(t_1)}\left[A-\left(\frac{\dot{p}(t_2)}{\Gamma^{vp}}\right)^{1/N}\right] \qquad (34)$$

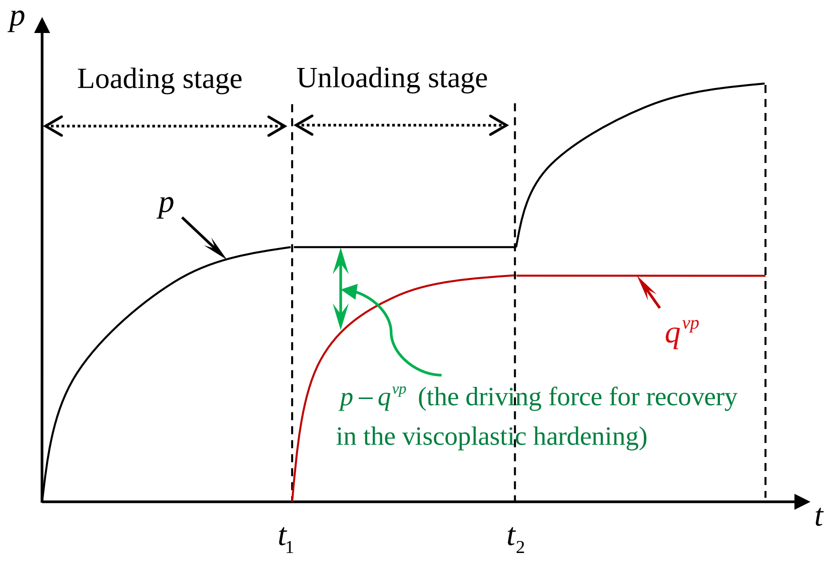

Figure B.7 Schematic representation of the evolution of the effective viscoplastic strain and the hardening-relaxation internal state variable during a cycle of RCRT-CLR.

- Plot $\kappa_1(t)$ and $p(t)$ versus the accumulative resting time t for the all RCRT-CLR tests.
- Integrate Eq. (32), such that:

$$-\frac{\kappa_1(t)-\kappa_1^{initial}}{S_2}=q^{vp}(t) \tag{35}$$

- Pick the average values of p and κ_1 at the end of the test for different rest periods. Set q^{vp} as the average p at the end of the tests (i.e. p^{final}) and calculate S_2, such that:

$$S_2=\frac{\kappa_1^{initial}-\kappa_1^{final}}{p^{final}} \tag{36}$$

- Calculate $\Delta q^{vp}(t)$ using Eq. (32) once S_2 is known, such that:

$$\Delta q^{vp}(t)=-\frac{\Delta\kappa_1(t)}{S_2} \tag{37}$$

where t is the accumulative unloading time.

- Calculate Δq^{vp}, q^{vp}, and p for all cycles of RCRT-CLR tests from experimental measurements and Eq. (37).
- Manipulate Eq. (31), such that:

$$\frac{\Delta q^{vp}}{\Delta t}=\Gamma^{h-r}\left(p-q^{vp}\right)^{S_1} \tag{38}$$

- Plot $\frac{\Delta q^{vp}}{\Delta t}$ versus $p-q^{vp}$ in log-log scale for all available data.
- Calculate Γ^{h-r} as the intersection of $\frac{\Delta q^{vp}}{\Delta t}$-$\left(p-q^{vp}\right)$ curve with Y-axis and S_1 as the slope of the fitted line using the following equation:

$$Ln\left(\frac{\Delta q^{vp}}{\Delta t}\right)=Ln\left(\Gamma^{h-r}\right)+S_1 Ln\left(p-q^{vp}\right) \tag{39}$$

10.5. Calibration of Viscodamage PANDA Model using Uniaxial Constant Strain Rate Tests

10.5.1. Viscodamage constitutive relationship and its associated parameters

The viscoelastic-viscoplastic constitutive relationships are coupled with damage within the context of continuum damage mechanics using the damage density variable ϕ, such that:

$$\sigma_{ij}=(1-\phi)\bar{\sigma}_{ij} \tag{40}$$

where σ_{ij} is the stress tensor in the nominal configuration which is identical to the experimentally measured stresses while $\bar{\sigma}_{ij}$ is the true stress tensor in the undamaged configuration which is the resulting stress if the damage density ϕ is assumed to be zero. The evolution function for damage density is expressed as (Darabi et al., 2013):

$$\dot{\phi} = \Gamma^{vd}\left(\frac{\bar{Y}}{Y_0}\right)^{q}\left(\varepsilon_{eff}\right)^{k}; \qquad \bar{Y} = \tau - \alpha I_1; \qquad \varepsilon_{eff} = \sqrt{\varepsilon_{ij}\varepsilon_{ij}} \tag{41}$$

where $\bar{Y}$ is the damage force and ε_{eff} is the total effective strain. The term Y_0 is the reference damage force which is used for dimensional consistency and can be assumed to be unity.

Table 7 lists the parameters associated with the viscodamage evolution function and their physical significance.

Table B.7 List of viscodamage parameters that should be identified.

Parameter	Physical meaning
Γ^{vd}	Viscodamage fluidity parameter controlling the rate of damage evolution.
q	Stress sensitivity parameter. Controls the effect of stress level on damage evolution and growth.
k	Strain sensitivity parameter. Controls the effect of total strain level on damage evolution and growth.

10.5.2. Calculation of damage density during uniaxial constant strain rate test

The first step in calibrating the damage evolution function is to calculate the damage density variable during the uniaxial constant strain rate test. The constant strain rate test should be conducted at minimum of three strain rates at low temperatures (e.g. 5°C).

- Select the constant strain rate tests at a low temperature (5°C is recommended) where the viscoplastic strain can be neglected. The strain input for constant strain rate test can be expressed as:

$$\varepsilon(t) = Ct \tag{42}$$

where C is the strain rate.

- Calculate the induced stress in the undamaged configuration, such that:

$$\bar{\sigma}(t) = C\int_0^t E(\tau)\,d\tau \tag{43}$$

where $E(t)$ is the relaxation modulus which is known from the dynamic modulus test.

- Calculate the damage density using the calculated stress in the undamaged configuration and the experimentally measured stress, such that:

$$\phi(t)=1-\frac{\sigma(t)}{\bar{\sigma}(t)} \tag{44}$$

- Calculate the rate of the damage density using the calculated damage density, such that:

$$\dot{\phi}=\frac{\Delta\phi}{\Delta t}=\frac{\phi(t+\Delta t)-\phi(t)}{\Delta t} \tag{45}$$

10.5.3. Identification of q parameter

- Select four arbitrary strain levels.
- Plot $\bar{Y}/Y_0$ versus rate of the damage density at different strain rates for each selected strain level in logarithmic scale.
- Figure 8 schematically shows the procedure to select and plot $\bar{Y}/Y_0$ versus $\dot{\phi}$

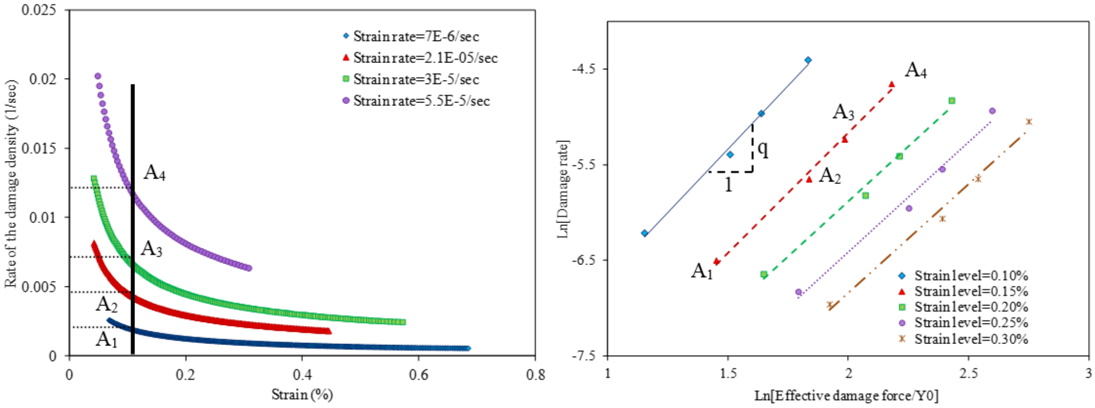

(a) (b)

Figure B.8 Schematic presentation of: (a) Rate of the damage density versus the effective strain plotted at different strain rates for the uniaxial constant strain rate tests; (b) Plot of the damage density rate versus the normalized effective damage force which is used to identify q.

- Calculate the slope of the fitted lines in the $\bar{Y}/Y_0$ versus $\dot{\phi}$ plot at each strain level.
- The parameter q is the average of the measured slopes.

10.5.4. Identification of k parameter

- Select four arbitrary calculated stress levels at undamaged configuration, $\bar{\sigma}$.
- Calculate $\bar{Y}/Y_0$ for each selected stress level.
- Plot ε_{eff} versus rate of the damage density at different stress levels in logarithmic scale.
- Figure 9 schematically shows the procedure to select and plot ε_{eff} versus $\dot{\phi}$.

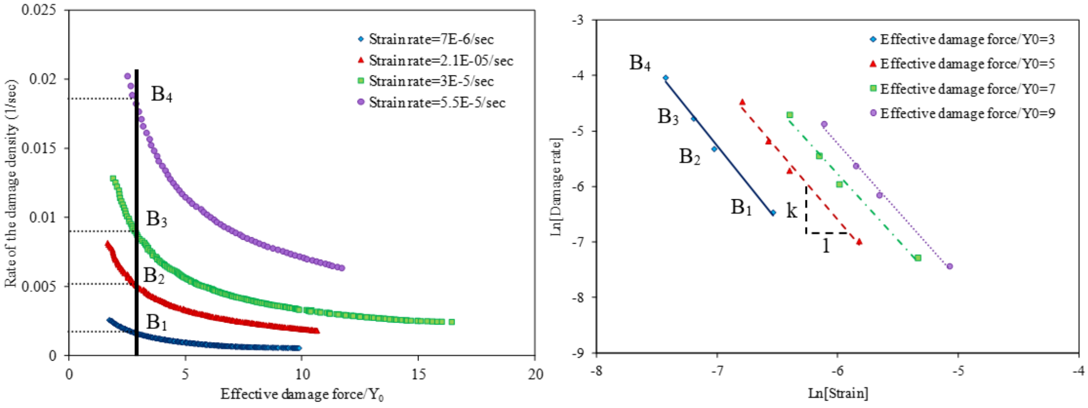

(a) (b)

Figure B.9 Schematic presentation of: (a) Rate of the damage density versus the dimensionless effective damage force (i.e. $\bar{Y}/Y_0$) plotted at different strain rates for the uniaxial constant strain rate tests; (b) Plot of the damage density rate versus the effective strain which will is used to identify k.

- Calculate the slope of the fitted lines in the ε_{eff} versus $\dot{\phi}$ plot at each strain level.
- The parameter k is the average of the measured slope.

10.5.5. Identification of Γ^{vd}

- Select the data points used to identify q and k.
- Calculate $\bar{Y}/Y_0$ and ε_{eff} for the selected data points.
- Calculate $qLn\left(\frac{\bar{Y}}{Y_0}\right)$ and $kLn\left(\varepsilon_{eff}\right)$ once q and k are identified.
- Record rate of the damage density for the selected data points.

- Calculate $Ln\left(\dot{\phi}\right)-qLn\left(\frac{\bar{Y}}{Y_0}\right)-kLn\left(\varepsilon_{eff}\right)$.
- Calculate Γ^{vd} for each data point as:

  $$Ln\left(\Gamma^{vd}\right)=Ln\left(\dot{\phi}\right)-qLn\left(\frac{\bar{Y}}{Y_0}\right)-kLn\left(\varepsilon_{eff}\right).$$
- Identify the parameter Γ^{vd} by averaging the calculated Γ^{vd} for each data point.

11. KEYWORDS

Asphalt Mixtures, Performance, PANDA, mechanical damage, viscoelastic, viscoplastic, and hardening-relaxation.

12. REFERENCES

Abu Al-Rub, R.K., Masad, E.A., Huang, C.W., 2009. Improving the sustainability of asphalt pavements through developing a predictive model with fundamental material properties. Southwest University Transportation Center, Texas Transportation Institute, College Station, TX, 1-45.

Darabi, M.K., Abu Al-Rub, R.K., Masad, E.A., Little, D.N., 2012a. A thermodynamic framework for constitutive modeling of time- and rate-dependent materials, part ii: Numerical aspects and application to asphalt concrete. International Journal of Plasticity 35, 67-99.

Darabi, M.K., Abu Al Rub, R.K., Masad, E., Huang, C.W., Little, D., 2012b. A modified viscoplastic model to predict the permanent deformation of asphaltic materials under cyclic-compression loading at high temperatures. International Journal of Plasticity 35, 100-134.

Darabi, M.K., Abu Al Rub, R.K., Masad, E., Little, D., 2013. Constitutive modeling of fatigue damage response of asphalt concrete materials with consideration of micro-damage healing International Journal of Solids and Structures In press.

Huang, C.W., 2008. Development and numerical implementation of nonlinear viscoelastic-viscoplastic model for asphalt materials. Ph.D. Dissertation, Texas A&M University.

Masad, E., Huang, C.W., Airey, G., Muliana, A., 2008. Nonlinear viscoelastic analysis of unaged and aged asphalt binders. Construction and Building Materials 22, 2170-2179.

Perzyna, P., 1971. Thermodynamic theory of viscoplastcity. Advances in Applied Mechanics 11, 313-354.

Rahmani, E., Darabi, M.K., Abu Al-Rub, R.K., Kassem, E., Masad, E., Little, D., 2013. Effect of confinement pressure on the nonlinear-viscoelastic response of asphalt concrete at high temperatures. Construction and Building Materials In press.

Schapery, R.A., 1969. Further development of a thermodynamic constitutive theory: Stress formulation. Purdue University, Purdue Resarch Foundation, Lafayette, IN.

APPENDIX C

PUI

ABAQUS provides wide flexibilities in terms of analysis type, material properties, mesh type, load and boundary conditions, etc. In order to allow users to utilize these versatile features without having in-depth knowledge of ABAQUS preprocessing functions, the PUI was developed at Texas A&M University by a team of researchers who are familiar with ABAQUS and who have expertise in the development of user-friendly interfaces. PUI is customized for pavement applications such that users can conduct performance simulations of pavements without having the in-depth knowledge of using ABAQUS. In PUI, users are required to specify the thickness of each layer, the properties of each layer, the wheel load magnitude, and the mode of analysis (e.g., 2D plane strain, 2D axisymmetric, or 3D). PUI translates these inputs into ABAQUS language and creates the input file that can be used directly by ABAQUS to perform the simulations. Therefore, users benefit from all preprocessing and postprocessing capabilities of ABAQUS through PUI.

The process for generating the input file is almost identical to the process in ABAQUS. Figure C.1 shows the main window for selecting the model and loading type. The interface provides four types of model and loading combinations:

- 2D axisymmetric model under pulse loading
- 3D model under equivalent loading
- 3D model under pulse loading

- 3D model under moving loading

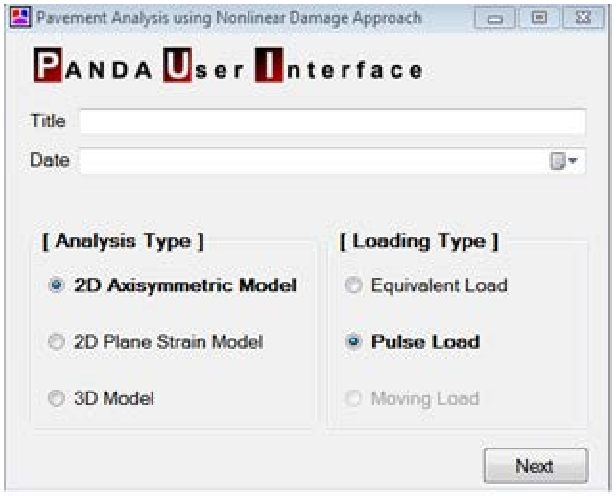

Pavement Analysis using Nonlinear Damage Approach

PANDA User Interface

Title

Date

[Analysis Type]

● 2D Axisymmetric Model

○ 2D Plane Strain Model

○ 3D Model

[Loading Type]

○ Equivalent Load

● Pulse Load

○ Moving Load

Figure C.1 Main Window of PUI

Figure C.2 shows an example of inputting the data required for a 3D model subjected to pulse loading. As shown in Figure C.2(a), the analysis model is composed of four layers, including an asphalt concrete layer, and the thickness of each layer is the only data required in the **Layer Thickness** tab to construct the 3D analysis model. The optimized longitudinal and transverse size of the model and mesh density (or element size) of each layer are predetermined in PUI based on comprehensive parametric studies conducted for different cases. Once the thickness of each layer is provided, the user can go to the **Material Properties** tab, as shown in Figure C.2(b), to select the type of constitutive relationship, such as elastic, viscoelastic, viscoelastic-viscoplastic, viscoelastic-viscoplastic-viscodamage, etc. Layers 2 to 4 are modeled as linear elastic. However, different constitutive relationships can be used for the asphalt layer (layer 1).

Moreover, the user can easily select several combinations of constitutive relationships by turning on and off each model.

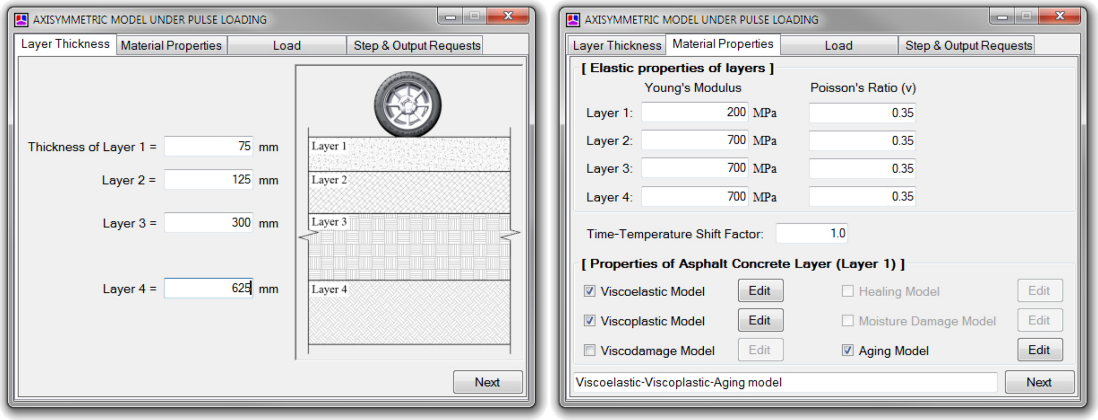

Thickness of Layer 1 = 75 mm
Layer 2 = 125 mm
Layer 3 = 300 mm
Layer 4 = 625 mm

[Elastic properties of layers]

	Young's Modulus	Poisson's Ratio (v)
Layer 1:	200 MPa	0.35
Layer 2:	700 MPa	0.35
Layer 3:	700 MPa	0.35
Layer 4:	700 MPa	0.35

Time-Temperature Shift Factor: 1.0

[Properties of Asphalt Concrete Layer (Layer 1)]

☑ Viscoelastic Model
☑ Viscoplastic Model
☐ Viscodamage Model
☐ Healing Model
☐ Moisture Damage Model
☑ Aging Model

Viscoelastic-Viscoplastic-Aging model

(a) Layer thickness

(b) Material properties

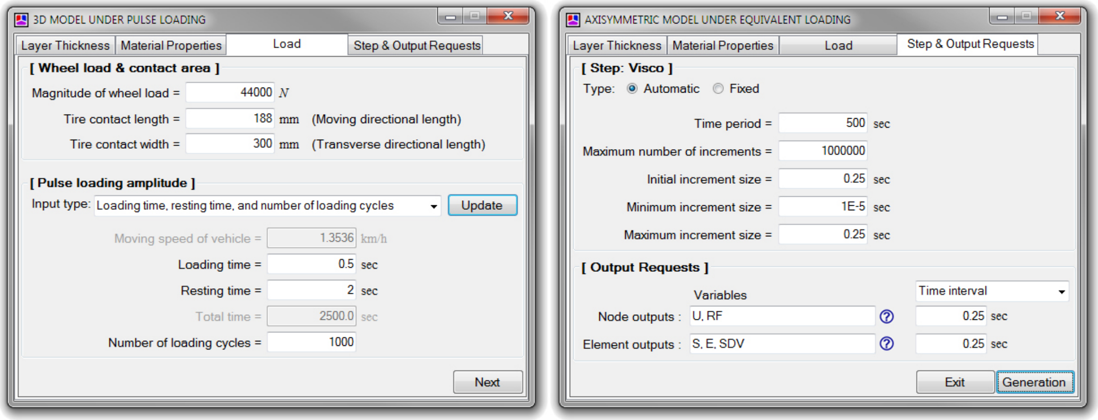

[Wheel load & contact area]

Magnitude of wheel load = 44000 N
Tire contact length = 188 mm (Moving directional length)
Tire contact width = 300 mm (Transverse directional length)

[Pulse loading amplitude]

Input type: Loading time, resting time, and number of loading cycles

Moving speed of vehicle = 1.3536 km/h
Loading time = 0.5 sec
Resting time = 2 sec
Total time = 2500.0 sec
Number of loading cycles = 1000

[Step: Visco]

Type: ● Automatic ○ Fixed

Time period = 500 sec
Maximum number of increments = 1000000
Initial increment size = 0.25 sec
Minimum increment size = 1E-5 sec
Maximum increment size = 0.25 sec

[Output Requests]

	Variables	Time interval
Node outputs :	U, RF	0.25 sec
Element outputs :	S, E, SDV	0.25 sec

(c) Magnitude and amplitude of pulse load

(d) Step and output requests

Figure C.2 Input Data Managing Process (3D Model Under Pulse Loading Case)

The magnitude of wheel load and pulse loading amplitude can be controlled in the **Load** tab, as shown in Figure C.2(c). A rectangular tire contact area is assumed for simplicity. A constant pressure is applied over the entire contact area. Moreover, the pulse loading amplitude is generated automatically based on the moving speed, loading time, resting time, total time, and number of loading cycles. Finally, the time increment size, increment size control type, and output data type preferred by the user can be managed in the **Step & Output Requests** tab, shown in Figure C.2(d). Similar to ABAQUS, both fixed and automatic incrimination techniques are offered in PUI.

Six different material constitutive relationships are available for the asphalt concrete layer, as shown in Figure C.2(b). Each parameter can be entered in its window, as shown in Figure C.3. The hardening-relaxation constitutive relationship is also available, and the user can activate the model simply by checking the option box on the viscoplastic parameters window. In addition, a default value for almost all parameters will be given for user convenience. Moreover, the format of the input file generated from the developed software is exactly the same as that generated from ABAQUS itself, such that advanced ABAQUS users can modify the input file once generated.

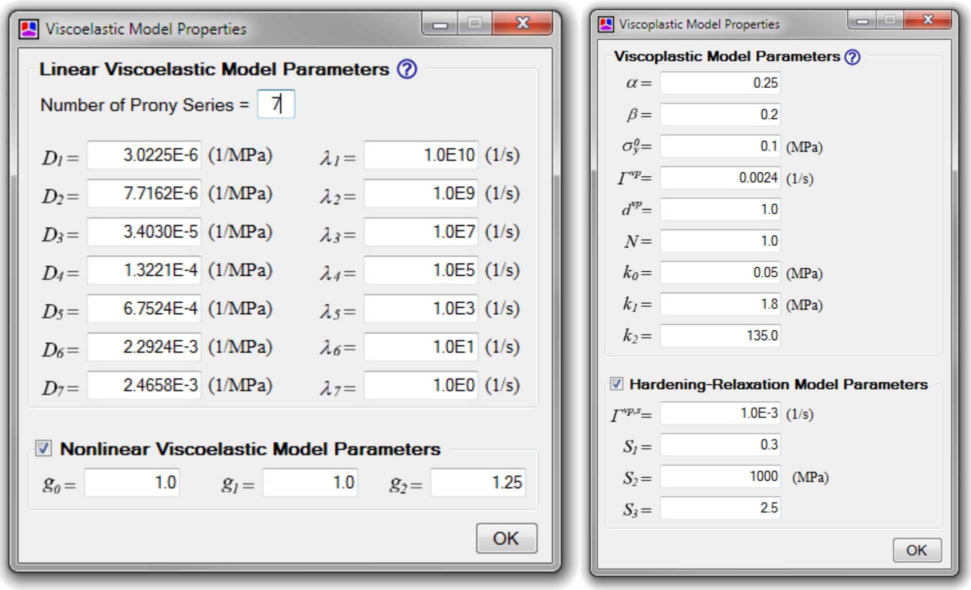

Linear Viscoelastic Model Parameters

Number of Prony Series = 7

$D_1 =$ 3.0225E-6 (1/MPa) $\lambda_1 =$ 1.0E10 (1/s)
$D_2 =$ 7.7162E-6 (1/MPa) $\lambda_2 =$ 1.0E9 (1/s)
$D_3 =$ 3.4030E-5 (1/MPa) $\lambda_3 =$ 1.0E7 (1/s)
$D_4 =$ 1.3221E-4 (1/MPa) $\lambda_4 =$ 1.0E5 (1/s)
$D_5 =$ 6.7524E-4 (1/MPa) $\lambda_5 =$ 1.0E3 (1/s)
$D_6 =$ 2.2924E-3 (1/MPa) $\lambda_6 =$ 1.0E1 (1/s)
$D_7 =$ 2.4658E-3 (1/MPa) $\lambda_7 =$ 1.0E0 (1/s)

☑ **Nonlinear Viscoelastic Model Parameters**

$g_0 =$ 1.0 $g_1 =$ 1.0 $g_2 =$ 1.25

Viscoplastic Model Parameters

$\alpha =$ 0.25
$\beta =$ 0.2
$\sigma_y^0 =$ 0.1 (MPa)
$\Gamma^{vp} =$ 0.0024 (1/s)
$d^{vp} =$ 1.0
$N =$ 1.0
$k_0 =$ 0.05 (MPa)
$k_1 =$ 1.8 (MPa)
$k_2 =$ 135.0

☑ **Hardening-Relaxation Model Parameters**

$\Gamma^{vp,s} =$ 1.0E-3 (1/s)
$S_1 =$ 0.3
$S_2 =$ 1000 (MPa)
$S_3 =$ 2.5

(a) Viscoelastic properties

(b) Viscoplastic properties

Figure C.3 Parameters Associated with the Constitutive Relationships

As illustrated through several figures, PUI is a powerful tool to create analysis models for simulating the performance of pavement structures. PUI can be utilized by users who do not have in-depth experience with the ABAQUS software. It is important to note that all constitutive relationships are integrated in PUI so that the user can take full advantage of the power of PANDA material characterization and constitutive relationships while utilizing the powerful and sophisticated ABAQUS FE model software.